THE PHANEROZOIC THERMO-TECTONIC EVOLUTION OF NORTHERN MOZAMBIQUE CONSTRAINED BY ^{40}AR/^{39}AR, FISSION TRACK AND (U-TH)/HE ANALYSES

Dissertation zur Erlangung des Doktorgrades der
Naturwissenschaften am Fachbereich Geowissenschaften
der Universität Bremen

Vorgelegt von
Matthias Ch. Daßinnies
Bremen, 2006

Tag des Kolloquiums:	22.12.2006
Gutachter:	Prof. Dr. J. Jacobs
	Prof. Dr. W. Bach
Prüfer:	Prof. Dr. T. Mörz
	Prof. A. Kopf

CONTENTS

ACKNOWLEDGEMENTS

This PhD study was funded by the University of Bremen (FNK) research grant ZF 05/101/01.

Special thanks go to my doctoral advisor Prof. Dr. J. Jacobs for the opportunity to carry out this research, for his supervision, interest and constant support throughout. Furthermore, I would like to thank Prof. Dr. W. Bach for taking on to be the second expert.

I am obliged to Prof. Dr. M. Olesch for providing working facilities as well as access to the fission track laboratory at University of Bremen. Dr. G. Grantham is especially acknowledged for providing sample material for thermochronological analyses. I am indebted to NGU and Dr. B. Thomas for the possibility to join the mapping project and using their logistic setup to accomplish field work in northern Mozambique. Prof. A. Gleadow and Dr. B. Kohn are thanked for their invitation to spend a research period in the (U-Th)/He and fission track laboratories at Melbourne University. I wish to thank Dr. J-A. Wartho for fruitful e-mail discussions on $^{40}Ar/^{39}Ar$ dating.

The technical and administrative support of V. Kolb, B. Schröder, P. Witte and the enthusiastic hints on sample preparation of Mr. Schulz are highly appreciated.

Many thanks go to my current and former colleges Dr. B. Emmel, PD Dr. F. Lisker, Dr. M. Geiger, Dr. E. Guasti, Dr. M. Lorencak, Dr. U. Weber, Dr. B. Ventura, M. Heldt and R.Tjalingii for helpful comments, suggestions and pleasant times at the Universities of Bremen and Melbourne.

Above all, I wish to express my thanks to my wife, my parents, my brothers and my friends, whose steady encouraging support gave motivation and balance to me.

SUMMARY

Results of thermochronometric investigations comprising $^{40}Ar/^{39}Ar$ hornblende and biotite, titanite and apatite fission track (FT) and apatite (U-Th)/He dating on 102 basement rock samples from northern Mozambique record a cooling and denudation history since Early Palaeozoic times. In the north Mozambican sector, these results place new temporal and geometric constraints on the initial rift and subsequent drift configuration during the Gondwana supercontinent dispersal as well as on the post break-up evolution of the sheared margin of central East Africa. Furthermore, they highlight the influence exerted by ductile basement structures of Pan-African age on the loci of tectonically active zone and associated denudation since the Late Palaeozoic.

$^{40}Ar/^{39}Ar$ hornblende and biotite ages range from c. 542 Ma to 456 Ma and c. 448 Ma to 428 Ma, respectively. They record the cooling from the latest Pan-African metamorphic imprint, presumably related to the formation of the Namama Thrust Belt at c. 550-500 Ma, at slow rates of about 11°-7°C/Ma from 525°C to 305°C in Early to Late Ordovician times. Locally, the thermal influences of syn- to post-tectonic granitoid / pegmatite emplacements at about 500-450 Ma delayed cooling. Widespread basement cooling to < 350°C occurred in Late Ordovician to Early Silurian times.

The titanite fission track ages fall into two age groups of c. 378 Ma to 327 Ma and c. 284 Ma to 219 Ma. Very slow cooling since the Late Ordovician/Early Silurian at rates of < 1°C/Ma to below 275 ± 25°C in the Late Devonian/Early Carboniferous is deduced from the older titanite FT ages. It is related to decreasing denudation in response to the establishment of pre-Karoo peneplains within central Gondwana. The younger titanite FT ages record the cooling of a denuding and approximately E-W trending uplifted rift flank whose formation marks the onset of rifting and incipient Gondwana disintegration in the Early to Late Permian. Associated crustal extension proceeded obliquely to a NW-SE tensional stress field by brittle reactivation of easterly trending ductile basement fabrics and presumably, linked to the Zambezi Rift system. Titanite FT results indicate ≤ 9-12 km of crust removal since the Permo-Carboniferous.

Apatite FT ages vary between c. 169 Ma and 61 Ma whereby ages of ≥ 100 Ma record complex, and in part multistage cooling and denudation histories that are generally restricted to zones of crustal weakness along the Mozambique Belt yielding northerly trending ductile fabrics; along the western Axial Granulite Complex and along the present eastern continental margin. Apatite FT data imply that denudation was related to brittle reactivation of ductile basement fabrics by rifting, transtension and/or transpression along southern Tanganyika-Rukwa-Malawi System and along the Davie Fracture Zone at the eastern margin. Modelled time-temperature paths indicate two periods of more rapid cooling (c. 5°-3°C/Ma) to below c. 110°C in the Early to Late Jurassic and Early to Late Cretaceous. The Early/Middle Jurassic rifting, break-up and subsequent seafloor spreading within the Somali and Mozambique basins triggered the Jurassic periods, which were accompanied by the deposition of up to 2.5 km of volcanic rocks and associated reheating along the eastern margin at about 180-160 Ma. Far field stresses linked to global plate reorganizations due to the opening of the Atlantic and Indian oceans are accounted for the Cretaceous cooling periods. The apatite FT results indicate < 6 km and < 7 km of maximum denudation in the Axial Granulite Complex and along the eastern margin since the Jurassic, respectively. Apatite FT ages ≤ 100 Ma from the central part of basement record a uniform cooling and denudation pattern. Modelled time-temperature paths indicate a more rapid cooling step (c. 5°-3°C/Ma) to below c. 110°C in Early to Late Cretaceous times. It is associated with the erosional compensation of a potential local base level gradient between the central southern basement and its bounding N-S trending zones of contemporaneous crustal extension and exhumation to the west and east. These apatite FT results indicate < 4 km of denudation since the Cretaceous. In Palaeogene times, a basement reheating to c. 60°C, presumably due to heat advection by fluids is inferred from time-temperature models of samples located in zones of crustal weakness and is synchronous with the initiation of the East African Rift System at c. 30 Ma.

Apatite (U-Th)/He ages span from 150 Ma to 40 Ma. Results of forward modelled time-temperature paths indicate a widespread slow and protracted cooling associated with persistent slow denudation from c. 80°C in the Late Cretaceous to subaerial conditions (c. 40°C) in Palaeogene/Neogene times. Along the eastern margin and the

Lurio Belt, these modelling results corroborate the occurrence of a reheating event localized to zones of crustal weakness in the Palaeogene.

ZUSAMMENFASSUNG

Die vorliegende Arbeit präsentiert die Ergebnisse thermochronometrischer Untersuchungen, die an 102 Grundgebirgsproben aus Nord-Mosambik durchgeführt wurden. Die dabei verwandten Methoden umfassen $^{40}Ar/^{39}Ar$ Datierungen an Hornblenden und Biotiten, Spaltspurdatierungen an Apatiten und Titaniten sowie Apatit-(U-Th)/He Altersbestimmungen. Die thermochronologischen Daten stellen eine Aufzeichnung der Abkühlungs- und Denundationsgeschichte des Grundgebirges seit dem frühen Paläozoikum dar. Sie liefern für das Gebiet von Nord-Mosambik neue zeitliche und geometrische Erkenntnisse über die initiale Rift- und anschließende Driftentwicklung während des Zerfalls des Gondwana Superkontinents ebenso wie über die Entwicklungsgeschichte des ostafrikanischen Transform-Kontinentalrandes nach dem Gondwana Aufbruch. Weiterhin geben diese Daten neue Erkenntnisse über den Einfluss duktiler, panafrikanischer Strukturtrends auf die Lage und den Verlauf von Zonen spröd-tektonischer Aktivität und die damit assoziierte Denundation seit dem späten Paläozoikum.

Die $^{40}Ar/^{39}Ar$ Datierungen ergaben Alter von ca. 542 bis 456 Ma für Hornblende und von ca. 448 bis 428 Ma für Biotit. Sie sind das Resultat einer langsamen Abkühlung nach der letzten panafrikanischen Metamorphose um ca. 550-500 Ma, wobei sich diese mit Abkühlraten von 11°-7°C/Ma, von 525°C im Unterordovizium auf 305°C im Oberordovizium vollzog. Syn- bis post-tektonische Granitoid- und Pegmatitintrusionen um 500-450 Ma führten zu einer lokalen Aufheizung und verzögerten die Abkühlung des Grundgebirges, so dass eine weitläufige Abkühlung unter 350°C für das Oberordovizium bis beginnendes Silur angenommen werden kann.

Die Titanit-Spaltspuralter weisen zwei Altersgruppen, eine ältere von ca. 378 bis 327 Ma und eine jüngere von ca. 284 bis 219 Ma, auf. Die ältere Population deutet auf eine sehr langsame Abkühlung (< 1°C/Ma) auf Temperaturen von $\leq 275 \pm 25$°C vom Oberordovizium / frühen Silur bis zum späten Devon / frühen Karbon hin. Sie ist assoziiert mit einer verminderten Denudation durch die zunehmende Einebnung Zentral-Gondwanas vor dem Beginn des Karoo-Rifting. Im Gegensatz dazu registrierten

die jüngeren Titanit-Spaltspuralter die durch Denundation verursachte Abkühlung einer annährend E-W verlaufenden Riftflanke. Ihre Heraushebung im Unter-/Oberperm markiert das beginnende intra-kontinentale Rifting zwischen Nord-Mozambique und der Ost-Antarktis während des einsetzenden Zerfalls Gondwanas. Die Extension der Kruste vollzog sich schräg zu einem NW-SE dehnenden Stressfeld und stand vermutlich in Verbindung zum Sambesi Riftsystem. Während der Krustenausdünnung kam es zu einer spröden Reaktivierung von östlich verlaufenden Foliationsflächen im Grundgebirge. Basierend auf den Spaltspuraltern der Titanite wurde eine Denundation von maximal 9-12 km an Krustenmaterial seit dem Permo-Karbon ermittelt.

Die Apatit-Spaltspuralter variieren zwischen ca. 169 und 61 Ma, wobei Alter von ≥ 100 Ma eine komplexe und teilweise mehrstufige Abkühlungs- und Denundations-geschichte anzeigen. Sie treten überwiegend entlang krustaler Schwächzonen, mit nördlich verlaufenden, duktilen Strukturtrends im Mozambique Belt auf. Im Unter-suchungsgebiet sind dies der westliche Axial Granulite Complex und der östliche Kontinentalrand. Weiterhin deuten diese Apatit-Spaltspurdaten darauf hin, dass es bei der Denudation und Exhumierung des Grundgebirges entlang des südlichen Tanganyika-Rukwa-Malawi Systems und entlang der Davie Fracture Zone am östlichen Kontinentalrand zu einer spröden Reaktivierung von N-S streichenden duktilen Strukturtrends während Phasen von Rifting, Transtension und/oder Transpression kam. Die Modellierungen von Zeit-Temperatur-Pfaden ergaben früh bis spät jurassische und früh bis spät kretazische Perioden zügigerer Abkühlung (ca. 5°-3°C/Ma) unter ca. 110°C. Das innerhalb des frühen/mittleren Juras einsetzende und zum Aufbruch des Gondwanas führende Rifting, sowie die sich anschließenden Ozeanisierung und Bildung des Somali und des Mosambik Beckens sind die Ursachen der jurassischen Abkühlungsphasen. Diese wurde von der Ablagerung basaltischer Vulkanite und einer damit verbundenen Aufheizung am östlichen Kontinentalrand um ca. 180-160 Ma begleitet. Weitreichende Stresseinflüsse globaler Plattenreorganisationen während der Öffnungen der Atlantischen und Indischen Ozeane kommen als Auslöser der kretazischen Abkühlungsphasen in Betracht. Für den Axial Granulite Complex und den östlichen Kontinentalrand deuten die Apatit-Spaltspurdaten auf maximale Denundationsbeträge von ≤ 7-6 km seit dem Jura hin. Im zentralen Bereich des

Grundgebirges wurden Apatit-Spaltspuralter von ≤ 100 Ma ermittelt, die ein einheitliches Abkühlungs- und Denudationsmuster aufweisen. Die Modellierungen ihrer Zeit-Temperatur-Pfade ergaben eine Phase zügigerer Abkühlung (ca. 5°-3°C/Ma) unter ca. 110°C für die frühe bis späte Kreidezeit. Diese Phase resultierte aus einer erosiven Kompensation eines topographischen Gradienten, welcher zwischen dem zentralen Teil des Grundgebirges und denen im Westen und Osten angrenzenden, N-S verlaufenden Zonen zeitgleicher Krustendehnung und Exhumierung bestand. Für den zentralen Bereich des Grundgebirges wurde, basierend auf den Apatit-Spaltspurergebnissen, ein Denudationsbetrag von < 4 km seit der Kreide ermittelt. Eine Temperierung des Grundgebirges im Paläogen auf ca. 60°C lässt sich aus den Zeit-Temperatur-Pfaden von Proben aus krustalen Schwächezonen ableiten. Diese ist vermutlich auf Wärme-advektion durch die Zirkulation von heißen Fluiden zurückzuführen und fällt zeitlich mit der einsetzenden Bildung des Ostafrikanischen Grabens um ca. 30 Ma zusammen.

Die Apatit-(U-Th)/He-Analysen erbrachten Alter von ca. 150 bis 40 Ma. Vorwärts modellierte Zeit-Temperatur-Pfade dieser Alter lassen auf eine sehr langsame, lang andauernde Abkühlung, ausgelöst durch beständig langsame Denundation, von ca. 80°C in der späten Kreide auf subaerische Temperaturen von ≤ 40°C im Paläogen / Neogen schließen. Entlang des östlichen Kontinentalrandes und des Lurio Belts stützen die modellierten Zeit-Temperatur-Pfade eine lokalisierte Temperierung des Grundgebirges innerhalb krustaler Schwächezonen im Paläogen.

Chapter 1

INTRODUCTION

1.1 Scope of the thesis

Since the advent of the concept of plate tectonics it has been become clear to geoscientists, that the consolidation and the decay of supercontinents, gigantic unifications of vast parts of continental crust, have been associated with major geodynamic processes that shaped the appearance of our planet through time. The present day plate configuration directly succeeded the disintegration of the Gondwana supercontinent in Late Palaeozoic to Mesozoic times.

Gondwana's initial disassembly was prominently favoured along the Mozambique Belt, a mobile belt that is now exposed over large parts of eastern Africa. The Mozambique Belt constitutes the orogenic root of an integral part of the formerly c. 8000 km N-S extending intra-Gondwanian East African-Antartic Orogen. This Himalayan-type orogen emerged from suturing proto E- and W-Gondwana fragments in Late Neoproterozoic/Early Cambrian times. Hence in the geological history of the Gondwana supercontinent, the crystalline basement of the East African continental margin played a dual role of contrasting tectonic nature. It has been the welding seam during its assembly and the locus of failure during its decay.

Northern Mozambique has been a site of such a dual evolution. Subsequent to the Gondwana formation, it was located in the centre of the supercontinent. Today, its basement exposes amphibolite to granulite facies high-grade metamorphic rocks of the southern Mozambique Belt. Their present marginal position in central East Africa clearly denotes the north Mozambican basement rocks as a prominent locus of crustal extension, rifting and drifting during Gondwana's dispersal in the Late Palaeozoic to Mesozoic.

Very little is known, however, about the earliest rift and subsequent drift evolution in the north Mozambican sector. The latest metamorphic imprint on the basement dates in the Late Neoproterozoic/Early Cambrian between c. 615-510 Ma. Sedimentary rocks of Palaeozoic to Mesozoic age are entirely absent on the north Mozambican basement and preclude inferences on the initial Gondwana rifting. Intracontinental rift basins, located adjacent to the west of crystalline basement, preserved continental deposits of Palaeozoic age. Whereas the fringing rift basins at the eastern continental margin solely permit access to mainly marine strata that record the passive continental margin evolution since the middle Mesozoic. These sedimentary basins, however, comprise discontinuous and very contrasting sedimentary records. They do not provide tight constraints on the timing and course of the initial rifting in the vicinity of northern Mozambique and, this therefore remains enigmatic.

Ductile basement fabrics, a heritage of the Gondwana amalgamation, display a broad parallelism with the present day outline of the north Mozambican coast that emerged from the rift and drift evolution. This could indicate an influence of the basement's ductile structural discontinuities on the geometric setting of the initial rifting. Unfortunately, the intensive degree of weathering on the basement likely obscures rift related tectonic features and strongly hinders structural analyses to unravel the initial rift setting.

Madagascar's southward passage along the East African margin in the Mesozoic indicates that the separation of E- and W-Gondwana did not simply proceed by pure orthogonal rifting. It strongly argues for a rather complex rift and drift setting involving transform related tectonics during the margin development in the north Mozambican sector.

The outlined geological setting suggests that the basement of the north Mozambican rift shoulder is a suited candidate to investigate the timing and the geometric configuration of initial rift and subsequent drift evolution of the Gondwana supercontinent within its central segment. Due to the failure of traditional methods, thermochronology provides at present the only tool to measure the timing and the rates at which rocks approach the surface and cool as a result of exhumation. These constraints can be used to derive

inferences on the thermo-tectonic and denudation history of the rift shoulder and thereby permit the investigation of the initial rift and subsequent drift evolution during Gondwana's disassembly.

1.2 Research objectives and methods

This study aims to reconstruct the thermal evolution of the north Mozambican basement since its latest metamorphic imprint at c. 615-510 Ma. This knowledge is achieved by conducting thermochronometric investigations combining $^{40}Ar/^{39}Ar$ hornblende and biotite, titanite and apatite fission track and apatite (U-Th)/He dating methods on basement rocks, which were sampled along a c. 250 km wide E-W traverse across northern Mozambique. These relatively well-understood systems have closure temperatures ranging from c. 550° to 60°C, making them sensitive to exhumation through crustal depths of a few tens to one kilometre. They permit the reconstruction of cooling histories, and furthermore, the discrimination between continuous and stepwise cooling phases.

The $^{40}Ar/^{39}Ar$ hornblende and $^{40}Ar/^{39}Ar$ biotite methods record the cooling to below c. 550°-450°C and c. 350°-300°C, respectively, and are employed to trace the basement's cooling paths subsequent to the latest metamorphism in the late Neoproterzoic/Early Cambrian. In addition, they provide a time-temperature anchor point for the low temperature fission track and (U-Th)/He analyses. The titanite and apatite fission track thermochronometers are sensitive to record cooling over a temperature range of 310°-265° ± 10°C and 110°-60° ± 10°C, respectively, probably linked to tectonic processes of brittle deformation taking place in the upper continental crust (c. 15-2 km). Numerical thermal history modelling of the apatite fission track data is used to resolve the cooling history of basement in more detail. Apatite (U-Th)He dating records the cooling between c. 80°C and 40°C and could reflect tectonic processes within less than 3 km depths. The apatite (U-Th)/He thermochronometer is complementary to the apatite fission track analysis. It aids to more tightly constrain the cooling to below c. 60°C and permits a more detailed modelling of *t-T* paths ranging from c. 110°C to 40°C. The obtained cooling paths are used to derive inferences on the thermo-tectonic evolution of the basement. They thereby aid to constrain the timing of

thermo-tectonic events such as e.g. the earliest rifting and to estimate the associated amounts of denudation. By evaluating spatial cooling patterns it is aimed to derive information on the geometry of initial rift setting.

A corresponding regional titanite and apatite fission track study by Emmel et al., (2004, 2006a, b, c) quantified the cooling and denudation history of an exposed rift shoulder in southern central Madagascar. A comparison of the denudation histories of the rift shoulders of north Mozambican and southern Madagascar, potentially infers information on symmetric or asymmetric rift processes within this sector of the initial Gondwana rifting.

1.3 Outline of thesis

The following second chapter provides an introduction into the applied thermo-chronological methods, their relevance regarding geological problems and a presentation of the analytical procedures involved. Chapter three comprises the results of the $^{40}Ar/^{39}Ar$ hornblende, $^{40}Ar/^{39}Ar$ biotite and titanite fission track investigations and is currently submitted as:

Daszinnies, M.C., Jacobs, J., Wartho, J-A. and Grantham, G.H, 2006. Post Pan-African thermo-tectonic evolution of the north Mozambican basement and its implication for the Gondwana rifting. Inferences from $^{40}Ar/^{39}Ar$ hornblende, biotite and titanite fission track dating. *Geological Society Special Publications.*

This paper outlines inferences on the basement's cooling paths since the latest metamorphism and on a thermo-tectonic record of the earliest rifting event in Permian times. This chapter also contains the geological setting of the north Mozambican rift shoulder. In the fourth chapter, an overview of the tectonic events of global and subcontinental scale is given that are important to the rift and drift evolution of central East Africa since the Mesozoic. A summery of previous fission track studies, relevant to this study, from regions in central Africa and East Antarctica is presented in chapter five. The sixth and seventh chapter comprise the presentation and interpretation of the apatite and (U-Th)/He analyses, respectively. Their discussion and significance to the thermo-tectonic evolution of the north Mozambican basement is depicted in chapter

eight. Chapter nine outlines the potential co-evolutionary relations and inferences on the modes of crustal extension between the two rift shoulders of northern Mozambique and south central Madagascar. The key aspects and results of this thesis are summarized in the last chapter.

Chapter 2

THERMOCHRONOLOGICAL METHODS AND ANALYTICS

2.1 $^{40}Ar/^{39}Ar$ dating method

The $^{40}Ar/^{39}Ar$ dating method is a derivate of the K/Ar isotope dating and was first proposed by Merrihue and Turner (1966). A comprehensive review of the theory and method of the $^{40}Ar/^{39}Ar$ geochronology is given by McDougall and Harrison (1999).

Of the three naturally occurring potassium isotopes ^{39}K (93.2581 %), ^{40}K (0.01167%) and ^{41}K (6.7302 %), ^{40}K is radioactive. It decays into ^{40}Ca (89.52 %) and ^{40}Ar (10.48 %) by different decay processes as illustrated in Fig. 2.1. ^{40}Ar represents radiogenic argon formed by ^{40}K decay in a mineral, and hence, an age can be calculated by using the general isotopic age equation and the quantitatively determined $^{40}Ar/^{40}K$ ratio.

For $^{40}Ar/^{39}Ar$ dating the determination of ^{40}K is based on two facts. First, the $^{39}K/^{40}K$ ratio is a natural constant and second ^{39}K if irradiated with fast neutrons can be converted into relatively stable ^{39}Ar (half-life of 269 ± 3 a, Stoenner et al., 1965) by capturing a neutron and emitting an electron. The advantage is that both argon isotopes can be measured simultaneously by argon gas extraction comprising a mixture of all argon isotopes. Compared to K/Ar dating, the $^{40}Ar/^{39}Ar$ method permits the coeval determination of the parent and daughter isotope concentrations on the same mineral specimen.

Generally, $^{40}Ar/^{39}Ar$ analysis is carried out by the incremental step heating technique, permitting argon isotope measurements during subsequent steps of incremental heating up to the mineral melting point or until all argon is released from the sample. After holding the sample at each particular temperature step, the degassed fraction of argon is admitted to a mass spectrometer and the relative abundances of the argon isotopes are determined. This provides the argon data necessary for the age calculation.

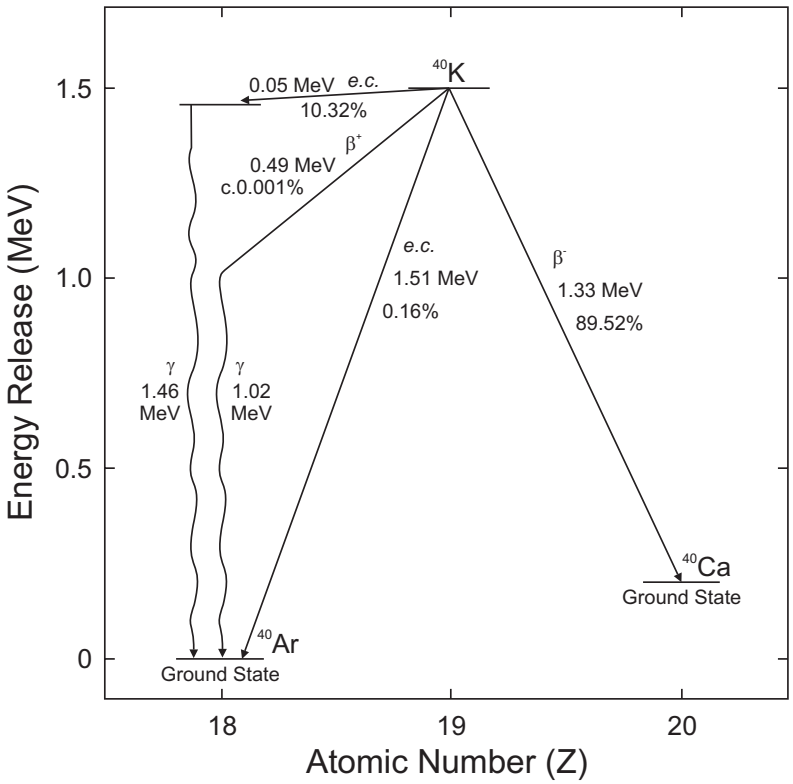

Figure 2.1: Illustration depicts the decay scheme of ^{40}K to ^{40}Ar and ^{40}Ca from McDougall and Harrison (1999); e.c. denotes electron capture.

2.1.1 Argon isotope measurements and age calculation

The obtained $^{40}Ar/^{39}Ar$ ratios have to be corrected for several interferences before an age can be calculated. Measured levels of mass spectrometer background are corrected for by subtracting them from the actual argon isotope determinations and similarly blanks in the extraction system are corrected for if necessary. A mass discrimination correction factor has to be applied to all measured volumes of argon isotopes if the present air $^{40}Ar/^{36}Ar$ ratio deviates from 295.5 (Nier, 1950).

Commonly some time elapses between the time of irradiation and actual $^{40}Ar/^{39}Ar$ analysis, therefore ^{37}Ar needs to be decay corrected back to the date of irradiation, due to its short half-life of 35.1±0.1 days (Stoenner et al., 1965). As the atmospheric ratio is assumed to be $^{40}Ar/^{36}Ar = 295.5$ (Nier, 1950), the amount of $^{40}Ar^*$ is obtained by:

(1) $$\frac{^{40}Ar}{^{39}Ar} = \left(\frac{^{40}Ar}{^{39}Ar}\right)_T - 295.5\left(\frac{^{36}Ar_A}{^{39}Ar}\right)_T$$

where indices denote T = total amount measured and A = all measured is assumed to be atmospheric.

Though the conversion from ^{39}K to ^{39}Ar is the major reaction during the fast neutron irradiation, small amounts of ^{36}Ar, ^{37}Ar and ^{39}Ar are produced from Ca and ^{40}Ar from K. Such interfering reactions have to be accounted for by applying corrections for the argon isotopes. Including equation (1) these corrections lead to a ^{40}Ar/^{39}Ar ratio calculated by:

(2)

$$\frac{^{40}Ar}{^{39}Ar_K} = \frac{\left(^{40}Ar/^{39}Ar\right)_T - 295.5\left(^{36}Ar/^{39}Ar\right)_T + 295.5\left(^{36}Ar/^{37}Ar\right)_{Ca}\left(^{37}Ar_{Ca}/^{39}Ar_T\right)}{1-\left(^{39}Ar/^{37}Ar\right)_{Ca}\left(^{37}Ar_{Ca}/^{39}Ar_T\right)} - \left(\frac{^{40}Ar}{^{39}Ar}\right)_K$$

where indices denote K = neutron induced on potassium and Ca = neutron induced on calcium.

For ^{40}Ar/^{39}Ar dating the standard age equation can be rewritten as:

(3) $$t = \frac{1}{\lambda}\ln\left(1 + J\frac{^{40}Ar}{^{39}Ar}\right)$$

where t = age, λ = decay constant (electron capture) for ^{40}K = 4.962×10^{-10} a^{-1} (Steiger and Jäger, 1977). J is a dimensionless irradiation parameter which is derived from a co-irradiated mineral age standard and incorporates and accounts for uncertainties about and the neutron flux and the neutron capture cross section. The J factor is calculated as:

(4) $$J = \frac{\left(e^{\lambda t} - 1\right)}{^{40}Ar*/^{39}Ar}$$

where λ = the total decay constant for ^{40}K = 5.543 × 10^{-10} a^{-1} (Dickin, 1995) and t = age of the age standard.
Errors for individual ages are calculated by:

(5) $$\sigma_t = \sqrt{\frac{J^2\sigma_F^2 + F^2\sigma_J^2}{\lambda^2\left(1+FJ^2\right)}}$$

where $F = {}^{40}Ar/{}^{39}Ar_K$ and σ = absolute errors related to parameters denoted by indices. The latter are generally given as standard deviations (McDougall and Harrison, 1999). Errors associated with standard age fluence monitor and the determination of the decay constants are neglected by this calculation.

2.1.2 Theoretical considerations and definitions

The release of argon isotopes by heating is generally dependant on the temperature, the duration of heating, the chemistry and the shape of the mineral specimen, which is being analysed.

In an ideal case, a mineral sample cools very rapidly and undisturbed after its crystallization. During degassing, each incremental heating step would release similar $^{40}Ar/^{39}Ar$ ratios, i.e. the sample will yield a horizontally flat, plateau-like age spectrum (Dalrymple and Lanphere, 1974) and the $^{40}Ar/^{39}Ar$ age would reflect the timing of a crystallization, e.g. igneous event (McDougall and Harrison, 1999). Many geological samples are subjected to metamorphic events or to slow cooling after their crystallization, i.e. to processes which exert an influence on the argon retention in the crystal or different parts of the crystal. At low temperatures, weakly bound argon isotopes are liberated from less retentive sites whereas at higher temperatures stronger bound argon is measured.

Age spectra (e.g. Fig. 3.3) are box plots of the apparent age versus the cumulative % of $^{39}Ar_K$ released during the step-heating experiment. The width of the box on the X-axis indicates the % of $^{39}Ar_K$ that each heating step contributed, and the width of the box on the Y-axis indicates the analytical error of the age for each individual step. As it is

standard practice, the age spectra were plotted using the step-heating ages with analytical errors only. Within an age spectrum, an age plateau is defined as:

a) Having three or more continuous steps comprising more than 50 % of the ^{39}Ar (Lanphere and Dalrymple, 1978);

b) The probability of fit of the weighted mean age of the steps is greater than 5 %;

c) The slope of the error weighted line through the plateau ages is not different from zero at 5 % confidence, i.e. steps are concordant within 2 σ;

d) The ages of the outermost two steps for either side of the plateau must not be significantly different at 1.8 σ confidence intervals than the weighted mean plateau age (six or more steps only);

e) The outermost two steps for either side of the plateau must not have non zero slopes at 1.8 σ confidence intervals with the same sign if nine or more steps are incorporated (Ludwig, 2001).

A pseudo-plateau age is defined as a plateau age but only contains 40-49.9 % of the cumulative % ^{39}Ar, which is marginally below the > 50 % cumulative ^{39}Ar threshold that defines a plateau age. If neither plateau nor pseudo-plateau ages were obtained weighted mean ages are quoted. The total fusion age is a cumulative age of all individual $^{40}Ar/^{39}Ar$ step releases and it is comparable to the conventional K/Ar age (Dalrymple and Lanphere, 1974).

An age spectra is considered discordant if the age of any gas fraction containing more than 3 % of the total ^{39}Ar is not part of the plateau and hence differs by more than ± 2 σ (Fleck et al., 1977). Concordant age spectra are characteristic for undisturbed samples which remain stable during in vacuo step heating.

Excess radiogenic $^{40}Ar^*$ is defined as the incorporation of ^{40}Ar into samples by other processes than by *in situ* radioactive decay of ^{40}K (Damon, 1968). It is often explained by the release $^{40}Ar^*$ from fluid inclusions with low partition coefficients between minerals and hydrous fluids (Kelley, 2002). Numerical modelling approaches have recently questioned the assumption that rocks are "infinite" argon reservoirs. Excess radiogenic $^{40}Ar^*$ in the mineral specimen analysed can be derived from internal build up

above the particular isotopic system's closure temperature and depends on the transmissive timescale τ_T (a bulk system property accounting for bulk effective Argon diffusivity and system geometry) and total local sink capacity (TLSC) of a rock (Baxter, 2003). Quartz in particular, is regarded as a key sink mineral to preserve excess radiogenic $^{40}Ar^*$ in enabling a high TLSC and preventing internal build up in rocks and hence in the analysed minerals specimen (Baxter, 2003; Baxter et al., 2002).

During irradiation ^{39}Ar is produced from inferring reactions of ^{42}Ca and ^{39}K within the mineral sample. ^{37}Ar entirely results from the conversion of ^{40}Ca and as the $^{42}Ca/^{40}Ca$ ratio is constant in nature, measurements of ^{37}Ar concentration permit the determination of the amount of ^{39}Ar produced from the reaction of ^{42}Ca. Additionally ^{36}Ar is produced from decay of ^{40}Ca and can influence the atmospheric correction. Therefore the $^{37}Ar_{Ca}/^{39}Ar_K$ ratio is important in $^{40}Ar/^{39}Ar$ dating and measured during step heating experiments in order to evaluate possible chemically mixed phases that may relate to alteration, contamination or exsolution (Harrison and Fitz Gerald, 1986). $^{37}Ar_{Ca}/^{39}Ar_K$ results are presented as box plots (e.g. Fig. 3.3, chapter 3) where the fraction $^{37}Ar_{Ca}$ is plotted versus the cumulative % of $^{39}Ar_K$ released during the step-heating experiment. The width of the box on the X-axis indicates the % of $^{39}Ar_K$ that each heating step contributed, and the width of the box on the Y-axis indicates the analytical error of the $^{37}Ar_{Ca}$ gas fraction for each individual step.

Inverse isochron diagrams are useful in recognizing the incorporation of atmospheric and excess ^{40}Ar in a mineral, which might not be revealed by age spectra plots. Inverse isochron diagrams contribute to a better $^{40}Ar/^{39}Ar$ age interpretation. A comprehensive review on the construction and interpretation of inverse isochron diagrams is given by Kuiper (2002). $^{40}Ar/^{39}Ar$ inverse isochron ages are calculated by fitting a negative slope line through the data points plotted on a $^{36}Ar/^{40}Ar$ versus $^{39}Ar/^{40}Ar$ inverse isochron diagram, using York's algorithm (York, 1969) and assuming an initial "atmospheric" $^{40}Ar/^{39}Ar$ ratio of 295.5. This technique yields errors that reflect not only the analytical errors of the analysis, but also the geological scatter caused by heterogeneity within the sample. Therefore, heterogeneous samples yield scattered data, often with high atmospheric argon contents, a high MSWD (Mean Square of Weighted Deviates), and high errors on the final ages. Most samples produce inverse isochron ages that reflect

simple mixtures of radiogenic and atmospheric components, although some samples can exhibit excess argon, reflected by a $^{40}Ar/^{36}Ar$ intercept value of greater than 295.5 (the $^{40}Ar/^{36}Ar$ ratio of the terrestrial atmosphere). The York (1969) algorithm assumes that the assigned errors are the only reason for the data points scatter from a straight line.

Some hydrous phases, such as hornblende and biotite tend to break down during in vacuo heating and produce flat age spectra, regardless of the spatial argon distribution with the mineral specimen (Gaber et al., 1988).

From studies of Lee et al. (1991) and Wartho et al. (1991), it is evident that hornblende heated in vacuo is unstable and that bulk argon release from hornblende correlates with temperatures of its structural decomposition. Argon release from hornblende by in vacuo step heating is not a solid-state volume diffusion process (Lee, 1993). At temperatures below c. 700°-800°C argon is released from hornblendes by multipath diffusion (Lee, 1993; Lee et al., 1991), a combined interaction of solid-state volume and "short circuit" (SC) diffusion. SC diffusion is the dominating and much faster mass transfer process. Here, extended defects (such as vacancies, dislocations, micropores etc.) serve as preferential highly diffusive pathways for migrating argon isotopes (Lee, 1995; Lo et al., 2000). At temperatures higher than c. 800°C argon release from pristine hornblende in vacuo is a complex process, correlated with the structural decomposition of the crystal lattice and is considered to be a function of the total iron/magnesium ratio, i.e. the argon retentivity of hornblende scales inversely with the total iron content (Lee, 1993). As argon is released through crystal lattice destabilisation and age gradients present in the crystal lattice are homogenized. Significant age spectra disturbances are, therefore, likely to result from degassing of impurities or experimental artefacts (Lee, 1993).

Recent studies have shown that in lower temperature regimes ($T < 600$°C) argon is released from biotite by multipath and dominantly SC diffusion. Thereby argon diffusivities and release patterns appear to be related to the biotite composition, i.e. that Fe-rich biotite yields higher diffusivities and degasses at lower temperatures than Mg-rich biotite (Lo et al., 2000). At temperatures above 600°C argon release from pristine biotite is strongly correlated with a crystal lattice decomposition-transformation process

(Di Vincenzo et al., 2003; Lo et al., 2000). Similar to hornblende argon release from biotite by in vacuo step heating is not a solid-state volume diffusion process and disturbed age spectra are likely to result from degassing of impurities or experimental artefacts. In chloritised biotites humped shaped age spectra have been observed and are attributed to $^{39}Ar_K$ redistribution by recoil during neutron irradiation and differential argon liberation from chlorite and biotite during in vacuo heating (Di Vincenzo et al., 2003). The effects of $^{39}Ar_K$ recoil are particularly significant in fine-grained material of less than 100 μm in diameter (McDougall and Harrison, 1999). It has been suggested that $^{39}Ar_K$ might be implanted by recoil into SC pathways during neutron irradiation (e.g. Lo, 2000).

Therefore, plateau ages of hornblende and biotite can not be unambiguously regarded as to reflect the time at which the mineral passes through its closure temperature (Lee, 1993; Lo et al., 2000).

Complex multipath (incl. SC diffusion) models are more capable of describing argon diffusion within hornblende and biotite than solid-state diffusion models. Unfortunately, they require diffusion parameters which due to the instability of the hydrous phases during in vacuo incremental heating experiments are either only crudely (e.g. Lo et al., 2000) or unlikely to be constrained (e.g. Lee, 1993) by $^{40}Ar/^{39}Ar$ analysis. Single domain, intra-crystalline, solid-state volume diffusion is the simplest model explaining argon transport in silicates like hornblende and biotite (Grove and Harrison, 1996; Harrison, 1981). It possesses, however, predictive values required for thermochronology and permits, by employing experimentally determined Arrhenius diffusion parameters the calculation of a bulk closure temperature (Dodson, 1973).

According to Dodson (1973), the diffusional closure temperature (T_c) of a mineral is calculated iteratively by:

$$T_c = \frac{E_a / R}{\ln\left(\frac{ART_c^{\,2}\left(D_0 a^2\right)}{E_a\left(dT/dt\right)}\right)} \tag{6}$$

where E_a = activation energy, R = gas constant, A = geometric parameter, a = effective diffusion radius, D_0 = frequency factor (diffusivity at infinite time) and dT/dt = cooling rate.

2.1.3 Analytical procedures

From forty-five rock samples thin section were prepared for petrographic inspection. Eight samples were finally selected for $^{40}Ar/^{39}Ar$ analysis. Their main constituents and the minerals intergrown/included in the hornblende and biotite specimen are listed in Tab. 2.1. All these samples display medium to coarse grained equi-granular textures and, excepting samples RMZ 45 and RMZ 13, weak to well developed planar fabrics, i.e. foliations. From optical thin section inspection (10-100x magnification) all samples reveal fresh, unaltered, euhedral to subhedral crystals of hornblende (BZ 216, GZ 90, PZ 37, RMZ 11, RMZ 13 and RMZ 45) and biotite (GZ 39, RMZ 11, RMZ 13) with grain sizes up to 1.5 mm and 1.2 mm, respectively. Except for RMZ 45 all samples yield minor amounts of hornblende (< 2-5 %) and biotite (< 3 %) exhibiting intergrowth with other mineral phases.

Table 2.1: Petrographic characteristics of the samples subjected to $^{40}Ar/^{39}Ar$ analysis

Sample No	Assamblage[a]	Rock type	Analysed minerals[b]
BZ 216	*hbl-plag-bio-(tit-opk-ap-ser)*	amphibolite	hbl *(opk-tit)*
GZ 90	*hbl-gt-plag-qtz-(bt-tit-opk)*	amphibolite	hbl *(opk-tit-ap)*
PZ 37	*hbl-plag-opx-qtz-(bt-ap-opk)*	amphibolite (charnockitic)	hbl *(opk-ap)*
RMZ 11	*K-fsp-plag-qtz-hbl-(bio-ser-ap-tit-carb-opk)*	monzonite	hbl *(opk)*
RMZ 45	*plag-K-fsp-qtz-hbl-(bio-car-opk)*	gneiss	hbl
RMZ 13	*qtz-plag-K-fsp-hbl-bio-(tit-ap-zir-opk)*	orthogneiss	hbl *(opk-tit)* bio *(zir-opk-tit-ap)*
GZ 39	*gt-hbl-plag-qtz-bio-op-(ep-ap-tit)*	amphibolitic gneiss	bio *(opk-ap)*
RMZ 18	*qtz-plag-K-fsp-bio-(ap-opk-zir)*	gneiss	bio *(opk-zir-ap)*

[a] accessories and [b] inclusions are given in parentheses. The abbreviations used for mineral specimen: *ap* – apatite, *bio* – biotite, *carb* – carbonates, *chl* – chlorite, *ep* – epidot, *gt* – garnet, *hbl* – hornblende, *K-fsp* – alkali-feldspar, *opk* – opake phases, *opx* – orthopyroxene, *plag* – plagioclase, *qtz* – quartz, *ser* – sericite, *tit* – titanite and *zir* – zircon.

Hornblende and biotite grains were extracted from the rock samples by crushing, sieving, magnetic separation and hand picking, then cleaned in methanol and then followed by deionised water in an ultrasonic bath. The largest grains of c. 0.3 mm were

selected from the sieving fraction of 150-315 μm. The mineral separates were wrapped individually in aluminium foil packets, and all the samples were loaded into an aluminium irradiation package. A biotite age standard Tinto B with the K-Ar age of 409.24 ± 0.71 Ma (Rex and Guise, 1995) was loaded at 5 mm intervals along the package to monitor the neutron flux gradient. The package was Cd-shielded and irradiated in the 5C position of the McMaster University Nuclear Reactor, Hamilton, Canada, for 90 h. Upon return, the samples were loaded into an ultra-high vacuum laser chamber with a Kovar viewport and baked to 120°C overnight to remove adsorbed atmospheric argon from the samples and chamber walls. A 110 W Spectron Laser Systems continuous-wave neodymium-yttrium-aluminium-garnet (CW-Nd-YAG) (λ = 1064 nm) infra-red laser, fitted with a TEM00 aperture, was used to slowly laser step-heat the mineral samples. The laser was fired through a Merchantek computer-controlled X-Y-Z sample chamber stage and microscope system, fitted with a high-resolution CCD camera, 6x computer controlled zoom, high magnification objective lens, and two light sources for sample illumination. The gases released by laser heating were 'gettered' using 3 SAES AP10 getter pumps to remove all active gases (CO_2, H_2O, H_2, N_2, O_2, CH_4, etc.). The remaining noble gases were equilibrated into a high sensitivity mass spectrometer (MAP 215-50), operated at a resolution of 570, and fitted with a Balzers SEV 217 multiplier. The automated extraction and data acquisition system was computer controlled, using a LabView program. The mean 5 minute extraction system blank argon isotope measurements that are obtained during the experiments were 1.18×10^{-12}, 1.32×10^{-14}, 4.65×10^{-15}, 6.70×10^{-14}, and 1.43×10^{-14} cm^3 (standard temperature and pressure) for ^{40}Ar, ^{39}Ar, ^{38}Ar, ^{37}Ar, and ^{36}Ar respectively. The ^{36}Ar, ^{37}Ar, ^{38}Ar, ^{39}Ar and ^{40}Ar isotope analyses were corrected for system blanks, the radioactive decay of ^{37}Ar, a mass discrimination of 295.5/281.0 (1.0516 amu), and minor interference reactions from Ca and K ($^{39}Ar/^{37}Ar_{Ca} = 0.00065$, $^{36}Ar/^{37}Ar_{Ca} = 0.000255$, and $^{40}Ar/^{39}Ar_{K} = 0.0015$).

The errors quoted on the ages in the Tabs. 3.1 and 3.2 are 1 sigma and include the *J* value error, and the $^{40}Ar/^{39}Ar$ ages were calculated using the decay constant of Steiger and Jäger, 1977. The *J* values and errors are noted on the sample $^{40}Ar/^{39}Ar$ data table (Tab. 3.2). The argon isotope data presented in this study were undertaken at the

Western Australian Argon Isotope Facility, operated by a consortium consisting of Curtin University and the University of Western Australia.

The calculation of the $^{40}Ar/^{39}Ar$ ages, and plotting of series of age spectra, inverse isochron diagrams and $^{37}Ar/^{39}Ar$ plots were undertaken using ISOPLOT 2.49 (Ludwig, 2001). In assessing whether all the data fit within the estimated error limits, indices of goodness-of-fit are used, including Mean Squared Weighted Deviates (MSWD) (McIntyre et al., 1966). MSWD values were calculated for weighted mean ages and inverse isochrones with n-1 and n-2 degrees of freedom, respectively. MSWD values ranging between 1 and 2.5 are accepted as a meaningful goodness of fit indicators (Roddick, 1978). Values of > 1 generally indicate either underestimated errors, or the presence of non-analytical scatter. MSWD values of < 1 generally indicate over-estimated analytical errors.

$^{40}Ar/^{39}Ar$ inverse isochron ages are quoted with 95 % confidence errors. Weighted mean ages were calculated using both the analytical and *J* value errors on a series of pseudo-plateau steps, quoted with their 95 % confidence errors. The total fusion age is calculated as an unweighted mean age of all the steps including the analytical and *J* value errors and quoted with its 1 sigma error in the $^{40}Ar/^{39}Ar$ data tables (Tabs. 3.1 and 3.2).

For the calculation of bulk closure temperatures using equation (6) the following parameter values were employed for hornblende (Harrison, 1981): $E_a = 64$ kcal/mol, $D_0 = 0.024$ cm^2/s, $R = 1.9872$ cal/(kgK), $A = 55$ (sphere), $a = 0.015$ cm (diffusion domain is the grain) and for biotite (Grove and Harrison, 1996): $E_a = 47.1$ kcal/mol, $D_0 = 0.075$ cm^2/s, $R = 1.9872$ cal/(kgK), $A = 27$ (cylinder), $a = 0.015$cm. The diffusion parameters of Cooma biotite with an intermediate composition (Mg/Fe ratio) were chosen as no chemistry was determined. Though it should be noted that a slightly higher argon retentivity in Fe-rich biotite is possibly related to a higher F content (Grove and Harrison, 1996). Some uncertainties exist regarding the diffusional radius of biotite. Effective radii of ~ 0.150 mm (Harrison et al., 1985) or of the natural grain size (Hess et al., 1993; Hodges et al., 1994) have been advocated, though it has been cautioned that multiple domains of varying radii may exist in biotite (Grove and Harrison, 1996; McDougall and Harrison, 1999). The natural grain radius has been used in this work.

2.2 Fission track dating method

Over the past years a number of comprehensive reviews of the theory, methods and application of fission track dating have been published, such as Gallagher et al., 1998; Gleadow et al., 2002; Wagner and Van den Haute, 1992.

Fission tracks are nuclear damage trails in solids which result from the spontaneous or induced nuclear fission of naturally abundant radioactive elements, such as uranium and thorium. A widely accepted theory of fission track formation is the "Coulomb explosion" or "ion explosion spike" model (Fleischer et al., 1965b; Fleischer et al., 1975). When for instance a ^{238}U atom in a mineral undergoes spontaneous nuclear fission two lighter, positively charged nuclides of different masses are produced, and fly off in opposite directions at high velocities with an initial energy of around 1 MeV/nucleous (Fig 2.2a). Both daughter particles “strip” electrons off the crystal lattice while leaving behind positively ionized lattice atoms along their track (Fig 2.2b). These positively charged atoms repel each other and thus produce a linear void, the fission track in an otherwise coherent and insulating crystal. Fission tracks accumulate through geological times (Fig 2.2c) and are randomly distributed in three dimensions within the host mineral. Depending on the solid, fission tracks are c. 10-20 μm long with a diameter of c. 50 Å and may be observed by transmission electron microscopy (Price and Walker, 1962a). Due to a higher chemical reactivity, tracks are routinely made optically visible by etching polished internal mineral surfaces and enlarging their size (Price and Walker, 1962b).

The usage of fission reactions for geochronological applications exploits the natural abundance of ^{238}U in certain rock forming minerals. Commonly the minerals apatite, zircon and titanite are employed, with apatite being the most comprehensively investigated specimen.

Spontaneous decay of ^{234}U, ^{235}U and ^{232}Th generally accounts for less than < 1 % of the total spontaneous fission reactions, principally due to lower concentrations and/or fission rates than ^{238}U. Thus, all spontaneous tracks are inferred to result from fission of ^{238}U. By knowing the concentration of ^{238}U, the number of decays and the decay

constant of ^{238}U it is often possible to calculate an age since the onset of fission track accumulation in a mineral.

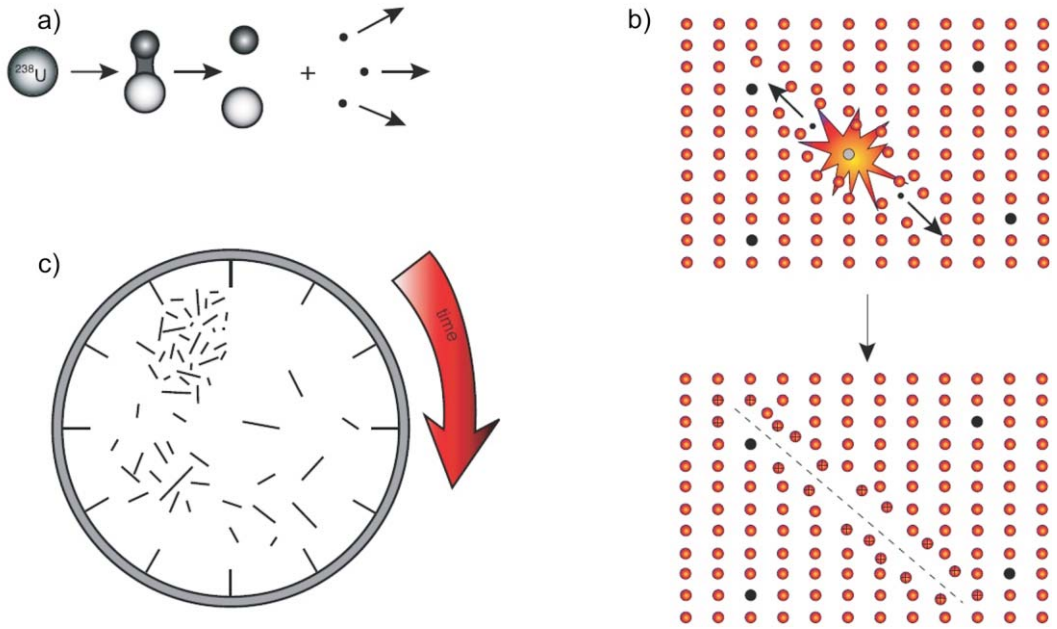

Figure 2.2 Schematic illustration of the concept of fission track formation. The spontaneous decay of ^{238}U (a) generates two each other repelling, positively charged nuclides, which damage the crystal lattice along their flight path and leave behind a fission track (b). These tracks accumulate trough time with the mineral specimen (c).

2.2.1 Fission track age and error calculations

Conventional radiometric dating methods are based on measured ratios of unstable parent to stable daughter isotopes and ages are obtained by derivations of the standard age equation:

$$t = \frac{1}{\lambda} \ln\left(1 + \frac{D}{P}\right) \tag{7}$$

where t = radiometric age, λ = decay constant, D and P are the daughter and parent isotope concentrations, respectively.

In fission track dating the daughter isotope is represented by the spontaneous track density of the ^{238}U decay in a mineral. The concentration of ^{238}U can not be directly

determined without destroying the investigated specimen. As the $^{235}U/\ ^{238}U$ ratio is constant in nature, an induced fission of ^{235}U by thermal neutron irradiation permits the determination of an induced track density, the concentration of the ^{235}U and hence the concentration of the ^{238}U. Thus fission track dating is based on the counting of spontaneous and induced fission track densities and ages are calculated by:

$$t = \frac{1}{\lambda_a} \ln\left[1 + g\left(\frac{\rho_s}{\rho_i}\right)\left(\frac{\lambda_a}{\lambda_f}\right) I\Phi\sigma\right] \tag{8}$$

where t = fission track age, ρ_s = spontaneous track density, ρ_i = induced track density, λ_a = total (alpha and fission) decay constant for $^{238}U = 1.55125 \times 10^{-10}\ a^{-1}$ (Jaffey et al., 1971), λ_f = spontaneous fission decay constant for $^{238}U = 8.46 \times 10^{-17}\ a^{-1}$ (Biagazzi, 1981), $I = ^{235}U/\ ^{238}U$ ratio of 7.2527×10^{-3} (Cowan and Adler, 1976), Φ = thermal neutron fluence (neutrons per cm^2), σ = thermal neutron capture cross section of $^{235}U = 548.25 \times 10^{-24}$ barn (Wagner and Van den Haute, 1992) and g = geometry factor of 0.5 for the external detector method (e.g. Wagner and Van den Haute, 1992).

In order to compensate for uncertainties about the spontaneous fission decay constant λ_f (Biagazzi, 1981) and imprecise determinations of the neutron fluence Φ, a zeta (ζ) calibration factor (Hurford and Green, 1983) is incorporated to:

$$\Phi = B\rho_d \tag{9}$$

where B = a constant calibration factor that relates the neutron fluence Φ to ρ_d = induced track density of an co-irradiated standard dosimeter glass (e.g. IRMM 540, CN5). Substituting equation (9) into equation (8) defines zeta as:

$$\zeta = \frac{B\sigma I}{\lambda_f} \tag{10}$$

Substituting ζ yields an age equation for dating a sample of an unknown age to:

(11) $$t = \frac{1}{\lambda_a} \ln\left[1 + g\left(\frac{\rho_s}{\rho_i}\right)\lambda_a \zeta \rho_d\right]$$

The value of the zeta factor is specific for a particular standard glass and is derived empirically from fission track determinations on age standards by rearranging (11) to:

(12) $$\zeta = \frac{\left(e^{\lambda_a t_{STD}} - 1\right)}{\lambda_a g\left(\rho_s / \rho_i\right)_{STD} \rho_d}$$

where t_{STD} = age of the age standard and $(\rho_s / \rho_i)_{STD}$ = corresponding spontaneous and induced track density ratio. Usually, zeta factors are calculated 3-10 times for each age standard from ideally different irradiations. These factors are than averaged to give an error weighted mean zeta. The zeta factor is unique for each observer, irradiation facility and microscope. A corresponding standard deviation is obtained by:

(13) $$S_\zeta = \zeta \sqrt{\frac{1}{N_s} + \frac{1}{N_i} + \frac{1}{N_d} + \left(\frac{\sigma\left(t_{STD}\right)}{t_{STD}}\right)^2}$$

where σ (t_{STD}) is the age error of the age standard. Commonly employed age standards are Fish Canyon Tuff (27.8 ± 0.2 Ma), Durango (31.4 ± 0.4 Ma), and Mount Dromedary Igneous Complex (98.7 ± 0.6 Ma). Details are given in Hurford (1990a, 1990b and references therein).

With the assumption that fission track statistics of track counting will follow a Poissonian distribution like radioactive decays, no further source of variation is assumed in the measured track densities. According to the "conventional analysis" (Green, 1981) the standard deviation S_t on the fission track age is calculated by:

(14) $$S_t = t \sqrt{\frac{1}{N_s} + \frac{1}{N_i} + \frac{1}{N_d} + \left(\frac{S_\zeta}{\zeta}\right)^2}$$

where N_s, N_i, and N_d are the total number of track counts for the spontaneous, induced and standard glass track densities, respectively. S_ζ = standard deviation of the empirically determined calibration factor ζ.

The usage of the external detector methods (see below) permits the determination of ρ_s/ρ_i ratios for individual crystals (Gleadow, 1981). It is therefore vital to assess whether the obtained range of single grain ages (equation 11) reflect a single or multiple age populations or if even other non poissonian sources of errors are present. Extensive and comprehensive reviews and discussions on fission track statistics are given by Green (1981), Galbraith and Laslett (1993) and references therein. In order to objectively test whether there is real variation in single grain ages beyond that expected from track counting alone Green (1981) suggested the determination of a χ^2 statistic to:

$$\chi^2 = \sum_{j=1}^{n} \frac{\left(N_{sj} - \overline{N}_{sj}\right)^2}{\overline{N}_{sj}} + \sum_{j=1}^{n} \frac{\left(N_{ij} - \overline{N}_{ij}\right)^2}{\overline{N}_{ij}} \tag{15}$$

with

$$\overline{N}_{sj} = \frac{N_s}{N_s + N_i}\left(N_{sj} + N_{ij}\right) \tag{16}$$

$$\overline{N}_{ij} = \frac{N_i}{N_s + N_i}\left(N_{sj} + N_{ij}\right) \tag{17}$$

where N_s, N_i are the total number of counted spontaneous and induced tracks, respectively. N_{sj}, N_{ij} represent the spontaneous and induced track counts in the j^{th}-grain, respectively.

If the χ^2 probability P(χ^2) value is > 5 % with (n-1) degrees of freedom (n = number of crystals counted), a sample age is derived as a *pooled age* calculated after equation 11 with the ρ_s/ρ_i ratio being the sum of track counts from all grains. If the χ^2 test fails [P(χ^2) < 5 %], meaning the Poisson distribution is not the only source of variation, a

mean age, where ρ_s/ρ_i ratio is an arithmetic mean of all individual grain ρ_s/ρ_i ratios represents a better estimation of the samples FT age.

In order to reduce the undue influence of grains with very few track counts a *central age* was introduced (Galbraith and Laslett, 1993). It is a weighted mean of the log normal distribution of single grain ages with an estimated standard deviation, i.e. age dispersion. For sample populations with high P(χ^2) values the pooled, mean and central ages are equal. The central age (t_c) and its associated standard deviation (S_{tc}) are calculated by:

(18) $$t_c = \frac{1}{\lambda_a} \ln\left[1 + g\left(\frac{\eta}{1-\eta}\right)\lambda_a \zeta \rho_d\right]$$

(19) $$S_{tc} = t_c \sqrt{\frac{1}{\eta^2 (1-\eta)^2 \sum_{j=1}^{n} w_j} + \frac{1}{N_d} + \left(\frac{S_\zeta}{\zeta}\right)^2}$$

where η and w are iteratively computed parameters derived from N_{sj} and N_{ij}.
A uranium concentration for each mineral grain U_{grain} is obtained by:

(20) $$U_{grain} = \frac{\rho_d}{\rho_i} U_{STD}$$

with U_{STD} = uranium concentration of a standard dosimeter glass, ρ_d = induced track density over the dosimeter glass and ρ_i = induced track density over the investigated grain.

2.2.2 External Detector Method

The External Detector Method (EDM) is a routinely applied standard procedure for fission track dating. It is usually the preferred dating method as it provides age information for individual grains and yields excellent reproducibility (Miller et al., 1990). The differentiation of intergrain age variability is in particular important for

detrital mineral dating from sedimentary rocks but it is also important for the application to igneous rocks (O'Sullivan and Parrish, 1995).

Fig. 2.3 illustrates the steps involved in the EDM fission track dating. Spontaneous fission tracks (1) are revealed on a polished internal mineral surface (2) by the application of an etchant onto it (3). An external detector, commonly used is mica with a low uranium content, is mounted onto the exposed internal mineral surface (4). During irradiation with thermal neutrons, fission fragments of ^{235}U induce tracks into the mineral grain and the external detector (5). After the irradiation the induced tracks are revealed by etching the external detector only. Thereby the external detector displays an induced fission track image of a corresponding mineral grain (6).

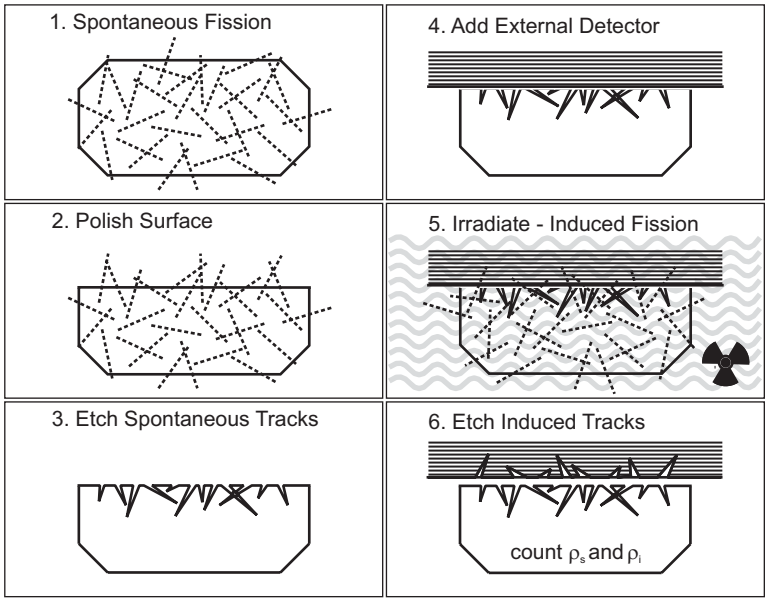

Figure 2.3: Illustration of the principal steps involved in the external detector method (EDM) (Gleadow et al., 2002). Dashed lines indicate unetched fission tracks and triangular spikes represent fission tracks revealed and enlarged by an etchant for optical inspection.

Usually a fission track sample mount comprises 50 to 100 mineral grains, is covered by one external detector mica and yields c. 5-25 grains suited for fission track dating. In order to determine a fission track age, the spontaneous track density (ρ_s) is counted in a suited mineral grain. By finding the corresponding mirror image area on the external detector, the induced track density (ρ_i) is counted over exactly the same area. The area matching is either facilitated by computer-controlled microscope stage systems (e.g.

Dumitru, 1993) or by repositioning the external detector back on the sample mount (Jonckheere et al., 2003).

Individual grain ages are calculated by equation (11) and a sample age is derived as a central age (equation 18). As the geometry of track registration is different for the internal mineral surface (4π) and for the external detector surface (2π) a geometric correction factor (g) is applied to the age calculation (equation 8, 11). This factor has a value of approximately 0.5 but not exactly as it is affected by small variations in the track etching efficiency and the fission track range between the external detector and the mineral grain (Gleadow and Lovering, 1977).

2.2.3 Fission track length and track annealing

Radiation damage caused by nuclides from fission decay is energetically metastable and represents an unstable state of the solid, which fades with time as the originally ordered structure gradually becomes restored. Fission track annealing is a temperature dependant diffusional process that affects the entire track and to which an Arrhenius relationship can be applied (Green et al., 1986; Laslett et al., 1987) (Fig. 2.4):

$$t_r = Ae^{\left(\frac{E}{kT}\right)} \tag{21}$$

where t_r = reaction rate, A = a mineral specific constant, E = activation energy, T = absolute temperature and with k being Boltzmann's constant.

It should be noted that it has been argued to refuse interpretations for both track shortening and reduction of track density by first-order reaction kinetics (Green et al., 1988b). During annealing tracks retain their linear shape but become shorter until the physical damage of the crystal lattice is restored (Fleischer et al., 1965a, b) and when its length is reduced to zero the tracks cease to exist. Temperature, time and chemical composition are the most dominant factors that control fission track annealing though pressure and ionizing radiation may also be important (Fleischer et al., 1965a). Consequently fission tracks will continue to shorten until they cool to lower

temperatures and the final length of each track represents an integrated record of its time-temperature path (Gleadow et al., 2002).

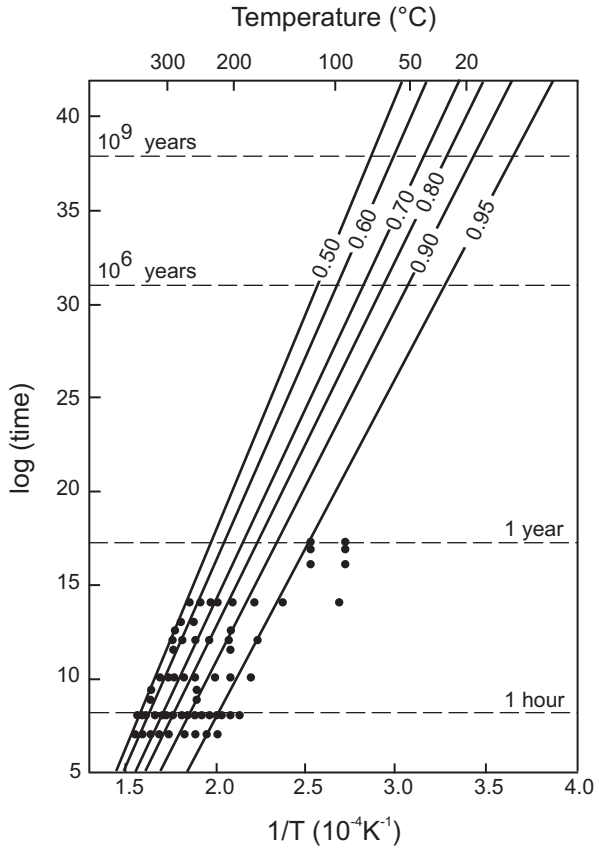

Figure 2.4: Arrhenius plot depicting the extrapolation of experimental annealing data on Durango apatite (Green et al. 1985) from laboratory scale to the geological scale (i.e. months to millions of years). In this illustration the iso-length contours (solid lines, numbers denote ratio between reduced and initial track length) are fitted using the fanning model of Laslett et al. (1987), modified after Gleadow et al., 2002.

The effect of annealing and track reduction has a fundamental influence on fission track age. While the track length diminishes, the probability of short track to intersect the polished internal surface decreases. As a result the track density at surfaces counted will be reduced and so will the obtained fission track age (Green, 1988a; Wagner, 1981). This effect becomes obvious by examination of fission track samples from boreholes where mineral specific fission track ages and track lengths decrease with increasing depth and temperature (Coyle and Wagner, 1998; Gleadow and Duddy, 1981; Naeser and Forbes, 1976). Several laboratory experiments were performed to constrain track

annealing kinetics and to extrapolate them onto geological time scales for different minerals (e.g. Carlson et al., 1999; Laslett et al., 1987; Jonckheere and Wagner, 2000; Yamada et al., 1998). The annealing of fission tracks starts at a mineral specific temperature and increases non-linearly in degree of fading with temperature. For geological timescales (c. 10^7 a) a temperature range can be defined, termed partial annealing zone (PAZ), over which fission tracks are produced and partially annealed. Above the upper high temperature threshold tracks will fade completely whereas below the lower temperature boundary tracks are permanently retained. Consequently, a sample's track length distribution is the net result of track production and track fading over geological times. It is therefore a crucial parameter as its histogram shape, the mean track length (MTL) and the standard deviation (SD) reflect the sample's thermal history (Fig. 2.5) (Gleadow et al., 1986).

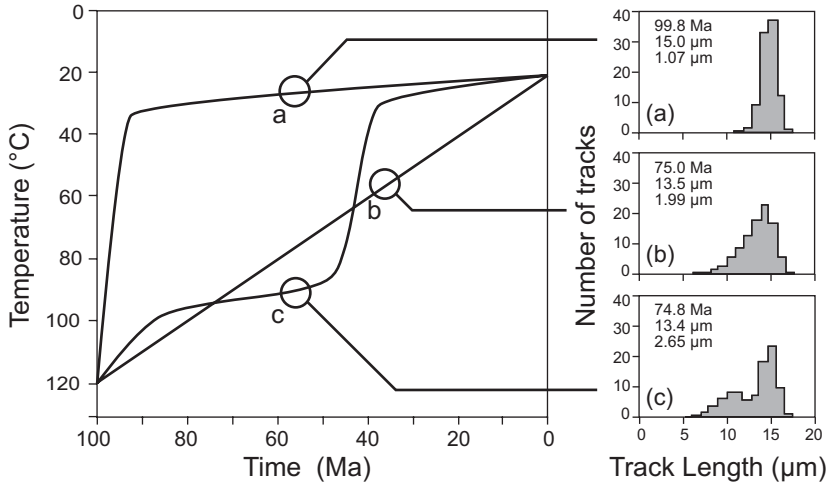

Figure 2.5: Illustration of three different hypothetical cooling histories (a-c) for apatite samples cooling through the temperature interval of 120°-20°C (Gleadow et al., 2002). The resulting length distribution histograms are depicted on the right side. Predicted apatite fission track ages, mean track lengths and associated standard deviations are given by numbers in the histograms from top to bottom, respectively. Example (a) shows a very rapidly cooled sample with an age closely approximating the timing of rapid cooling. Cases (b) and (c) depict a slow monotonous and a two-stage cooling path with broad, negatively skewed unimodal and bimodal track length distributions, respectively.

The apparent fission track age corresponds to time spans over which the sample has resided within the PAZ and at lower temperature regimes. Solely in samples that cooled

more rapid and fairly linear through the PAZ, the fission track age will correspond to the time of a cooling event (Fig. 2.5).

Titanite

The titanite fission track (TFT) thermochronometer is estimated to partially retain fossil fission tracks over a temperature range of 310°-265° ± 10°C (Coyle and Wagner, 1998) and to record cooling to below 275° ± 25°C for cooling rates of 10°C/Ma (Kohn et al., 1993). Extrapolations of experimental titanite annealing results to geological time scales predicted significantly higher temperature ranges (e.g. see compilation of Wagner and Van den Haute, 1992). They were discounted as they were less compatible with geological observations from other radiometric dating systems, in particular Rb/Sr and K/Ar of biotite (e.g. Kohn et al., 1993).

Recent annealing experiments (Jonckheere and Wagner, 2000) indicate that the reduction of track length and density take place in a complex manner with heating time and may be related to coeval annealing of α-recoil-tracks or atomic scale differences in the defect structure along the fission track. Still, the relationship between track length and track density decrease is similar to that in apatite (Jonckheere and Wagner, 2000).

Revelation of fission tracks in titanites by etching is none uniform due to the anisotropic crystal structure of titanite; i.e. tracks are etched differentely in different crystallographic planes and in certain orientations are not revealed at all. As a result the spontaneous track density is underestimated (Gleadow, 1978) and no reliable information on cooling histories can be derived from the track length distributions. The track etching becomes more isotropic with increasing partial metamictisation that entails gradual loss of anisotropy towards a more isotropic, glass-like crystal structure (Gleadow, 1978). Therefore, fission track lengths are not routinely measured in titanite and the interpretation of TFT ages is mainly based on single-grain age distributions and their statistics (Galbraith, 1990).

However, investigations on the influence of radiation damage on the annealing behaviour of titanite age standards Mt. Dromedary and Fish Canyon Tuff indicate isotropic fossil track revelation even below the level of incipient metamictisation. These results suggest that ζ – values obtained from these standards are suitable to date

different titanite samples with fossil track densities of 10^5-10^6 cm^{-2} (Enkelmann et al., 2005).

Apatite

Apatite fission track (AFT) analyses from deep drill holes (e.g. Gleadow et al., 1983; Naeser and Forbes, 1976) and extrapolation of annealing experiments on Durango apatite in geological time scales (Laslett et al., 1987) estimate the apatite PAZ to range between 110°-60° ± 10°C (Fig. 2.6). A simplified model suggests a closure temperature of c. 100°C for the AFT dating system (e.g. Wagner and Van den Haute, 1992).

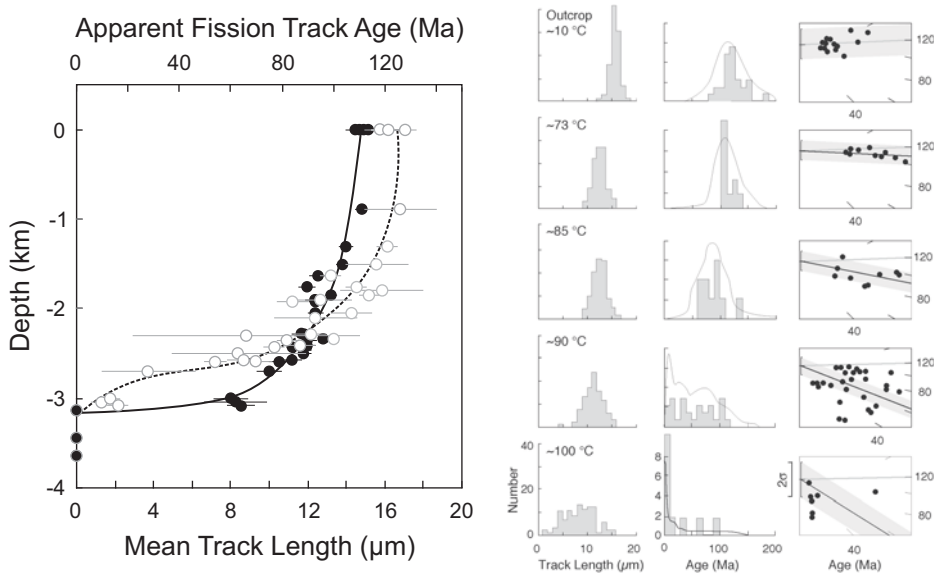

Figure 2.6: Left diagram depicts the observed decrease in apparent apatite fission track ages (open grey circles) and mean track length (black circles) with increasing depth. Apparent is the concave upward form of trend decrease for both, the apparent apatite fission track ages (dashed line) and the mean track lengths (black line). Data are compiled from several wells from the central Otway Basin, south eastern Australia (Gleadow and Duddy, 1981; Green et al., 1989). The illustration to the right displays fission track length distributions, single crystal age histograms and single crystal age radial plots (Galbraith, 1990) of four representative samples from datasets of the Otway Basin wells, illustrated on the left diagram. The stratigraphic age in all samples is c. 120 Ma as shown by the thin gray line on the radial plots. The four samples correspond from top to bottom to increasing temperatures and depths. They clearly depict the progressive increase in annealing as the mean apparent age (black line on the radial plots) and mean track length decrease while the single grain age distribution and the track length distribution progressively broaden. The increase of dispersion in single grain ages and track length distributions is attributed to differences in apatite annealing kinetics by variable chemical composition i.e. Cl/F ratio and annealing anisotropy (Brown et al., 1994; Gallagher et al., 1998; Green et al., 1989). Figures modified after Gleadow et al. (2002).

The chemical composition of apatite may exert an important control on the track annealing rate. In particular influences of the Cl and F proportions have been known for some time (Donelick, 1991; Gleadow and Duddy, 1981; Green et al., 1986; O'Sullivan and Parrish, 1995). While fluorine-rich apatites, such as Durango typically display complete annealing at temperatures of 90°-100°C chlorine-rich apatites are more resistant and totally anneal at temperatures around 110°-150°C (Burtner et al., 1994). Little is known about the influence of other chemical species on the annealing processes such as OH and Mn (Bergmann and Corrigan, 1996; Ravenhurst et al., 1992) or rare earth elements, which are significant trace constituents of apatite (Hughes et al., 1991; Hurford et al., 2000). Besides chlorine, particularly REE appear to exert influences on the annealing behaviour of fluorine-rich apatites and so does in rare cases Sr substituted for Ca (Barbarand et al., 2003b).

Burtner et al. (1994) have related the degree of annealing to composition and to etching characteristics of apatite. Etch figures (etch pits) are the two-dimensional cross-sections of etched tracks intersecting the polished internal crystal surface (Honess, 1927). Their size and geometry are considered to reflect the apatite's solubility and thus the bulk apatite composition. It has been inferred, that for etch figures, whose long axis parallel the crystallographic c-axis (Fig. 2.7a), that their long axis length (termed D_{par}) scales directly with the chlorine concentration and inversely with fluorine content of apatite crystals (Burtner et al., 1994; Donelick, 1993).

Recently, it has been shown that the degree of fission track annealing rather relates to the crystal lattice structure i.e. unit cell parameters, which in turn depends on the bulk chemical composition (Barbarand et al., 2003b). The etch pit size is also clearly related to crystal structure and hence to the bulk chemical composition and therefore, it provides a valuable estimate of the annealing rate of an individual apatite grain (Barbarand et al., 2003b). It is important to note that neither etch pit figures nor single chemical compositional variables, including the chlorine content, are completely reliable and robust predictors for the annealing behaviour. As an example, an increase in OH content can result in a large etch pit figure size without an increase in resistance to annealing (Ketcham et al., 2000).

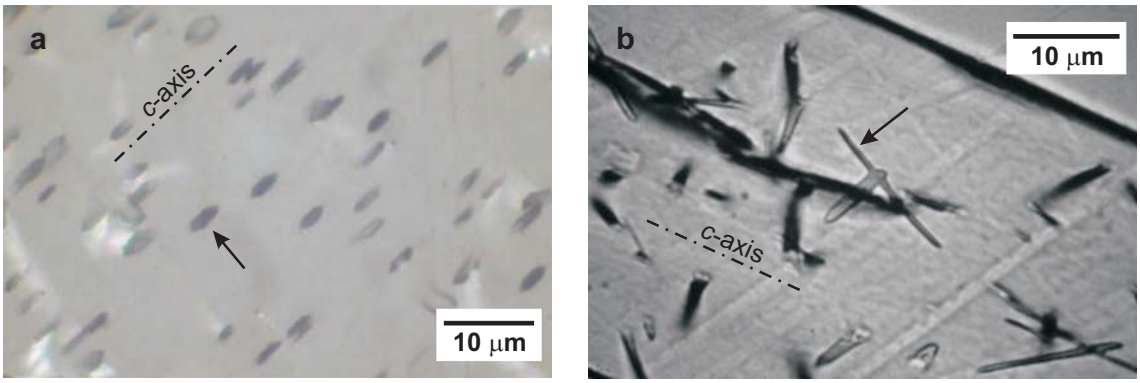

Figure 2.7: a) Hexagonal etch pit (arrow) in apatite. The perfectly aligned long axis of the etch pits parallel the crystallographic *c*-axis of the apatite, indicated by the dashed lines. This alignment provides a reliable assessment of the prismatic surfaces in apatites. b) Transmitted light image of apatite with an etched horizontally confined fission track (arrow).

Another influence on the annealing of randomly orientated fission tracks is given by the anisotropy of the apatite crystal lattice itself (Hughes et al., 1990; Sudarsanan and Young, 1978). Anion columns in the apatite crystal (Hughes et al., 1990) appear to define channels parallel to the crystallographic *c*-axis, and thereby provide preferential pathways for diffusing species (Gleadow et al., 2002). As a consequence fission tracks orientated orthogonally to the *c*-axis anneal more rapidly (Green and Durrani, 1977) whereas tracks orientated parallel to the c-axis appear to be influenced by less favoured diffusion in the lattice and hence anneal more slowly. The track length distribution of an apatite crystal ranges between these two extremes and the annealing anisotropy becomes more obvious as annealing takes place (Wagner and Van den haute, 1992). Polished internal surfaces orientated parallel to the *c*-axis display the entire angular spectrum (Green et al., 1986). Therefore track lengths are measured in planes parallel to *c*-axis and solely horizontally confined tracks (Fig. 2.7b), i.e. tracks that run parallel to and due not intersect with the polished internal surface are chosen (Gleadow et al., 1986). Confined tracks are revealed by etchant percolating through cross-cutting fractures (tincle = track in cleavage) or tracks (tint = track in track), though only the latter are used for track length measurements (Barbarand et al., 2003a). Further comprehensive descriptions on the investigations of crystallographic induced anisotropic annealing, length-bias in track shortening and their effects on fission track ages are given by Green (1988); Donelick et al. (1990, 1999) and Donelick (1991).

2.2.4 Modelling of *t-T* paths from apatite fission track data

Advances in the quantitative descriptions of the annealing behaviour of apatite fission tracks led to the development of numerical models for extracting quantitative information on the thermal history of a rock sample from apatite fission track data. In principle isothermal annealing algorithms are adopted in fission track data modelling. They conventionally describe fanning linear contours of constant annealing on the Arrhenius plots (fanning Arrhenius model, e.g. Fig 2.4) and relate track length reduction r to temperature T (K) and annealing time t (s) in a form like:

$$\frac{\left\{\left[\frac{\left(1-r^{b}\right)}{b}\right]^{a}-1\right\}}{a}=C_0+C_1\frac{\left[\ln(t)+C_2\right]}{\left[1/T-C_3\right]} \tag{22}$$

where $r = l/l_0$ is the ratio of the annealed (l) to unannealed, i.e. initial (l_0) track length and a, b, $C_{0\text{-}3}$ are constants derived by fitting experimental laboratory annealing data of a single type of apatite (Carlson, 1990; Crowley et al., 1991; Laslett and Galbraith, 1996; Laslett et al., 1987). Ketcham et al. (1999) developed an isothermal annealing model in the form:

$$\frac{\left\{\left[\frac{\left(1-r^{b}\right)}{b}\right]^{a}-1\right\}}{a}=C_0+C_1\frac{\left[\ln(t)+C_2\right]}{\left[\ln(1/T)-C_3\right]} \tag{23}$$

which describes fanning curvilinear contours of constant annealing of apatite fission track data sets on the Arrhenius plot; so called “curvilinear model” (Carlson et al., 1999). In contrast to previous annealing models, the track length reduction r is linked to the apatites bulk chemistries inferred from etch pit diameters (D_{par}; see Ketcham et al., 1999) and thus permits the modelling of naturally occurring apatites with a broad range

of chemical compositions and annealing kinetics. Additionally, this model permits the employment of a correction model that accounts for the crystallographic annealing anisotropy (Donelick et al., 1999).

Forward modelling predicts apatite fission track data for a given *t-T* paths. Thereby equations (22) or (23) are used to generate track length distributions from incremental isothermal annealing steps and subsequently a fission track age is derived, which generally is a sample's pooled age (e.g. Ketcham et al., 1999; Green, 1988a). All numerical models of apatite fission track annealing rely on the principle of time equivalence (Duddy et al., 1988). It presumes that a fission track, which has been annealed to a certain degree, will behave during further annealing independent from the previous annealing conditions. Thus, further track reduction solely depends on the preceding degree of annealing and the prevailing *t-T* conditions whereas the order of occurrence of isothermal annealing steps is not important. In principle, forward modelling solely permits inferences on cooling. It fairly precisely constrains the timing of cooling into the AFT PAZ, approximately below 110°C and the palaeo-temperature value prior to the latest cooling step out of the PAZ. The timings of this paleao-temperature and of the cooling out of the PAZ, approximately below 60°C are rather poorly defined.

Inverse model approaches are designed to determine a range of *t-T* paths which are consistent with a given fission track data set and additional geological constraints. Inverse model attempts are not strictly mathematical inversions but rather statistical processes to determine a range of possible thermal histories that may underlie the measured fission track data. Components of inverse models comprise a candidate *t-T* paths generator, a statistical means to evaluate the goodness-of-fit between measured data and predicted data sets from each generated *t-T* path and a searching algorithm for extracting best-fit solutions among various permissible *t-T* paths generated (e.g. Gallagher and Sambridge, 1994, Ketcham et al. 2000). The computer program AFTSolve 1.3.1 (Ketcham et al., 2000), used in this study, permits maximum and minimum cooling rates and fixed time-temperature points as input parameters. In order to test the goodness-of-fit (G.O.F.) of model results, predicted track length distribution and fission track age are tested against measured fission track data individually. They

are then combined into one merit function to evaluate different thermal histories against each other (Ketcham et al., 2000). As a result, a wider 0.05 ("acceptable fit") and a narrower 0.5 ("good fit") probability envelop are created. They define a *t-T* space that comprises all *t-T* paths which are consistent with additional geological constraints and pass the principle baseline statistical criteria. The Monte Carlo method and the Constrained Random Research (CRC) are employed as routines for extracting best-fit *t-T* path solutions.

2.2.5 Analytical procedures

Titanite and apatite separates, (grain sizes of c. ≤ 315 μm) were extracted from rock samples using conventional preparation techniques including crushing, sieving, Wilfley table, heavy liquid and magnetic separation. Figure 2.8 illustrates schematically the mineral separation process.

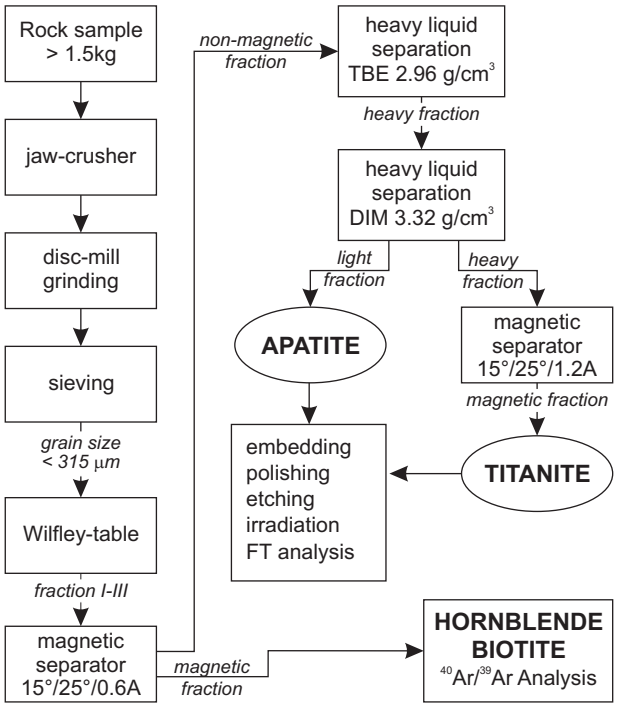

Figure 2.8: Flowchart of mineral separation technique for deriving and concentrating apatite and titanite separates. TBE = 1,1,2,2 tetrabromethane, DIM = di-iodomethane are heavy liquids with specific densities denoted. Values in the magnetic separator boxes indicate used forward slope, side slope and direct current, respectively.

Titanite

Batches of titanite grains were embedded in epoxy resin, then ground and polished with corundum powder (c. 20 and 0.05 μm graining, respectively) to expose internal crystal surfaces. Fission tracks were revealed by etching polished crystal mounts in an acid solution (conc. HF : conc. HNO_3 : conc. HCl : H_2O = 1 : 2 : 3 : 6). Samples were etched individually at room temperature for 17-27 minutes (Naeser and McKee, 1970). Distinctly recognizable terminations of confined tracks were used as an evaluation criterion for sufficient track revelation. Induced tracks were recorded in white micas following the external detector approach (Gleadow, 1981) and revealed after irradiation by exposing the micas for 15 minutes to 40% HF etchant at 21°C.

All the samples were loaded into aluminium capsules and irradiated at the FRM II research reactor facility in Munich-Garching (Germany). Corning dosimeter glasses were used to monitor a neutron fluence gradient. An irradiation time of 60 s was applied to obtain a total thermal neutron (n) fluence of 0.5×10^{16} ncm^{-2}.

Table 2.2: Zeta values for titanite fission track calibration

Age standard	No. of grains	ρ_s (× 10^6cm^{-2}) (N_s)	ρ_i (× 10^6cm^{-2}) (N_i)	ρ_d (× 10^6cm^{-2}) (N_d)	P(χ^2) (%)	ζ - factor ± 1σ
Fish Canyon	18	0.311 (366)	0.770 (906)	1.146 (2049)	66.0	120.8 ± 8.2
Fish Canyon	30	0.336 (780)	0.820 (1902)	1.141 (2049)	99.0	119.5 ± 6.1
Fish Canyon	30	0.337 (829)	0.796 (1955)	1.129 (2049)	33.7	116.8 ± 5.9
Mt. Dromedary	29	0.812 (1588)	0.629 (1230)	1.002 (2049)	8.4	153.8 ± 6.8
Mt. Dromedary	30	1.075 (1623)	0.701 (1058)	1.006 (2049)	13.7	128.9 ± 5.9
Mt. Dromedary	25	0.862 (1593)	0.644 (1189)	1.011 (2049)	71.8	146.9 ± 6.6
Mt. Dromedary	20	0.929 (1287)	0.691 (957)	1.015 (2049)	8.9	145.7 ± 7.1
Mt. Dromedary	30	1.604 (1682)	1.270 (1332)	1.137 (2049)	30.2	138.6 ± 6.0
Mt. Dromedary	30	2.012 (2588)	1.562 (2009)	1.125 (2049)	72.3	137.3 ± 5.2
Mt. Dromedary	13	1.426 (828)	1.161 (674)	1.133 (2049)	1.8	142.9 ± 8.1

All samples were irradiated at the reactor facility FRM II Munich-Garching (Germany) and ζ values were determined for CN2 standard glasses. ρ_d is the standard glass track density, ρ_s and ρ_i represent sample's spontaneous and induced track densities, with the total number of track counts given in parentheses (N_s, N_i, N_d). P (χ^2) represents the probability of the chi-square test

Track densities in mounts and micas were measured using a Zeiss® Axiophot microscope equipped with a drawing tube, a Kintec® stage and a Calcomp® digitizer with the latter two being operated by the FT-Stage software (Dumitru, 1991). Dry objectives, calibrated against stage micrometers, were used for track density counts in

transmitted light at 2000× magnification. Only pristine titanite grains without inclusions and lattice defects e.g. dislocations were used for age dating. TFT central ages were calculated according to zeta calibration method (Galbraith and Laslett, 1993; Hurford, 1990a) using a weighted mean zeta factor of $\zeta = 134 \pm 2$. Individual zeta values and counting statistics of age standards are provided in Tab. 2.2. TFT age errors are quoted at the 1σ confidence level throughout this study and were derived according to the conventional method (Green, 1981). Due to the high yield of titanite crystals, granite sample YG3 was selected for internal cross validation. The separate was split in two and analysed independently.

Apatite

Apatite grains were embedded in epoxy resin, then ground and polished with corundum powder (20 μm and 0.05 μm graining) to expose internals crystal surfaces. The fission tracks were revealed by etching polished crystal mounts with 5 M HNO_3 for 20 s at 21°C. Induced tracks were recorded in white micas following the external detector approach (Gleadow, 1981) and revealed after irradiation by exposing the micas for 15 min to 40 % HF etching at 21°C.

One set of sample mounts was loaded into polyethylene capsules and irradiated at the thermal neutron channel 8 of the Thesis reactor facility in Ghent (Belgium). IRMM 540 dosimeter glasses were used to monitor a neutron fluence gradient and a total thermal neutron (n) fluence of c. 1×10^{16} ncm^{-2} was applied.

Track densities in mounts and micas were measured using a Zeiss® Axiophot microscope equipped with a drawing tube, a Kintec® stage and a Calcomp® digitizer with the latter two being operated by the FT-Stage software (Dumitru, 1991). Dry objectives, calibrated against stage micrometers, were used for track density counts in transmitted light at 1250× magnification. Only pristine apatite grains without inclusions and lattice defects e.g. dislocations were used for fission track analyses. Solely grains, exposing internal surfaces parallel to the crystallographic *c*-axis were used for track density and track length measurements. Confined track length (tints only) and etch pit diameter were measured with dry objectives, calibrated against a stage micrometer at 2000× magnification in transmitted light and reflected light, respectively. Four etch pits

per grain dated and three etch pits per crystal used for track length measurement were determined. Arithmetic mean D_{par} values were used for each grain and track of samples employed in the *t-T* path modelling. An overall sample's arithmetic mean D_{par} value was calculated as a bulk kinetic proxy for each AFT sample (Tabs. 6.1-6.4). The AFT central ages were calculated according to the zeta calibration method (Galbraith and Laslett, 1993; Hurford, 1990a) with a weighted mean zeta factor of $\zeta = 325 \pm 7$. Individual zeta values and counting statistics of age standards are provided in Tab. 2.3.

All other apatite sample mounts were loaded into aluminium capsules and irradiated at the FRM II research reactor facility in Munich-Garching (Germany). An irradiation time of 100 s was applied to obtain a total thermal neutron fluence of 1×10^{16} ncm^{-2}. Grain selection, track length and etch pit measurements were conducted as given above.

The track densities were determined using the repositioning technique (Jonckheere et al., 2003) at a magnification 1250× in transmitted light. AFT central ages were calculated according to zeta calibration method (Galbraith and Laslett, 1993; Hurford, 1990a) with a weighted mean zeta factor of $\zeta = 322 \pm 9$ for IRMM 540 dosimeter glasses. Individual zeta values and counting statistics of age standards are provided in Tab. 2.4. Throughout this study AFT age errors are quoted at the 1σ confidence level and were derived according to the conventional method (Green, 1981).

The modelling of apatite fission track data was performed for representative samples that yield a minimum of 5 grains dated and of 30 track lengths measured. The software AFTSolve 1.3.1 (Ketcham et al., 2000) using the Ketcham AFT annealing algorithm (Ketcham et al., 1999) was employed. Single grain ages, track length measurements and corresponding D_{par} values are used as model inputs. The annealing model of Ketcham et al. (2000, 1999) is calibrated for a track revelation procedure using 5.5 M HNO_3 etchant for 20 s at 21°C (Carlson et al., 1999). Therefore, samples employed in *t-T* path modelling were corrected for slightly deviating etching conditions by multiplying the measured etch pit diameter (D_{par}) values with a calibration factor of 1.0145, according to suggestion of R. A. Donelick (pers. comm., 2004). The calibration factor represents the ratio between the D_{par} measurements obtained from two different track revelation

Table 2.3: Zeta values used for apatite fission track calibration (Ghent reactor)

Age standard	No. of grains	ρ_s (× 10^6cm^{-2}) (N_s)	ρ_i (× 10^6cm^{-2}) (N_i)	ρ_d (× 10^6cm^{-2}) (N_d)	P(χ^2) (%)	ζ - factor ± 1σ
Durango	16	0.128 (73)	0.867 (495)	1.520 (11498)	97.1	280.8 ± 35.6
Durango	23	0.133 (86)	1.071 (692)	1.606 (11498)	99.9	315.4 ± 36.5
Fish Canyon	21	0.181 (84)	1.558 (725)	1.577 (11498)	99.8	306.1 ± 35.8
Fish Canyon	21	0.198 (109)	1.554 (855)	1.557 (11498)	97.5	278.2 ± 28.8
Mt. Dromedary	18	1.083 (234)	3.027 (654)	1.554 (11498)	55.1	357.8 ± 27.5
Durango	6	0.143 (84)	1.035 (607)	1.589 (11803)	43.3	286.3 ± 33.7
Durango	10	0.194 (36)	1.351 (251)	1.587 (11803)	99.9	276.6 ± 49.6
Fish Canyon	20	0.211 (76)	1.952 (702)	1.591 (11803)	99.9	324.7 ± 39.8
Mt. Dromedary	20	0.737 (191)	2.185 (566)	1.586 (11803)	99.9	371.7 ± 31.4
Durango	14	0.140 (48)	1.052 (360)	1.481 (7238)	97.5	318.8 ± 49.4
Fish Canyon	7	0.171 (24)	1.520 (214)	1.478 (7238)	100.0	337.4 ± 73.0
Mt. Dromedary	19	0.711 (324)	1.699 (774)	1.484 (7238)	20.1	320.2 ± 21.6
Durango	10	0.151 (27)	1.051 (188)	1.487 (7246)	99.9	294.8 ± 61.0
Fish Canyon	6	0.205 (15)	1.814 (133)	1.486 (7246)	93.4	333.7 ± 91.2
Mt. Dromedary	25	0.801 (293)	2.145 (784)	1.488 (7246)	99.9	357.7 ± 25.0
Durango	10	0.136 (103)	0.954 (723)	1.506 (7359)	71.7	293.4 ± 31.4
Mt. Dromedary	22	0.704 (406)	1.880 (1084)	1.503 (7359)	70.3	353.4 ± 21.1
Durango	25	0.216 (231)	1.498 (1605)	1.481 (11436)	93.3	295.3 ± 21.5
Mt. Dromedary	25	0.742 (436)	1.971 (1158)	1.485 (11436)	95.4	355.8 ± 20.4

All samples were irradiated at the reactor facility Thetis in Ghent (Belgium) and ζ values were determined for IRMM 540 standard glasses. ρ_d is the standard glass track density, ρ_s and ρ_i represent sample's spontaneous and induced track densities, with the total number of track counts given in parentheses (N_s, N_i, N_d). P (χ^2) represents the probability of the chi-square test.

Table 2.4: Zeta values used for apatite fission track calibration (Munich reactor)

Age standard	No. of grains	ρ_s (× 10^6cm^{-2}) (N_s)	ρ_i (× 10^6cm^{-2}) (N_i)	ρ_d (× 10^6cm^{-2}) (N_d)	P(χ^2) (%)	ζ - factor ± 1σ
Durango	17	0.127 (185)	0.736 (1075)	1.143 (7775)	99.8	320.0 ± 26.2
Durango	21	0.127 (238)	0.795 (1488)	1.140 (7775)	96.1	345.3 ± 25.0
Durango	15	0.130 (163)	0.782 (977)	1.147 (7775)	96.4	329.0 ± 28.6
Durango	11	0.133 (112)	0.856 (720)	1.121 (7775)	67.9	361.0 ± 37.3
Fish Canyon	14	0.217 (123)	1.226 (696)	1.136 (7775)	96.8	278.6 ± 27.9
Fish Canyon	25	0.222 (183)	1.527 (1260)	1.128 (7775)	99.8	341.3 ± 28.0
Fish Canyon	23	0.218 (216)	1.177 (1164)	1.132 (7775)	99.0	266.2 ± 20.5
Mt. Dromedary	26	0.835 (706)	1.649 (1394)	1.125 (7775)	92.7	349.1 ± 16.7

All samples were irradiated at the reactor facility FRM II Munich-Garching (Germany) and ζ values were determined for IRMM 540 standard glasses using the repositioning technique (Jonckheere et al., 2003). ρ_d is the standard glass track density, ρ_s and ρ_i represent sample's spontaneous and induced track densities, with the total number of track counts given in parentheses (N_s, N_i, N_d). P (χ^2) represents the probability of the chi-square test.

procedures of the same apatite standard. Multiple D_{par} ratio determinations were derived for Durango and Fish Canyon apatite standards (Tab. 2.5). An overall mean D_{par} ratio value of both standards was used as the calibration factor (1.0145).

Table 2.5: Etch pits diameter values of apatite standards used for D_{par} calibration

Age Standard	No. of etch pits	D_{par} (µm)	SD (µm)	ratio D_{par}
Durango	58	1.80	0.20	1.02
Durango	61	1.85	0.16	0.99
Durango	47	1.79	0.17	1.02
Weighted mean	166	1.82	0.01	1.01

Age Standard	No. of etch pits	D_{par} (µm)	SD (µm)	ratio D_{par}
Fish Canyon	34	2.38	0.18	1.02
Fish Canyon	56	2.40	0.30	1.01
Fish Canyon	58	2.39	0.22	1.02
Fish Canyon	41	2.34	0.27	1.04
Weighted mean	189	2.38	0.02	1.02

D_{par} represents arithmetic mean of all measured etch pits in a sample and SD is the associated standard deviation. Ratio D_{par} is the ratio between D_{par} values quoted by Donelick et al. (1999) (5.5 M HNO_3, 20 s, 21°C; Durango = 1.83 ± 0.13 µm, Fish Canyon = 2.43 ± 0.21 µm) and measured D_{par} values.

All fission track annealing models are calibrated against a reduced track length ($r = l/l_0$) and rely on the usage of an initial unannealed track length (e.g. $l_0 = 16.3$ µm in Laslett et al., 1987; Ketcham et al., 1999). Uncertainties about this initial track length and the lack of knowledge about the AFT annealing behaviour below c. 60°C are accounted for to result in major cooling from c. 60°C to present-day surface temperatures in the geologically recent past (see Kohn et al., 2002 and references therein). The AFT-Solve 1.3.1 (Ketcham et al., 2000) modelling software uses a compensation factor to account for some uncertainties about the initial spontaneous track length to reduce the effect of the recent rapid cooling events. However, it does not account for the poorly constrained annealing behaviour of apatite fission tracks below c. 60°C. Therefore such "recent" cooling episodes could be modelling artefacts and hence they are regarded as less reliable unless independent evidences exist. Throughout this study, cooling path models are discussed in terms of the best-fit model path.

2.2.6 Fission track data presentation

The results of the TFT and AFT analyses are presented in Table 3.3 and Tables 6.1-6.4, respectively. Individual titanite and apatite single grain age data are presented as radial plots (Appendix A and B), a graphical device for comparing crystals of different ages

and precisions (Galbraith, 1990). In radial plots the position of the *x* axis represents the precision of individual grain age estimates (dependant on the number of track counts), with precision increasing to the right. Each datum has the same standard error in the y direction (indicated by the vertical +2 to -2 bar). The age of each grain is proportional to the slope of a line from the origin passing through the datum's x, y coordinates. It can be read from the radial age scale by extrapolating this line to its intersection with the age scale. Sample's apatite track length data are shown as track length histograms, binned at 1 μm intervals (Appendix B). The kinetic parameters (D_{par}) determined in each AFT sample, are presented in *x-y* scatter plots versus a) their single grain ages and b) their single track lengths (Appendix B).

2.3 (U-Th)/He dating of apatite

The application of the (U-Th)/^{4}He radioactive decay series for age dating of rocks is the oldest known physical chronometric method and it had already been proposed at the begin of the 20th century (Rutherford, 1906; Strutt, 1908; Strutt, 1909). With the advent of the K-Ar dating method the (U-Th)/He method was excepting minor research efforts (e.g. Fanale and Kulp, 1962; Ferreira et al., 1975; Turekian et al., 1970) essentially abandoned. In particular as (U-Th)/He results derived from different mineral phases often yielded unreliable and unusually low ages, probably as a consequence of diffusive ^{4}He loss paired with radiation damage (Boschmann-Käthler, 1986; Hurley, 1954).

By the mid 80's, the (U-Th)/He dating method gained renewed interest. It had been suggested that at least in the case of apatite, He ages might be thermochronometers, which record cooling through very low temperatures (Zeitler et al., 1987). Important aspects on the technique, calibration, application and laboratory studies of the apatite (U-Th)/He thermochronometry are given by Ehlers and Farley, 2003; Farley et al., 1996; Farley, 2000; Farley, 2002; House et al., 1999; Lippolt et al., 1994; Reiners and Farley, 2001; Stockli et al., 2000; Warnock et al., 1997; Wolf et al., 1998; Wolf et al., 1996a; Wolf et al., 1996b.

2.3.1 Helium isotope measurements and age calculation

In minerals, the overwhelming majority of ^{4}He nuclei (α-particles) are produced by actinide radioactive decay series. They are mainly derived from ^{238}U, ^{235}U, ^{232}Th and to a lesser extent from ^{147}Sm. The (U-Th)/He dating method is based upon a chain of decays from the nuclides ^{238}U, ^{235}U and ^{232}Th into their stable end products ^{206}Pb, ^{207}Pb and ^{208}Pb, respectively. Thereby α and β particles are emitted (Fig. 2.9) according to the net-balances:

$$^{238}U \rightarrow {}^{206}Pb + 8\alpha + 6\left(\beta^{-} + \bar{\nu}_{e}\right) + E$$
$$^{235}U \rightarrow {}^{207}Pb + 7\alpha + 4\left(\beta^{-} + \bar{\nu}_{e}\right) + E$$
$$^{232}Th \rightarrow {}^{208}Pb + 6\alpha + 4\left(\beta^{-} + \bar{\nu}_{e}\right) + E$$

where α is a ^{4}He nucleus, β^{-} is an electron, ν_{e} is an electronic antineutrino and E represents the decay energy.

The emitted α particles possess an energy- and solid matter-specific travel distance. After having released all energy, i.e. coming to rest they capture two electrons and form neutral ^{4}He atoms. These ^{4}He atoms are interpreted as stable daughter nuclides and their production per time can be described by the standard radioactive decay law.

For (U-Th)/He dating the fundamental He production equation is given by:

$$^{4}He = 8^{238}U \cdot \left(e^{\lambda_{238}t} - 1\right) + 7^{235}U \cdot \left(e^{\lambda_{237}t} - 1\right) + 6^{232}Th \cdot \left(e^{\lambda_{232}t} - 1\right) \quad (24)$$

where t = the time since the closure of the (U-Th)/^{4}He system, ^{4}He is the number of the helium daughter nuclides at time t. ^{238}U, ^{235}U and ^{232}Th are the number of the specific parent nuclides at time t. λ_{238} is the decay constant for ^{238}U = 1.5513×10^{-10} a^{-1}, λ_{235} is the decay constant for ^{235}U = 9.8485×10^{-10} a^{-1} and λ_{232} is the decay constant for ^{232}Th = 0.4948×10^{-10} a^{-1} after Steiger and Jäger (1977).

The time since system closure, t, cannot be derived analytically from equation (24) for determined parent and daughter nuclide concentrations. It is either obtained iteratively or by calculating the first two terms of Taylor expansion to derive a

simplified linear age equation (see Wolf et al., 1998). Recently, a noniterative solution for approximating *t* from equation (24) has been proposed (Meesters and Dunai, 2005).

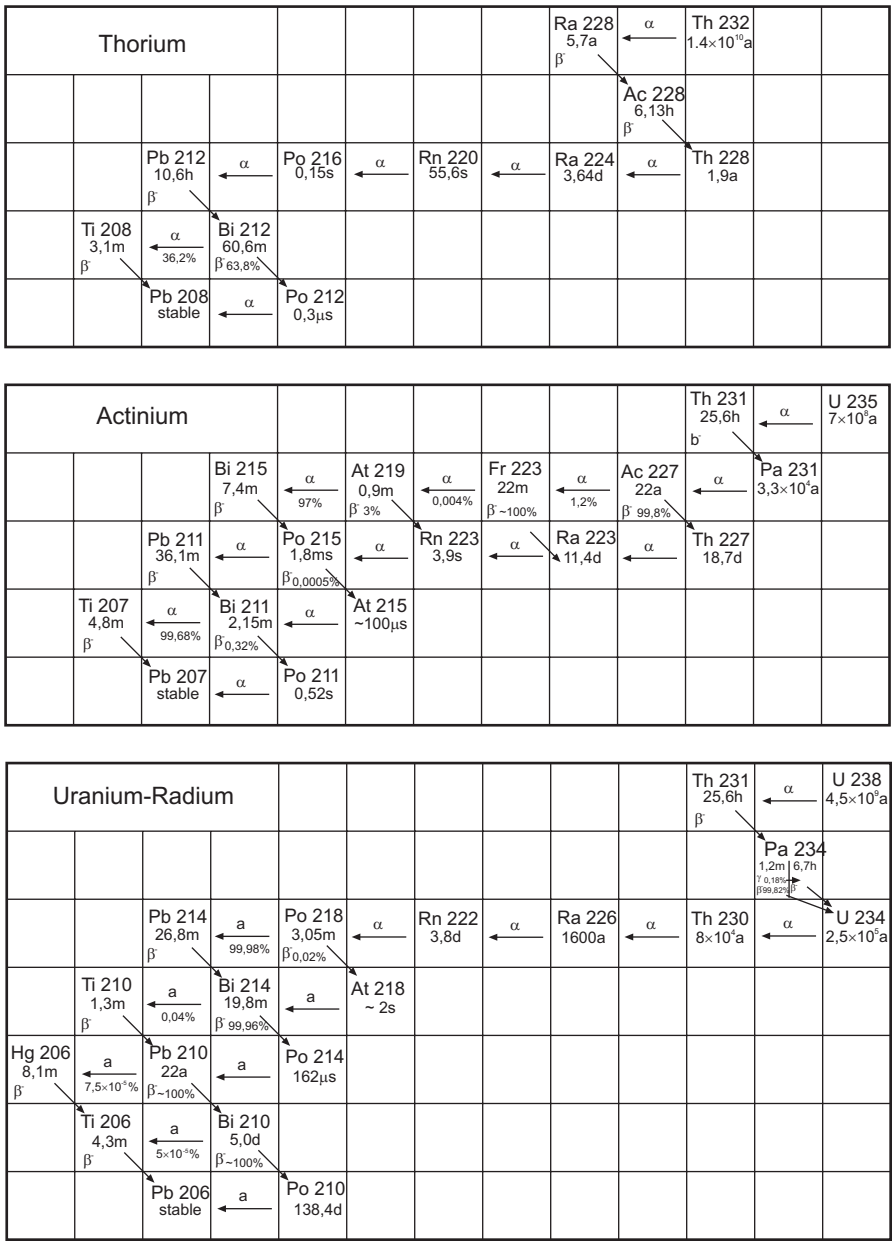

Figure 2.9: Illustration depicts the thorium and uranium decay series modified after Seelmann-Eggebert et al. (1981). Specific half-lives are quoted below isotopes and α, β and γ indicate the type of decay.

Equation (24) assumes a secular equilibrium among all daughter nuclides of the decay chain and is determined by the lifetime of the most long-lasting interim daughter

nuclide, i.e. $^{234}U = 3.6 \times 10^5$ a. For most applications this condition is valid, i.e. crystals have formed more than ~360 ka prior to onset of helium accumulation. In practice equation (24) assumes no initial ^4He within the mineral specimen analysed. As the atmosphere contains 0.5 ‰ helium, trapped atmospheric helium can be neglected though other sources like fluid inclusions carrying crustal or mantle helium and/or impurities may be important. A detailed overview on helium isotopes is given by Mamyrin and Tolstikhin (1984).

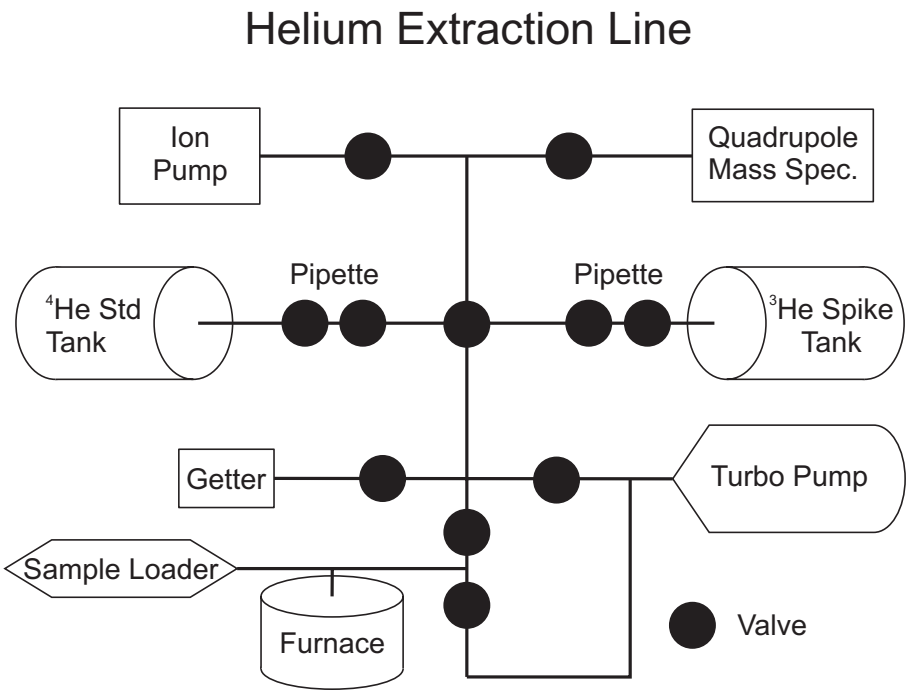

Figure 2.10: Schematic setup of the helium extraction line used at School of Earth Sciences; Melbourne University (D.X. Belton, pers. comm.).

The determination of the ^4He and U, Th nuclide concentrations is commonly done in two steps. First, ^4He gas is extracted in vacuo from apatite by either furnace (Farley et al., 1999) or laser heating (House et al., 2000), spiked with ^3He and admitted to a quadrupole mass spectrometer for measuring the He concentration as a ratio ($^3He/^4He$) via isotope dilution. Measured helium concentration levels of mass spectrometer background and extraction line blanks are corrected for (if necessary) by subtracting them from actual helium isotopic determinations. The precision on the helium gas measurement throughout this work is on the order of 1.4 %. It is based on multiple

measurements of a calibrated volume from a dedicated ^{4}He tank (Fig. 2.10) (D.X. Belton, pers. comm., 2003). In a second step, degassed apatite grains are dissolved in nitric acid. The obtained solution is spiked with ^{235}U and ^{230}Th and the concentrations of U and Th are measured as ratios (^{235}U/^{238}U) and (^{230}Th/^{232}Th) using ICPMS (inductively coupled plasma mass spectrometry) via isotope dilution. The precisions on the isotope measurements are determined from multiple measurements of a known standard solution that is measured between the actual sample analyses. Typical precisions throughout this work are 4.1 % and 4.5 % for U and Th, respectively (D.X. Belton, pers. comm., 2003).

2.3.2 α-emission balance and helium age correction

The α particles of the U and Th decay chains are emitted with sufficient kinetic energy to travel between c. 13-34 μm in apatite, with average stopping distances between 20-23 μm (Tab. 2.6). Consequently, the α decay induces a spatial separation between parent and daughter isotopes. The important implication is that α particles produced along the outermost rim of c. 20 μm of an apatite crystal may not entirely retained and hence alter the helium concentration within the apatite grain (Fig. 2.11). Depending on the shape and size of a grain the proportion of helium loss may significantly affect the calculated helium age. As an example, for a sphere with a radius of 100 μm only 82 % of the ^{4}He produced is retained (Farley et al., 1996).

Fleischer (1983) proposed an analytical solution for determining the fraction of α particles retained (F_T) within a sphere containing homogeneously distributed uranium and being surrounded by negligible amounts of uranium, hence neglecting possible α implantation:

$$F_T = 1 - \frac{3S}{4R} + \frac{S^3}{16R^3} \quad (25)$$

where S = alpha stopping distance and R = radius of the sphere. Using Monte Carlo simulations, Farley et al. (1996) extended this approach to cubic and cylindrical

geometries (applicable for apatite and zircon) and yielded for grains being considerably larger than the α stopping distance ($R >> S$):

$$F_T = 1 - \frac{S}{4} \cdot \beta \tag{26}$$

where β is the surface to volume ratio of the mineral grain; for a hexagonal prism of apatite β =(2.31L+2R)/(R/L), R is the half prism width and L is the crystal length.

Table 2.6: Stopping distances of α-particles in apatite for the decay series of ^{238}U, ^{235}U and ^{232}Th

Nuclide	α - energy (MeV)	Stopping distance in apatite (µm)
^{238}U	4.18	13.54
^{234}U	4.76	16.26
^{230}Th	4.67	15.84
^{226}Ra	4.77	16.31
^{222}Rn	5.49	20.09
^{218}Po	6.00	22.89
^{214}Bi	7.69	33.39
^{210}Po	5.31	19.10
^{238}U average	5.36	19.68

Nuclide	α - energy (MeV)	Stopping distance in apatite (µm)
^{235}U	4.38	14.48
^{231}Pa	5.00	17.39
^{227}Th	5.93	22.50
^{223}Ra	5.65	20.97
^{219}Ra	6.68	26.89
^{215}Po	7.38	31.40
^{211}Bi	6.57	26.18
^{235}U average	5.94	22.83

Nuclide	α - energy (MeV)	Stopping distance in apatite (µm)
^{232}Th	3.98	12.60
^{228}Th	5.35	19.32
^{224}Ra	5.67	21.08
^{220}Rn	5.49	20.09
^{216}Po	6.78	27.53
^{212}Bi / ^{212}Po	6.0 / 8.7	34.14
^{232}Th average	5.85	22.46

Data after Farley et al., 1996

In order to account for slightly higher mean kinetic energies of α-particle from the ^{232}Th decay series (Tab. 2.6), a mean F_T value (Farley et al., 1996), weighted by the fraction of helium (a) derived from each parent is calculated to:

$$^{mean}F_T = a_{238} \cdot {}^{U238}F_T + (1 - a_{238}) \cdot {}^{Th232}F_T \tag{27}$$

Due to very similar α decay energies of ^{235}U and ^{232}Th this weighting approach associates ^{4}He from both parent isotopes as a single value, $^{Th232}F_T$. The value of a_{238} (fraction of ^{4}He produced by ^{238}U) is either derived directly from equation (24) or for integrated time periods < c. 200 Ma approximated from measured Th/U ratio by:

(28) $$a_{238} = \left(1.04 + 0.245 \cdot \left(Th / U\right)\right)^{-1}$$

Fig. 2.12 illustrates the influence of the grain size on the F_T correction factor. It demonstrates that the uncertainty on the F_T correction factor increases significantly with decreasing grain size and that for grain radii smaller than c. 30 μm the F_T value growth very rapidly and hence exerts a significant influence on the helium age. For a batch of apatite grains, a mean F_T is calculated for the entire population, weighted by the individual grain mass, which itself is derived from the grain dimensions. This weighting implicitly assumes that larger grains contribute helium proportional to their mass (Farley et al., 1996). Correction for loss of alpha particles is accounted for by:

(29) $$t_{corr} = \frac{t_{raw}}{{}_{mean}F_T}$$

where t_{corr} = the corrected ^{4}He age and t_{raw} = ^{4}He age calculated from equation (24).

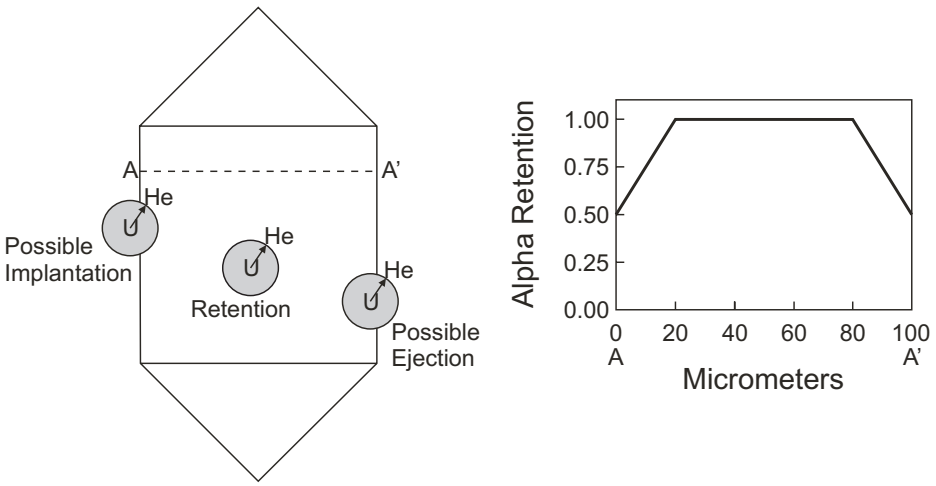

Figure 2.11: Illustration depicts the effect of long α-stopping distances on the retention of ^{4}He in apatite. Left figure depicts sites of possible α-retention, α-ejection and α-implantation within a schematic crystal. U denotes the location of the parent nuclides (U or Th) and the surrounding sphere indicating the possible radial stopping distance of the emitted α particle. One possible trajectory is given by the arrow, pointing to the possible point of stop of a ^{4}He nucleus. Diagram on the right displays a schematic cross section of the crystal and illustrates the change of ^{4}He retention from rim to rim (after Farley et al., 1996).

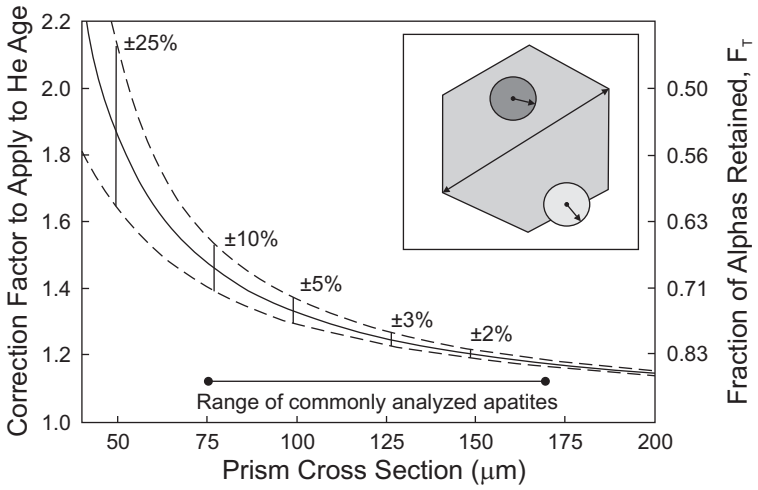

Figure 2.12: Diagram shows the relation between grain size and alpha particles retained (right Y-axis line) i.e. applicable correction factor to raw He age (left Y-axis). Black line represents α particles retention for the ^{238}U decay series in a hexagonal apatite prism with a length/width ratio of 3. Dashed lines indicate 1σ error on the FT factor derived from grain measurement uncertainties and percentage values are 2σ uncertainties for related cross sections. Inset depicts a cross section of hexagonal apatite prism (grey hexagon) with one ^{4}He particle being retained within the crystal (dark circle) and one being ejected outside of the grain (light circle). Cross section is determined between opposing apices. Figure modified after Ehlers and Farley, 2003.

2.3.3 Age error estimation

The absolute analytical error on the corrected ^{4}He age (σ_{rel}) is estimated according to a procedure used at Melbourne University:

$$\sigma_t = \frac{t_{corr} \cdot \sqrt{\sigma_{^4He}{}^2 + \sigma_{Th}{}^2 + \sigma_U{}^2 + \sigma_{FT}{}^2}}{100} \tag{30}$$

where σ_{4He}, σ_{Th} and σ_U are the relative analytical errors on the helium, thorium and uranium determinations, respectively and σ_{FT} is the estimated relative error on the mean F_T factor given to:

$$\sigma_{FT} = \frac{-0.0987 \times {}^{mean}F_T + 0.0934}{{}^{mean}F_T} \cdot 100 \tag{31}$$

The relationship between the grain radius and the F_T factor is non-linear and a calibration curve has been fitted based on 400 grain radii determinations (30-200 μm range) to establish the relative error (σ_{FT}) on the F_T factor (D.X. Belton, pers. comm., 2003). A relative error on the corrected ^{4}He age (σ_t) is obtained by:

(32) $$\sigma_{rel} = \frac{100 \cdot \sigma_t}{t_{corr}}$$

2.3.4 Helium diffusion in apatite

In (U-Th)/He dating, it is crucial to understand the ^{4}He diffusion behaviour in minerals. For apatite, notably Durango apatite, it has been shown by laboratory step degassing experiments that for temperatures below c. 265°C ^{4}He diffusion is a thermally activated process that can be described by an Arrhenius relationship. The physical grain remains

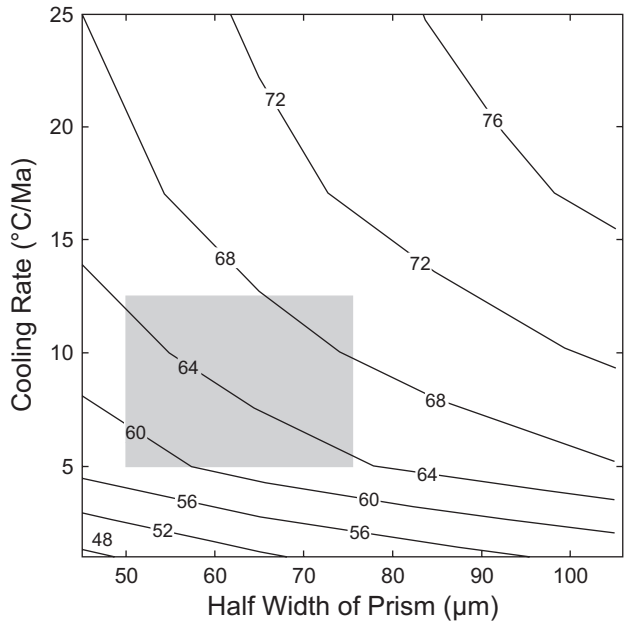

Figure 2.13: Diagram depicts the effective helium closure temperatures (T_c) for infinite cylinders as a function of apatite grain radii (half prism width) and cooling rates. Shaded area represents ranges typically observed in nature (after Farley, 2000).

stable during heating and is the diffusion domain whereby diffusion in Durango apatite is nearly isotropic. The estimates on the Arrhenius diffusion parameters are

$E_a = 33 \pm 0.5$ kcal/mol and $log(D_0) = 1.5 \pm 0.6$ cm^2/s [$D_0 = 31.6$ cm^2/s] (Farley, 2000) and they may be applied to calculate a closure temperature according to Dodson (1973) using equation (6). In Fig. 2.13 closure temperatures are displayed for a range of grain radii and cooling rates. As a good approximation, the effective closure temperature of the (U-Th)/He dating method is c. 68°C for cooling rates of 10°C/Ma and grain radii of c. 90 μm (Farley, 2000).

The time of ^{4}He accumulation calculated from equation (24) solely accounts for production of α-particles and does not incorporate diffusive loss of ^{4}He. Therefore only in the special case where cooling proceeds fairly rapidly the assumption of a cooling age is justified. In other cases where uncertainties exist about the diffusive closure of the (U-Th)/He system the term "helium indices" has been suggested (Keevil, 1941). If diffusion is the only source of ^{4}He loss in the (U-Th)/He system the age equation can be stated as followed for a spherical diffusion domain:

(33)

$$\frac{\partial^4 He(r,t)}{\partial t} = \frac{D(t)}{a^2}\left[\frac{\partial^2 {}^4 He(r,t)}{\partial r^2} + \frac{2}{r}\frac{\partial^4 He(r,t)}{\partial r}\right] + 8\lambda_{238}{}^{238}U(t) + 7\lambda_{235}{}^{235}U(t) + 6\lambda_{232}{}^{232}Th(t)$$

where $^4He(r,t)$ is concentration of helium at time t as a function of the radial position r with a spherical diffusion domain of radius a. $U(t)$ and $Th(t)$ represent the parent isotope concentrations at time t and $D(t)$ is the time-temperature dependant diffusion coefficient obeying an Arrhenius relationship.

For high temperatures the diffusive term dominates and virtually all helium is lost from the mineral. With decreasing temperature, helium starts to accumulate and for even further temperature lowering the diffusive term becomes negligible and all helium produced is retained. Wolf et al., (1998) used an analytical solution of equation (33) for isothermal conditions and showed that with increasing depth and temperature, helium ages will decrease and in dependence of the isothermal holding time a helium partial retention zone (HePRZ), analogous to fission track PAZ, will establish. This model predicts that a ^{4}He age will always be younger than its corresponding apatite fission track. The HePRZ does not overlap with the fission track PAZ. Solely for very rapidly

cooled samples ($t_{cooling}$ << ^{4}He age), a ^{4}He age and its corresponding AFT age will be equal. The example given in Fig. 2.14 demonstrates that the HePRZ locates c. 35°C cooler than the corresponding FTPAZ. Over geological timescales of 10^6-10^8 Ma, the HePRZ resides between c. 45-85°C and for typical geothermal gradients 25°C/km, it is located at 2 ± 1km (Wolf et al., 1998). Studies from boreholes broadly confirmed the supposed decrease in apparent age with increasing depth and temperature (House et al., 1999; Warnock et al., 1997). Field investigation confirmed the existence of apatite HePRZ within a temperature range of c. 45°-85°C (Stockli et al., 2000). Equation (33) allows the modelling of helium ages for given time-temperature paths but does not account for α-particle emission.

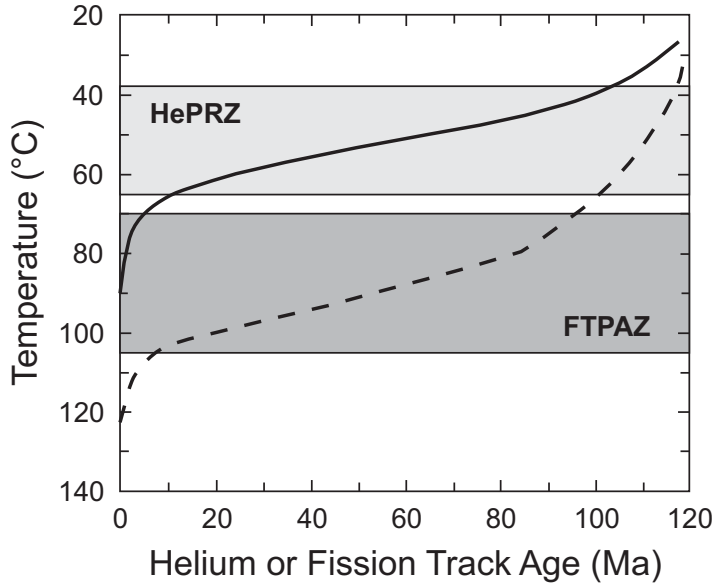

Figure 2.14: Variation of ^{4}He (solid line) and fission track ages (dashed line) with temperature (depth) for apatites exposed to isothermal conditions for 120 Ma. Light grey and dark grey shaded areas represent HePRZ and FTPAZ, respectively. The HePAZ is defined as the range, were the ^{4}He ages decrease from 90% to 10% of the isothermal holding time, i.e. $0.1 \leq t_{He}/t_{hold} \leq 0.9$. Diagram modified after Wolf et al. (1998).

At the time of analysis, the helium content in a mineral is the net result of two inter-woven processes: the ejection of α-particles and the helium diffusion (Meesters and Dunai, 2002a; Meesters and Dunai, 2002b). Meesters and Dunai (2002a, 2002b) presented an algorithm to calculate helium ages for given *t*-*T* paths that incorporates both processes. Their model demonstrates that the average ^{4}He age tends to be universal

for identical surface to volume ratios. Therefore the He content evolving in a finite geometry can be translated into one evolving in the simpler geometry of a sphere.

2.3.5 Analytical procedures

Apatite grains for (U-Th)/He analysis were obtained from concentrates separated from whole rock material as described in chapter 2.5. Furnace heating and laser heating analyses were performed at Melbourne University in cooperation with B. Kohn and at CSIRO in Perth in cooperation with P. Crowhurst, respectively.

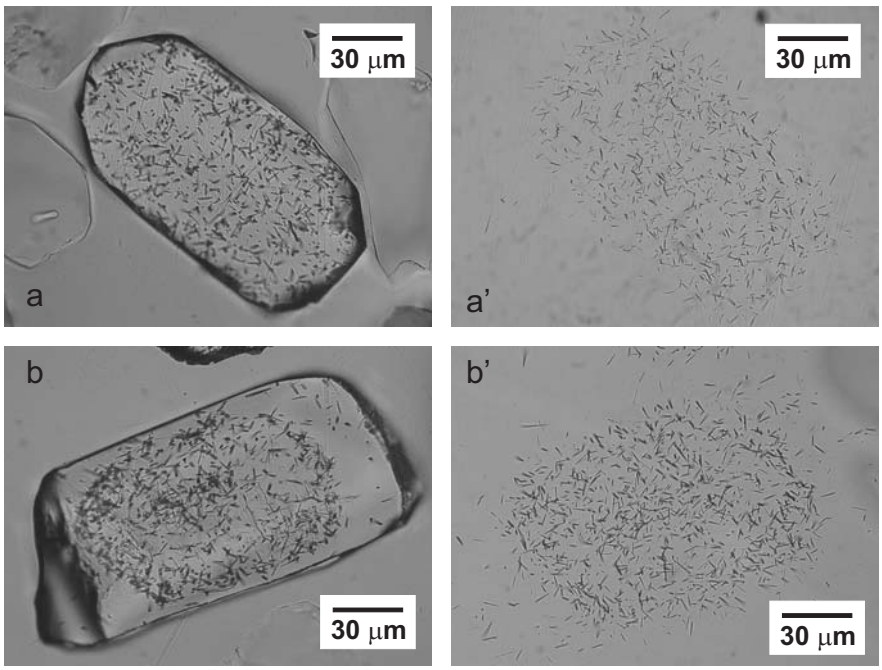

Figure 2.15: Upper images show homogenous ^{238}U and ^{235}U distribution patterns in an etched euhedral apatite crystal (a) and corresponding detector mica print (a'), respectively. The lower image depicts an etched subheadral apatite (b) displaying strong zoning with moderate and extremely low ^{238}U concentrations occurring in the core and rim, respectively. Its corresponding detector mica print (b') reveals a similar zoning in the ^{235}U distribution pattern.

Heterogeneous distributions of U and Th exert strong influences on the helium retention (F_T) and on the helium age. And so do the grain shape and grain diameter. Therefore apatite samples were screened in a two step process for selecting inclusion free samples with homogeneous parent nuclide distributions and preferred euhedral and cylindrical grain shapes. At first, apatite samples prepared for fission track analysis (embedded,

polished, etched and irradiated) were inspected as etched tracks in crystal mounts and extern mica detector reveal information on ^{238}U and ^{235}U distribution patterns, respectively (Fig. 2.15). Inspection was performed using dry objects in transmitted light at 50-500x magnification. From high quality samples c. 10-15 apatites were picked per

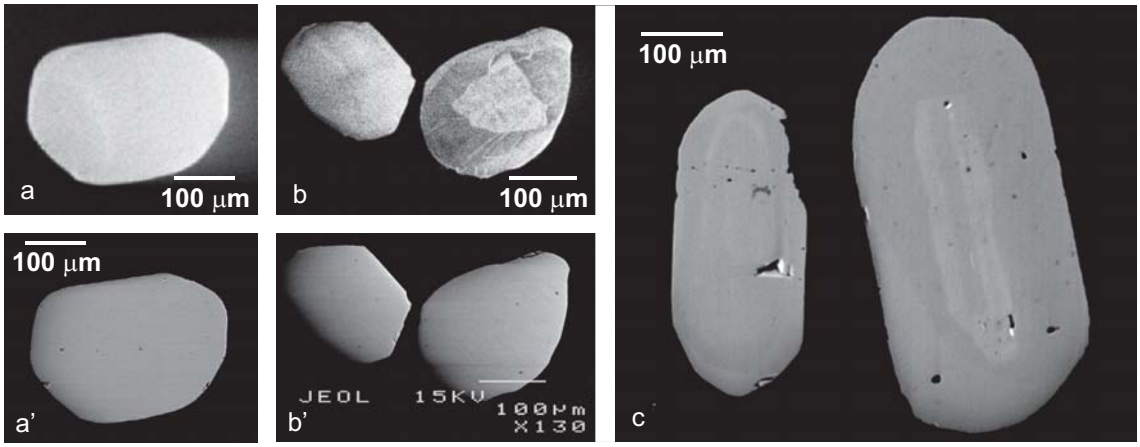

Figure 2.16: Image of a stubby, euhedral apatite crystal displaying homogenous CL SEM (a) and backscatter SEM (a') of a sample suited for (U-Th)/He analysis. Anhedral apatite crystals with a homogenous appearance in the backscattered SEM image (b'). Their CL SEM images (b) reveal zoning (triangular core) and sub parallel bright streaks in the larger grain. These crosscutting, streaky alterations are likely to be a source of helium loss and this sample has been excluded from (U-Th)/He analysis. Image (c) shows two euhedral apatite crystals with alternating zoning from rim to core. This possibly indicates zoned uranium and thorium distributions.

sample and investigated more detailed using SEM CL (cathodoluminescence) and SEM backscatter imaging (Fig. 2.16). CL microscopy is a useful tool to detect lattice defects and/or trace activator cations such as $REE^{2+/3+}$, Fe^{3+}, Cr^{3+}, Al^{3+}, Mn^{2+}, Pb^{2+} Cu^{2+}, Sn^{2+} (Götze, 2002). By using coupled CL and Laser-ICP-MS analysis, it has been demonstrated that within zoned crystals different colours of luminescence produced by e.g. Mn or REE are in direct relationship to U, Th and Ce concentrations (Jolivet et al., 2003). In backscatter SEM images of apatite crystals brighter regions are generally enriched in Y, Ce and La and often strongly correlate with U and Th (Ehlers and Farley, 2003). Apatite samples showing strong internal structures e.g. zoning were excluded. Thereafter, grain selection was done by handpicking batches of pristine crystals (8-15) of similar grain diameter (> 60 μm) and undamaged surfaces. Picking was performed using a binocular microscope fitted with a polarizer and calibrated digital camera in

transmitted and polarized light at 50x magnification. Apatites were immersed in ethanol and rotated in polarized light to detect inclusions (e.g. zircon, monazite) and cracks. Digital images were taken from selected apatite batches (Fig. 2.17). Subsequently, their grain dimensions were determined by an automated image analysis routine using edge detection and threshold algorithms to define the grains and then measure them by means of minimum and maximum fitted ellipses. This approach has a precision of c. ± 5 μm (D.X. Belton, pers. comm., 2003).

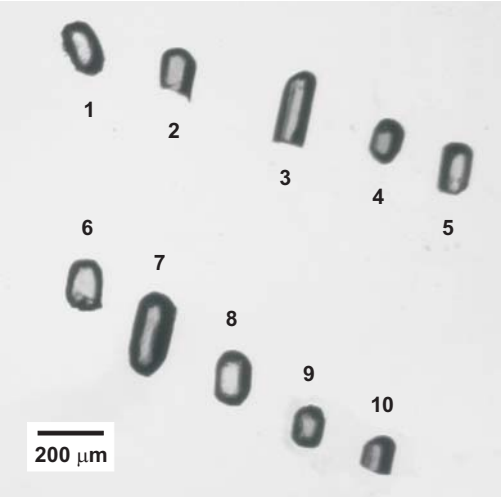

Grain measurements

grain	length (μm)	width (μm)
1	186.1	113.2
2	154.3	113.9
3	256.7	108.4
4	145.2	97.9
5	175.3	100.9
6	171.5	119.4
7	278.8	133.3
8	180.5	121.1
9	139.5	104.2
10	124.9	105.1

Figure 2.17: Digital image of an apatite crystal batch selected for (U-Th)/He dating. The table to the right shows the corresponding grain dimensions derived by digital image analysis.

Apatite batches were placed in stainless steel capsules and sealed by welding on a lid. Up to 6 capsules were loaded into the helium extraction line (Fig. 2.10), a stainless steel system connected to a dedicated, on-line Balzers Prisma^{TM} 200 quadrapole mass spectrometer. The extraction line was maintained at c. 10^{-8} mbar between analyses and the automated extraction and data acquisition system was computer controlled, using a Lab View program. The sample was heated in a sealed vacuum furnace to c. 870°C for approximately 20 min and gases released were "gettered" using a titanium sponge getter to remove all active gases (CO_2, H_2O, H_2, N_2, O_2, CH_4, e.t.c.). ^{4}He abundances were determined via isotope dilution using a pure ^{3}He spike, which is calibrated on a regular basis against an independent ^{4}He standard tank. ^{4}He 're-extracts' hot line blank measurements were performed routinely after each analysis to determine whether all of

the trapped He gas has been removed or not. Every sixth sample analysis was a Durango apatite standard to control consistency of analyses.

Apatite single grain analyses were performed at CSIRO Perth and grain selection followed routine outlined above. Picked grains were sealed in Pt tubes (1 mm width) and up to 25 individual aliquots were placed into pits in a Cu planchette prior to heating with the laser in an ultra-high vacuum system. The CSIRO He extraction and analysis facility comprises a fully automated, stainless steel system connected to a dedicated, on-line Balzers Prisma^{TM} 200 quadrupole mass spectrometer. Gas extraction was performed by using a US Laser Corporation, 16W Nd-YAG, continuous-wave infra-red laser system ($\lambda = 1064$ nm) with a 1000 μm beam, and samples were heated to c. 1000°C for c. 5 min using 1-2 W of power. The extraction line was maintained at c. 10^{-8} mbar between analyses. Active gases were removed using SAES getters (AP10N). The analytical procedure was controlled by a LabVIEW^{TM} based, automated procedure. ^{4}He abundances were determined via isotope dilution using a pure ^{3}He spike, which is calibrated on a regular basis against an independent ^{4}He standard tank. ^{4}He 're-extracts' were performed routinely after each analysis to determine whether all of the trapped He gas has been removed or not. The re-extract gas levels were consistently as low as ~0.0034 ncc ^{4}He.

Apatites degassed by furnace heating were removed from capsules whereas laser heated samples remained within Pt tubes during the U and Th content determinations on a Perkin Elmer Sciex 5000a ICP-MS using the Isotope Ratio application. 100 μl of a ^{235}U and ^{230}Th spike solution (approximately 50 ng/ml U and Th) prepared in 7.1 M $HNO_{3(aq)}$ was used to dissolve the apatite. Each acidified Pt/aliquot package was placed in an ultrasonic bath for ~10 minutes. A dilute stock solution (Johnson Matthey) containing 250 ng/ml U and Th (prepared on a weight/weight basis in 1M $HNO_{3(aq)}$) was also acidified, spiked and analysed with the samples.

2.3.6 Forward modelling of ^{4}He ages

The apatite (U-Th)/He thermochronometer is sensitive to record cooling between c. 80°-40°C (Farley et al., 1996). The measured apatite helium age results from helium loss and accumulation during the samples passage through a *t-T* space (cooling path)

that is a priori unknown. Therefore, the interpretation of helium ages is not straight forward. It has to be linked to independent *t-T* constraints which enable the derivation of a *t-T* path that reproduces the measured helium age. Inverse *t-T* path modelling of AFT data provides such constraints. The AFT system records the cooling between c. 110°-60°C but the timing of cooling to below c. 60°C is fairly poorly constrained (see section 2.2.5.2). Both dating systems yield an overlapping sensitivity to record cooling between c. 80°-60°C. Corresponding AFT and apatite helium ages should therefore yield consistent cooling paths over this temperature interval. Forward modelling of the (U-Th)/He ages using AFT *t-T* models as an independent input could thereby assist to more tightly constrain the timing of the sample's cooling to below c. 60°C and further to below c. 40°C.

The forward modelling of He *t–T* paths is performed using the software "Decomp" (Meesters and Dunai, 2002a; Meesters and Dunai, 2002b). The interpretation of the ^{4}He data by means of the model proposed by Meesters and Dunai (2002a, 2002b) is applicable in slowly cooled environments. In this approach the raw ^{4}He age is regarded as the result of a thermal history experienced. The interplay of α-emission with diffusion is continuously incorporated in the thermal histories modelled. Sample aliquots and single grains radii are accordingly recalculated to fit a spherical geometry with an identical surface to volume ratio. The resulting sphere radius is used for modelling of *t–T* paths. To account for breakage of grains, the average lengths of selected aliquots and grains were multiplied by a factor of 1.5, according to the routine described by Farley (2002).

Best-fit cooling paths of corresponding AFT *t-T* models (c. 110°-60°C), are used as starting points for the ^{4}He data modelling. All samples are modelled assuming a homogenous parent nuclide distribution. To enable intra-sample comparability of different ^{4}He models only the temperature is modified and the numbers (*n*) and time (*T*) of the *t-T* nodes are kept fixed in each sample. Intra-sample cooling path variations among individual analyses are assessed by estimating their average temperature deviations from an overall arithmetic mean *t-T* path. This mean *t-T* path is taken as reference and the deviates of the individual *t-T* paths from it are calculated for the

temperature range between c. 80°-40°C; i.e. the HePRZ. The root mean square (RMS) deviate of all ^{4}He models in a sample is calculated to:

$$He_{RMS} = \sqrt{\frac{\sum_{i=1}^{m}\sum_{j=1}^{n}\left(x_{ij} - \bar{x}_j\right)^2}{m \cdot n}} \quad (34)$$

where m = number of modelled analyses in a sample, n = number of *t-T* nodes, x_{ji} = the modelled temperature of the i^{th} analysis at the j^{th} *t-T* step. $\bar{x}_j$ = arithmetic mean temperature of all modelled analyses at the j^{th} *t-T* step.

The average deviation of the mean ^{4}He *t-T* path from the input AFT model path is estimated by a similar approach. Thereby the AFT *t-T* path is taken as reference and the deviates of the individual *t-T* paths are calculated for the temperature range between c. 80°-60°C; i.e. where the cooling paths pas through the AFT PAZ and the HePRZ. The deviation is calculated to:

$$AFT_{RMS} = \sqrt{\frac{\sum_{i=1}^{n}\left(\bar{x}_{He} - x_{AFT}\right)^2}{n}} \quad (35)$$

where, n = number of *t-T* nodes, $\bar{x}_{He}$ = arithmetic mean temperature of all modelled helium analyses and x_{AFT} = temperature of AFT model at the i^{th} *t-T* step, respectively.

2.3.7 Remarks on the sample pre-screening and on excess ^{4}He

In principle the pre-screening approach permits the selection of potentially high quality samples. However, discrepancies persist as the grains dated are not identical with the ones inspected. CL and fission track sample mount/print images are only 2D representations of the uranium distributions in apatite grains. Hence complex, e.g. none concentric parent nuclide distributions may not be readily detected during the pre-screening. Consequently, the difference between pre-screened and dated apatites might account for some awkward intra-sample ^{4}He age results.

In analogy to the definition of excess radiogenic $^{40}Ar^*$ (Damon, 1968), the term "excess $^4He^*$" is used to designate the incorporation of ^4He into samples by processes other than by *in situ* radioactive decay of ^{238}U, ^{235}U and ^{232}Th. ^4He ages are total fusion ages. Besides the previously outlined relations between corresponding AFT and ^4He ages (Wolf et al, 1998), no independent control exists to reliably identify the influences of excess $^4He^*$.

Recent advances in the ^4He dating systematic indicated a number of potential sources for excess $^4He^*$. Undetected U- or Th-rich micro or fluid inclusions, could account for excess helium (Ehlers and Farley, 2003). Inhibited ^4He diffusion due to a none zero ^4He concentration grain boundary condition or implantation of α-particles from the neighbouring minerals with high U, Th contents (e.g. epidote, Fe-oxides, titanite and zircon) may also result in excess $^4He^*$ and anomalously old ages (Baxter, 2003; Belton et al., 2004a; Spencer et al., 2004). The radioactive decay of ^{147}Sm via α-emission into stable ^{143}Nd is capable of accounting for 0.1-10 % and in extreme cases for more than 25 % of the ^4He age in apatite. Routinely, ^{147}Sm concentrations are not determined. In principle, ^{147}Sm is not considered to be a major source for excess helium but it likely implies a systematic ^4He age overestimation (Belton et al., 2004b). However, none of these excess $^4He^*$ contributing effects can be assessed quantitatively and thus they are collectively regarded as the potential source of excess $^4He^*$.

Microscopic inspections of thin sections yield titanite, zircon and occasionally epidote quantities of typically less than 5-10 %. Therefore α-particle implantation from these mineral phases is considered less significant. A comprehensive review on the effects of zoned parent nuclide distributions and excess $^4He^*$ is given by Fitzgerald et al. (2005).

2.4 Denudation estimates

Estimates on the amount of denudation can be obtained by dividing the palaeo-temperature information, derived from thermochronological analyses, by an estimate of the appropriate palaeo-geothermal gradient. The amount of denudation for a given time interval is then,

(36) $$D = \frac{\Delta T}{G}$$

where D is the amount of denudation during the time interval, ΔT is the estimated change in palaeo-temperature over the time interval, and G is the palaeo-geothermal gradient, assumed to be constant over the time interval. In principle, the parameter G is always unknown because the geothermal gradient present at the time of denudation existed within the now vanished rock column. In low temperature thermochronology, however, it is a common practice to approximate a palaeo-geothermal gradient from present day heat flow measurements divided by the thermal conductivities for the lithologies considered (e.g van der Beek et al., 1998). It is given then,

(37) $$G_P = \frac{hf}{k}$$

where G_P is the present day geothermal gradient, hf is the present day heat flow measurement, and k is the lithology dependant thermal conductivity.

A regional study in southern and eastern Africa of Nyblade et al. (1990) indicates heat flow values of c. 60-80 mW/m^2 for Late Neoproterozoic/Early Cambrian ('Pan African') mobile belt regions (including the Karoo age and recent rifts) and much lower values of c. 35 mW/m^2 for the Archean cratons. Using a thermal conductivity of crystalline upper crustal rocks of c. 2.5 W/mK suggests a present day geothermal gradients of 25°-30°C/km for the southern Mozambique Belt and has been used throughout this study. Surface temperatures of 20°C are assumed, corresponding to values used in the modelling of *t-T* histories from AFT and (U-Th)/He data.

Chapter 3

Post Pan-African thermo-tectonic evolution of the north Mozambican basement and its implication for the Gondwana rifting. Inferences from $^{40}Ar/^{39}Ar$ hornblende, biotite and titanite fission track dating

Daszinnies, M.C.[1], Jacobs, J.[1,2], Wartho, J-A.[3] and Grantham, G.H.[4]

[1] *Department of Geosciences, University of Bremen, P.O.Box 330440, Bremen, Germany 28334*

[2] *Department of Earth Sciences, University of Bergen, Allegaten 41, Bergen, Norway N-5007*

[3] *John de Laeter Centre of Mass Spectrometry, Department of Applied Geology, Curtin University, Perth, WA 6845, Australia*

[4] *Council for Geosciences, P/Bag X112, Pretoria, South Africa 0012*

Abstract

This study presents the thermochronological results of six $^{40}Ar/^{39}Ar$ hornblende, three $^{40}Ar/^{39}Ar$ biotite and twenty five titanite fission track analyses from basement rocks of northern Mozambique. It elucidates the thermo-tectonic basement history since the latest Pan-African imprint and its implication for the initial Gondwana dispersal in Late Palaeozoic to Early Mesozoic times. $^{40}Ar/^{39}Ar$ hornblende and biotite ages of c. 474 Ma to 476 Ma and 448 Ma to 444 Ma, respectively, record the cooling of the eastern part of the southern basement subsequent to the latest Pan-African metamorphic imprint of the Namama Thrust Belt evolution at c. 550-500 Ma. Cooling took place at slow rates of c. 11°-7°C/Ma from c. 525°C to 305°C in the Early to Late Ordovician, respectively. Syn- to post tectonic granitoid/pegmatite emplacements at c. 500-450 Ma caused localized basement reheating and delayed basement cooling as recorded by younger $^{40}Ar/^{39}Ar$ hornblende and biotite ages of c. 456 Ma and 428 Ma, respectively. The titanite fission track (TFT) ages fall into two age groups of c. 378 Ma to c. 327 Ma and c. 284 Ma to 219 Ma. A protracted basement cooling from around 350°-305°C to below 275 ± 25°C at very slow rates of < 1°C/Ma is recorded by the older TFT age population

between the Late Ordovician/Early Silurian and the Late Devonian/Early Carboniferous. The decrease in cooling rates with time is attributed to a reduction in denudation, possibly linked to an establishment of pre-Karoo peneplains. The younger TFT ages record the cooling of a denuding, approximately E-W trending rift flank that was uplifted in the Early to Late Permian. Its formation marks the onset of rifting and incipient Gondwana disintegration in the north Mozambican sector. The corresponding rift basin was probably located to the south of the basement, proximate to the present continental margin and linked to the Zambezi rift system via the Zambezi pre-transform system. Associated crustal extension proceeded obliquely to a NW-SE tensional stress field by brittle reactivation of easterly trending ductile basement fabrics. Titanite FT results indicate ≤ 9-12 km of crust removal on the basement since the Permo-Carboniferous.

3.1 Introduction

Since its amalgamation in Late Neoproterozoic/Early Cambrian times (Pan-African), the crystalline basement of northern Mozambique was located in the central part of the Gondwana supercontinent. Its present location at the East African margin documents that northern Mozambique has been a prominent site of continental extension and separation (Reeves et al., 2002). The supercontinent's disintegration was favoured along large scale Pan-African structural discontinuities (Visser and Praekelt, 1998), and its history is generally constrained and resolved through the investigation of sediments (Karoo Group equivalents), which were deposited in coeval rifts structures across eastern Africa (Catuneanu et al., 2005).

Rift basins located adjacent to the north (Metangula Basin) and west (Shire Valley) of the basement (cf. Fig. 3.2) contain Late Palaeozoic to Late Triassic/Early Jurassic and Late Palaeozoic to Late Triassic/Early Jurassic plus Early Cretaceous sediments, respectively (Castaing, 1991; Catuneanu et al., 2005). The marginal Rovuma and Mozambique rift basins to the east and south comprise Early-Middle Jurassic to Cenozoic strata. On the basement itself, solely Late Mesozoic to Cenozoic sedimentary deposits are preserved (Pinna et al., 1993; Salman and Abdula, 1995). All sedimentary records provide very limited aid as they draw a spatially contrasting and temporally

discontinuous picture. Thus, the geological evolution since the latest Pan-African imprint is not adequately to constrain and the timing of the Gondwana break-up remains enigmatic for this region.

The current outline of the southern coastal margin conspicuously coincides with E to NE ductile litho-trends in the basement. This could suggest an influence of the Pan-African age structural inventory on the locus and geometry of crustal extension during the incipient rifting.

In the absence of rift related continuous sedimentary records, thermochronological methods provide a valuable tool to investigate the cooling history of crystalline basement rocks. Cooling paths could provide information of the regional denudation history and thereby allow the interpretation of the regional thermo-tectonic history. This study combines medium- and low-temperature thermochronology involving $^{40}Ar/^{39}Ar$ dating of hornblende and biotite, and titanite fission track analyses of basement rocks sampled along a 260 km wide E-W trending profile. It aims to constrain the thermo-tectonic evolution of the north Mozambican basement following the latest metamorphic imprint and to elucidate the earliest timing of Gondwana dispersal. By evaluating spatial cooling patterns, it is attempted to delineate constraints on the spatial configuration of the extension and to investigate a possible influence of the Pan-African structural heritage on the Gondwana dispersal in northern Mozambique.

The $^{40}Ar/^{39}Ar$ dating method of minerals yields ages, which can record the cooling to below their specific closure temperatures (Dodson, 1973). For cooling rates of 100-1°C/Ma and grain radii of c. 150 µm, hornblende and biotite yield closure temperatures ranging from 570-483°C and 345-281°C, respectively (McDougall and Harrison, 1999). In the case of TFT dating, the thermochronometer is estimated to partially retain fossil fission tracks over a temperature range of 310-265°C ± 10°C (Coyle and Wagner, 1998), and to yield ages that can record cooling to below 275° ± 25°C (Kohn et al., 1993). A combination of these three thermochronometers permits inferences to trace the cooling path of rocks from temperature conditions of the lower amphibolite metamorphic facies into regimes equal to around 15-10 km depth.

3.2 Geological setting and previous geochronology

The Precambrian basement in northern Mozambique is of Mesoproterozoic juvenile origin and was subjected to intense amphibolite to granulite facies tectono-metamorphic overprints during the amalagamtion of the Gondwana supercontinent in Pan-African times (Kröner et al., 1997; Kröner et al., 2001). In East Africa, it represents the southern termination of the N-S trending Mozambique Belt (MB) (Fig. 3.1), which constitutes a fundamental suture in the assembly of Gondwana and possibly extends southward into Dronning Maud Land, Antarctica (Jacobs et al., 1998). It is still disputed if the supercontinent formed by suturing various parts of proto East and West Gondwana along the MB in a continent-continent collision on a scale of a modern Alpine-Himalayan orogen between c. 650-500 Ma (Jacobs and Thomas, 2004) or by a multiphase assembly from a collage of continental blocks. In the latter model, the north Mozambican basement may experienced an early N-S trending (East African orogeny, c. 750-620 Ma) and/or a late E-W trending (Kuunga orogeny, c. 570-530 Ma) orogenic overprint in Pan-African times (Meert, 2003).

The crystalline basement is divided into a western domain, the Mozambican Axial Zone (Axial Granulite Complex) and an eastern domain of granulitic nappes and amphibolitic rocks (Pinna et al., 1993; Pinna and Marteau, 1987a).

3.2.1 Axial Granulite Complex (Unango Group)

The Axial Granulite Complex extends from north-western Mozambique into southern Malawi and south-eastern Zambia (Andreoli, 1984; Barr et al., 1984; Bloomfield, 1968; Carter and Bennett, 1973; Daly, 1986; Kröner et al., 2001). In northern Mozambique, the axial granulite complex is termed the Unango Group, and comprises calc-alkaline to alkaline granulitic orthogneisses and leucocratic charnockites. These occur in three lithostructural units, the Lichinga, Cuamba and Meponda, (Pinna et al., 1993). In its western part the Meponda Unit contains interlayer of amphibolite facies supracrustal assemblages, the Metangula Group (e.g. Kröner et al., 2001).

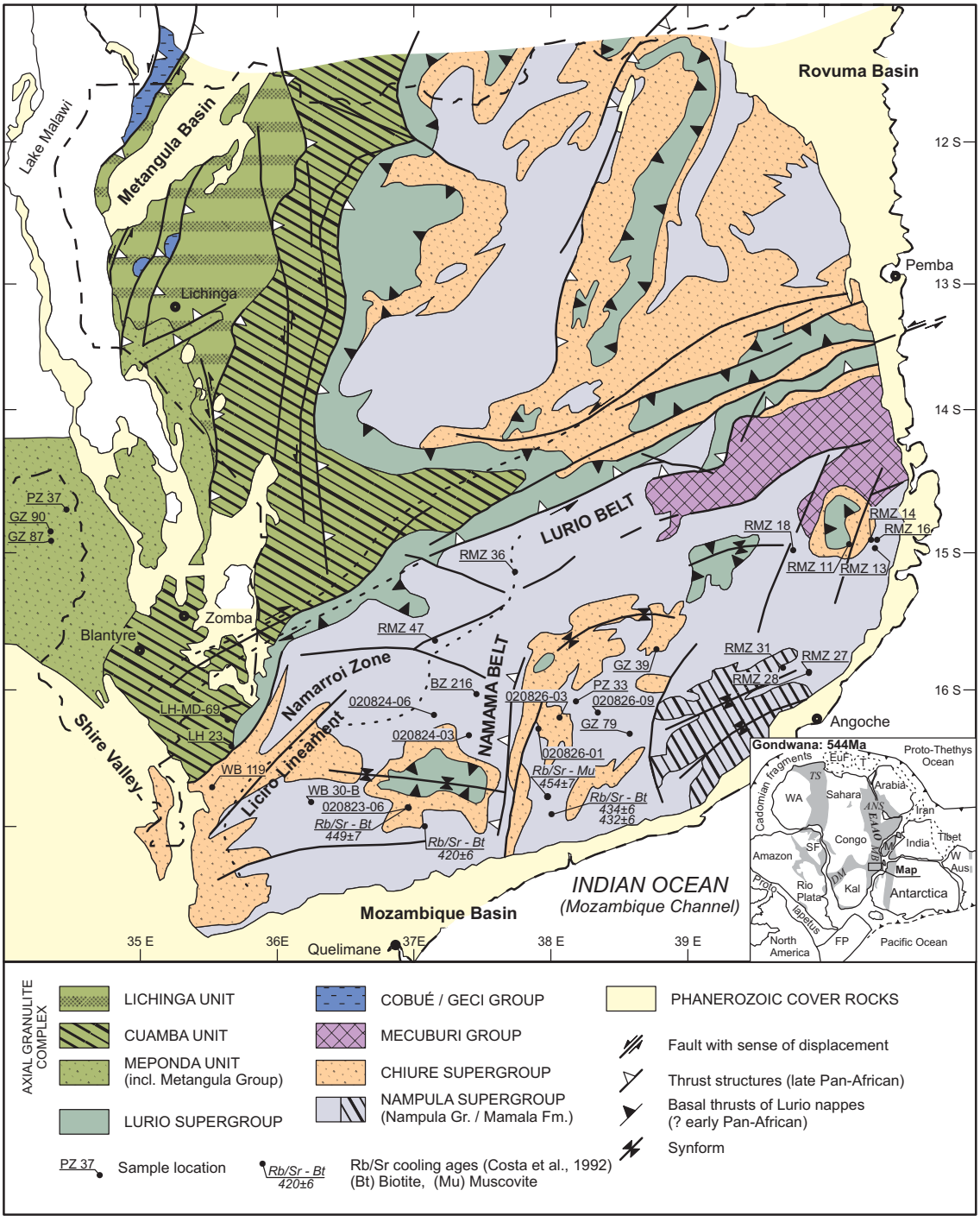

Figure 3.1: Generalized map depicting major litho-tectonic units of the crystalline basement in northern Mozambique and southern Malawi. The map was modified after Pinna et al. (1993), Andreoli (1984), Kröner et al. (2001) and Perits et al. (2002) with superimposed locations of samples used for $^{40}Ar/^{39}Ar$ and TFT analyses. The inset depicts Pan-African Mobile Belts (grey) in a Gondwana reconstruction (Kusky et al., 2003, Jacobs and Thomas, 2004). Abbreviations: ANS = Arabian Nubian Shield, DM = Damara Belt, EAAO = East African-Antartic Orogen, EuF = European fragments, FP = Falkland Plateau, Kal = Kalahri craton, M = Madagascar, MB = Mozambique Belt, SF = San Francisco craton, T = Turkey, TS = Trans-Saharan, W Aus = Western Australia, WA = West Africa craton.

The prominent D_{M2} ductile fabrics in the Unango group display oscillating NW-SE to NE-SW trends (Pinna et al., 1993). A static, post-kinematic (D_{M2}) granulite facies metamorphism is dated between 571-549 Ma, based on U/Pb Sensitive High Resolution Ion Micro-Probe (SHRIMP) and Pb/Pb evaporation analyses of individual metamorphic zircon grains (Kröner et al., 2001). Isobaric cooling led to a subsequent strain-free retrograde amphibolite facies overprint (Kröner et al., 2001; Pinna et al., 1993). Post D_{M2} ductile, amphibolite facies deformations D_{P1}, D_{P2} and D_{P3} of likely Pan-African age, exemplified in the Geci Group (Lulin, 1985), are mainly confined to transpressive thrust zones ranging in trends from ENE-WSW to NW-SE (e.g. Costa et al., 1992).

3.2.2 The eastern domain and the Lurio Belt foreland

The eastern domain is subdivided into a northern and southern basement region by the ENE-WSE trending Lurio Belt (Fig. 1), which extends from the Indian Ocean into southern Malawi (Cadoppi et al., 1987; Kröner et al., 1997; Pinna et al., 1993). This belt is a discontinuous high-strain zone of dismembered layers, pods and lenses of granulite facies rocks (Thomas, 2006). In the area studied (Fig. 3.1), the basement consists of the following units (see also Pinna et al., 1993; Costa et al., 1992; and references therein).

Nampula Supergroup: Amphibolite facies "basement" (*Mocuba Complex* of Costa et al., 1992) is composed of meta-granitoid biotite-hornblende gneisses, meta-basic dykes, concordant leucocratic granite-gneiss bodies, and migmatites, plus charnockites in the Namarroi zone. Autochthon migmatic leucocratic gneisses of the *Mamala Formation* rest unconformably on the "basement" and are interpreted as meta-rhyolites.

Chiure Supergroup: These medium to high grade amphibolite facies (*Rio Molocue Group* of Sacci et al., 1984) allochthonous supracrustals cover the Nampula Supergroup and comprise metasedimentary composites, leucocratic paragneisses and meta-mafic lithologies.

Mecuburi Group: This autochthonous supracrustal sequence (*Cavarro Formation* of Sacci et al., 1984) covers the Nampula Supergroup in the east of the southern basement (Fig. 1) and consists of amphibolitic leucogneisses that contain basal meta-sediments.

Granulite Klippen: Allochthonous ortho- and paragneisses of granulite to high grade amphibolite facies rest in synforms as unrooted klippen on the Nampula and Chiure Supergroup.

Late to post-kinematic Pan-African intrusions: Gabbroic to granitic intrusives of late Pan-African age (c. 500 Ma) cross cut all previous units. Some bodies exhibit weak, linear fabrics and elliptic shapes that parallel the Lurio Belt trend. It is interpreted to indicate their syn- to late-kinematic emplacement (Pinna et al., 1993). Rb/Sr biotite cooling ages (Fig. 3.1) range between 420-434 Ma (Costa et al., 1992; Sacchi et al., 1984). Undeformed pegmatites occurrences in the southern basement are largely regarded as Pan-African in age (Afonso, 1976; Araujo, 1976; Costa et al., 1992) and Costa et al. (1992) reported a Rb/Sr muscovite age of 454 ± 7 Ma (Fig. 3.1).

The principle D_{M2} ductile basement fabrics display easterly, NE-SW to NW-SE oscillating trends; broadly parallel the Lurio Belt (Pinna et al., 1993). Curvilinear basin and dome structures are observed in the Mocuba Complex (Cadoppi et al., 1987; Sacchi et al., 1984). Pb/Pb evaporation and U/Pb SHRIMP ages of c. 615 Ma from single metamorphic zircon grains are interpreted to date the syn-D_{M2} granulite facies metamorphism in the southern basement and the Lurio Belt (Kröner et al., 1997). It is post-dated by an temporally unconstrained retrograde amphibolite facies overprint (Pinna et al., 1993). One Rb/Sr biotite cooling age of 449 ± 7 Ma is reported from a meta-granitoid of the Nampula Supergroup (Costa et al., 1992) (Fig. 1).

The NNE-SSW trending Namama Thrust Belt (NTB) in the central southern basement (Fig. 1) displays a series of thrust sheets, imbricate stacks and indicates eastward thrusting. It alters the main ductile fabric (D_{M2} of Pinna et al., 1993) at all scales into a strongly E-W trending ductile fabrics (Cadoppi et al., 1987) and for the purposes of distinction is hereby termed $D_{N1.}$ The NTB is considered to be younger than the Lurio Belt (Cadoppi et al., 1987) and probably of Pan-African age (Sacchi et al., 2000). Across the NTB (from west to east) a post-kinematic (D_{N1}) increase from amphibolite to granulite metamorphic facies assemblages is attributed to thrusting and crustal stacking (Cadoppi et al., 1987).

3.2.3 Late Palaeozoic to Early Mesozoic intracontinental rift basin

In the Late Carboniferous to Late Triassic/Early Jurassic, the regional tectonic regime of Gondwana was governed by compressional stresses due to accretion along its southern margin and by tensional stress regimes in the northeast. Latter propagated from the diverging southern Tethyan margin southwards into the supercontinent (Wopfner, 2002). Within the present East African sector it resulted in the formation of graben and subsequent extended intracratonic rift structures filled with thick, mainly terrigenous sedimentary deposits (Karoo Group equivalents). These deposits display remarkable similarities across central east and north eastern Africa, indicating an evolution controlled by similar forces (Reeves et al., 2002; Visser and Praekelt, 1996; Wopfner, 1993, 1994). In the entire region, Late Triassic successions are terminated by a major unconformity. This is interpreted to reflect the incipient Gondwana break-up and to mark the termination of the intracratonic rift stage (Catuneanu et al., 2005 and references therein).

West of the north Mozambican basement, the oldest Karoo basin infillings are preserved in the transtensional Mwabvi and Lengwe Basins (Shire Valley; Fig. 3.2) and are Early/Late Permian (Late Ecca-Early Beaufort) in age. Syn-sedimentary faulting and the initiation of the sinistral Zambesi pre-transform system occurred in response to a prominent NW-SE and a subordinate NE-SW tensional stress fields (Castaing, 1991). Terrestrial Karoo sedimentation probably lasted until the Late Permian (Early Beaufort). Late Triassic/Early Jurassic clastic sediments, with Stormberg Group affinities (Karoo Supergroup) and were followed by the deposition of fissure type basaltic lava flows of probable Early Jurassic age (Castaing, 1991; Habgood, 1963). Within the Cabora Bassa Basin (Fig. 3.2) incipient Karoo sedimentation coincides with tectonic activity in the Early Permian (Catuneanu et al., 2005 and references therein) and is probably linked to the evolution of the Zambesi pre-transform system (Castaing, 1991). The Permian-Triassic boundary strata are not preserved and solely younger Permo-Triassic to Early Jurassic sediments are found (Johnson et al., 1996). In the Metangula Basin in northern Mozambique, earliest Karoo sedimentation and earliest rifting commenced in the Early Permian and sedimentation lasted until the Middle Triassic (Catuneanu et al., 2005; Verniers et al., 1989). Distinct NW-SE trending graben-like faulting occurred during the

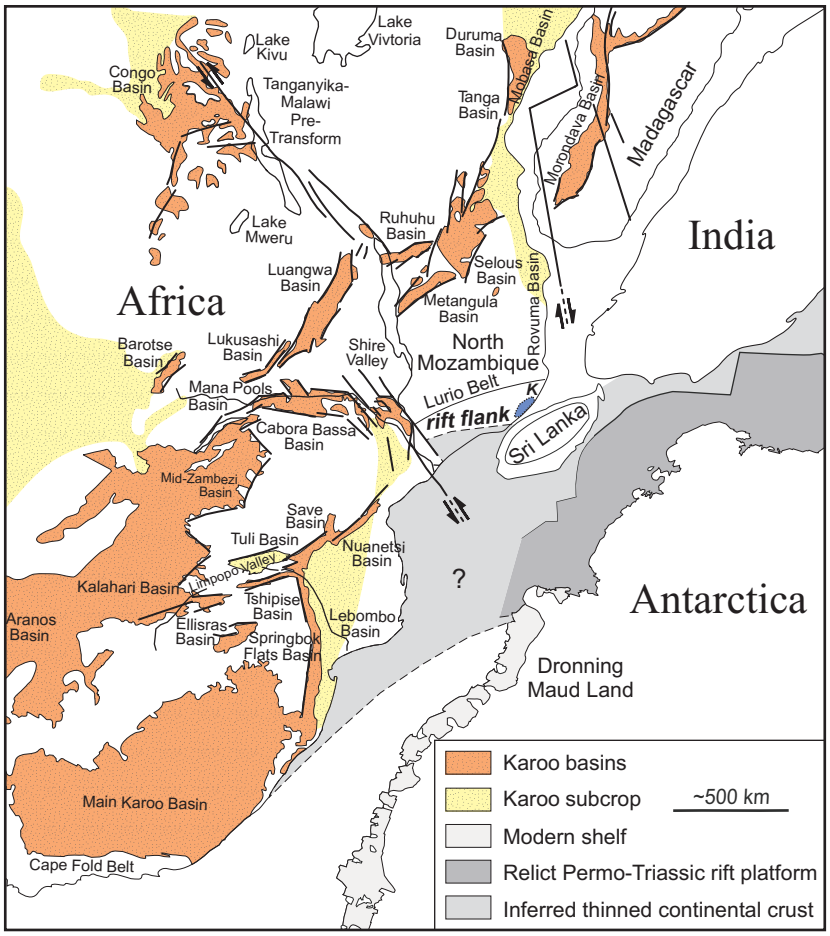

Figure 3.2: Illustrations of the distribution of the Karoo basins in central Gondwana. It also depicts the north Mozambican rift structure and its westward extension into the Middle Zambezi Basin as well as a possible eastward linkage with proposed Permo-Triassic rift basin between India and Antarctic (Harrowfield et al., 2005). Dashed lines represent supposed boundaries. Intercontinental white areas are thinned continental crust. *K* represents isolated outcrops of Karoo age volcanics of c.180-160 Ma in age (Grantham et al., 2005b; Jaritz et al., 1977). The map was compiled and modified after Castaing, 1991; Catuneanu et al., 2005 and Harrowfield et al., 2005.

Late Permian/Early Triassic (Verniers et al., 1989). In south-eastern Tanzania, active normal faulting along the NW margin of the Selous Basin (Uluguru Horst) occurred in the Late Permian and Karoo sediment infill comprises Late Permian to Late Triassic deposits, though older rift-related Karoo deposits are inferred at depth (Wopfner and Kaaya, 1991). In south-west Madagascar, intracontinental Karoo basins contain Late Carboniferous/Early Permian to Late Triassic strata (Besairie and Collignon, 1972). Earliest pull-apart basins formed along NE-SW trending zones of sinistral strike slip

deformation in the Early-Late Permian. During Permo-Trissic times transtension stress regimes developed. From the Early Triassic onwards a NW-SE tensional stress field prevailed and resulted in increasing formation of orthogonal half graben (e.g. Morondava Basin) (Schandelmeier et al., 2004).

3.2.4 Marginal rift basins

The Southern Rovuma Basin (Fig. 3.1 and 3.2) is located along the north-eastern Mozambican basement and represents the southern termination of the pericratonic East African marginal basin. Sedimentary deposits comprise Middle Jurassic to Cenozoic strata and Karoo age deposits are inferred below, based on seismic correlations with the Tanzanian Selous Basin (Salman and Abdula, 1995). The Mozambique Basin is located to the south of the basement (Fig. 3.1) and contains basin infillings ranging from volcanic rocks of Early Jurassic age to Cenozoic sedimentary deposits. Older Karoo related sedimentary deposits are not evident but their presence is inferred underneath the Mesozoic strata (Salman and Abdula, 1995).

3.3 Analytical procedures

3.3.1 $^{40}Ar/^{39}Ar$ Analysis

Optical thin section inspection (10-100× magnification) revealed that all samples contain fresh, unaltered mineral phases and euhedral to subhedral crystals of hornblende (BZ 216, GZ 90, PZ 37, RMZ 11, RMZ 13, RMZ 45) and biotite (GZ 39, RMZ 11, RMZ 13) with grain sizes ranging up to 1.5 mm and 1.2 mm, respectively. All samples, with exception of RMZ 45 contain minor amounts of hornblende (< 2-5 %) or biotite (< 3 %) partially intergrown with other mineral phases. Hornblende samples BZ 216, GZ 90, PZ 37, RMZ 11 and RMZ 13 yield opaque inclusions. Inclusions of titanite were observed in hornblende samples BZ 216, GZ 90, RMZ 13 and inclusions of apatite were found in hornblende samples GZ 90 and PZ 37. Biotite samples GZ 39, RMZ 13 and RMZ 18 contained inclusions of opaques and apatite. Zircon and zircon plus titanite inclusions were detected in biotite samples RMZ 18 and RMZ 13, respectively.

Hornblende and biotite grains were extracted from the rock samples by crushing, sieving, magnetic separation and hand picking. The grains were then cleaned in methanol, followed by deionised water in an ultrasonic bath. Approximately 300 μm-sized grains were selected from the 150-315 μm sieve fraction. The mineral separates were individually wrapped in aluminium foil packets, and all the samples were inserted into an aluminium irradiation package. Biotite age standard Tinto B [(K/Ar age of 409.2 ± 0.7 Ma (Rex and Guise, 1995)] was placed at 5 mm intervals along the package to monitor the neutron flux gradient. The package was Cd-shielded and irradiated in the 5C position of the McMaster University Nuclear Reactor, Hamilton, Canada, for 90 h. Upon return, the samples were loaded into an ultra-high vacuum laser chamber fitted with a Kovar viewport and baked to 120°C overnight to remove adsorbed atmospheric argon from the samples and chamber walls.

A 110 W Spectron Laser Systems continuous-wave neodymium-yttrium-aluminium-garnet (CW-Nd-YAG) (λ = 1064 nm) infra-red laser, fitted with a TEM00 aperture, was used to slowly laser step-heat the mineral samples. The laser was fired through a Merchantek computer-controlled X-Y-Z sample chamber stage and microscope system, fitted with a high-resolution CCD camera, 6x computer controlled zoom, high magnification objective lens, and two light sources for sample illumination. The gases released by laser heating were 'gettered' using 3 SAES AP10 getter pumps to remove all active gases. The remaining noble gases were equilibrated into a high sensitivity mass spectrometer (MAP 215-50), operated at a resolution of 570, and fitted with a Balzers SEV 217 multiplier. The automated extraction and data acquisition system was computer controlled, using a LabView program. The mean 5 minute extraction system blank Ar isotope measurements obtained during the experiments were 1.18×10^{-12}, 1.32×10^{-14}, 4.65×10^{-15}, 6.70×10^{-14}, and 1.43×10^{-14} cm^3 STP (standard temperature and pressure) for ^{40}Ar, ^{39}Ar, ^{38}Ar, ^{37}Ar, and ^{36}Ar respectively. The Ar isotope analyses were corrected for system blanks, mass discrimination ($^{40}Ar/^{36}Ar = 281.0$), radioactive decay of ^{37}Ar, and minor interference reactions from Ca and K ($^{39}Ar/^{37}Ar_{Ca} = 0.00065$, $^{36}Ar/^{37}Ar_{Ca} = 0.000255$, and $^{40}Ar/^{39}Ar_K = 0.0015$). Errors quoted on the ages in the Tabs. 1 and 2 are 1 sigma and include the *J* value error. The $^{40}Ar/^{39}Ar$ ages were calculated using the decay constant of Steiger and Jäger, 1977. *J* values and errors are

noted on the sample $^{40}Ar/^{39}Ar$ data tables (Tab. 2). The $^{40}Ar/^{39}Ar$ data presented in this study were undertaken at the Western Australian Argon Isotope Facility (Curtin University and the University of Western Australia).

In order to assess the geological significance of $^{40}Ar/^{39}Ar$ ages, a series of age spectra and $^{37}Ar/^{39}Ar$ plots are presented. Isoplot version 2.49 (Ludwig, 2001) was used to plot the figures and calculate the ages (Figs. 3.3a-f and 3.4a-c). Within $^{40}Ar/^{39}Ar$ age spectra, age plateaus were defined according to criteria outlined by Ludwig (2001). $^{40}Ar/^{39}Ar$ inverse isochron ages were calculated by fitting a negative regression line through the data points plotted on a $^{36}Ar/^{40}Ar$ versus $^{39}Ar/^{40}Ar$ inverse isochron diagram, using York's algorithm (York, 1969) and quoted with 95% confidence errors. In assessing whether all the data fit within the estimated error limits, indices of goodness of fit are used, including Mean Squared Weighted Deviates (MSWD) (McIntyre et al., 1966). MSWD values were calculated for weighted mean ages and inverse isochrons with n-1 and n-2 degrees of freedom, respectively (Ludwig, 2001). MSWD values ranging between 1 and 2.5 are accepted as meaningful goodness of fit indicators (Roddick, 1978). MSWD values of > 1 generally indicate either underestimated errors or the presence of non-analytical scatter whereas values of < 1 suggest overestimated analytical errors. Weighted mean ages were calculated using both the analytical and *J* value errors on a series of pseudo-plateau steps, quoted with 95% confidence errors. The total fusion age is an unweighted mean age of all the steps including the analytical and *J* value errors, quoted with 1 sigma errors in the $^{40}Ar/^{39}Ar$ data tables (Tabs. 3.1 and 3.2).

3.3.2 Titanite fission track analysis

Titanite separates with grain sizes of 150-315 μm were extracted using conventional preparation techniques including crushing, sieving, Wilfley table, heavy liquid and magnetic separation. Batches of titanite grains were embedded in epoxy resin, then ground and polished to expose internal crystal surfaces. The titanite fission tracks (TFT) were revealed by etching the polished crystal mounts in an acid solution of 1 part concentrated HF, 2 parts concentrated HNO_3, 3 parts concentrated HCl, and 6 parts H_2O. Samples were etched individually at room temperature for 17-27 minutes (Naeser

and McKee, 1970). Distinctly recognizable terminations of confined tracks were used as an evaluation criterion for sufficient fission track etching. All the samples were loaded into aluminium capsules and irradiated at the FRM II research reactor facility in Munich-Garching, Germany. Corning dosimeter glasses were used to monitor the neutron fluence gradient. An irradiation time of 60 seconds was applied to obtain a total thermal neutron fluence of 0.5×10^{16} neutrons/cm^{-2}. Induced tracks were recorded in white micas following the external detector approach (Gleadow, 1981) and revealed after irradiation by etching the micas for 15 minutes in 40% HF at 21 ± 1°C. Track densities in mounts and micas were measured using a Zeiss® Axiophot microscope equipped with a Kintec® stage, a Calcomp® digitizer, and a drawing tube operated by the FT-Stage software (Dumitru, 1991). Dry objectives, calibrated against stage micrometers, were used for track density counts in transmitted light at 2000x magnification. Fission track ages were calculated according to the zeta calibration method (Galbraith and Laslett, 1993; Hurford, 1990) using a weighted mean zeta factor (ζ) of 134.5 ± 4.1 (M.D.) obtained from Fish Canyon Tuff and Mt. Dromedary TFT age standards. Errors are quoted at the 1σ level and were derived according to conventional method (Green, 1981).

3.4 Results

3.4.1 $^{40}Ar/^{39}Ar$ hornblende analysis

The $^{40}Ar/^{39}Ar$ results of six hornblende samples (BZ 216, GZ 90, PZ 37, RMZ 11, RMZ 13 and RMZ 45) are presented in Tab. 1, 2 and Fig. 3. All hornblende samples exhibit disturbed age spectra and yield no plateau or inverse isochron ages. All the hornblende samples contained very high $^{40}Ar^*$ concentrations of 95-99 % (Tab. 3.2), with only the occasional presence of 11-36 % atmospheric ^{40}Ar in the first low-temperature steps of sample PZ 37 (Tab. 3.2). The predominance of $^{40}Ar^*$ results in the limited distribution of data points in the inverse isochron plots that yield either no or statistically invalid inverse isochron ages (Tab. 3.1). Therefore inverse isochron plots are omitted.

Pseudo-plateau and weighted mean ages of 462.5 ± 2.2 Ma, 550.7 ± 3.2 Ma, 542.1 ± 0.3 Ma, 473.8 ± 2.4 Ma, 475.8 ± 2.8 Ma, and 455.5 ± 6.2 Ma are obtained for

samples BZ2 16, GZ 90, PZ 37, RMZ 13, RMZ 11 and RMZ 45, respectively. These ages are statically unreliable as they either comprise less than 45 % of the cumulative ^{39}Ar (BZ 216, PZ 37) or yield MSWD and probability values higher than 2.5 and lower than 0.05 (GZ 90, RMZ 11, RMZ 13, RMZ 45), respectively.

All the hornblende samples preserved old ages in the low temperature steps (Figs. 3a-f) with some of these ages being anomalously old up to 3.8 Ga (e.g., sample BZ 216, Fig. 3a), thus indicating the presence of excess Ar in the samples. Amphibolite samples BZ 216, PZ 37 and GZ 90 yield large age differences of c. 3.4 Ga, 718 Ma and 162 Ma between their oldest low-temperature step ages of 3869.4 ± 12.9, 1259.5 ± 7.9 and 712.8 ± 3.2 Ma and their weighted mean ages of 462.5 ± 2.2, 541.9 ± 2.7 and 550.7 ± 3.2 Ma, respectively. Samples BZ 216 and PZ 37 yield total fusion ages of 1003.3 ± 1133.6 and 651.7 ± 210.1 Ma that are distinctly older than their corresponding weighted mean ages of 462.5 ± 2.2 and 541.9 ± 2.7 Ma, respectively. This suggests the incorporation of significant amounts of excess ^{40}Ar in these samples.

3.4.2 ^{40}Ar/^{39}Ar biotite analysis

The ^{40}Ar/^{39}Ar results of three biotite samples GZ 39, RMZ 18 and RMZ 13 are given in Figs. 3.4a-c, Tabs. 3.1 and 3.2. The biotite samples contain high concentrations of ^{40}Ar* (92-100 %) with only the occasional presence of 11-28 % atmospheric ^{40}Ar in the first low-temperature steps of samples GZ 39 and RMZ 13 (Tab. 3.2) linked to the youngest preserved ^{40}Ar/^{39}Ar ages in these two samples. The predominance of ^{40}Ar* resulted in the limited distribution of data points on the inverse isochron plots, which yield either no or statistically invalid inverse isochron ages (Tab. 3.1). Therefore inverse isochron plots are omitted.

Biotite samples GZ 39 and RMZ 18 yield plateau ages of 443.8 ± 0.4 Ma and 428.4 ± 0.3 Ma (Tab. 3.1). The highest-temperature steps (i.e. > 80 % cumulative ^{39}Ar) of both samples revealed discordant ^{40}Ar/^{39}Ar age spectra (Figs. 3.4a, 3.4c). Sample RMZ 13 yielded a discordant ^{40}Ar/^{39}Ar age spectrum (Fig. 3.4b) with no plateau or inverse isochron age. A calculated weighted mean age of 448.2 ± 3.7 Ma (steps 2-6) is consistent with the sample's total fusion age (Tab. 3.1).

Table 3.1: Results of $^{40}Ar/^{39}Ar$ hornblende and biotite analyses

Step	$^{36}Ar/^{39}Ar$	± 1σ	$^{37}Ar/^{39}Ar$	± 1σ	$^{40}Ar^*/^{39}Ar$	± 1σ	% $^{40}Ar^*$	Cum. % 39Ar	Age (Ma)	± 1σ
Hornblende										
BZ216										
1	0.031968	0.006445	0.986919	0.028020	349.732503	2.212949	97.37	0.20	3869.41	12.85
2	0.006243	0.001156	2.728420	0.021142	220.124316	0.512934	99.17	1.33	3154.44	8.23
3	0.001416	0.000095	3.399730	0.017253	23.044950	0.031808	98.22	8.18	727.71	3.11
4	0.001222	0.000085	3.543060	0.025649	15.612262	0.030807	97.74	15.84	523.42	2.45
5	0.000720	0.000241	3.791943	0.031466	13.846273	0.071766	98.49	21.24	471.28	2.99
6	0.001581	0.000122	3.161398	0.045993	13.558327	0.036948	96.67	31.88	462.64	2.33
7	0.001013	0.000050	3.641793	0.036380	14.773656	0.015967	98.01	46.47	498.85	2.23
8	0.001071	0.000030	3.812191	0.042203	14.231090	0.014135	97.82	57.47	482.77	2.16
9	0.001079	0.000068	3.762541	0.037817	13.613811	0.022209	97.71	67.05	464.31	2.16
10	0.000603	0.000074	4.005727	0.024829	13.470823	0.025718	98.69	79.48	460.00	2.18
11	0.001267	0.000146	3.625625	0.016354	13.527152	0.048550	97.31	83.94	461.70	2.51
12	0.000653	0.000041	3.957767	0.020543	13.591164	0.016215	98.60	100.00	463.63	2.11
Total fusion age = 1003.4 ± 1133.6 Ma, *J* value = 0.021560 ± 0.000108										
GZ90										
1	0.002301	0.000146	2.456882	0.016064	22.476271	0.047316	97.06	2.59	712.84	3.20
2	0.000992	0.000064	2.387667	0.015752	18.514820	0.049140	98.44	8.52	605.95	2.92
3	0.000362	0.000110	2.456473	0.026630	16.822836	0.043184	99.37	11.97	558.29	2.70
4	0.000538	0.000045	2.316737	0.022783	16.721306	0.018715	99.06	20.38	555.39	2.45
5	0.000500	0.000021	2.495926	0.010075	16.737354	0.021711	99.13	29.23	555.85	2.48
6	0.000410	0.000014	2.476219	0.006787	16.653821	0.014297	99.28	43.26	553.46	2.42
7	0.000238	0.000031	2.590435	0.007219	16.399811	0.016299	99.57	49.38	546.17	2.41
8	0.000403	0.000000	2.400349	0.005985	16.592527	0.004636	99.29	61.34	551.70	2.38
9	0.000471	0.000033	2.202266	0.020097	16.346616	0.020737	99.16	67.03	544.65	2.43
10	0.000224	0.000018	2.476167	0.017132	16.456251	0.011906	99.60	77.46	547.80	2.39
11	0.000339	0.000020	2.408623	0.009644	16.677319	0.022609	99.40	86.81	554.13	2.48
12	0.000363	0.000014	2.468989	0.020111	16.467898	0.014588	99.35	100.00	548.13	2.40
Total fusion age = 569.5 ± 45.9 Ma, *J* value = 0.021559 ± 0.000108										
PZ37										
1	0.027605	0.000105	4.795990	0.052506	27.301070	0.104714	76.99	0.56	834.98	4.22
2	0.089966	0.001109	5.335098	0.045883	46.849253	0.335388	63.80	1.18	1259.48	7.92
3	0.012678	0.000028	6.435820	0.032841	29.971019	0.069612	88.89	2.51	899.20	3.91
4	0.003188	0.000004	5.030265	0.049770	17.610746	0.024486	94.92	5.54	580.62	2.58
5	0.001446	0.000357	4.687974	0.026548	16.655755	0.106100	97.50	10.29	553.49	3.86
6	0.001057	0.000154	4.498755	0.018551	16.158381	0.046009	98.10	22.14	539.20	2.69
7	0.001356	0.000226	4.439132	0.031948	16.870235	0.073552	97.68	25.14	559.62	3.20
8	0.000966	0.000064	4.155384	0.034079	16.280563	0.021442	98.28	40.21	542.72	2.43
9	0.000912	0.000025	4.536082	0.015826	16.181961	0.008882	98.36	53.81	539.88	2.35
10	0.001674	0.000077	4.052126	0.016037	16.098877	0.024255	97.02	58.20	537.48	2.43
11	0.000998	0.000078	3.948953	0.030853	16.240262	0.026588	98.22	73.93	541.56	2.47
12	0.000774	0.000060	4.271916	0.035165	16.238207	0.020075	98.61	90.86	541.50	2.41
13	0.000541	0.000000	4.276148	0.034619	16.272831	0.014912	99.03	100.00	542.50	2.39
Total fusion age = 651.7 ± 210.1 Ma, *J* value = 0.021558 ± 0.000108										
RMZ11										
1	0.002071	0.000001	1.805152	0.011411	16.135771	0.010117	96.35	3.77	538.51	2.35
2	0.000713	0.000000	1.631983	0.013544	13.703791	0.012508	98.49	9.29	466.93	2.10
3	0.000196	0.000000	2.083660	0.006827	13.986771	0.008592	99.59	13.84	475.41	2.11
4	0.000419	0.000000	1.799740	0.028872	13.934258	0.015722	99.12	21.78	473.84	2.14
5	0.000167	0.000054	2.161815	0.020805	14.043136	0.022280	99.65	37.09	477.09	2.20
6	0.000367	0.000055	1.895692	0.008180	14.019303	0.017721	99.23	50.47	476.38	2.16
7	0.000255	0.000000	2.032152	0.006206	13.951377	0.011752	99.46	59.96	474.35	2.12
8	0.000549	0.000073	1.849881	0.007221	13.751567	0.023784	98.84	65.00	468.37	2.19
9	0.000482	0.000001	1.478668	0.049551	13.825448	0.040317	98.98	73.12	470.58	2.40
10	0.000000	0.000000	2.106406	0.013741	14.004789	0.016991	100.00	80.96	475.95	2.16
11	0.000167	0.000000	1.862911	0.010342	13.996620	0.006078	99.65	83.82	475.70	2.10
12	0.000340	0.000000	1.957515	0.008483	14.028065	0.007438	99.29	100.00	476.64	2.11
Total fusion age = 479.2 ± 18.2 Ma, *J* value = 0.021556 ± 0.000108										
RMZ13										
1	0.002836	0.000212	2.988312	0.013327	17.243466	0.064602	95.37	3.00	570.16	3.06
2	0.001289	0.000001	3.046942	0.036717	14.266128	0.014036	97.40	9.45	483.72	2.17
3	0.000327	0.000046	3.205138	0.022329	14.047255	0.016597	99.32	16.39	477.20	2.16
4	0.000273	0.000085	3.245300	0.025361	14.006588	0.032799	99.43	20.14	475.98	2.31
5	0.000507	0.000095	3.081394	0.031997	13.959224	0.033506	98.94	30.21	474.57	2.32
6	0.000848	0.000081	2.728519	0.026984	13.908267	0.028004	98.23	44.40	473.04	2.25
7	0.000717	0.000078	2.964814	0.034257	13.879942	0.026517	98.50	52.59	472.20	2.23
8	0.000721	0.000090	2.899146	0.062228	14.204426	0.039599	98.52	62.59	481.88	2.42
9	0.000562	0.000000	3.462113	0.015176	13.977041	0.010603	98.83	73.58	475.10	2.12
10	0.000930	0.000080	2.931609	0.028501	13.830189	0.027456	98.05	81.52	470.71	2.23
11	0.000740	0.000119	3.175439	0.021192	13.874109	0.036536	98.45	86.85	472.02	2.35
12	0.001685	0.000195	2.573737	0.024448	13.558608	0.058774	96.46	90.11	462.55	2.70
13	0.000070	0.000091	3.499486	0.011615	14.071987	0.028740	99.85	100.00	477.94	2.27
Total fusion age = 482.1 ± 25.9 Ma, *J* value = 0.021555 ± 0.000108										

Tab. 3.1: continued

Step	$^{36}Ar/^{39}Ar$	± 1σ	$^{37}Ar/^{39}Ar$	± 1σ	$^{40}Ar^*/^{39}Ar$	± 1σ	% $^{40}Ar^*$	Cum. % ^{39}Ar	Age (Ma)	± 1σ
Hornblende										
RMZ13										
1	0.002836	0.000212	2.988312	0.013327	17.243466	0.064602	95.37	3.00	570.16	3.06
2	0.001289	0.000001	3.046942	0.036717	14.266128	0.014036	97.40	9.45	483.72	2.17
3	0.000327	0.000046	3.205138	0.022329	14.047255	0.016597	99.32	16.39	477.20	2.16
4	0.000273	0.000085	3.245300	0.025361	14.006588	0.032799	99.43	20.14	475.98	2.31
5	0.000507	0.000095	3.081394	0.031997	13.959224	0.033506	98.94	30.21	474.57	2.32
6	0.000848	0.000081	2.728519	0.026984	13.908267	0.028004	98.23	44.40	473.04	2.25
7	0.000717	0.000078	2.964814	0.034257	13.879942	0.026517	98.50	52.59	472.20	2.23
8	0.000721	0.000090	2.899146	0.062228	14.204426	0.039599	98.52	62.59	481.88	2.42
9	0.000562	0.000000	3.462113	0.015176	13.977041	0.010603	98.83	73.58	475.10	2.12
10	0.000930	0.000080	2.931609	0.028501	13.830189	0.027456	98.05	81.52	470.71	2.23
11	0.000740	0.000119	3.175439	0.021192	13.874109	0.036536	98.45	86.85	472.02	2.35
12	0.001685	0.000195	2.573737	0.024448	13.558608	0.058774	96.46	90.11	462.55	2.70
13	0.000070	0.000091	3.499486	0.011615	14.071987	0.028740	99.85	100.00	477.94	2.27
Total fusion age = 482.1 ± 25.9 Ma, *J* value = 0.021555 ± 0.000108										
Irradiation standard used = Tinto B biotite (409.24 ± 0.71 Ma)										
Biotite										
GZ 39										
1	0.011680	0.002009	0.000000	0.000000	8.965713	0.594464	72.20	0.99	318.75	19.43
2	0.003772	0.000539	0.002945	0.021168	12.114483	0.159828	91.57	4.27	418.55	5.27
3	0.000682	0.000076	0.007890	0.002870	12.982153	0.029098	98.47	27.59	445.10	2.17
4	0.000324	0.000108	0.000000	0.000000	12.935932	0.034885	99.27	35.79	443.70	2.24
5	0.000204	0.000068	0.000000	0.000000	12.933735	0.022260	99.54	48.82	443.63	2.08
6	0.000255	0.000064	0.002128	0.002101	12.924705	0.019603	99.42	62.67	443.36	2.06
7	0.000190	0.000048	0.000528	0.001563	12.877354	0.014933	99.57	81.31	441.92	2.02
8	0.000117	0.000040	0.012501	0.002493	12.850149	0.013735	99.73	92.32	441.09	2.00
9	0.000081	0.000085	0.015071	0.005261	12.853508	0.027671	99.81	97.55	441.19	2.13
10	0.000000	0.000000	0.030525	0.006027	13.033229	0.007971	100.00	99.16	446.65	2.00
11	0.001047	0.000001	0.035236	0.011596	12.724409	0.015440	97.63	100.00	437.25	2.00
Total fusion age = 429.2 ± 35.7 Ma, *J* value = 0.021554 ± 0.000108										
RMZ 13										
1	0.005050	0.000103	0.000000	0.000000	12.300142	0.037992	89.18	3.23	424.31	2.23
2	0.000920	0.000013	0.001692	0.000003	13.107143	0.020349	97.97	28.88	448.95	2.08
3	0.000743	0.000000	0.006078	0.001491	12.937691	0.008148	98.33	39.60	443.81	1.99
4	0.000119	0.000000	0.004797	0.000963	13.110753	0.007466	99.73	56.21	449.06	2.00
5	0.000102	0.000035	0.005773	0.000554	13.185036	0.012573	99.77	85.09	451.31	2.04
6	0.000628	0.000379	0.013758	0.002717	13.066838	0.114919	98.60	87.73	447.73	4.01
7	0.000000	0.000000	0.044075	0.014505	13.474908	0.400574	100.00	88.22	460.07	12.24
8	0.000087	0.000091	0.016849	0.000979	13.064757	0.029675	99.80	95.54	447.67	2.18
9	0.000330	0.000168	0.027560	0.016723	13.347708	0.050315	99.28	99.49	456.23	2.53
10	0.002616	0.001317	0.071897	0.127766	12.481085	0.390841	94.17	100.00	429.87	12.13
Total fusion age = 445.9 ± 10.4 Ma, *J* value = 0.021557 ± 0.000108										
RMZ 18										
1	0.002598	0.000173	0.015448	0.010784	12.685405	0.055949	94.29	2.56	436.05	2.59
2	0.000683	0.000018	0.001561	0.000771	12.522462	0.008021	98.41	27.91	431.06	1.94
3	0.000348	0.000032	0.001412	0.001558	12.428754	0.011991	99.18	55.96	428.19	1.95
4	0.000000	0.000113	0.000000	0.000000	12.462420	0.034782	100.00	63.80	429.22	2.19
5	0.000139	0.000047	0.004156	0.002294	12.442172	0.014372	99.67	82.87	428.60	1.96
6	0.001139	0.000163	0.003685	0.032744	12.230228	0.050871	97.32	85.60	422.09	2.45
7	0.000000	0.000000	0.002661	0.007882	12.435996	0.012731	100.00	96.93	428.41	1.95
8	0.001587	0.000227	0.000000	0.000000	11.963503	0.069610	96.23	98.89	413.87	2.84
9	0.000980	0.000985	0.022325	0.066121	12.234369	0.294736	97.69	99.34	422.22	9.26
10	0.002021	0.000674	0.000000	0.000000	11.628928	0.203067	95.11	100.00	403.49	6.57
Total fusion age = 424.3 ± 9.0 Ma, *J* value = 0.021553 ± 0.000108										
Irradiation standard used = Tinto B biotite (409.24 ± 0.71 Ma)										

See method and analytic chapters for analytical and data processing details.

Table 3.2: Summary of $^{40}Ar/^{39}Ar$ ages for biotite and hornblende samples

Samples					Age spectrum			Inverse isochron				Total fusion	Weighted mean		
ID	Location			Rock type	Age ± 1σ (Ma)	n (N)	MSWD	Age ± 1σ (Ma)	$^{40}Ar / ^{36}Ar$	n	MSWD	Age ± 1σ (Ma)	Age ± 1σ (Ma)	n	MSWD
	Longitude	Latitude	Elevation (m)			% ^{39}Ar	P		intercept		P			% ^{39}Ar	P
Hornblende															
BZ 216	37.44806	-16.03861	428	amphibolite	*no plateau to establish*	*(12)*		*no isochron to regress*				1003.4 ± 1133.6	*462.5 ± 1.1*	*9-12 42.4*	*0.8 0.49*
GZ 90	34.34167	-14.84944	1150	amphibolite	*no plateau to establish*	*(12)*		*514 ± 16*	*3484 ± 1300*	*12*	*7.6 0*	569.5 ± 45.9	*550.7 ± 1.6*	*4-12 88.03*	*3 0.003*
PZ 37	34.45778	-14.68889	1300	amphibolite	*542.05 ± 0.31*	*11-13 (13) 41.8*	*1.2 0.3*	*543.6 ± 2.6*	*216 ± 110*	*11-13*	*0.79 0.37*	651.7 ± 210.1	*541.9 ± 1.35*	*11-13 41.81*	*0.054 0.95*
RMZ 11	40.16833	-14.94222	184	monzonite	*no plateau to establish*	*(12)*		*465.5 ± 3.75*	*1434 ± 250*	*12*	*532 0*	479.2 ± 18.2	*473.8 ± 1.2*	*2-12 80.05*	*2.7 0.03*
RMZ 13	40.37083	-14.91000	117	orthogneiss	*no plateau to establish*	*(13)*		*467.4 ± 2.85*	*719 ± 150*	*2-9*	*7.6 0*	482.1 ± 25.9	*475.8 ± 1.4*	*2-13 90.55*	*3.3 0*
RMZ 45	37.15000	-15.43194	946	gneiss	*no plateau to establish*	*(7)*		*no isochron to regress*				466.9 ± 29.9	*455.5 ± 3.1*	*2-7 92.3*	*7.3 0*
Biotite															
GZ 39	38.76139	-15.71056	271	amphibolitic gneiss	443.79 ± 0.37	3-6 (11) 58.4	0.93 0.42	440.4 ± 1.2	553 ± 160	3-10	0.49 0.82	429.2 ± 35.7	443.9 ± 1.05	3-6 58.39	0.13 0.94
RMZ 13	40.37083	-14.91000	117	orthogneiss	*no plateau to establish*	*(10)*		*449.1 ± 2.65*	*128 ± 50*	*10*	*15 0*	445.9 ± 10.4	448.2 ± 1.85	2-6 55.3	1.9 0.11
RMZ 18	39.75833	-14.98472	317	gneiss	428.42 ± 0.27	3-5 (10) 55.0	0.56 0.57	*427.2 ± 2.35*	*456 ± 150*	*1-5*	*2.9 0.032*	424.3 ± 9.0	428.6 ± 1.15	3-5 54.96	0.062 0.94

N = total number of heating steps, n = number of heating steps used to calculate the plateau age (including the % of ^{39}Ar contributing to the plateau age) or inverse isochron age. MSWD values for plateau ages and inverse isochron ages were calculated with n-1 and with n-2 degrees of freedom, respectively. *Italics:* rejected results due to the plateau ages containing < 50% of the cumulative % ^{39}Ar, disturbed spectra or significant differences of individual steps at 2 σ level [(MSWD > 2.5 and P (probability) < 0.05)].

The first low-temperature steps of GZ 39 and RMZ 13 yielded ages that are younger than the plateau and weighted mean ages (Figs. 3.4b, 3.4c and Tab. 2). Sample RMZ 18 (Fig. 3.4a and Tab. 3.2) exhibits low-temperature step ages that are slightly older than the obtained plateau age.

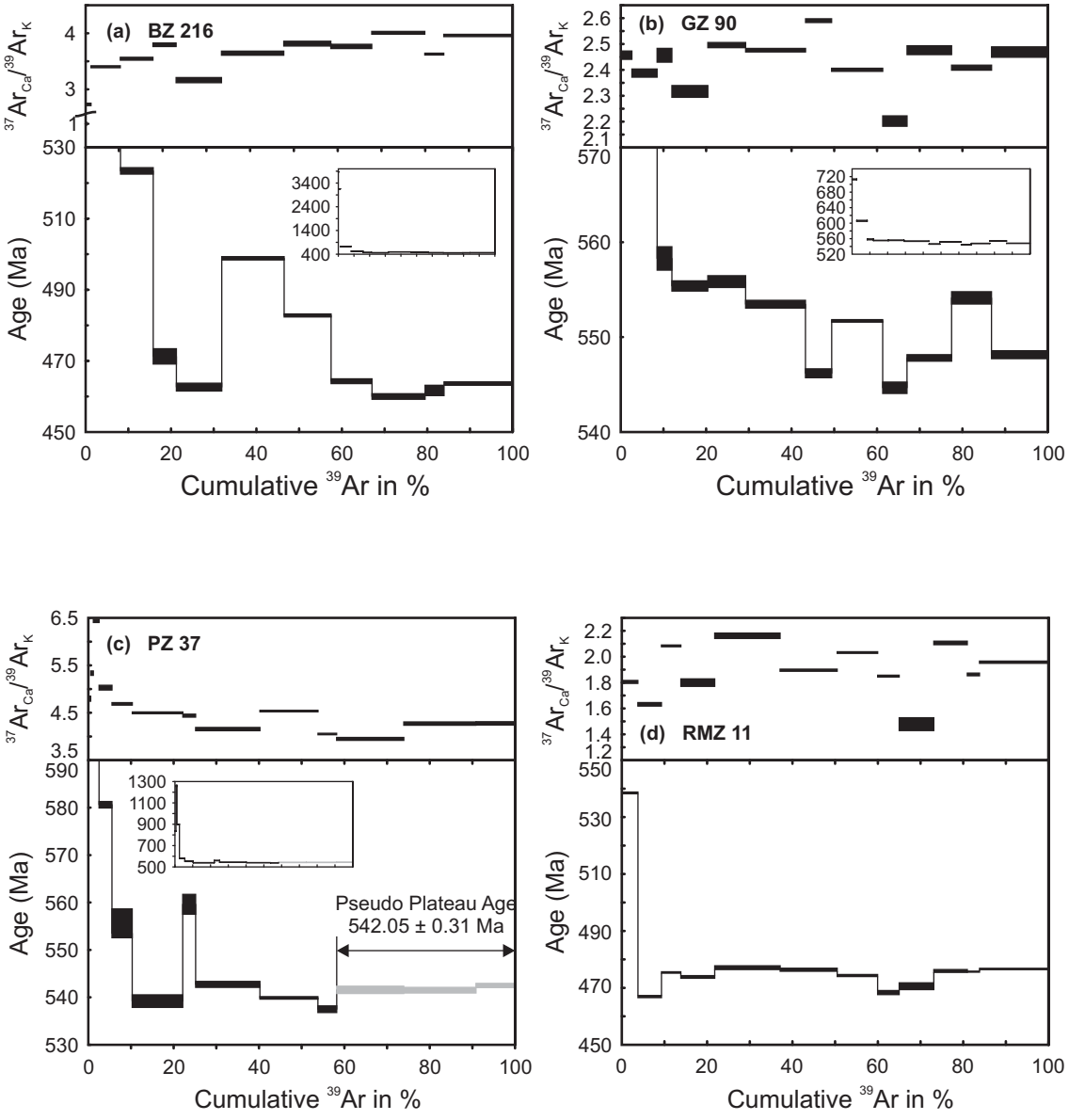

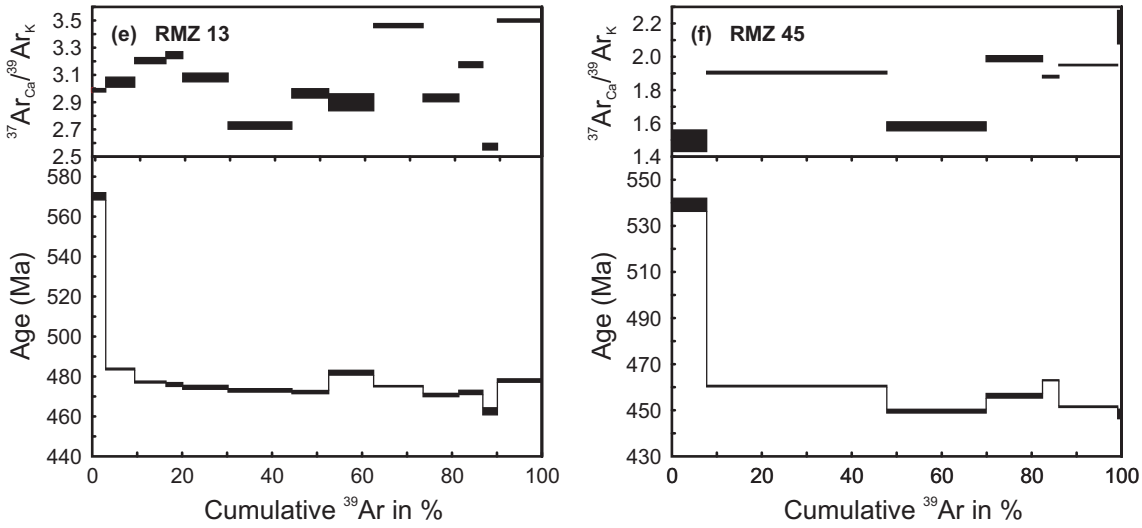

Figure 3.3: $^{37}Ar/^{39}Ar$ and apparent age spectra plots of incremental heating steps from hornblende samples analyses (a-d: previous page and e-f: this page). Insets are presented for samples exhibiting strongly discordant spectra and depict entire age range of incremental heating steps. Errors for each step are ± 1 σ and do not include error of *J* value.

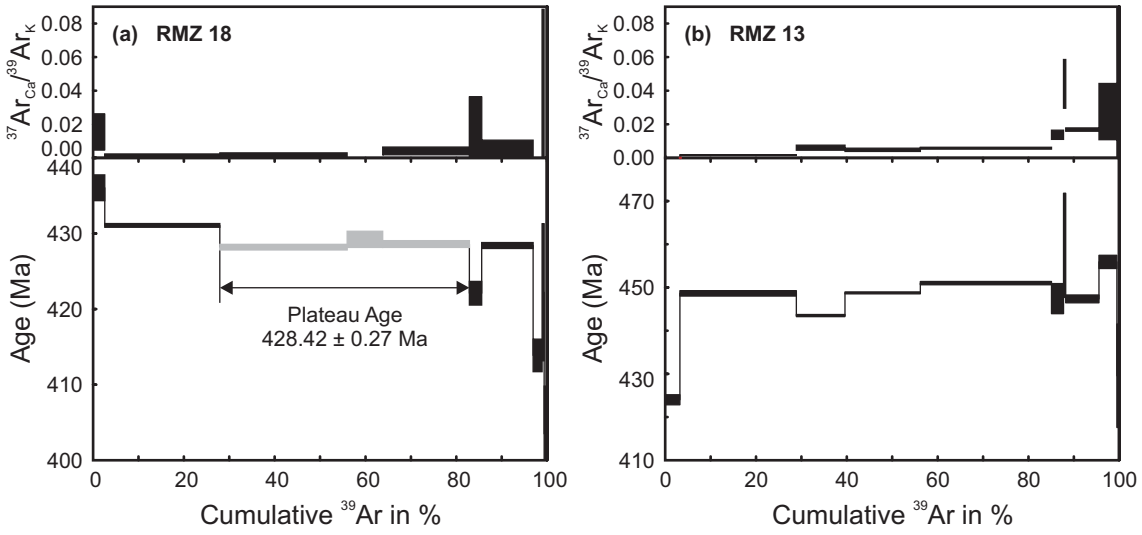

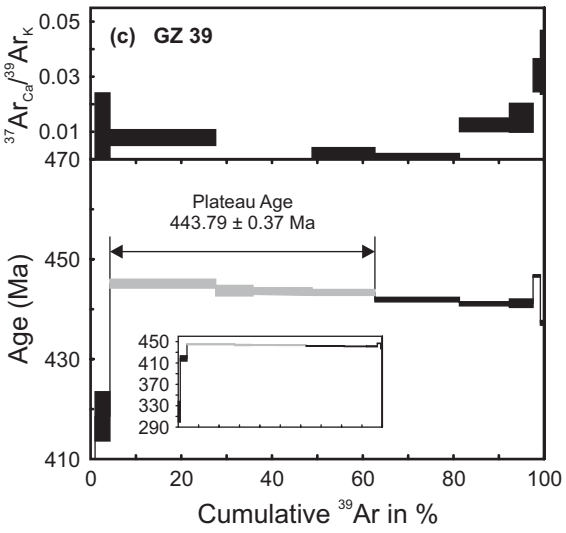

Figure 3.4: $^{37}Ar/^{39}Ar$ and apparent age spectra plots of incremental heating steps from biotite samples analyses (a-b previous page and c: this page). Insets are presented for samples exhibiting strongly discordant spectra and depict entire age range of incremental heating steps. Errors for each step are ± 1 σ and do not include error of *J* value.

3.4.3 Titanite fission track analysis

The ages and analytical details of 27 TFT analyses are presented in Tab. 3.3 and their spatial distribution pattern is depicted in Figs. 3.5 and 3.6. The TFT ages range between 384 ± 20 Ma and 219 ± 12 Ma; the associated errors are quoted at their 1 σ confidence level. All TFT ages are younger than the latest Pan-African thermo-tectonic event at c. 500 Ma (Pinna et al., 1993). The χ^2 probability values of all samples demonstrate that the dispersion of the individual grain ages (Appendix A) is explained by a poissonian distribution, suggesting that the single grain ages are derived from a single population. Granite sample YG3 was employed for internal cross validation by two independently analysed splits (Tab. 3). The two data sets reveal concordant TFT results and indicate internally consistent TFT analyses.

The TFT ages show no distinct trend with elevation, suggesting a non-uniform TFT age-elevation relationship (e.g. Braun, 2002), probably related to presents of diverse cooling paths records (Fig. 3.5b). Samples GZ 87 and GZ 90 were collected from in the western Axial Granulite Complex at 1200 m elevation. These are vertically offset by approximately 500 m against the majority of the TFT samples by the Neogene Malawi rift zone (Chorowicz, 2005 and references therein) (Figs. 3.5b, 3.6 and Tab. 3.3).

Table 3.3: Results of titanite fission track analysis

Sample	Lithology	Longitude	Latitude	Elevation (m)	No. of grains	ρ_s ($\times 10^7 cm^{-2}$) (N_s)	ρ_i ($\times 10^7 cm^{-2}$) (N_i)	ρ_d ($\times 10^7 cm^{-2}$) (N_d)	P(χ^2) (%)	Central age ± 1σ (Ma)	U (ppm)
RMZ 13†	orthogneiss	40.37083	-14.91000	142	24	0.695 (2553)	0.134 (492)	0.102 (2049)	36.5	348 ± 20	46.1
RMZ 14†	orthogneiss	40.35556	-14.97000	58	25	0.586 (1527)	0.131 (342)	0.116 (2049)	59.9	338 ± 22	46.6
RMZ 16†	orthogneiss	40.32722	-14.91028	47	21	0.853 (1915)	0.189 (423)	0.111 (2049)	39.7	330 ± 20	72.8
RMZ 36†	bt-gneiss	37.72972	-15.14361	657	25	0.171 (614)	0.031 (112)	0.106 (2049)	92.6	378 ± 40	14.0
GZ 87†	gt-amphibolite	34.34556	-14.91611	1150	25	0.697 (2661)	0.148 (565)	0.104 (2049)	30.8	327 ± 19	49.2
GZ 90†	amphibolite	34.34167	-14.84944	1150	30	0.456 (3349)	0.093 (682)	0.102 (2049)	15.5	329 ± 18	31.8
LH-MD-69†	felsic gneiss	35.63489	-16.22693	599	20	0.861 (5667)	0.399 (2625)	0.231 (4492)	71.7	327 ± 10	64.1
RMZ 31	gneiss	39.68361	-15.84694	31	25	0.631 (2224)	0.152 (537)	0.113 (2049)	55.4	306 ± 17	51.3
RMZ 11	monzonite	40.16833	-14.94222	184	23	1.102 (2368)	0.283 (608)	0.114 (2049)	99.6	291 ± 15	92.4
BZ 216††	amphibolite	37.44806	-16.03861	500	20	0.941 (1813)	0.294 (566)	0.107 (2049)	22.0	230 ± 14	101.4
GZ 39††	amphibolitic gneiss	38.76139	-15.71056	250	25	0.322 (1957)	0.089 (541)	0.105 (2049)	11.6	254 ± 16	40.3
GZ 79††	amphibolite	38.56639	-16.32750	50	24	0.296 (1176)	0.078 (308)	0.107 (2049)	19.9	271 ± 21	28.0
PZ 33††	amphibolite	38.17444	-16.09139	250	13	0.430 (1541)	0.12 (431)	0.110 (2049)	23.5	260 ± 16	45.3
RMZ 27††	granite	39.87333	-15.87722	91	13	1.015 (1084)	0.272 (291)	0.116 (2049)	95.8	284 ± 20	82.9
RMZ 28††	granite	39.87167	-15.88444	92	13	1.005 (1216)	0.279 (338)	0.111 (2049)	43.7	262 ± 18	90.9
RMZ 47††	granitic gneiss	37.14708	-15.64833	575	14	1.024 (836)	0.287 (234)	0.115 (2049)	9.2	271 ± 24	97.6
020823-06††	orthogneiss	36.95478	-16.87181	180	5	1.288 (349)	0.410 (111)	0.120 (2049)	69.5	248 ± 28	129.1
020824-03††	migmatite	37.39403	-16.33947	352	32	0.613 (2656)	0.185 (800)	0.119 (2049)	72.7	260 ± 13	63.5
020824-06††	migmatite	37.13939	-16.19142	330	25	0.796 (3020)	0.243 (922)	0.116 (2049)	44.4	252 ± 12	79.7
020826-01††	gneiss	37.90036	-16.29083	240	13	1.060 (987)	0.351 (327)	0.117 (2049)	16.1	231 ± 17	123.7
020826-03††	granite	38.05367	-16.21033	380	24	0.959 (1596)	0.341 (567)	0.118 (2049)	97.9	219 ± 12	116.7
020826-09††	granite	38.33333	-16.17339	290	12	1.438 (955)	0.396 (263)	0.119 (2049)	22.2	284 ± 24	127.1
LH 23††	amphibolite	35.66108	-16.41903	454	15	0.605 (2245)	0.375 (1394)	0.242 (4492)	31.2	257 ± 11	60.3
WB-30B††	hbl-bt-gneiss	36.24128	-16.82791	336	22	0.510 (2708)	0.301 (1597)	0.235 (4492)	12.9	263 ± 11	49.9
WB 119††	metagabbro	35.52135	-16.71980	127	20	0.698 (5169)	0.433 (3207)	0.236 (4492)	17.2	251 ± 8	67.0
YG 3*	granite	33.25958	-18.81886	1500	22	0.589 (2767)	0.118 (555)	0.118 (2049)	61.7	384 ± 21	39.4
YG3 II*	granite	33.25958	-18.81886	1500	23	0.511 (2222)	0.104 (453)	0.117 (2049)	91.7	376 ± 22	31.3

N_s, N_i, and ρ_s, ρ_i, denote counted spontaneous and induced fission tracks and fission track densities, respectively. N_d and ρ_d are fission tracks and fission track densities of co-irradiated dosimeter glasses IRMM 540. n = number of counted grains, P = probability of inferred poissonian distribution of single grain ages. See method and analytic chapters for analytical and data processing details. Samples marked † are *O* group samples, †† are *Y* group samples and * are used for internal cross validation.

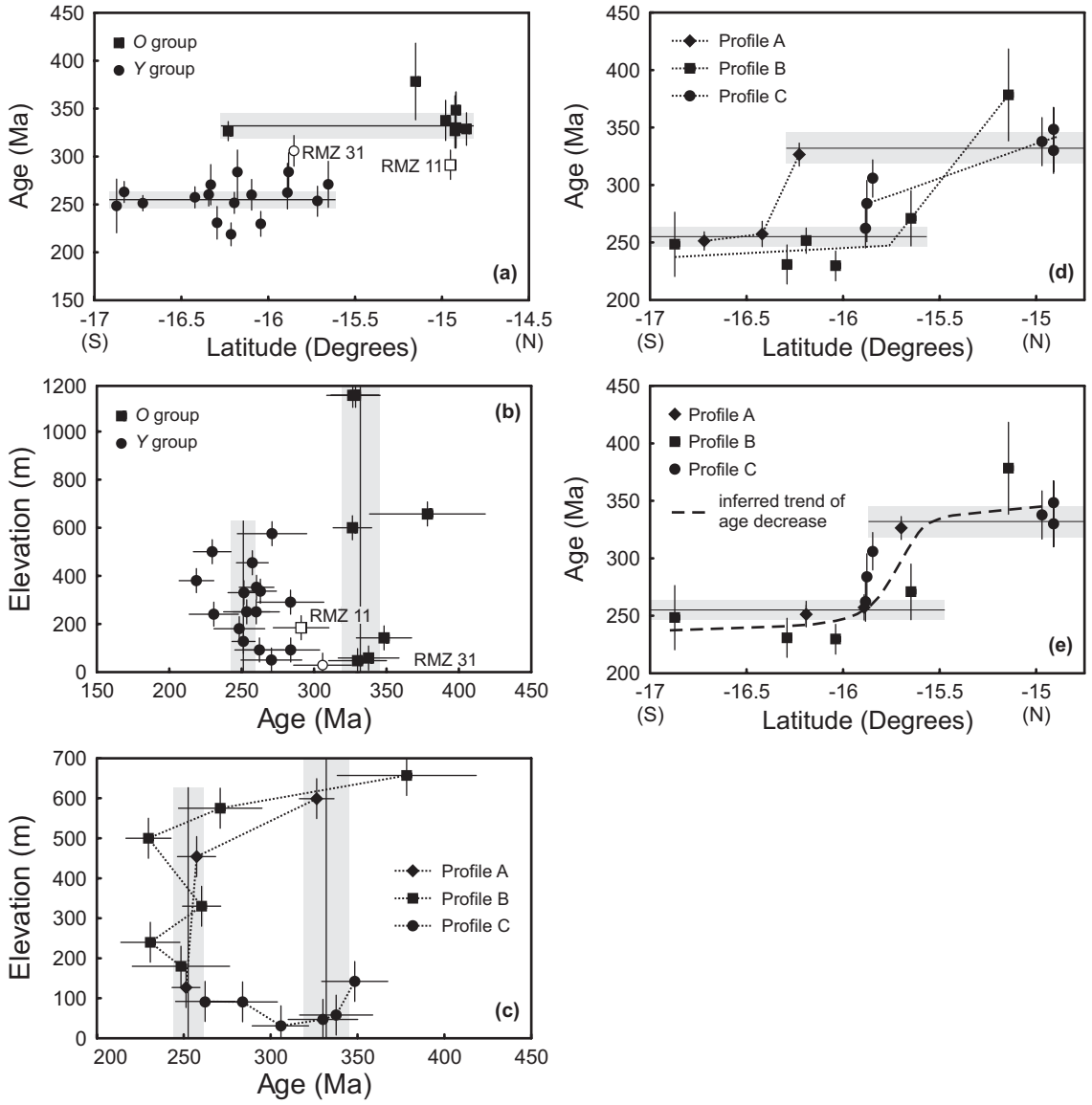

Figure 3.5: Diagrams depicting the results of the TFT analyses; weighted mean ages of *Y* and *O* populations are depicted as black horizontal or vertical lines and the grey bars indicate the associated ± 2 σ confidence intervals. (a) Latitude versus age plot: open symbols represent samples excluded from discriminant analysis and calculation of weighted mean ages. (b) Age versus elevation plot: open symbols represent samples excluded from discriminant analysis and calculation of weighted mean ages. (c) Age versus elevation plot of selective profiles A, B and C. (d) Latitude versus age plot of selective profiles A, B and C. (e) Latitude versus age plot for ~ N-S trending synthetic profile.

The age versus latitude plot (Fig. 3.5a) indicates two age groups: Seven TFT ages ranging from 378 ± 40 to 327 ± 18 Ma yield a weighted mean age of 328 ± 7 Ma. A younger TFT age population of 16 samples ranges from 284 ± 23 to 219 ± 12 Ma and

clusters around a weighted mean age of 255 ± 4 Ma. For easier distinction, the older and the younger TFT age populations are termed *O* and *Y* group, respectively. The grouping is confirmed by a discriminant analysis (Bahrenberg et al., 1992), using the TFT ages, latitudes, longitudes and elevations (Tab. 3) as grouping parameters. A Wilks' Λ value of 0.110808 indicates a distinct class separation, and a probability value of P (χ^2) > 99 % shows that the estimated discriminant functions are significant. Samples RMZ 11 and RMZ 31 were excluded from the discriminant analysis and weighted mean age calculation. Sample RMZ 11 (291 ± 15 Ma) does not overlap within its 1 σ error with the weighted mean ages of the *O* or *Y* group (Figs. 3.5b, 3.6 and Tab. 3.3). Its age, however, is statistically identical to proximately located *O* group samples RMZ 13, RMZ 14 and RMZ 16 (Fig. 3.1). Sample RMZ 31 yields a TFT age of 306 ± 16 Ma that overlaps within 1 σ error with the weighted mean age of the *O* populations (Figs. 3.5b, 3.6 and Tab. 3.3) but RMZ 31 is proximately located to *Y* group samples RMZ 27 and RMZ 28 (Fig. 3.1).

TFT samples from three N-S traverses A, B and C delineate the age versus latitude trends across the region from west to east (Fig. 3.6). Profile B covers the largest section whereas profile C represents a composite of two locations (Figs. 3.5c, d, and 3.6). In general, the TFT ages decrease from N to S and remain constant in E-W direction between longitude 37° E and 40.5° E (Fig. 3.6). East of longitude c. 40.5° E, the ages appear to align along an NE-SW to ENE-WSW trend (Fig. 3.6). Traverses A and B exhibit a steep gradient of TFT age decrease from the *O* to *Y* group (Fig. 3.5c, d). The steep gradient of profile A appears to be shifted towards the south compared to profile B. This shift attributed to the NE alignment similar age east of c. 40.5° E (Figs. 3.5d and 3.6). The offset is accounted for as follows and a "corrected" synthetic traverse is shown in Fig. 3.5e. Along traverse B no significant change in the youngest TFT ages is observed further south than latitude c. 16.1° S (Figs. 3.5d and 3.6). At this point the *Y* group samples BZ 216, 020824-06 and 020824-03 yield identical TFT ages (within their 1 σ errors) and indicates a plateau-like TFT age pattern (Figs. 3.5d, 3.6 and Tab. 3.3). South of latitude c. 16.5° S, traverse B crosses the interpolated TFT age isolines obliquely and may not reflect a true TFT age trend (Figs. 3.5d and 3.6). Therefore profile A is shifted by 0.5 degrees towards the north, such that sample WB 119 (251 ±

8 Ma) of traverse A aligns with sample 020824-06 (251 ± 11 Ma) of traverse B, and the plateau-like trends of both traverses overlap (Figs. 3.5d, e and 3.6). This amount of shift is considered to be a conservative estimate as it accounts for a good overlap of both the plateau-like age trends but does not artificially extend the plateaus. This is particularly important as the inflection points between the shallow and steep age gradients are not tightly constrained along the traverses. The synthetic profile shows that the change from the older towards the younger age population occurs fairly rapidly over a distance of approximately 0.5° latitude, i.e. c. 55 km. A general sigmoid trend line is approximated for the observed age decrease pattern between the *O* and *Y* groups from north to south (Fig. 3.5e).

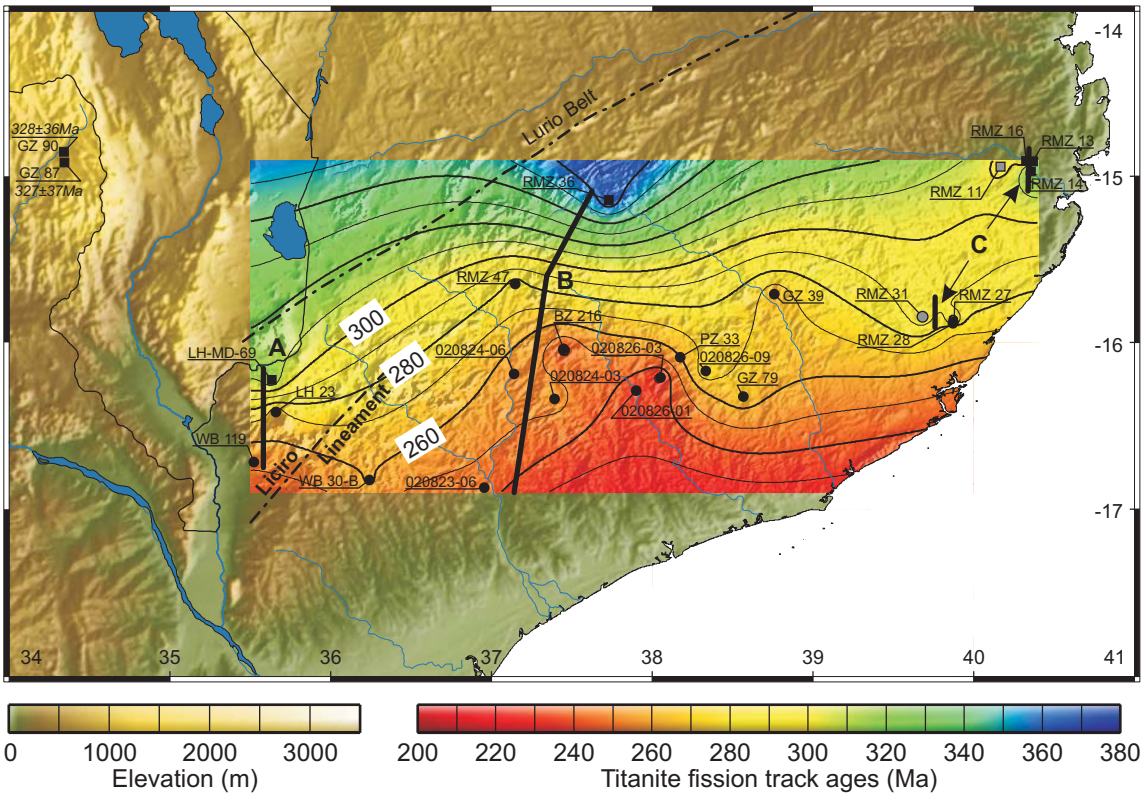

Figure 3.6: Topographic map of northern Mozambique with superimposed spatial distribution pattern of TFT ages. Contour lines were calculated using GMT 4.0, module surface. Sample locations are given as black squares and black circles for the *O* and *Y* groups, respectively. The open grey boxes indicate ungrouped samples.

3.5 Interpretation

3.5.1 $^{40}Ar/^{39}Ar$ hornblende data

Experiments suggest that some hydrous mineral like hornblende and biotite do not remain stable during in vacuo heating and produces flat argon age spectra, irrespective of the spatial argon distribution. Significant age spectra disturbances can be produced by the degassing of impurities or experimental artefacts (Lee, 1993; Lee et al., 1991). Accordingly, the observed discordant hornblende age spectra (Figs. 3.3a-f) result from an influence of degassing inclusions or impurities. The discordant hornblende age spectra commonly show similar variations in the $^{37}Ar/^{39}Ar$ ratios (Figs. 3.3a-f), which may further suggest degassing of inclusions or impurities (Di Vincenzo et al., 2003).

In all the hornblende samples (Figs. 3.3a-f) the old ages in the low temperature steps likely reflect the release of excess ^{40}Ar (Damon, 1968) from extended crystal defects by short circuit diffusion (Lee, 1995, 1993; Lee et al., 1991; Lo et al., 2000). Consequently, the weighted mean and pseudo-plateau ages of all hornblende samples might be affected by excess ^{40}Ar.

The very high radiogenic $^{40}Ar^*$ and very low atmospheric ^{40}Ar concentrations in all hornblende samples (Tab. 3.1) suggest that they were not significantly altered by mixing with meteoric fluids. Sample PZ 37 shows the largest concentration of atmospheric ^{40}Ar in their low-temperature degassing steps and probably indicates some sample alteration by meteoric fluids containing a modern atmospheric $^{40}Ar/^{36}Ar$ ratio. However, as optical thin section inspection reveal fresh, unaltered mineral phases in all samples, large-scale external input of excess ^{40}Ar by fluids is considered less likely.

The observed excess ^{40}Ar may either accumulated during original mineral formation or may be derived from internal build up above the isotopic system closure (Baxter, 2003). Hornblende analyses BZ 216 and GZ 90 are derived from amphibolite rock samples with < 5 % quartz and analyses PZ 37 is derived from an amphibolite with quartz content of 5-10 %. Quartz is regarded as a key sink mineral to preserve excess ^{40}Ar, to enable high total local sink capacity and to prevents internal build up (Baxter, 2003; Baxter et al., 2002). Eventually, the low amounts of quartz in these three amphibolite samples resulted in a low total local sink capacity and enabled an internal

build up of excess radiogenic argon. However, some of the low-temperature excess ^{40}Ar in PZ37 appears to be associated with a Ca-rich phase (Fig. 3.3c).

The total fusion and weighted mean ages of samples BZ 216, GZ 90 and PZ 37 may be significantly altered by excess ^{40}Ar and degassing of non-hornblende phases and therefore may not provide geologically meaningful $^{40}Ar/^{39}Ar$ cooling ages. The weighted mean ages of samples RMZ 11, RMZ 13 and RMZ 45 are probably disturbed by the degassing of inclusions. A good agreement betweeen the total fusion 479.2 ± 18.2, 482.1 ± 25.9 and 466.9 ± 29.9 and weighted mean ages of 473.8 ± 2.4 Ma, 475.8 ± 2.8 Ma, and 455.5 ± 6.2 Ma of samples RMZ 11, RMZ 13 and RMZ 45, respectively suggests that these samples are least affected by excess ^{40}Ar (Figs. 3.3d-f and Tabs. 3.1, 3.2). Consequently, their weighted mean ages of c. 474-476 Ma provide the best estimation for hornblende $^{40}Ar/^{39}Ar$ cooling ages in this region.

3.5.2 $^{40}Ar/^{39}Ar$ biotite data

Discordant age spectra are observed for all $^{40}Ar/^{39}Ar$ biotite samples. The discordant $^{40}Ar/^{39}Ar$ age spectra pattern observed in sample RMZ 13, and in the high-temperature degassing steps (at cumulative ^{39}Ar values of > 80 %) of samples GZ 39 and RMZ 18, show similar variations in their corresponding $^{37}Ar/^{39}Ar$ ratios (Figs. 3.4a-c, Tab. 3.1) and likely result from degassing of non pristine biotite phases, e.g. inclusions (Di Vincenzo et al., 2003; Kuiper, 2002; Lo et al., 2000).

The low ages in the first low-temperature degassing steps of GZ 39 and RMZ 13 could either reflect loss of ^{40}Ar, degassing of non biotite phases or the degassing of ^{39}Ar by multipath diffusion, which was implanted into short circuit pathways by recoil effects during neutron irradiation (Lo et al., 2000). The low-temperature degassing steps of both samples are not accompanied by significantly lower $^{37}Ar/^{39}Ar$ ratios (Figs 3.4b-c and Tab. 3.1). This indicates that RMZ 13 and GZ 39 biotites either suffered some ^{40}Ar loss or experienced degassing of non-biotite phases. The slightly older ages in the first low temperature degassing steps of biotite sample RMZ 18 may reflect the degassing of minor amounts of excess ^{40}Ar from extended defects by short circuit diffusion (Lo et al., 2000).

Minor influences of ^{40}Ar loss in biotite sample RMZ 13 and of excess ^{40}Ar in sample RMZ 18, suggest that their weighted mean and plateau ages of 448.2 ± 3.7 Ma and 428.4 ± 0.3 Ma, respectively provide good $^{40}Ar/^{39}Ar$ biotite cooling age estimate in the region. Due to a possible influence of ^{40}Ar loss, the plateau age of 443.8 ± 0.4 Ma for sample GZ 39 is regarded as a minimum estimate of the $^{40}Ar/^{39}Ar$ biotite cooling age.

3.5.3 Cooling rates for $^{40}Ar/^{39}Ar$ hornblende and biotite results

The following diffusion parameters were adopted to calculate of the closure temperatures and cooling rates for hornblende: a frequency factor ($D_{0)}$ of 0.024 cm^2/s, an activation energy (E) of 64.1 kcal/mol, a diffusion geometry (A) of 55 for spherical diffusion (Harrison, 1981), and for biotite: $D_0 = 0.075$ cm^2/s, $E = 47.1$ kcal/mol (Grove and Harrison, 1996), and $A = 27$ for cylindrical diffusion that is appropriate for mica (Hames and Bowring, 1994; Onstott et al., 1991). A mineral closure temperature (T_c) is directly related to the cooling rate (Dodson, 1973). The closure temperatures for corresponding $^{40}Ar/^{39}Ar$ hornblende and biotite cooling ages were calculated using cooling rates ($\Delta T/\Delta t$) that are in turn consistent with the age difference (Δt) between them.

$^{40}Ar/^{39}Ar$ analyses of sample RMZ 13 yield hornblende and biotite cooling ages of 475.8 ± 2.8 Ma and 448.2 ± 3.7 Ma, respectively (Fig. 3.1, Tab. 3.2). These ages differ by $\Delta t = 21$-34 Ma. Derived cooling rates range from c. 10.5° to 6.5°C/Ma suggesting closure temperatures of c. 524° to 513°C and 311° to 305°C for hornblende and biotite, respectively. Similar cooling rates and closure temperature values are inferred for hornblende sample RMZ 11 due to a similar cooling age of 473.8 ± 2.4 Ma and its proximate location to sample RMZ 13 (Fig. 3.1, Tab. 3.2). Identical biotite $^{40}Ar/^{39}Ar$ cooling ages of sample RMZ 13 (448.2 ± 3.7 Ma) and sample GZ 39 (443.8 ± 0.4 Ma) imply similar minimum cooling rates of 10.5°-6.5°C/Ma and closure temperatures of 311°-305°C for GZ 39. Hornblende sample RMZ 45 (455.5 ± 6.2 Ma) and biotite sample RMZ 18 (428.4 ± 0.3 Ma) yielded younger ages than the hornblende and biotite cooling ages of sample RMZ 13. Therefore, the approximated cooling rates of 50°-5°C/Ma and associated closure temperatures of 556°-511°C and 334°-302°C are applied for RMZ 45 hornblende and RMZ 18 biotite, respectively. A closure temperature of T_c

~ 350°C (Möller et al., 2000) is estimated throughout this study for cited Rb/Sr cooling ages (Fig. 3.1).

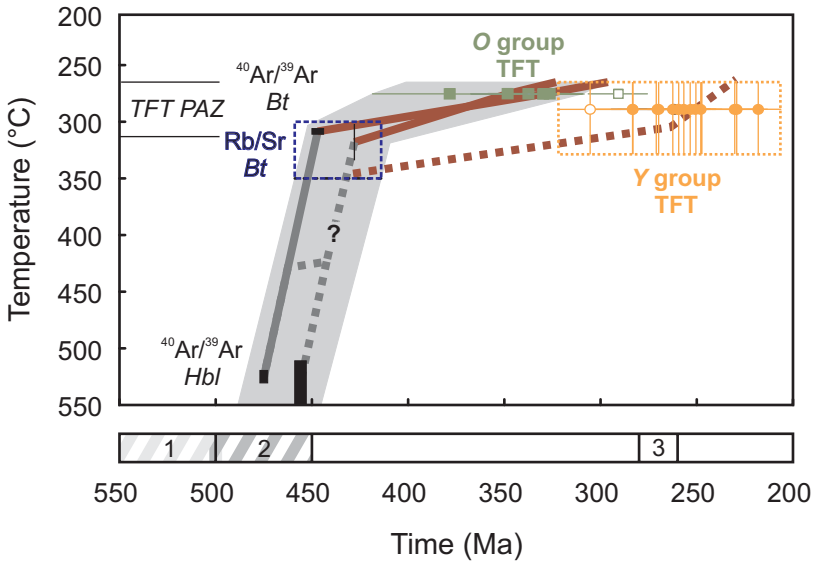

Figure 3.7: Diagram illustrating the *t-T* cooling paths of the southern basement in northern Mozambique. Black rectangles represent *t-T* spaces constrained by the $^{40}Ar/^{39}Ar$ hornblende (*Hbl*) and biotite (*Bt*) analyses. Rb/Sr biotite (*Bt*) cooling ages of Costa et al. (1992) are represented by the blue dashed outlined box. Older (*O*) and younger (*Y*) TFT age groups are depicted by green squares and orange circles, respectively. Constrained and inferred cooling paths are shown in solid and dashed brown lines, respectively. The light grey area denotes a general *t-T* trend envelope, inferred from error intervals of thermochronological data and cooling rates. An inferred temperature range, where *Y* group TFT samples resided prior to their uplift and cooling is indicated by the orange dotted outlined box. Open symbols depict ungrouped TFT ages. Numbers 1, 2 and 3 indicate periods of the Pan-African metamorphism, granite and pegmatite intrusions and incipient rifting in the Early to Late Permian, respectively. The question mark denotes an exemplary cooling path for the post-metamorphic thermally influenced basement.

3.5.4 Titanite Fission Track data

Annealing characteristics of titanite fission tracks are fairly complex and rather sparsely constrained (Jonckheere and Wagner, 2000). Therefore the TFT age of sample RMZ 31 may either be a "transitional age" between the *O* and the *Y* populations, or it reflects a variation in annealing characteristics with respect to proximate samples RMZ 27 and RMZ 28. The similarities in age and location may argue for a common cooling history for samples RMZ 31, RMZ 27 and RMZ 28 (*Y* group). Similarly, the TFT age of sample RMZ 11 may either represent a "transitional age" between the two age populations, or

differences in annealing characteristics. Due to the close spatial relations, a similar cooling history of samples RMZ 11, RMZ 13, RMZ 14 and RMZ 16 (*O* group) is inferred.

Excepting the two samples RMZ 11 and RMZ 31, no TFT ages of c. 300 Ma have been observed. Therefore, the spatial separation between the *O* and *Y* TFT age groups is roughly approximated by the interpolated 300 Ma age contour (Figs. 3.5a and 3.6). A TFT age span of 65 Ma of the *Y* group is slightly larger than the 51 Ma age span of the *O* group (Figs. 5a and 5b). This could either reflect data scatter in the larger sample population (*Y* group: 16 samples versus *O* group: 7 samples) or the incorporation of a minor N-S TFT age gradient in the *Y* group (Figs. 3.5d and 3.6).

As no track length information could be obtained, the *O* and *Y* group TFT ages are regarded as minimum cooling ages, with a TFT closure temperature of 275° ± 25°C (Kohn et al., 1993). Because the samples GZ 87 and GZ 90 from the Axial Granulite Complex yield similar TFT ages as the *O* group samples from the southern basement east of the Malawi Rift System, (Figs. 3.5b, 3.6 and Tab. 3.3) their ages likely indicate a common cooling *O* group history in the north Mozambican basement to either side of the Malawi rift, irrespective of the present day elevation difference.

Relating the $^{40}Ar/^{39}Ar$ biotite results of RMZ 13 (T_c ~ 311°-305°C, 448.2 ± 3.7 Ma) to corresponding TFT *O* group samples RMZ 13 (348 ± 19 Ma) and RMZ 16 (330 ± 20 Ma) suggests cooling rates of less than 0.6°C/Ma between Late Ordovician to Early Carboniferous times (Tabs. 3.1, 3.3 and Figs. 3.1, 3.7). These rates are one order of magnitude lower than the cooling rates of c. 10.5-6.5°C/Ma derived from $^{40}Ar/^{39}Ar$ hornblende and biotite analyses of sample RMZ 13. Similarly, a low cooling rate of < 0.9°C/Ma is determined for $^{40}Ar/^{39}Ar$ biotite sample RMZ 18 (428.4 ± 0.3 Ma, c. 334-302°C) and its closest corresponding TFT samples RMZ 14 (338 ± 21 Ma) (Tabs. 3.1, 3.3 and Figs. 3.1, 3.7). The very low cooling rate estimates could indicate that the *O* group samples cooled very slowly through the TFT partial annealing zone (PAZ), 310°-265°C ± 10°C (Coyle and Wagner, 1998), and experienced a significant amount of track annealing. The *O* group samples probably cooled through the TFT PAZ (T < 265°C) in Late Carboniferous to Early Permian times (c. 320-290 Ma). A cooling rate of less than 0.3°C/Ma was calculated from sample GZ 39 based on its $^{40}Ar/^{39}Ar$ biotite results

(443.8 ± 0.4 Ma, c. 311-305°C) and its corresponding *Y* group TFT age (254 ± 16 Ma) (Tabs. 1, 3 and Fig. 1). This rate could indicate an apparent further decrease in cooling rates towards the south. Cooling rate estimated were solely obtained from samples RMZ 13 and GZ 39, and hence may not be unrestrictedly representative for the oldest *O* group (378 ± 40 Ma of RMZ 36) and youngest *Y* group (219 ± 12 Ma of 020826-03) TFT samples (Tab. 3.3, Fig. 3.6). However, the consistent NE to ENE alignment of similar N-S decreasing TFT age trends (Figs. 3.5c-e and 3.6) argues for a common origin for the TFT age distribution across the north Mozambican basement. The prominent N-S gradient between the TFT age groups (Figs. 5d-e) indicates that a solely continuous decrease in cooling rates towards the south is very unlikely. It rather suggests that the *O* and *Y* group TFT samples experienced distinctly different cooling paths and that in turn the cooling rates derived from the *Y* group samples are of no significance as the *Y* group TFT ages likely resulted from a complex cooling history. The occurrence of similar *Y* group TFT ages over a small elevation range (c. 600 m; Fig. 3.5b) could indicate that these samples experienced a period of more rapid cooling (cf. Braun, 2002), whereby the youngest TFT age, located furthest south, cooled at latest through the TFT PAZ.

The Rb/Sr bitotite (Costa et al., 1992,) and $^{40}Ar/^{39}Ar$ biotite cooling ages (Tab. 3.1, 3.2 and Fig. 3.1) indicate cooling to below c. 350°-300°C in the southern basement at 450-420 Ma. This could rather suggest that subsequently, both TFT age groups cooled at fairly similar rates of < 1°C/Ma. Thereby the *Y* group samples were located at a deeper crustal level than the *O* group samples. During, presumably, Late Carboniferous/Early Permian times (c. 300-290 Ma) the *O* group samples had cooled through the TFT PAZ whereas the *Y* group samples still resided within and/or above the high temperature threshold of the TFT PAZ (c. > 310°C). The *Y* group cooled to below c. 275 ± 25°C, probably more rapidly, at a younger time (c. < 280 Ma) (Fig. 3.7).
Alternatively, the *O* and *Y* group samples could have resided at similar crustal levels and cooled at similar rates from c. 450-420 Ma onward. Then, the *Y* group samples experienced a thermal overprinting causing partial or entire age resetting at a younger time (c. < 280 Ma).

3.6 Discussion

3.6.1 Proterozoic to Early Palaeozoic cooling in the south western Axial Granulite Complex

The $^{40}Ar/^{39}Ar$ ages of hornblende samples GZ 90 and PZ 37 (Tab. 3.1 and Fig. 3.2), are younger than the peak post-kinematic (D_{M2}) granulite facies metamorphic event at c. 571-549 Ma in the Axial Granulite Complex in southern Malawi (Kröner et al., 2001). These $^{40}Ar/^{39}Ar$ hornblende ages appear to be in agreement with cooling from the latest granulite facies imprint at c. 571-549 Ma in the region. Unfortunately, a significant alteration by excess ^{40}Ar observed within both analyses precludes reliably time-temperature estimates on the regional cooling paths.

Post-granulite facies metamorphism and D_{M2} fabrics reworking events are recognized in southern Malawi (temporally unconstrained in the Metangula Group; Pinna et al., 1993) and further north in the Cobue-Geci Group at c. 538 Ma (Lulin, 1985; Pinna et al., 1993). There, the protholiths of the metasedimentary units (Fig. 1) were sourced from the Axial granulites and were subsequently metamorphosed under amphibolite facies conditions. U/Pb SHRIMP zircon dating on gneisses and granites from Eastern Zambia yielded ages of c. 500-480 Ma (De Waele, 2006). U/Pb SHRIMP dating on metamorphic overgrowths of detrital zircon from the Alto Benfica Group (Namarroi Zone, Fig. 1; Jacobs 2005, unpubl.) yield ages of c. 490 Ma. Both results indicate high *T* metamorphic overprints within the basement rocks to the east and west of the Unango granulites at c. 500 Ma. The $^{40}Ar/^{39}Ar$ hornblende ages of samples GZ 90 and PZ 37 (Tab. 3.1, 3.2 and Figs. 3.3b-c) could therefore also result from excess argon alteration, accumulated during cooling periods following metamorphic overprints between c. 550-500 Ma in the western Axial Granulite Complex.

3.6.2 Early Palaeozoic cooling in the southern basement

$^{40}Ar/^{39}Ar$ hornblende cooling ages of samples RMZ 13 and RMZ 11 date the cooling to below 524°C at 476-474 Ma in the eastern part of the southern basement. The syn-tectonic granulite facies metamorphism (D_{M2}) in the Mugeba Klippe basement is dated at c. 615 Ma (Kröner et al., 1997) although new U-Pb SHRIMP zircon ages of c. 551

Ma (Grantham et al., 2005a) and of c. 510 Ma from the Nampula basement (Jacobs unpublished data) have challenged these earlier results. This deformation (D_{M2}) is post-dated by an unconstrained, mainly amphibolite facies overprint (Pinna et al., 1993). A time difference of c. 30-80 Ma exists between the peak granulite facies meta-morphism and the $^{40}Ar/^{39}Ar$ hornblende cooling ages of RMZ 11 and RMZ 13. Both $^{40}Ar/^{39}Ar$ hornblende ages are also younger than the inferred timing (c. 500 Ma) of the syn-to late-tectonic granitic intrusions (Pinna et al., 1993). Therefore, both $^{40}Ar/^{39}Ar$ hornblende cooling ages could either indicate a period of very slow cooling or a protracted, yet not completely resolved multiphase evolution of the basement during Pan-African times.

The temporally unconstrained evolution of the Namama Thrust Belt probably post-dates the peak granulite facies metamorphism (c. 615-551 Ma). It likely accounts for the distribution of some late phase, high grade metamorphic assemblages (Sacchi et al., 2000). The associated D_{N1} deformation, presumably reworked a large region of the southern basement, and affected some of the granitoids emplaced at c. 500 Ma. Therefore, the $^{40}Ar/^{39}Ar$ hornblende results of RMZ 13 and RMZ 11 most probably record the cooling below 524°C at 476-474 Ma from a thermo-tectonic overprint at c. 615-500 Ma at with subsequent cooling rates of 10.5-6.5°C/Ma (Fig. 3.7). This could in turn indicate that the amphibolite to granulite facies D_{N1} metamorphic overprint of the Namama Thrust Belt dates between c. 615-500 Ma.

Sillimanite bearing metasedimentary rocks of the Alto Benfica Group (Thomas, 2006) near the Namaroi Zone (Fig. 3.1) and yielded detrital zircons with metamorphic zircon overgrowths. U-Pb SHRIMP analyses revealed ages of c. 490 Ma and c. 610 Ma for the metamorphic rims and the youngest detrital grains, respectively (Jacobs, 2005 unpublished). These findings record the deposition of sediments after 610 Ma with protolith sources of Late Proterozoic to Archean ages. They further suggest exposure and erosion after a granulite facies metamorphism at c. 615 Ma as well as post-sedimentary reworking and metamorphism up to at least sillimanite grade at c. 490 Ma in the western part of the southern basement. In the eastern part of the southern basement (Fig. 1), the autochthonous, sillimanite-bearing metasedimentary rocks of the Mecuburi Group show evidences of reworking of Nampula gneisses (Sacchi et al., 1984). With respect to proximate $^{40}Ar/^{39}Ar$ hornblende results of RMZ 13 and RMZ 11

(Fig. 3.1), the Mecuburi Group might also indicate exhumation, erosion, sedimentation, and amphibolite facies metamorphism between c. 615-500 Ma in the eastern part of the southern basement.

An $^{40}Ar/^{39}Ar$ hornblende cooling age of 455.5 ± 6.2 Ma (RMZ 45) coincides with a pegmatite Rb/Sr muscovite cooling age of 454 ± 7 Ma (Costa et al., 1992; Fig. 1). Recent monazite U/Pb CHIME (Chemical Isochron Method) dates of pegmatites yield a broad scatter of intrusion ages around c. 450 Ma (Grantham, 2005a). U-Pb SHRIMP zircon analysis from two undeformed granites yielded intrusion ages of c. 500 and 450 Ma (Grantham et al., 2005a). These data indicate localized thermal influences by igneous activity in the central southern basement between c. 500-450 Ma. The preserved younger $^{40}Ar/^{39}Ar$ hornblende age of RMZ 45 is thus inferred to record cooling to below 556°-511°C at c. 456 Ma (Fig. 3.7) from a late- to post-metamorphic reheating at c. 500-450 Ma.

$^{40}Ar/^{39}Ar$ biotite sample RMZ 13 and GZ 39 recorded the cooling to below c. 310-305°C at 448.2 ± 3.7 Ma and 443.8 ± 0.4 Ma, respectively at rates of 10.5-6.5°C/Ma in the eastern part of the southern basement (Fig. 3.7). Both cooling ages coincide with a Rb/Sr biotite cooling age of 449 ± 7 Ma (Costa et al., 1992) from a basement gneiss in the Namama Thrust Belt hinterland (Fig. 3.1). These results likely indicate widespread cooling of the southern basement gneisses at c. 450 Ma to below c. 350°-305°C (Fig. 3.7). Younger Rb/Sr biotite cooling ages of 434-420 Ma from mainly undeformed granitoids (Costa et al., 1992; Sacchi et al., 1984) coincide with the 428.4 ± 0.3 Ma $^{40}Ar/^{39}Ar$ biotite cooling age of sample RMZ 18. This likely suggests that biotite sample RMZ 18 records cooling to below 334-302°C from a basement reheating between c. 500-450 (Fig. 3.7). Consequently, the pegmatite and granite emplacements, locally delayed final basement cooling to below 350°C to c. 434-420 Ma (Fig. 3.7).

Conclusively, the $^{40}Ar/^{39}Ar$ biotite and Rb/Sr biotite cooling ages (Fig. 3.1 and Tab. 3.2) indicate that the southern basement experienced widespread, ultimate cooling to below c. 350°-305°C from the youngest Pan-African thermo-tectonic events between c. 615 Ma to 450 Ma at c. 450-420 Ma, i.e. in Late Ordovician to Early Silurian times (Fig. 3.7).

3.6.3 Late Palaeozoic cooling and denudation history

Further cooling to below c. 275 ± 25°C occurred in Late Devonian to Early Carboniferous times. It was accompanied by a decrease in cooling rates to values of < 1°C/Ma (Fig. 3.7) and presumably reflects a reduction in denudation rates. The establishment of pre-Karoo peneplains (< Late Carboniferous), subsequent to a prolonged period of denudation (erosion) in central Gondwana (Catuneanu et al., 2005; Wopfner and Kaaya, 1991) most probably corresponds to the observed decrease in denudation in northern Mozambique.

Preliminary apatite fission track results (Daszinnies et al., 2004) and isolated outcrops of Karoo age lavas (Grantham et al., 2005b; Jaritz et al., 1977) along the continental margin, (Fig. 3.2) indicate basement cooling to ≤ 110°C in Early to Middle Jurassic times. Conclusively, the *Y* group TFT ages probably record basement cooling to below 275 ± 25°C between the Late Carboniferous/Early Permian (c. < 280 Ma) and Late Triassic/Early Jurassic (c. > 200-180 Ma).

Permo-Triassic rift basins adjacent to the north Mozambican basement consistently indicate incipient rifting in Early to Late Permian times (c. 280-260 Ma) (Castaing, 1991; Catuneanu et al., 2005). This timing post-dates the cooling of the *O* group TFT samples but pre-dates and overlaps with the basement cooling period of the *Y* group TFT samples. This suggests that the cooling of the *Y* population is maybe related to regional incipient rifting activity in Early to Late Permian times. Their cooling might result from rift related denudation and exhumation by: (a) crustal extension, i.e. rift basin formation, (b) erosion of an uplifted rift flank adjacent to a rift basin, (c) erosional base level lowering due to incipient rifting. Alternatively, their cooling could also represent the fading of a thermal influence that accompanied the formation of a rift structure (e.g. Bott, 1995; Ziegler and Cloething, 2004).

In the north Mozambican basement south of the Lurio Belt, besides remnant basal shear zones of the granulites nappes and Namama Thrust Belt (Fig. 3.1), regional ductile high strain zones (Pinna, 1995; Thomas, 2006) and regional brittle structures are absent (Thomas, 2006). This apparent lack of potential regional scale extensional structures indicates that the inferred *Y* group cooling pattern (Fig. 3.6) is less likely explained by denudation due to crustal extension on the north Mozambican basement.

The TFT age trends of profiles A-B and the composite profile (Figs. 3.5d, e) show a rapid sigmoid shaped age decrease over a distance of c. 50 km. Both, the profile shape and the distance of TFT age decrease strongly resembles sigmoidal AFT age patterns (a) observed at rifted continental margins displaying prominent escarpments (Gallagher et al., 1994), and (b) predictions from numerical modelling combining lithosphere extension and surface processes (Van der Beek, 1995). The youngest TFT ages (c. < 250 Ma) are located furthest south and pre-date the regional timing of incipient rifting (c. 280-260 Ma). They were likely exhumed from below the TFT PAZ (T > 310°C) at times < c. 280 Ma. This is in good agreement with previous AFT studies which document that the youngest AFT ages are found on the uplifted rift flanks close to the basin edge commonly pre-date the timing of rifting as they were exhumed from below the AFT PAZ (Gallagher et al., 1998; Van der Beek et al., 1995). The observed TFT age patterns of the N-S profiles (Figs. 3.5d, e) are interpreted as traverses across the thermochronological imprint of an E to ENE trending rift flank that was uplifted during Karoo times. Thereby the *O* group TFT ages record the cooling of the unaffected hinterland, inland of the uplifted region. Towards the south the TFT ages rapidly approach the *Y* group age values that record the cooling from the denuding uplifted rift flank, cooling that result from interwoven processes of tectonic uplift, denudation and local isostatic compensation. This suggests further that the youngest TFT age samples may represent the zone of highest denudation, highest tectonic and isostatic uplift of the rift flank, proximate to the edge of a rift basin (Fig. 3.8a).

Rift flanks are fairly linear, narrow (≤ 200 km) zones which adjoin continental rifts that are associated with broad domal swells (~1000 km wavelength), for instance the East African rift system (e.g. Fairhead, 1976). Rift flank uplifts may persist for long times (> 60 Ma) and are capable to produce spectacular topography such as the Transantarctic Mountains which rise > 3 km over the surface of the adjoining rifts (Fitzgerald et al, 1992). Thermal, mechanical and combined concepts have been advocated to support rift flank uplift (e.g. Royden and Keen, 1980; Buck, 1986, Kooi, 1991). However, mechanically supported flexural uplift compared to thermal uplift is much more effective and more capable to explain the long term persistence of rift flank uplifts (Van der Beek et al., 1994 and references therein).

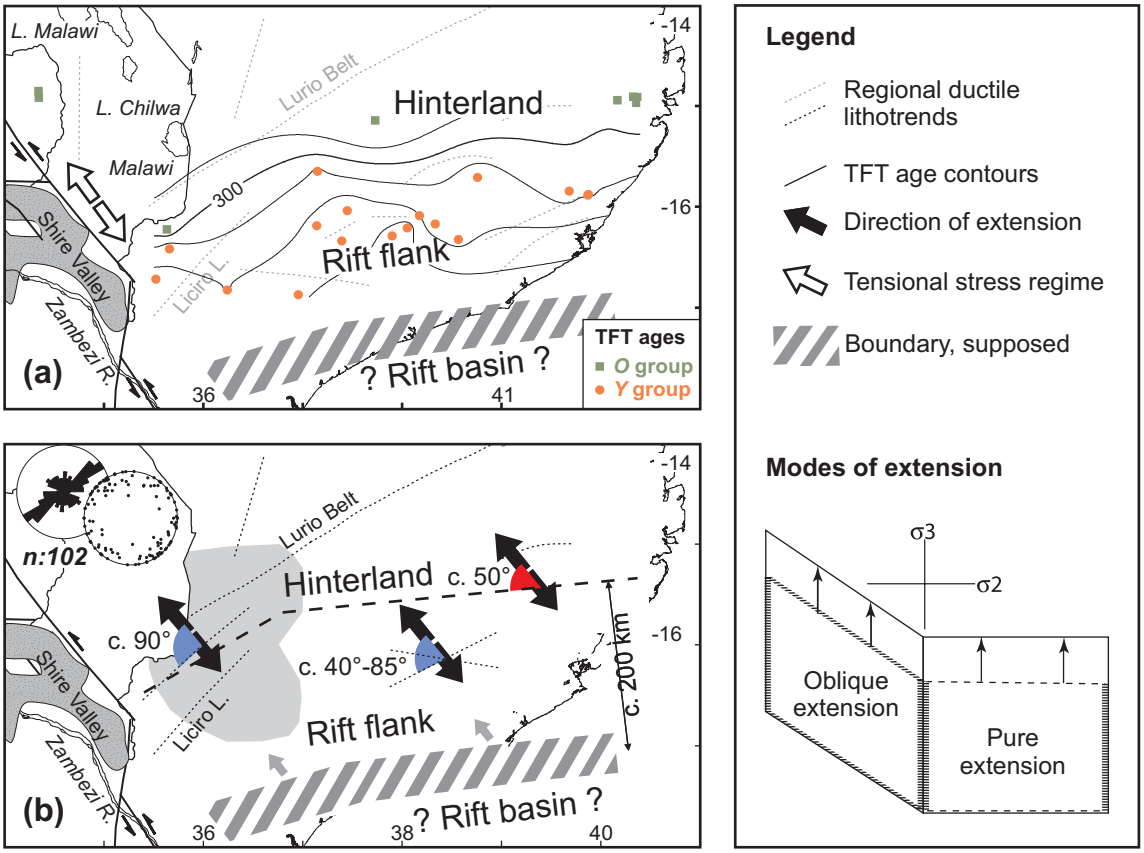

Figure 3.8: Illustration (a) depicts the spatial TFT age pattern in northern Mozambique and the inferred rift flank. The green squares and orange dots show the sample locations of the older and younger TFT age populations, respectively. The interpolated TFT age contours are represented by black lines. The ductile basement fabrics are derived from Pinna et al., 1993 and the orientation of the Permian tensional stress field is obtained from Castaing, 1991. Illustration (b) shows the inferred rift geometry. Thick dashed lines trace the approximated boundary between the hinterland and the rift flank. Thin dashed lines show the generalized ductile litho-trends. The blue and red circle segments are graphical representations of the acute angles formed by trends of ductile fabrics and the rift structure with the tension stress field, respectively. Large black and small grey arrows indicate the regional tensional stress orientation and the supposed local extension direction. Orientation measurements of joints obtained from the light grey area shown in the Rose and Schmidt diagrams.

In depth dependant pure shear crustal extension models, the rheologically layered lithosphere retains a finite strength during rifting; necks around its strongest layer and for sufficiently deep levels of necking an upward state of flexure is induced that mechanically supports the rift flanks (Braun and Beaumont, 1989; Kooi et al., 1992). The uplift results from regional isostatic compensation of the mechanically thinned

lithosphere and/or from foot wall uplift due to unloading and flexural rotation of rift basin border faults (e.g. Ziegler and Cloething, 2004) (Fig. 3.9). Rift flank uplift is flexural in nature (e.g. Bott, 1995) and this fact appears to be in good agreement with the lack of regional extensional structures on the basement.

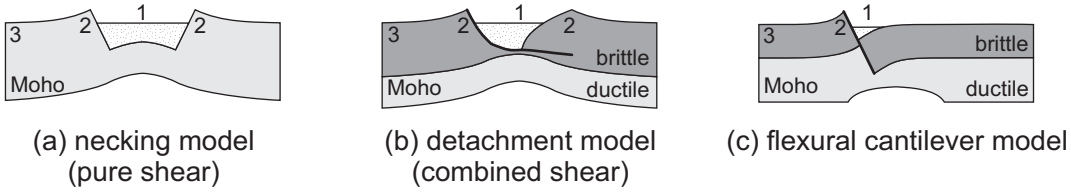

Figure 3.9: Cartoons depicting three models of kinematic extension and their regional isostatic response: (a) the necking model for a deep level of necking (Braun and Beaumont, 1989; Kooi et al., 1992), (b) the detachment model (Weissel and Karner, 1989) and (c) the flexural cantilever model (Kusznir and Ziegler, 1992). In models (a) and (b) rift flank uplift is supported by regional isostatic compensation and passive upwelling of the asthenosphere into the mechanically attenuated mantle lithosphere (Ziegler and Cloething, 2004). In model (c) rift flank uplift results from foot wall unloading and flexural rotation of the normal fault (Buck, 1988). Numbers 1, 2 and 3 indicate the extensional rift basin, the uplifted rift flank and the unaffected interior, respectively. Extensional faults are represented by thick black lines.

A corresponding rift basin was probably located in the vicinity of the southern continental margin (Fig. 3.8b), suggestive that the uplifted rift flank could be up to approximately 200 km wide. This is quite a large distant but it is in consistency with numerical modelling predictions (Van der Beek et al., 1994, 1995) which indicate that the extent of the uplifted section depends on the pre-existing surface elevation. However, the Permo-Carboniferous pre-rifting surface elevation of the north Mozambican basement is unknown. The occurrence of thinned continental crust to the south (Nairn et al., 1991; Salman and Abdula, 1995) and to the southeast (Mascle et al., 1987; Mougenot et al., 1986) of the north Mozambican margin could support the existence of a rift basin to the south of the present basement.

Model results of denudation induced cooling from base level lowering triggered by incipient rifting yielded AFT age patterns that decrease very continuously in age from the interior towards the rift basins (Van der Beek, 1995). Hence a base level lowering is therefore less likely suited to explain the TFT ages pattern in northern Mozambique.

All post Pan-African igneous activity in northern Mozambique is younger than c. 180 Ma (e.g. Eby et al., 1995, Grantham et al, 2005). This suggests that an intense rift related thermal activity by magmatism was less dominant or absent. A thermal overprinting is therefore considered less likely to explain the TFT age distribution. This could further indicate passive rifting conditions in the region (Bott, 1995; Ziegler and Cloething, 2004) and suggests that rift flank uplift supposedly occurred synchronous with incipient rifting (Braun and Beaumont, 1989) in Early to Late Permian times, at c. 280-260 Ma.

Between longitudes 37°-40.5 °E and SE of the Liciro lineament, the regional ductile basement fabrics and the TFT age distribution display a very similar easterly trend (Fig. 3.8a). Such an easterly trend is also inferred for the uplifted rift flank (Fig. 3.8a, b). The regional easterly trends of the basement fabrics (Pinna et al., 1993; Cadoppi et al., 1987; Thomas, 2006) enclose acute angles of c. 85°-40° with the NW-SE orientated Early Permian tensional stress regime (Castaing, 1991) (Fig 3.8b). The inferred general trend of the rift structure forms an acute angle of c. 50° with it (Fig 3.8b). This could suggest that pre-existing basement fabrics trending at high angles of 45°-50° to the tensional stress direction were activated by oblique extensional faulting during rifting (Morley et al., 2004) (Fig. 3.8b). West of longitude 37°E, to the NE of the Liciro lineament, the inferred TFT age trend approaches an NE-SW orientation (Figs. 3.1, 3.6 and 3.8a,b) and coincides with NE trending lithologies (Thomas, 2006). Here, steeply dipping joints trend parallel to ductile basement patterns (Fig. 3.8b). It could indicate brittle, extensional reactivation of ductile basement fabrics. Extension west of longitude 37°E might therefore have taken place in a more orthogonal mode.

The E-W orientated extensional fault trends in the Cabora Bassa Basin (Fig. 3.2), are attributed to reactivation of easterly trending crystalline basement fabrics (Castaing, 1991). It is supposed that the Cabora Bassa Basin and the inferred rift basin south of the north Mozambican basement were linked via the Zambesi pre-transform system during incipient rifting in the Early to Late Permian (Fig. 3.2). Harrowfield et al. (2005) envisioned the formation of an extensive Permo-Triassic rift basin bordering Australia/Antarctica and India. If this is true, a branch could extended from the Australo-Antarctic rift basin into central Africa via northern Mozambique (Fig. 3.2).

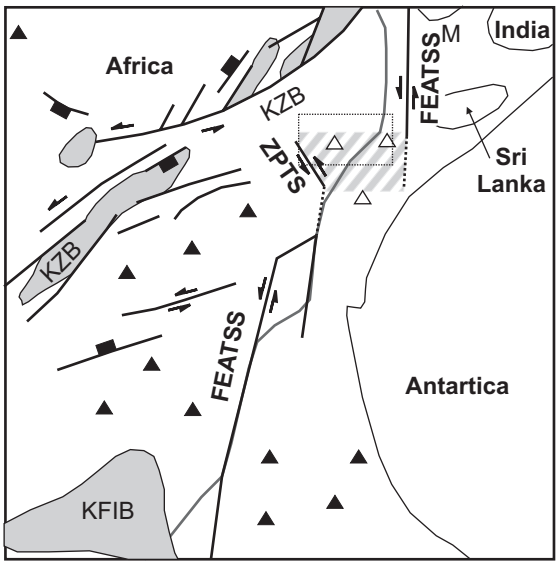

Figure 3.10: Illustration of the tectono-geographic setting in central Gondwana during the Late Permian to Early Triassic; modified after Visser and Praekelt (1996, 1998). The study area is depicted by the dotted line box. Black and open triangles indicate areas and supposed areas of uplift and erosion, respectively. The grey hashed box highlights the right stepping restraining band. Abbreviations used: M – Madagascar, KZB – Kalahari-Zambezi Basins, KFIB – Karoo-Falkland Islands Basins and FEATSS – Falkland-East Africa-Tethys shear system.

Alternatively, the inferred cooling path of the *Y* group TFT samples could also be interpreted to record cooling from erosion of a region uplifted by transpression. In Late Permian to Early Triassic times, the north Mozambican basement could have been a site of lithospheric buckling, uplift and erosion around a regional-scale right stepping restraining bend in the sinistral Falkland-East Africa-Tethys shear system (FEATSS) (Visser and Praekelt, 1996, 1998) (Fig. 3.10). This alternative can not be strictly excluded but is considered less likely. As kinematic investigation in SW Madagascar do not evidence sinistral strike slip faults parallel to the present East African margin in Permo-Triassic times (Schandelmeier et al., 2004), the existence of the FEATSS along the east Mozambican margin during that time is questionable. Additionally, the lack of regional brittle structures in the north Mozambican basement rather precludes the existence of transpression structures. In the southern basement, cooling through denudation recorded by the TFT ages in Permo-Triassic times solely appears to have occurred parallel to the present southern costal margin. This could suggest that the present eastern coastal margin evolved at a distinctly younger time. If it formed

coevally, then it was not recorded by the TFT thermochronology. Either the amount of exhumation was too small or the location of margin formation was further in the east.

At rifted margins, geothermal gradients are fairly constant as the upper crustal isotherms are not significantly disturbed (Brown and Summerfield, 1997; Stüwe et al., 1994) by the sufficiently low (<100 m/Ma) exhumation rates (Leeder, 1991; Van der Beek, 1995). Estimating the amount of denudation is generally difficult as no direct measurements of palaeo-heat flow are available. A geothermal gradient of 30°-25°C/km, inferred from present heat flow records and vitrinite reflectance data through the Karoo basins of southern Tanzania, has been used to constrain the Late Paleozoic to Cenozoic denudation history in the Malawi and Rukwa rift flanks (located in Pan-African mobile belt) (Van der Beek et al., 1998). These values are adopted here. As the youngest TFT samples of the *Y* population were likely exhumed from below the TFT PAZ (T > 310°C), c. 10-12 km of crust are estimated to have been removed by denudation from the rift flank since its uplift in the Early to Late Permian times. Further inland, the TFT ages of the *O* group indicate an amount of c. 9-11 km of denudation since the Early Carboniferous (c. 330 Ma and T_c = 275 C°). Importantly, the denudation estimates are rough approximations as they assume a constant geothermal gradient over very long time periods, though transient geothermal gradient are more reasonable but inaccessible. Therefore, these high amounts of removed crustal material are regarded as extreme upper limit estimations. According to Jacobs and Thomas (2004), the thickened continental crust in the central part of East African-Antarctic Orogen was thinned by an orogenic collapse at c. 530-490 Ma. This could suggest that subsequently continental crust of average thickness (c. 30-50 km) existed in the area of northern Mozambique. If high amounts of up to 12 km (equal to c. 1/3-1/5 of the average thick continental crust) of denudation occurred since the Early Carboniferous, the question arises to which extent it can be evidenced by other observations. As a consequence of such amounts of denudation, the present day crustal thickness in northern Mozambique should be distinctly thinner than in formerly adjacent and less thinned regions of Africa and East Antarctica. Compared to them, the Mohorovičić discontinuity underneath northern Mozambique should be located at a shallower depth due to high degree of crustal thinning.

An alternative interpretation to the rift margin uplift model (preferred by one of us, GHG) is as follows. The data clearly show that the TFT ages young southwards, implying greater degrees of exhumation southwards. Early workers have interpreted the Lurio Belt as a significant high strain zone and have interpreted the Mugeba and Monapo structures as overthrust klippen of granulite grade lithologies derived from the Lurio Belt (e.g. Sacchi, 2002 Pinna et al., 1993). Grantham et al. (2003) have suggested that the Lurio Belt is correlatable with the shear zone which separates the Central Highlands Complex from the Vijayan Complex in Sri Lanka (see tight fit reconstruction of Gondwana after Lawver et al., (1998) and others including Reeves used in Grantham et al. (2003). Similar klippen structures of Highland Complex rocks overlying Vijayan Complex rocks in Sri Lanka are also recognised (Kriegsman, 1995; Kröner, A., 1991). Recent P-T estimates from the Mugeba structure show that the meta-pelitic and meta-basic gneisses have peak metamorphic assemblages which show high strain syn-tectonic textures and indicate conditions of ~10kb and 900°C after which post-tectonic static cooling to ~8kb and ~700°C occurred (Roberts et al., 2005). U/Pb SHRIMP data indicate that the high grade metamorphism occurred at ~556 Ma. Data from the same Mugeba Klippe yielded marginally older ages (Kröner et al., 1997) however the data from Kröner et al. (1997) were obtained using the evaporation method which does not have the spatial resolution of SHRIMP. Consequently these data for the Mugeba Klippen are considered unreliable because the SHRIMP data show complex zircons with concordant ages of ~556 Ma and discordant zircons suggesting an upper intercept of ~1120 Ma Consequently during the period from ~550 Ma at ~8 kb and 700°C, rapid exhumation of the area (at least in the vicinity of sample 020823-6) to ~3.5 kb and ~280°C at 245 Ma followed (assuming a typical geothermal gradient of 25°C/km) or 2.8 kb and 280°C at 245Ma (assuming a geothermal gradient of 30°C/km). Using the typical geothermal gradient implies an uplift rate of ~15 km (4.5 kb) over ~300 my or 50 m/my. The area south of the Lurio lineament, here termed the Nampula Terrane for convenience, contains a significant volume of largely undeformed granites whose ages vary from ~453 Ma to ~530 Ma (Grantham et al., 2005a) with most being ~500 Ma in age. The hornblende $^{40}Ar^{39}Ar$ ages (blocking temperature ~550°C) are broadly

consistent with these conditions with the granite minimum melt temperatures being ~650-700°C. The large scale genesis of the granites from ~550-500 Ma is consistent with the Nampula Terrane being depressed in the footwall of the overthrust Lurian rocks now represented by the Mugeba and Monapo Klippen. The increase in temperature due to burial in the footwall would promote dehydration reactions at depth contributing to extensive partial melting of the ~1100 Ma gneisses to form the ~450-530 Ma granites. Rapid exhumation and inversion of the Nampula terrane after the collision along the Lurio front would have followed. On a larger scale, if one considers a cross section from Cobue-Geci (at surface ~550-600 Ma ago) to the Urfjell in southern Kirwanveggan (also at surface ~550 Ma ago) the central portion of Mugeba/Sverdrupfjella experienced depths of 6-8 kb at ~500 Ma ago. The orogenic belt between these two areas has been exhumed. If one looks at the cooling rate from 550 Ma, 900°C and 10 kb with all the points plotted until Karoo times i.e. surface at Gondwana breakup at 180-200 Ma, the data define an almost constant slope with a cooling rate of ~2.5°C/Ma.

3.7 Conclusions

Within the south western Axial Granulite Complex, the c. 542-551 Ma $^{40}Ar/^{39}Ar$ hornblende ages revealed a significant alteration by excess $^{40}Ar^*$ and do not permit reliable inferences on its post-metamorphic cooling history. In the eastern part of the southern basement cooling from the Pan-African thermo tectonic imprint at c. 550-500 Ma was slow with low cooling rates of 10.5-6.5°C/Ma between 524°C and 310-305°C, as recorded by the $^{40}Ar/^{39}Ar$ 476-474 Ma hornblende and c. 448-444 Ma biotite ages, respectively, and is probably linked to the development of the Namama Thrust Belt. Widespread cooling from this youngest thermo-tectonic event in the southern basement to below 350°C was already achieved by c. 450 Ma. The emplacement of granite and pegmatite bodies between c. 500-450 Ma, partly influenced by the youngest deformation event at c. 500 Ma, probably resulted in localized re-heating and hence locally delayed cooling in the region to below 350°C until 434-420 Ma. It cannot be excluded that the Axial Granulite Complex and the southern basement regions coevally experienced significant Pan-African overprints between 550-

500 Ma, subsequent to their granulite facies metamorphic imprints at c. 571-549 Ma (Kröner et al, 2001) and 615-551 Ma (Grantham et al., 2005a; Kröner et al., 1997), respectively. The south-eastern termination of the Lurio Belt in the Unango Group and the adjacent Namarroi Zone are likely key areas to further resolve a younger (< 550 Ma) Pan-African thermo-tectonic evolution in northern Mozambique and southern Malawi.

In both regions, the similar TFT ages of the *O* group samples indicate a common cooling to below 275 ± 25°C during the Late Devonian to Early Carboniferous. It likely further suggests that up to c. 9-11 km of denudation have occurred since. In the southern basement an accompanying decrease in cooling rates to < 1°C/Ma between the Late Ordovician/Early Silurian to Late Devonian/Early Carboniferous is attributed to a reduction in denudation, probably linked to the establishment of pre-Karoo peneplains (< Late Carboniferous) as inferred by Wopfner and Kaaya (1991). A younger group of TFT ages records the cooling induced by erosion of a broadly E-W trending uplifted rift flank. This rift flank probably initiated between Early to Late Permian times. Its formation marks the onset of rifting and incipient Gondwana dispersal in the north Mozambican segment. The TFT data suggest that up to 10-12 km of material has been denuded since the onset of rifting. A corresponding rift basin was probably located adjacent to the south of the basement and linked to the Zambezi rift system via the Zambezi pre-transform system. The basin potentially formed by oblique crustal extension in response to a regional NW-SW tensional stress regime while exploiting pervasive, easterly trending Pan-African ductile fabrics by brittle extensional reactivation. The development of an oblique extensional rift basin, superimposed onto a Pan-African mobile belt corresponds to a network of Karoo-age African rift basins which formed by transtensional and extensional fracturing of weak anisotropic lithosphere that was metamorphosed in late Neoproterozoic/Early Cambrian times (Rogers et al., 1995; Visser and Praekelt, 1998). The spatial TFT age pattern solely recorded rift related cooling and exhumation parallel to the present southern coastal margin in the Early to Late Permian.

Acknowledgements

This research is part of the Ph. D. studies of M. C. Daszinnies. The funding by the University of Bremen, ZF 05/101/01 is gratefully acknowledged. B. Emmel and F. Lisker are thanked for constructive reviews and valuable comments for improvements of a previous version of the manuscript. NGU is thanked for the possibility to join the mapping project in northern Mozambique.

References

Afonso, R.S., 1976, A geologica de Moçambique Notiçia explicativa da carta de Moçambique, *in* Moçambique, S.G.M., ed., Open-File Report.

Andreoli, M.A.G., 1984, Petrochemistry, tectonic evolution and metasomatic mineralisations of Mozambique Belt granulites from S Malawi and Tete (Mozambique): Precambrian Research, v. 25, p. 161-186.

Araujo, J.R., 1976, Mozambique Belt: uma interpretaçao geochronologica: Memoir Notice Publication Museum Mineralogica Geologica Universidad Coimbra Centro Estudidar Geologica, v. 81, p. 85-102.

Bahrenberg, G., Giese, G. and Nipper, J., 1992, Statistische Methoden in der Geographie, Bd.2.: Stuttgart, Borntraeger, p. 220.

Barbarand, J., Carter, A., Wood, I., and Hurfurd, T., 2003, Compositional and structural control of fission-track annealing in apatite: Chemical Geology, v. 198, p. 107-137.

Barbarand, J., and Pagel, M., 2001, Controle de la cicatrisation des traces de fission dans les cristaux d'apatite; le role de la composition chimique: Comptes Rendus de l'Academie des Sciences, Serie II. Sciences de la Terre et des Planetes, v. 332, p. 259-265.

Barr, M.W.C., Donning, K.N., Hammil, M., Harding, A.E., Loughlin, W.P., and Potts, J.G., 1984, Geological and prospecting survey in north Eastern Mozambique, Tete Area., Hunting Geology and Geophysics, Open-File Report: Maputo, Instituto Naçinal de Geological.

Baxter, E.F., 2003, Quantification of the factors controlling the presence of excess ^{40}Ar or ^{4}He: Earth and Planetary Science Letters, v. 216, p. 619-634.

Baxter, E.F., DePaolo, D.J., and Renne, P.R., 2002, Spatially correlated anomalous $^{40}Ar/^{39}Ar$ "age" variations in biotites about a lithologic contact near Simplon Pass, Switzerland; a mechanistic explanation for excess Ar: Geochimica et Cosmochimica Acta, v. 66, p. 1067-1083.

Besairie, H., and Collignon, M., 1972, Géologie de Madagascar; I. Les terraines sédimentaires: Annales Géologiques de Madagascar, v. 35, p. 1-463.

Bloomfield, K., 1968, The pre-Karroo geology of Malawi: Memoir Geological Survey Malawi, v. 5, p. 51.

Bott, M.H.P., 1995, Mechanisms of rifting: Geodynamic modeling of continental rift systems, *in* Olsen, K.H., ed., Continental Rifts: Evolution, Structure, Tectonics, Volume 264: International Lithosphere Program: New York, Elsevier, p. 27-43.

Braun, J., 2002, Quantifying the effect of recent relief changes on the age-elevation relationships: Earth and Planetary Science Letters, v. 200, p.331-343.

Braun, J., and Beaumont, C., 1989, A physical explanation of the relation between flank uplift and the breakup unconformity at rifted continental margins: Geology, v. 17, p. 760-764.

Brown, R., and Summerfield, M.A., 1997, Some uncertainties in the derivation of rates of denudation from thermochronologic data: Earth Surface Processes and Landforms, v. 22, p. 239-248.

Buck, W.R., 1986, Small-scale convection induced by passive rifting: the cause for uplift of rift shoulders: Earth and Planetary Science Letters, v. 77, p. 362-372.

Cadoppi, P., Costa, M., and Sacchi, R., 1987, A cross section of the Namama Thrust Belt (Mozambique): Journal of African Earth Sciences, v. 6, p. 493-504.

Carter, G.S., and Bennett, J.D., 1973, The Geology and Mineral Resources of Malawi: Bulletin Geological Survey Malawi, v. 6, p.141.

Castaing, C., 1991, Post Pan-African tectonic evolution of South Malawi in relation to the Karroo and Recent East African Rift Systems: Tectonophysics, v. 191, p. 53-73.

Catuneanu, O., Wopfner, H., Eriksson, P.G., Cairncross, B., Rubige, B.S., Smith, R.M.H., and Hancox, P.J., 2005, The Karoo basins of south-central Africa: Journal of African Earth Sciences, v. 43, p. 211-253.

Chorowicz, J., 2005, The East African rift system: Journal of African Earth Sciences, v. 43, p. 379-410.

Costa, M., Ferrara, G., Sacchi, R., and Tonarini, S., 1992, Rb/Sr dating of the Upper Proterozoic basement of Zambesia, Mozambique: Geologische Rundschau, v. 81, p. 487-500.

Coyle, D.A., and Wagner, G.A., 1998, Positioning the titanite fission-track partial annealing zone: Chemical Geology, v. 149, p. 117-125.

Daly, M.C., 1986, The intracratonic Irumide Belt of Zambia and its bearing on collision orgogeny during the Proterozoic of Africa, *in* Coward, M.P., and Ries, A.C., eds., Collision tectonics, Volume 19: London, Special Publications Geological Society of London, p. 321-328.

Damon, P.E., 1968, Potassium-argon dating of igneous and metamorphic rocks with applications to the Basin ranges of Arizona and Sonora, *in* Hamilton, E.I., and Farquhar, R.M., eds., Radiometric dating for geologists: London, Intersciences, p. 1-71.

Daszinnies, M.C., Jacobs, J., Kohn, B., and Grantham, G.H., 2004, A combined apatite fission track and (U-Th)/He study of the passive continental margin of northern Mozambique: preliminary results, *in* Scientific committee, ed., Joint earth sciences meeting: Société Géologique de France - Geologische Vereinigung: Strasbourg, p. 29.

Di Vincenzo, G., Viti, C., and Rocchi, S., 2003, The effect of chlorite interlayering on ^{40}Ar-^{39}Ar biotite dating; an ^{40}Ar-^{39}Ar laser-probe and TEM investigations of variably chloritised biotites: Contributions to Mineralogy and Petrology, v. 145, p. 643-658.

Dodson, M.H., 1973, Closure temperature in cooling geochronological and petrological systems: Contributions to Mineralogy and Petrology, v. 40, p. 259-274.

Dumitru, T., 1991, A new computer-automated microscopic stage system for fission track analysis: On Track, v. 1, p. 1-7.

Eby, G.N., Roden Tice, M., Krueger, H.L., Ewing, W., Faxon, E.H., and Woolley, A.R., 1995, Geochronology and cooling history of the northern part of the Chilwa alkaline province, Malawi: Journal of African Earth Sciences, v. 20, p. 275-288.

Fairhead, J.D., 1976, The structure of the lithosphere beneath the Eastern Rift, East Africa, deduced from gravitiy studies: Tectonophysics, v. 30, p. 269-298.

Galbraith, R.F., and Laslett, G.M., 1993, Statistical models for mixed fission track ages: Nuclear Tracks and Radiation Measurements, v. 21, p. 459-470.

Gallagher, K., Brown, R., and Johnson, C., 1998, Fission track analysis and its applications to geological problems: Annual Reviews in Earth and Planetary Sciences, v. 26, p. 519-572.

Gallagher, K., Hawkesworth, C.J., and Mantovani, M.J.M., 1994, The denudation history of the onshore continental margin of SE Brazil inferred from apatite fission track data: Journal of Geophysical Research, v. 99, p. 18117-18145.

Gleadow, A.J.W., 1981, Fission track dating methods: What are the real alternatives? Nuclear Tracks and Radiation Measurements, v. 5, p. 3-14.

Grantham, G.H., Maboko, M., and Eglington, B.M., 2003, A review of the evolution of the Mozambique Belt and implications for the amalgamation and dispersal of Rodinia and Gondwana, *in* Yoshida, M., Windley, B.F., and Dasgpta, S., eds., Proterozoic East Gondwana: Supercontinent Assembly and Breakup, Volume 206: London, Special Publications Geological Society of London, p. 401-425.

Grantham, G.H., Keidan, H., Hokada, T., Ingram, B.A., Macey, P., Shiraishi, K., Kagashima, S., and Azevedo, S., 2005a, New U-Pb SHRIMP Zircon data from NE Mozambique: implications for Mozambique Belt evolution and Gondwana E-W or N-S? *in* Pankhurst, R.J., and Veiga, G.D., eds., Gondwana 12: Mendoza, p. 182.

Grantham, G.H., Macey, P., Ingram, B.A., Rademeyer, M., Eglington, B., Keidan, H., and Azevedo, S., 2005b, The chemistry and age of Karoo-age andesitic lavas along the northern Mozambique coast, *in* Pankhurst, R.J., and Veiga, G.D., eds., Gondwana 12: Mendoza, p. 183.

Green, P.F., 1981, A new look at statistics in fission-track dating: Nuclear Tracks and Radiation Measurements, v. 5, p. 77-86.

Grove, M., and Harrison, T.M., 1996, $^{40}Ar^*$ diffusion in Fe-rich phlogopite: American Mineralogist, v. 81, p. 940-951.

Habgood, F., 1963, The geology of the country west the Shire River between Chikwawa and Chiromo: Bull. geol. Surv. Nyasaland, v. 14, p. 172.

Hames, W.E., and Bowring, S.A., 1994, An empirical evaluation of the argon diffusion geometry in muscovite: Earth and Planetary Science Letters, v. 124, p. 161-167.

Harrison, T.M., 1981, Diffusion of ^{40}Ar in hornblende: Contributions to Mineralogy and Petrology, v. 78, p. 324-331.

Hurford, A.J., 1990, International Union of Geological Sciences Subcommission on Geochronology Recommendation for standardization of fission track dating calibration and data reporting: Nuclear Tracks and Radiation Measurements, v. 17, p. 233-236.

Jacobs, J., Fanning, C.M., Henjes-Kunst, F., Olesch, M., and Paech, H.-J., 1998, Continuation of the Mozambique Belt into East Antarctica: Grenville-age metamorphsim and polyphase Pan-African high-grade events in central Dronning Maud Land: Journal of Geology, v. 106, p. 385-406.

Jacobs, J., and Thomas, B., 2004, Himalayan-type indenter-escape tectonics model for the southern part of the late Neoproterozoic-early Palaeozoic East African Antarctic orogen: Geology, v. 32, p. 721-724.

Jaritz, W., Kreuzer, H., Mueller, P., and Harre, W., 1977, Die Vulkanitserien im Küstengebiet von Nordmoçambique: Geologisches Jahrbuch. Reihe B: Regionale Geologie Ausland, v. 26, p. 147-165.

Johnson, M.R., Van Vuuren, C.J., Hegenberger, W.F., Key, R., and Shoko, U., 1996, Stratigraphy of the Karoo Supergroup in southern Africa: an overview: Journal of African Earth Sciences, v. 23, p. 3-15.

Jonckheere, R.C., and Wagner, G.A., 2000, On the thermal stability of fossil and neutron-induced fission-tracks in natural titanite: Nuclear Instruments and Methods - Physics Research B, v. 168, p. 78-87.

Kohn, B.P., Wagner, M.E., Lutz, T.M., and Organist, G., 1993, Anomalous Mesozoic thermal regime, central Appalachian Piedmont; evidence from sphene and zircon fission-track dating: Journal of Geology, v. 101, p. 779-794.

Kriegsman, L.M., 1995, The Pan-African event in East Antarctica: a view from Sri Lanka and the Mozambique Belt: Precambrian Research, v. 75, p. 263-277.

Kröner, A., 1991, African linkage of Precambrian Sri Lanka: Geologische Rundschau, v. 80, p. 429-440.

Kröner, A., Sacchi, R., Jaeckel, P., and Costa, M., 1997, Kibaran magmatism and Pan-African granulite metamorphism in northern Mozambique: single zircon ages and regional implications: Journal of African Earth Sciences, v. 25, p. 467-484.

Kröner, A., Willner, A.P., Hegner, E., Jaeckel, P., and Nemchin, A., 2001, Single zircon ages, PT evolution and Nd isotopic systematics of high-grade gneisses in southern Malawi and their bearing on the evolution of the Mozambique belt in southeastern Africa: Precambrian Research, v. 109, p. 257-291.

Kuiper, Y.D., 2002, The interpretation of inverse isochron diagrams in $^{40}Ar/^{39}Ar$ geochronology: Earth and Planetary Science Letters, v. 203 , p. 499-506.

Kusky, T.M., Abdelsalam, R.D., Tucker, R.D., and Stern, R.J., 2003, Evolution of the East African and related orogens, and the assembly of Gondwana: Precambrian Research, v. 123, p. 81-85.

Lawyer, L.A., Gahagan, L.M., and Dalziel, I.W.D., 1998, A tight fit early Mesozoic Gondwana, a plate reconstruction perspective: Special Issue, Memoir of the National Institute of Polar Research, v. 53, p. 214-229.

Lee, J.K.W., 1993, The Argon release mechanisms of hornblende in vacuo: Chemical Geology, v. 106, p. 133-170.

—, 1995, Multipath diffusion in geochronology: Contributions to Mineralogy and Petrology, v. 120, p. 60-82.

Lee, J.K.W., Onstott, T.C., Cashman, K.V., Cumbest, R.J., and Johnson, D., 1991, Incremental heating of hornblende in vacuo: Implications for ^{40}Ar-^{39}Ar geochronology and the interpretation of thermal histories: Geology, v. 19, p. 872-876.

Leeder, M.R., 1991, Denudation, vertical crustal movements and sedimentary basin infill: Geologische Rundschau, v. 80, p. 441-458.

Lo, C.H., Lee, J.K.W., and Onstott, T.C., 2000, Argon release mechanisms of biotite in vacuo and the role of short-circuit diffusion and recoil: Chemical Geology, v. 165, p. 135-166.

Ludwig, K.R., 2001, Isoplot 2.49 - A Geochronological Toolkit for Microsoft Excel, Berkeley Geochronology Center Special Publication 1a, v. 4.

Lulin, J.M., 1985, Un nouveau gîte à Nb, Ta, U, REE d'origin magmatique en Afrique orientale: le complexe alcalin tectonisé de Meponda, Précambrien, province de Niassa, Moçambique [PhD thesis]: Orléans, University Orléans.

Mascle, J., Mougenot, D., Blarez, E., Marinho, M., and Virlogeux, P., 1987, African transform continental margins; examples from Guinea, the Ivory Coast and Mozambique, *in* Bowden, P., and Kinnaird, J., eds., African geology reviews, v. 22: Geological Journal: Chichester-New York, United Kingdom, Wiley & Sons, p. 537-561.

McDougall, I., and Harrison, T.M., 1999, Geochronology and Thermochronology by the $^{40}Ar/^{39}Ar$ Method: New York, Oxford University Press, p. 269.

McIntyre, G.A., Brooks, C., Compston, W., and Turek, A., 1966, The statistical assessment of Rb-Sr isochrons: Journal of Geophysical Research, v. 71, p. 5459.

Meert, J.G., 2003, A synopsis of events related to the assembly of eastern Gondwana: Tectonophysics, v. 362, p. 1-40.

Möller, A., Mezger, K., and Schenk, V., 2000, U-Pb dating of metamorphic minerals: Pan-African metamorphism and prolonged slow cooling of high pressure granulites in Tanzania, East Africa: Precambrian Research, v. 104, p. 123-146.

Morley, C.K., Haranya, W., Phoosongsee, S., Pongwapee, S., Kornsawan, A., and Wonganan, N., 2004, Activation of rift oblique and rift parallel pre-existing fabrics during extension and their effect on deformation style: examples from the rifts in Thailand: Journal of Structural Geology, v. 26, p. 1803-1829.

Mougenot, D., Recq, M., Virlogeux, M., and Lepvrier, C., 1986, Seaward extension of the East African Rift: Nature, v. 321, p. 599-603.

Naeser, C.W., and McKee, E.H., 1970, Fission-track and K-Ar ages of Tertiary ash-flow tuffs, north-central Nevada: Geological Society of America Bulletin, v. 81, p. 3375-3384.

Nairn, A.E.L., Lerche, I., and Iliffe, J.E., 1991, Geology, basin analysis, and hydrocarbon potential of Mozambique and the Mozambique Channel: Earth Science Reviews, v. 30, p. 81-124.

Norgett, M.J., and Liaiard, A.B., 1968, The migration of inert gases in ionic crystals: Philosophical Magazin, v. 18, p. 1193-1220.

Onstott, T.C., Phillips, D., and Pringle-Goodell, L., 1991, Laser microprobe measurement of chlorine and argon zonation in biotite: Chemical Geology, v. 90, p. 145-168.

Pinna, P., 1995, On the dual nature of the Mozambique Belt, Mozambique to Kenya: Journal of African Earth Sciences, v. 21, p. 477-480.

Pinna, P., Jourde, G., Caluez, J.-Y., Mroz, J.P., and Marques, J.M., 1993, The Mozambique Belt in northern Mozambique: Neoproterozoic (1100-850 Ma) crustal growth and tectogenesis and superimposed Pan-African (800-550 Ma) tectonism: Precambrian Research, v. 62, p. 1-59.

Pinna, P., and Marteau, P., 1987, Carta geologica de Moçambique, 1:1,000,000 scale, with explanatory notes.

Reed, D.J., 1977, A review of recent theoretical developments in the understanding of the migration of helium in metals and its interaction with lattice defects: Radiation Effects, v. 31, p. 129-147.

Reeves, C.V., Sahu, B.K., and de Wit, M., 2002, A re-examination of the paleo-position of Africa's eastern neighbours in Gondwana: Journal of African Earth Sciences, v. 34, p. 101-108.

Roberts, M.P., Grantham, G.H., Cronwright, M., Sacchi, R., Ingram, B., Azevedo, S., Walliser, A., and August, R.B., 2005, Preliminary pressure temperature determinations on granulitefacies rocks of the Mugeba Klippe, north central Moçambique, GEO 2005, Abstract Volume: Durban, South Africa, University of Kwazulu-Natal, p. 193-194.

Roddick, J.C., 1978, The application of isochron diagrams in $^{40}Ar/^{39}Ar$ dating: A discussion: Earth and Planetary Science Letters, v. 41, p. 233-244.

Rogers, J.J.W., Unrug, R., and Sultan, M., 1995, Tectonic assembly of Gondwana: Journal of Geodynamics, v. 19, p. 1-34.

Royden, L., and Keen, C.E., 1980, Rifting processes and thermal evolution of the continental margin of eastern Canada determined from subsidence curves: Earth and Planetary Science Letters, v. 51, p. 343-361.

Sacchi, R., Cadoppi, P., and Costa, M., 2000, Pan-African reactivation of the Lurio segment of the Kibaran Belt system: a reappraisal from recent age determinations in northern Mozambique: Journal of African Earth Sciences, v. 30, p. 629-639.

Sacchi, R., Marques, J., Costa, M., and Casati, C., 1984, Kibaran events in the southernmost Mozambique Belt: Precambrian Research, v. 25, p. 141-159.

Salman, G., and Abdula, I., 1995, Development of the Mozambique and Ruvuma sedimentary basins, offshore Mozambique: Sedimentary Geology, v. 96, p. 7-41.

Schandelmeier, H., Bremer, F., and Holl, H.-G., 2004, Kinematic evolution of the Morondava rift basin of SW Madagascar - from wrench tectonics to normal extension: Journal of African Earth Sciences, v. 38, p. 321-330.

Steiger, R.J., and Jäger, E., 1977, Subcommission on geochronology: Convention on the use of decay constants in geo- and cosmochronology: Earth and Planetary Science Letters, v. 36, p. 359-362.

Stüwe, K., White, L., and Brown, R., 1994, The influence of eroding topography on steady-state isotherms. Application to fission track analysis: Earth and Planetary Science Letters, v. 124, p. 63-74.

Thomas, R.J. et al., 2006, Field Report. Mineral Resources Management Capacity Building Project, Report B5.1, Republic of Mozambique, p. 41.

Van der Beek, P., 1995, Tectonic evolution of continental rifts: inferences from numerical modelling and fission track thermochronology [PhD thesis]: Amsterdam, Vrije University.

Van der Beek, P., Andriessen, P., and Cloethingh, S., 1995, Morphotectonic evolution of rifted continental margins: inferences from a coupled tectonic-surface process model and fission track thermochronology: Tectonics, v. 14, p. 406-421.

Van der Beek, P., Cloethingh, S., and Andriessen, P., 1994, Mechanisms of extensional basin formation and vertical motions at rift flanks: Constraints from tectonic modelling and fission track thermochronology: Earth and Planetary Science Letters, v. 121, p. 417-433.

Van der Beek, P., Mbede, E., Andriessen, P., and Delvaux, D., 1998, Denudation history of the Malawi and Rukwa Rift flanks (East African Rift System) from

apatite fission track thermochronology: Journal of African Earth Sciences, v. 26, p. 363-385.

Verniers, J., Jourdan, P.P., Paulis, R.V., Frasca-Spada, L., and Bock, F.R.D., 1989, The Karroo Graben of Metangula Northern Mozambique: Journal of African Earth Sciences, v. 9, p. 137-158.

Visser, J.N.J., and Praekelt, H.E., 1996, Subduction, mega-shear systems and Late Palaeozoic basin development of Gondwana: Geologische Rundschau, v. 86, p. 632-646.

—, 1998, Late Palaeozoic crustal block rotations within the Gondwana sector of Pangea: Tectonophysics, v. 287, p. 201-212.

Wagner, G.A., and Van den Haute, P., 1992, Fission Track Dating: Stuttgart, Enke Verlag, p. 285.

Wopfner, H., 1993, Structural development of Tanzania Karoo basins and the break-up of Gondwana, *in* Finlay, A., ed., Gondwana Eight: Hobart, Balkema, p. 531-539.

—, 1994, The Malagasy, a chasm in the Tethyan margin of Gondwana: Journal of Southeast Asian Earth Sciences, v. 9, p. 451-461.

—, 2002, Tectonic and climatic events controlling deposition in Tanzanian Karoo basins: Journal of African Earth Sciences, v. 34, p. 167-177.

Wopfner, H., and Kaaya, C.Z., 1991, Stratigraphy and morphotectonics of Karoo deposits of the northern Selous Basin, Tanzania: Geological Magazine, v. 128, p. 319-334.

York, D., 1969, Least squares fitting of a straight line with correlated errors: Earth and Planetary Science Letters, v. 5, p. 320-324.

Ziegler, P.A., and Cloething, S., 2004, Dynamic processes controlling the evolution of rifted basins: Earth-Science Reviews, v. 64, p. 1-50.

Chapter 4

CENTRAL EASTERN AFRICA DURING GONDWANAS RIFT, BREAK-UP AND DRIFT EVOLUTION SINCE THE MESOZOIC

In the eastern part of central Africa, graben and extended intra-cratonic rift structures, filled with Karoo Group equivalent deposits formed during the Late Carboniferous to Late Triassic/Early Jurassic period of rifting (e.g. Catuneanu et al., 2005). Since the Late Permian to Early Triassic the tectonic regime of eastern Africa was governed by a NW-SE orientated tensional stress field (Castaing, 1991; Catuneanu et al., 2005; Schandelmeier et al., 2004; Verniers et al., 1989) (Figs. 4.1 and 4.2). During this time the rift structures were connected by transcontinental mega-shear systems. One of them, the Falkland-East Africa-Tethys shear system split the supercontinent into an eastern and western part but failed to break it apart (Visser and Praekelt, 1996; 1998) (Fig. 4.1). It remarkably coincides in trend with the Mozambique Belt and the East African-Antarctic Orogen (Jacobs et al., 1998), suggesting a Pan-African shear zone/mobile belt control on its location and orientation.

Based on palaeo-geographic reconstruction attempts it has been argued that the supercontinent's separation into two rigid plates of East and West Gondwana is an oversimplification (Reeves et al., 2002). An improvement has been proposed by subdividing the continental plates into smaller crustal segments that are bounded by shear zones. These shear zones repeatedly accommodated the long distance transfer of stresses and allow limited rotation of the connected crustal segments (Reeves et al., 2004).

During the Early to Middle Jurassic, a widespread intracontinental magmatism occurred in southern Gondwana and evidences the continuing stress by extensional forces (Brewer et al., 1992; Hawkesworth et al., 1999). In southern Africa the Karoo Large Igneous Province (LIP) erupted between 184-179 Ma and virtually synchronously, the Ferrar Group igneous activity took place along the margin of eastern

Antarctica (Duncan et al., 1997; Jones et al., 2001). The Karoo and Ferrar magmatism have been associated with a thermal anomaly of the Bouvet mantle plume (Fig. 4.2). This plume activity potentially caused further crustal weakening within southern Gondwana and thereby contributed to the rifting and final break-up between East Gondwana (Antarctica/ India/Australia) and West Gondwana (Africa/South America) (Fig. 4.1) (Storey, 1995) .

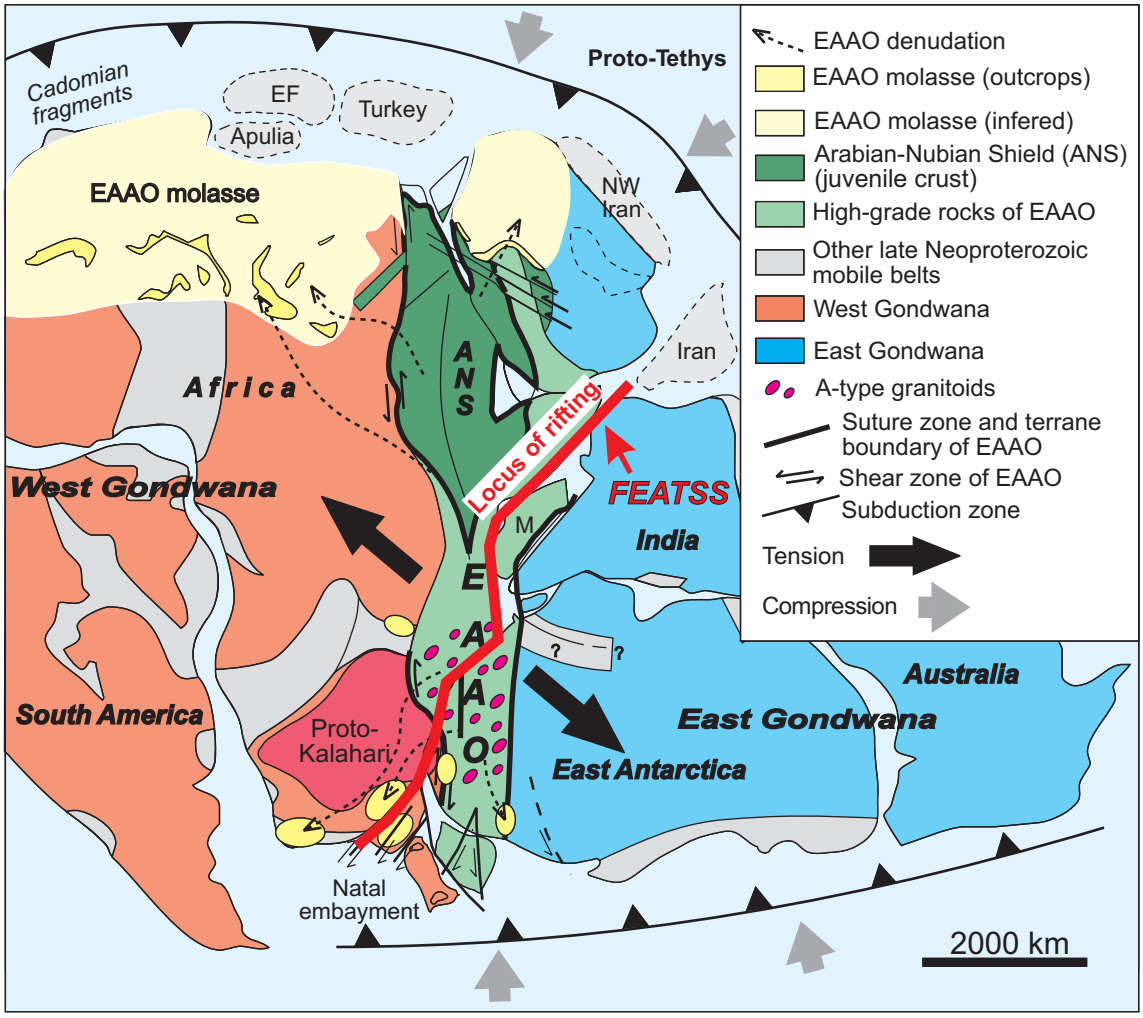

Figure 4.1: Gondwana reassembly with outlined present-day continents and approximated axis of separation between East and West Gondwana modified after Jacobs and Thomas (2004). The *EAAO* is the East African-Antarctic Orogen, *EF* denotes European fragments and the *FEATSS* is the Falkland-East Africa-Tethys Shear System (Visser and Praekelt, 1996; 1998).

The tensional stresses that prevailed in central eastern Africa since in Late Palaeozoic Early Mesozoic times progressively changed in orientation from NW-SE to NE-SW during the Jurassic to Early Cretaceous (Castaing, 1991; Delvaux, 2001).

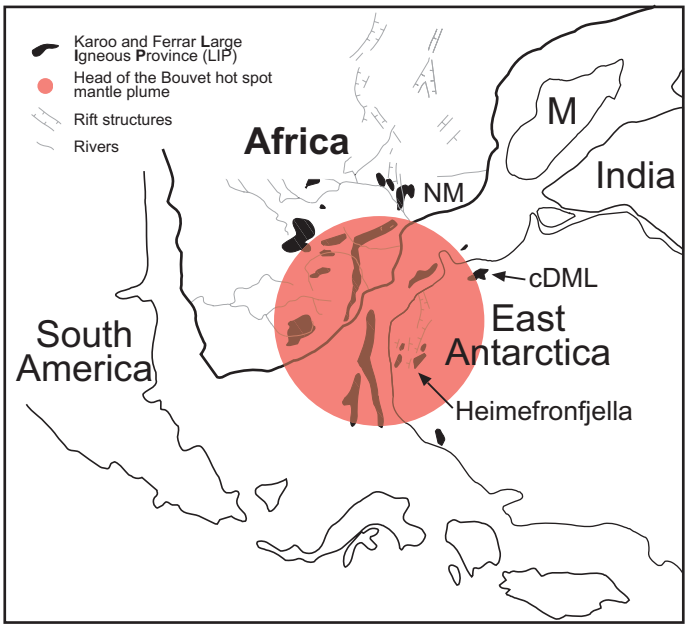

Figure 4.2: Sketch map of Gondwana illustrating the location of the Karoo and Ferrar Large Igneous Province (LIP) in the Middle Jurassic. The map was modified from Storey et al. (1995). Abbreviations: cDML = central Dronning Maud Land, M = Madagascar and NM = northern Mozambique.

The southward movement of East Gondwana relative to West Gondwana proceeded during the Jurassic to Early Cretaceous (Fig 4.3) along the Davie Fracture Zone (DFZ) and an associated sub parallel system of fracture zones along the coast of eastern Africa (e.g. Mozambique Ridge) and Madagascar. They coincide in trend with prominent Pan-African lineaments, such as the Bongolava-Rantosara Shear Zone in Madagascar (Fig. 4.3) (Droz and Mougenot, 1987; Roeser et al., 1996). The DFZ is a remnant transform fault with a dextral shear sense that edges the north Mozambican margin and localized transpressional and transtensional stresses during the southward drift of Madagascar (Coffin and Rabinowitz, 1987; Coffin and Rabinowitz, 1992). The stresses probably also affected the adjacent continental margins, such as the south western margin of Madagascar (Malod et al., 1991). East Gondwana's southward drift was accompanied by the evolution of the Somali and Mozambique basins (Fig 4.3). The rift

to drift transition, i.e. the timing of the Gondwana break-up is marked by the first production of oceanic crust. In the Somali Basin it is assigned to the first magnetic anomaly M 25 in the Late Jurassic at c. 154 Ma (Oxfordian-Kimmerigdian). The formation of oceanic crust ceased in the Early Cretaceous at c. 118 Ma (M 0) as did the southward drift of Madagascar (Coffin and Rabinowitz, 1992). Based on tectono-sedimentary patterns from the Morondava Basin in Madagascar a late Early Jurassic timing (Toarcian-Aalenian) is inferred for the break-up in the Somali Basin (Geiger et al., 2004a). In the Mozambique Basin/Riiser-Larsen Sea, the first oceanic crust formed around c. 155 Ma (Jokat et al., 2003). Episodes of marine transgressions of the southern Tethys occurred from the northern margin of the supercontinent and accompanied sea-floor spreading. In the southern Rovuma Basin marine conditions prevailed since the Middle to Late Jurassic. In contrast, in the Mozambique Basin earliest marine transgressions occurred later in the Early Cretaceous and document the gradually southward extending marine corridor between East and West Gondwana (Salman and Abdula, 1995).

Within central East Africa, the southern segment of the Tanganyika-Rukwa-Malawi System that emerged from the Permo-Triassic rifting period (Fig. 4.4), experienced renewed rifting during the Late Jurassic to Early Cretaceous (Delvaux, 2001 and references therein). In the Early Cretaceous crustal extension and rifting in the southern Tanganyika-Rukwa-Malawi System and its continuation via the Urema Graben into southern Mozambique were accompanied by alkaline and basaltic magmatism (Flores, 1973; Nairn et al., 1991; Woolley and Garson, 1970).

The Cretaceous was a time of major plate reorganisations. It was accompanied by the productions of large amounts of seafloor, associated with the extension of the world ocean ridge system during the Early Cretaceous and with an increase in the amount of spreading ridges and rise in spreading rates since the middle Cretaceous (Summerfield, 1985; Summerfield, 1991). In the southern Gondwana hemisphere, a significant re-arrangement in the plate tectonic pattern occurred in the Early Cretaceous at c. 130 Ma. The two plate drift configuration of East and West Gondwana was replaced by a three plate drift setting due to the opening of the southern Atlantic Ocean (Figs 4.4 and 4.5).

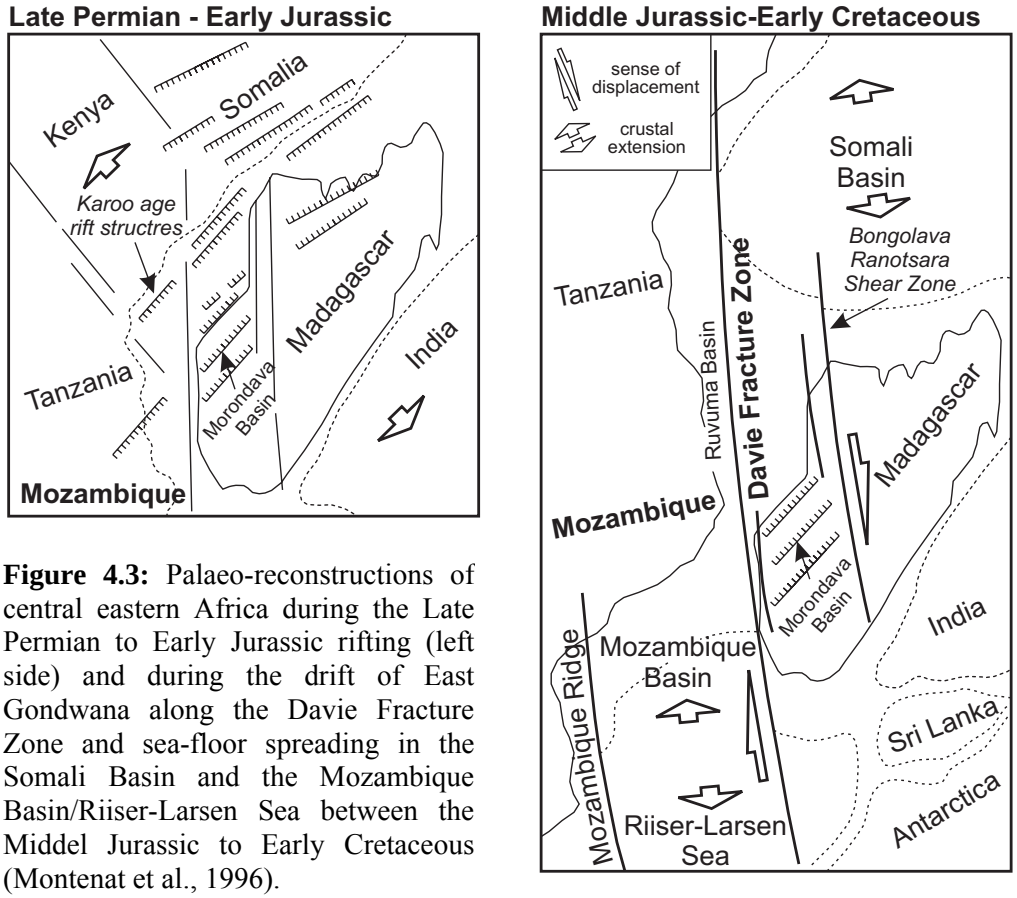

Figure 4.3: Palaeo-reconstructions of central eastern Africa during the Late Permian to Early Jurassic rifting (left side) and during the drift of East Gondwana along the Davie Fracture Zone and sea-floor spreading in the Somali Basin and the Mozambique Basin/Riiser-Larsen Sea between the Middel Jurassic to Early Cretaceous (Montenat et al., 1996).

A triple junction formed between the crustal segments of South America, Africa and the India/Madagascar/Sri Lanka/Antarctica/Australia block. Synchronously, rifting between India/Madgascar, Sri Lanka and Antarctica/Australia initiated at c. 135-130 Ma (Lawver et al., 1991; Roeser et al., 1996; Storey, 1995). The northward drift of the India/Madagascar block started with an accelerated seafloor spreading at c. 96 Ma (Lawver et al., 1991; Powell et al., 1988; Storey, 1995). India rifted off Madagascar in the Late Cretaceous, broadly synchronous to the cessation of strike-slip motion along the DFZ (Malod et al., 1991).

The changes in plate motion as e.g. the opening of the Atlantic and Indian oceans exerted a significant tectonic influence on the African plate. It resulted in the re-activation of Pan-African age shear zones expressed by repeated crustal extension, rifting, strike-slip motion and the development and reactivation of superimposed sedimentary basins (Janssen et al., 1995). The Central African Shear Zone and the Mwembeshi Shear Zone are such regional scale transcontinental Pan-African age shear

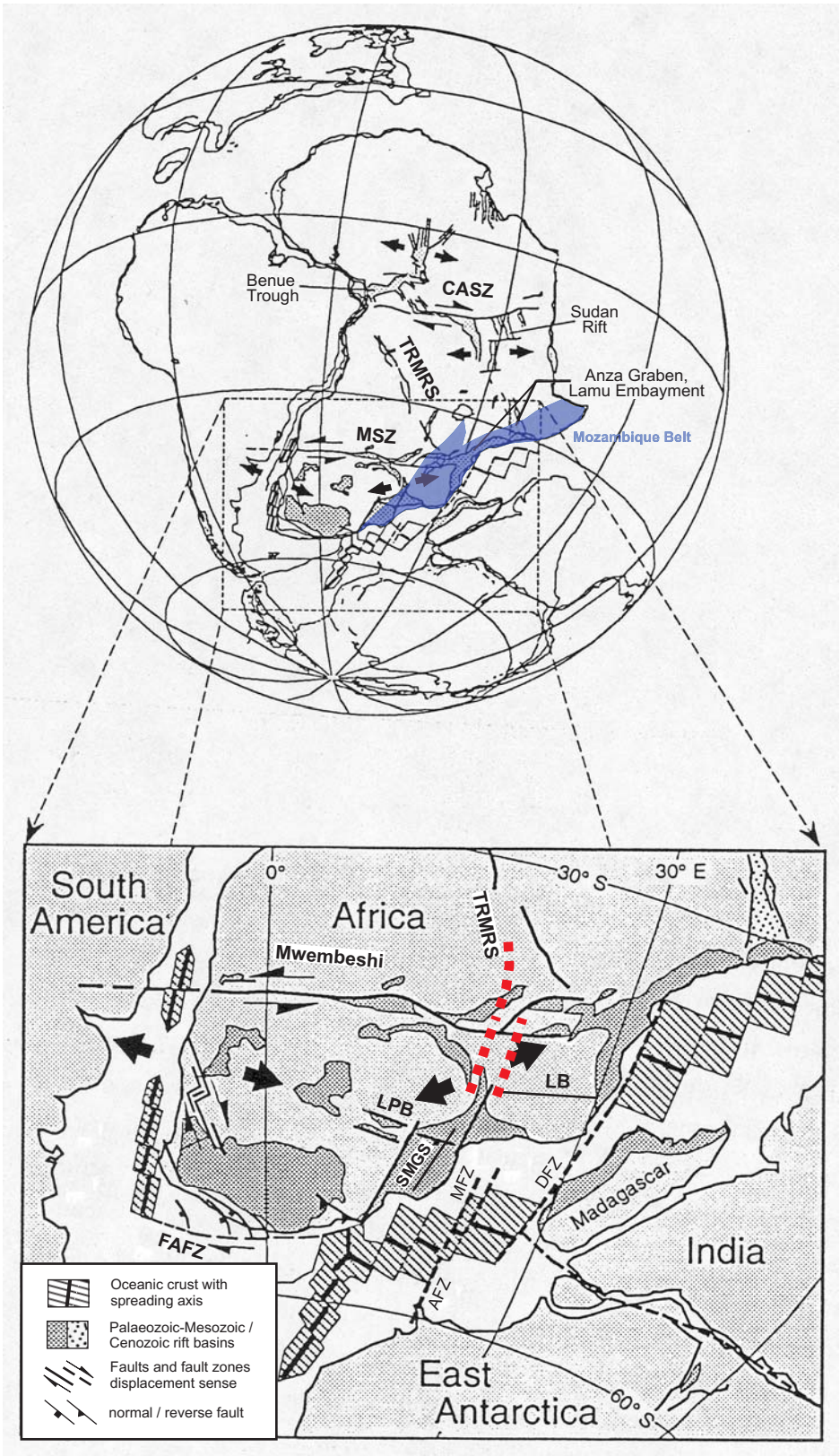
Benue Trough
CASZ
Sudan Rift
TRMRS
Anza Graben, Lamu Embayment
MSZ
Mozambique Belt
South America
0°
Africa
30° S
30° E
TRMRS
Mwembeshi
LB
LPB
SMGS
MFZ
DFZ
Madagascar
India
FAFZ
AFZ
East Antarctica
60° S
Oceanic crust with spreading axis
Palaeozoic-Mesozoic / Cenozoic rift basins
Faults and fault zones displacement sense
normal / reverse fault

Figure 4.4: Palaeogeographic reconstruction the Gondwana fragments during the Early Cretaceous (c. 130 Ma). The map depicts active trans- and intracontinental tectonic lineaments and Karoo (Permo-Triassic) and Jurassic-Cretaceous rift basins in Africa. The red dotted lines broadly trace zones of post Triassic crustal extension, indicated by AFT analysis of Van der Beek et al. (1998) and this study. Map modified and compiled after Brown (1992), Castaing (1991), Dingle and Scrutton (1974), Delvaux (2001), Reeves et al. (2002) and references therein. Abbreviations: AFZ = Astrid Fracture Zone (Ridge), CASZ = Central African Shear Zone, DFZ = Davie Fracture Zone, FAFZ = Falkland-Africa Fault Zone, LB =Lurio Belt, LPB: Limpopo Belt, MFZ = Mozambique Fracture Zone (Ridge), MSZ = Mwembeshi Shear Zone, SMGS = South Mozambican Graben System, TRMS = Tanganyika-Rukwa-Malawi Rift System.

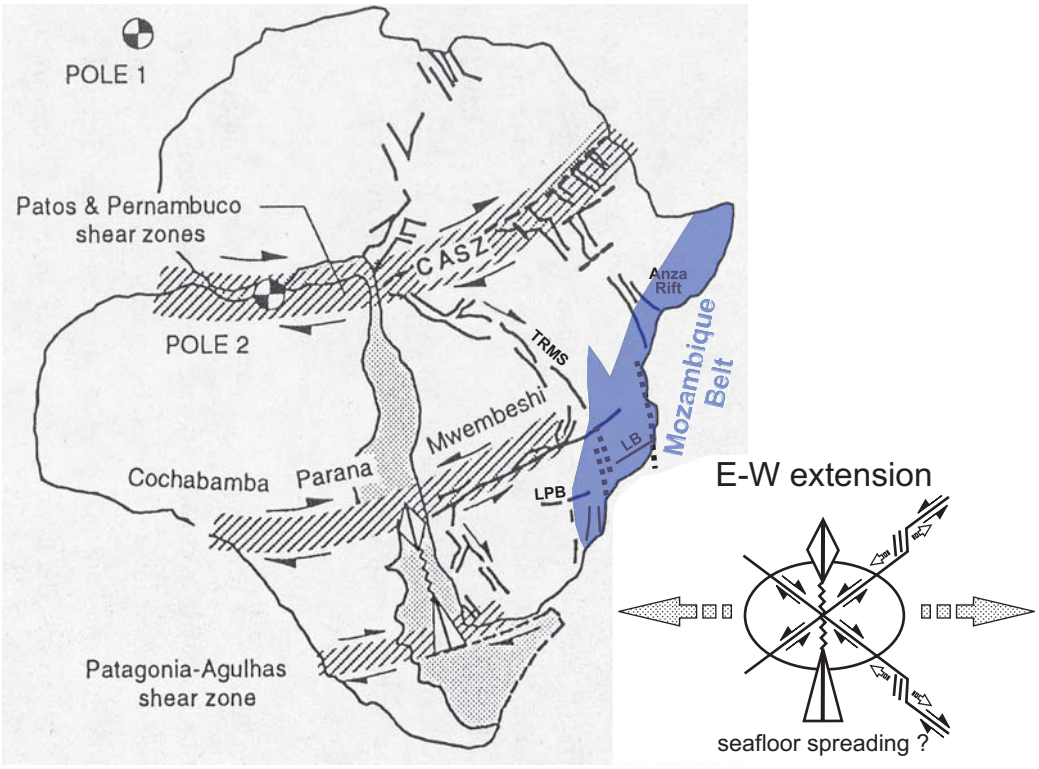

Figure 4.5: Palaeo-geographic reconstruction of the pre-drift configuration between South America and Africa in the Early Cretaceous (c. 130 Ma). Trans-African shear zones reactivated during the seafloor spreading are highlighted by hashed patterns. The inset depicts theoretical relationships for a conjugated set of shear zones and associated structures in response to E-W extension after Brown (1992 and references therein). It also illustrates the anticipated sense of sinistral shear for the Mwembeshi and the dextral sense of shear for the Central African shear zones. The left stepping sinistral and right stepping dextral shears and zones of consequent extensional faulting are shown as a possible interpretation of the renewed rifting in southern segment of the TRMS. The thick black dotted lines broadly trace zones of post Triassic crustal extension, indicated by AFT analysis of Noble et al. (1997), Van der Beek et al. (1998) and this study. The Poles 1 and 2 are the poles of relative motion for the northern and southern domains of South America, relative to southern Africa, respectively. Map and inset after Brown (1992) and references therein. Abbreviations: CASZ = Central African Shear Zone, LB = Lurio Belt, LPB = Limpopo Belt, TRMS = Tanganyika-Rukwa-Malawi-Rift System.

zone reactivating structures (Figs. 4.4 and 4.5), which experienced multiple episodes of crustal extension and strike slip deformation during the Phanerozoic (Daly et al., 1989; Daly et al., 1991). They both accommodated long distance transfer of stresses through Africa in response to Atlantic opening (Fairhead, 1988; Popoff, 1988; Unternehr, 1988) and link-up to the N-S trending Mozambique Belt (MB) in eastern Africa. During Cretaceous times their tectonic activities led to repeated crustal extension in the Sudan rift and its extension into Kenya/Tanzania (Fairhead, 1988; Foster and Gleadow 1992, 1996; Noble et al., 1997 and references therein). The geometric setting of these transcontinental shear zones and associated perpendicular orientated extensional rift basins (Figs 4.4 and 4.5) in West, Central and East Africa apparently resembles a regional conjugated fault system (Brown, 1992 and references therein). Synchronously, Cretaceous rifting activity along the Tanganyika-Rukwa-Malawi System (Delvaux, 2001), and the MB in southern Mozambique (e.g. Nairn et al., 1991) is reported.

An Early Tertiary period of extension and rifting is reported from the southern Tanganyika-Rukwa-Malawi System (≤ 50-40 Ma) in Malawi and along the upcoming eastern branch of the East African Rift System (Fig. 4.6) within the Sudan to northern Kenya basins and the Anza Rift (Delvaux, 2001).

In Palaeogene times at c. 30 Ma, the Afar hot spot activity initiated the development of the East African Rift System (Fig. 4.6) in the Afar and Ethiopian plateau (Hoffmann et al., 1997) through triggering the formation of a triple junction (Chorowicz et al., 1998). Subsequently, the rift system propagated from north to south. Its southern terminations of the western and eastern branches enclose the north Mozambican basement (see Chorowicz, 2005 and references therein). They are of late Miocene-Pliocene to recent and of middle Miocene to recent in age, respectively (Chorowicz, 2005; Mougenot et al., 1986). The south western branch coincides with the southern Tanganyika-Rukwa-Malawi System while the south eastern branch coincides in trend and location with the DFZ (Figs. 4.4-4.6). In the Palaeogene extensional faulting and graben formation along the DFZ formation is attributed to the extensional reactivation of fossil strike-slip faults (Mougenot et al., 1986).

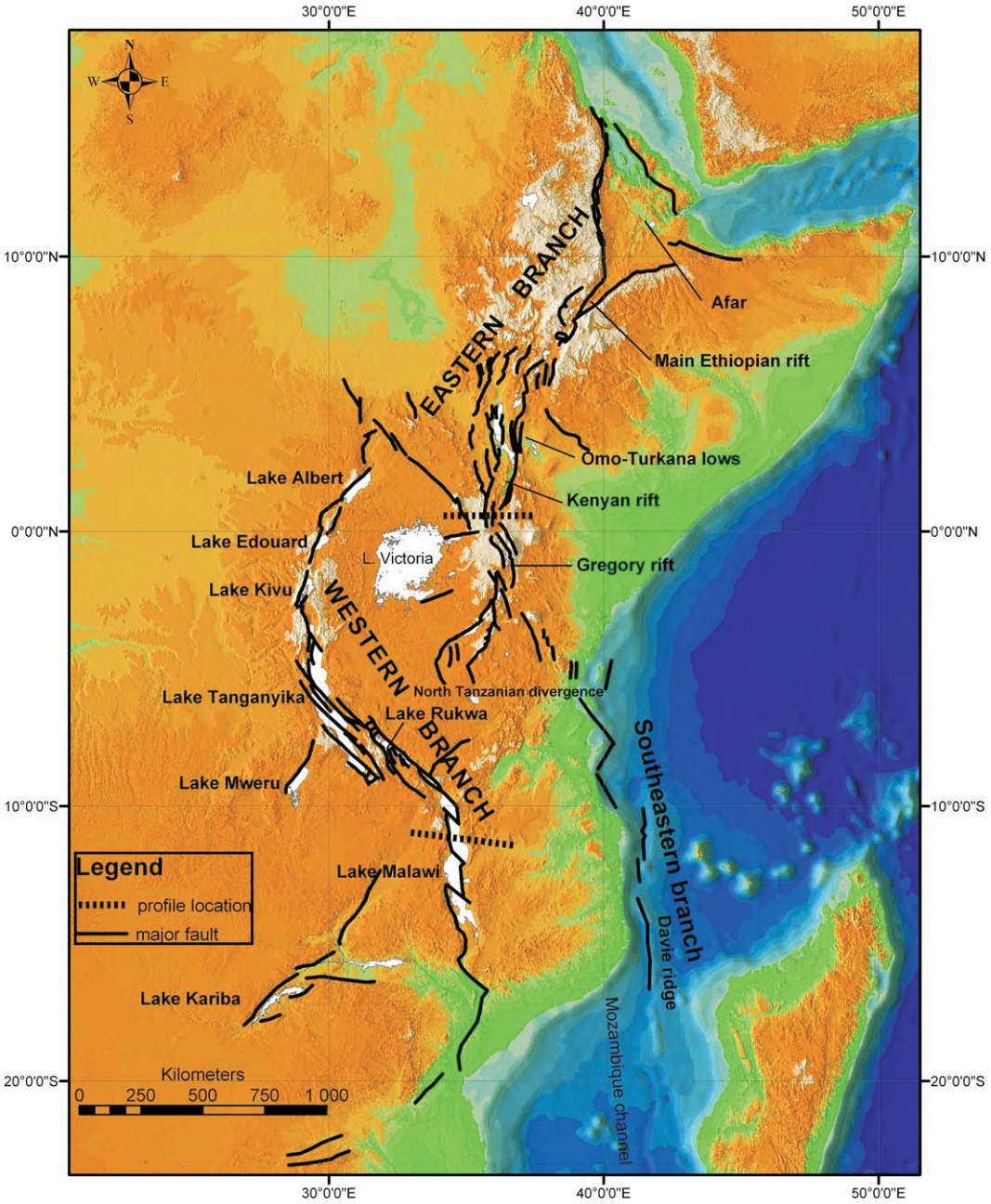

Figure 4.6: Hypsographic digital elevation model of the East African Rift System from Chorowicz (2005). Black lines represent the main faults, white surfaces display lakes and colour levels from green to brown indicate the elvations from low to high, respectively.

Chapter 5

PREVIOUS APATITE FISSION TRACK STUDIES IN CENTRAL EAST AFRICA AND EAST ANTARCTICA

Previous AFT studies in central East Africa comprise a reconnaissance study around the East African Rift System in Kenya (Wagner et al., 1992), detailed studies of four mountain ranges surrounding the central Kenya Rift (Foster and Gleadow, 1992; 1996), a regional study in eastern Tanzania (Noble et al., 1997) a detailed study around the Malawi and Rukwa rift segments of the East African Rift System in south western Tanzania and northern Malawi (Van der Beek et al., 1998), regional studies in central and southern Madagascar (Emmel et al., 2004; 2006a-c) and a regional study of Madagascar as an entity (Seward et al., 2004). Following the late Neoproterozoic/Early Cambrian amalgamation of Gondwana, East Antarctica was adjoined to northern Mozambique and Madagascar. During the Palaeozoic-Mesozoic supercontinent's disintegration, East Antarctica rifted off northern Mozambique but was still joined to central Africa until the early Mesozoic. Therefore, zircon fission track (ZFT) and AFT data of a study from two mountain ranges in the central Dronning Maud Land (Fig. 4.2), East Antarctica, are presented too (Meier et al., 2004). A combined study using the AFT data set of Meier (1999) and single grain apatite (U-Th)/He data provides refinements on the cooling paths of central Dronning Maud Land (Emmel et al., 2006d).

AFT data from Kenya (Wagner et al., 1992) indicate a slow continuous cooling of the basement throughout the past 400 to 300 Ma and suggest earliest cooling to below 60° C in the Late Carboniferous at around 310 Ma. Solely AFT data proximate to the Tanganyika and Kenya rifts indicate a Tertiary cooling period after a reheating of the rift flanks.

Foster and Gleadow (1992, 1996) presented composite age-elevation profiles from AFT data surrounding the central Kenya Rift. They identified three periods of more rapid denudation during the Mesozoic to Cenozoic at $\geq$ 220 Ma, 130-110 Ma, and

70-60 Ma. Both Mesozoic events yielded c. 0.5 km of denudation; whereas up to 2.5 km of denudation are associated with the Early Tertiary event. Foster and Gleadow (1992) attributed the more rapid denudation to be caused by block faulting and local uplift in response to intracontinental tectonic phases correlated to changes in plate motion. Inverse modelling approaches of their AFT data from the eastern Kenya Rift flanks also indicate a denudation period in the Neogene at c. 10 Ma. However, the denudation history derived from their AFT data is inconsistent with classical correlations of regional erosion surfaces (Foster and Gleadow, 1992 and references therein). Samples from inferred Mesozoic erosion surfaces were not exhumed from depth ≥ 2 km until after Early Paleogene times (c. 60 Ma).

The AFT data of Noble et al. (1997) showed a post Pan-African development of the basement in eastern Tanzania that is characterized by long periods of slow cooling. They are punctuated by three episodes of more rapid cooling at 140-120 Ma, 80-60 Ma and 40 Ma. Noble et al. (1997) associated them with rapid denudation. Their estimated total amounts of post-Late Cretaceous denudation range between c. 2 to 6 km. Similar to Foster and Gleadow (1992, 1996), they linked accelerated cooling and denudation to block faulting during phases of intracontinental tectonics.

Van der Beek et al. (1998) presented AFT data from basement rocks along the Malawi and Rukwa rift flanks. Their data show a protracted regional cooling history since the Permian. Three periods of more rapid cooling and by inference denudation of the flanks were identified at c. 250-200 Ma, c. 150 Ma and ≤ 50-40 Ma. The estimated amounts of denudation for the Permo-Triassic and the Late Jurassic-Early Cretaceous episodes are c. 2 km each, whereas the Cenozoic denudation amounted to ≤ 1 km. The total post-Karoo denudation in the region varied between c. 3-5 km. These three periods are linked to different rifting events in the region and correlate with the deposition of sedimentary units within the rift basins. Importantly, Van der Beek et al. (1998) showed that the denudation history derived from their AFT data is inconsistent with correlations of regional erosion surfaces. Samples from inferred erosional "Gondwana surfaces" were exhumed to temperatures of 60-70° C in Karoo times but exposed to sub-aerial conditions at times ≤ Early Tertiary.

Emmel et al. (2004, 2006b,c) presented TFT and AFT data from basement rocks of south and central Madagascar and detrital AFT data from Middle Jurassic strata of the Morandava basin. In total four Palaeozoic-Mesozoic periods of more rapid cooling were identified from these data. The basement rock TFT and AFT data show a long and protracted cooling and denudation since the Late Neoproterozoic/Early Cambrian. More rapid cooling and by inference denudation occurred in the Early Carboniferous and during Permo-Triassic times. During the Early Carboniferous, enhanced denudation is potentially related to glacial abrasion and/or to intracontinental compression, uplift and erosion in central Gondwana. The Permo-Triassic episode is associated with crustal extension during the intracontinental Karoo rifting. It is linked to the formation of the western passive continental margin of Madagascar. Differential cooling and likely denudation patterns suggest a brittle reactivation of NW-SE trending ductile basement fabrics (e.g. Bongolava-Ranotsara Shear Zone) during that time. The fission track data of Emmel et al. (2004, 2006b, c) depict the basement of southern and central Madagascar as a region of continuous denudation during the intracontinental Karoo rifting, and furthermore indicate that the basement rocks along the western margin of Madagascar were subsequently reheated due to burial by Permo-Triassic sediments after their Palaeozoic exhumation. Detrital AFT data from the Morondava Basin indicate a reworking of Palaeozoic sediments, associated with renewed rifting and the break-up of Gondwana in the Early to Middle Jurassic (Emmel et al., 2006a). The youngest cooling event in the Late Cretaceous is linked to a thermal overprint from the Marion hot spot that accompanied the Madagascar–India/Seychelles break-up. The regional study results of Seward et al. (2004) displays distinct consistencies to the AFT data of Emmel et al. (2004, 2006a, b, c) but suggest a thermochronological subdivision of Madagascar into a southern, central and northern region.

Meier et al. (2004) presented fission track data from two vertical profiles of basement rocks in central Dronning Maud Land, East Antarctica. The ZFT ages are interpreted to indicate a slow post Pan-African cooling and denudation of the basement from middle Palaeozoic to Triassic times. Inverse modelling approaches of their AFT data yield three Mesozoic episodes of more rapid cooling in the Early to Middle Jurassic (c. 190-180 Ma), in the Late Jurassic (c. 150-140 Ma) and in the Early

Cretaceous (c. 100-90 Ma). The Early to Middle Jurassic period is associated with differential denudation during the evolution of a high elevation passive rift margin. Both younger cooling episodes appear to be related to major plate reorganisations in the Mesozoic. The Late Jurassic cooling and denudation period coincides temporally with the onset of seafloor spreading in the Riiser-Larsen Sea at c. 155 Ma. Synchronous to the late Early Cretaceous cooling period, the spreading pattern between India, Antarctica and Australia changed and India started its accelerated northward drift. Meier et al. (2004) inferred a total removal of 5.5 to 9.5 km of crust since the middle Palaeozoic. Between 2.5 to 3.2 km and 0.3 to 1.2 km of denudation amounted during the Early to Middle and the Late Jurassic cooling periods, respectively. Recently, apatite (U-Th)/He analyses from central Dronning Maud Land yielded ages of c. 312 Ma to 135 Ma. A combined analysis of new (U-Th)/He and the AFT data set of Meier et al. (2004) suggests rather two distinct cooling periods of the basement in the Phanerozoic (Emmel et al. 2006c). A Late Carboniferous cooling phase is related to far field stresses associated with convergent tectonics within Gondwana. In the Early Jurassic a second period of cooling indicates the erosion of an evolving rift shoulder. The post-Jurassic cooling history appears to be restricted to temperatures of ≤ 40° C.

Chapter 6

APATITE FISSION TRACK ANALYSIS - RESULTS AND INTERPRETATION

Fission track ages and analytical details of 96 AFT analyses are presented in Tabs. 6.1-6.4, Figs 6.1-6.10 and in Appendix B.1-B.4. The AFT ages range from 169 ± 19 Ma to 61 ± 8 Ma. Their mean track lengths (MTL) span from 14.5 ± 0.2 μm to 11.5 ± 0.2 μm with associated standard deviations (SD) ranging between 3.2 to 0.3 μm. The mean etch pit diameters (D_{par}) span between 4.97 ± 0.08 μm to 1.04 ± 0.04 μm. In all samples, the χ^2 probability values are higher than 5 %. This indicates that in each sample the single grain age dispersion is explained by a poissonian distribution and the single grain ages are considered to be derived from one population. The spatial distribution patterns of the AFT ages, the MTL, the associated SD and the D_{par} values are depicted in Figs. 6.2 and 6.3. All contour images were computed using GMT 4.0, module surface (bash script is given in Appendix C).

AFT central ages derived from less than 5 apatite grains analysed and track length information obtained from less than 20 track length measurements are statistically not trustworthy. Such critical data are denoted in the following sections but are not considered for interpretation. AFT data sets comprising either critical AFT ages or track length data are specially designated on the diagrams whereas samples yielding entirely critical AFT data sets (ages and length data) are not presented.

In the following, the AFT results are presented and interpreted in three sections according to their sampling locations and these are the western *Axial Granulite Complex, Mount Tumbine* and the *Southern basement*. Within theses sections, samples yielding statistically critical AFT data are listed at first. Subsequently, the remaining AFT samples are interpreted and grouped. Fission track ages and track length data are interpreted according to inferences of Gleadow et al. (1986) and D_{par} kinetic parameters are interpreted in accordance with implications of Barbarand et al. (2003a, b), Burtner et

al. (1994) and Donelick et al. (1999). At last, modelled AFT time-temperature (*t-T*) paths are presented. The AFT *t-T* paths are derived by using the following modelling parameters and strategy:

(a) For all models the starting *t-T* constraints are set by the corresponding TFT ages or by TFT ages of proximate samples (see chapter 3, section 3.4.3). In addition, 4-6 *t-T* constraints with large temperature intervals ($T \sim$ 250°-20°C) are set randomly at time points between c. 200-20 Ma to enable a high degree of freedom for initial model runs. The present day surface temperature is set to 20°C in all models.

(b) If the first model runs generated *t-T* paths, some *t-T* constraints are varied and clustered more tightly in *t-T* space to further constrain the timing of a sample's cooling into AFT PAZ; approximately to below c. 110°C. If no *t-T* paths were obtained with the initial random *t-T* constraints setting, the *t-T* constraints are modified manually to derive geologically reasonable *t-T* paths.

(c) The quality of the "best fit" modelled AFT data set (AFT age, MTL ± SD) is evaluated by the indices of "goodness of fit" (G.O.F) and the model quality of the track length frequency distribution is assessed by visual comparison of the shape of the graphs (model versus measured).

In the following interpretation and discussion of the samples AFT *t-T* path models the expression "(more) rapid cooling" refers to cooling rates of approximately 5°-3°C/Ma whereas "slow cooling" designates cooling rates < 3°-1°C/Ma. The ranges of rates are chosen somewhat arbitrarily, based on the variety of obtained model results and used to provide a fairly uniform measure for differently steep *t-T* paths segments among samples.

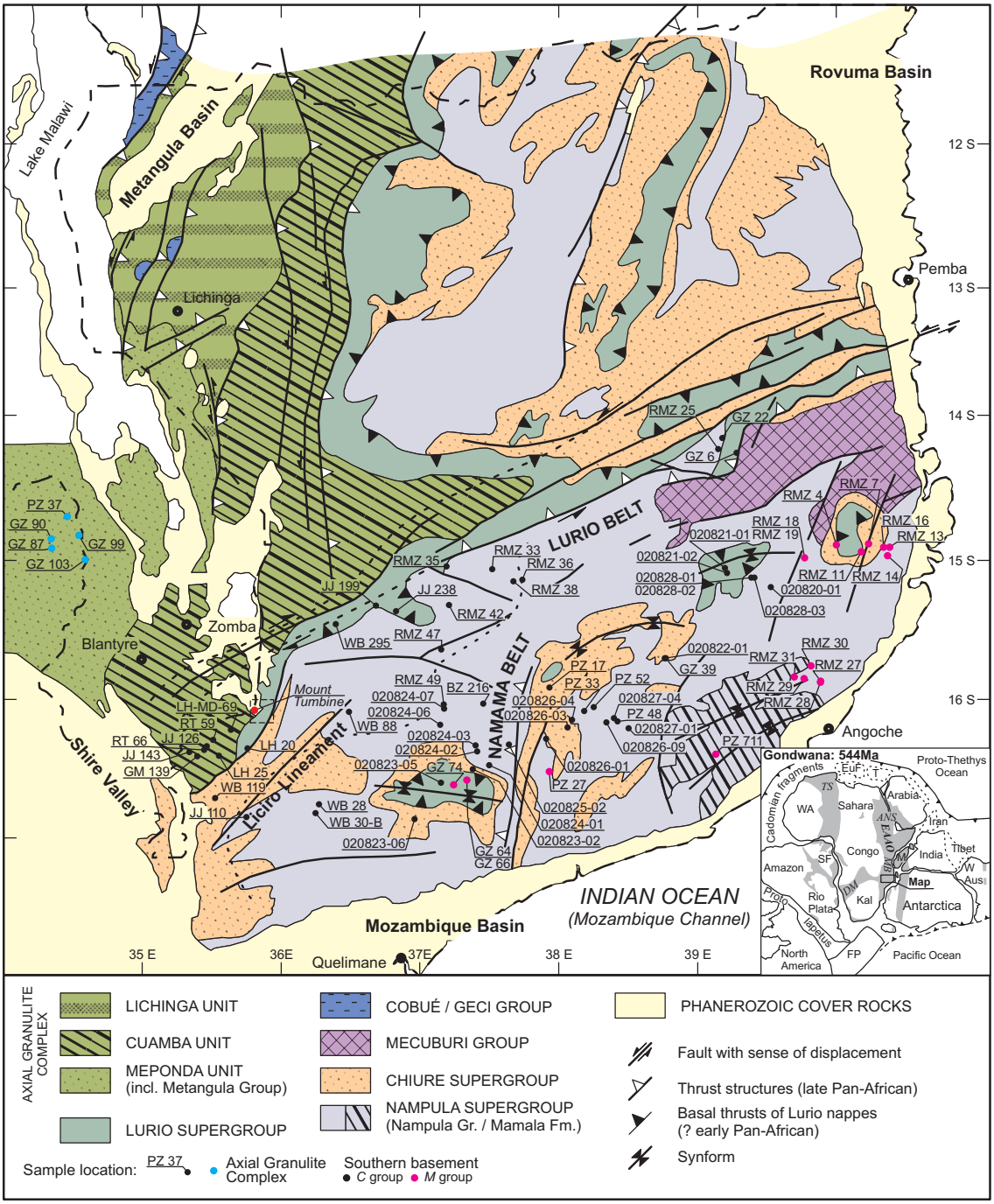

Figure 6.1: Generalized map depicting major litho-tectonic units of the crystalline basement in northern Mozambique and southern Malawi. The map was modified after Pinna et al. (1993), Andreoli (1984), Kröner et al. (2001) and Perits et al. (2002). Superimposed are the sample locations of the AFT and (U-Th)/He analyses. The dashed outlined rectangle represents the Mt. Tumbine area displayed in Fig. 6.5. The inset depicts Pan-African Mobile Belts in a Gondwana reconstruction (Kusky et al., 2003, Jacobs and Thomas, 2004). Abbreviations: ANS = Arabian Nubian Shield, DM = Damara Belt, EAAO = East African-Antartic Orogen, EuF = European fragments, FP = Falkland Plateau, Kal = Kalahri craton, M = Madagascar, MB = Mozambique Belt, SF = San Francisco craton, T = Turkey, TS = Trans-Saharan, W Aus = Western Australia, WA = West Africa craton.

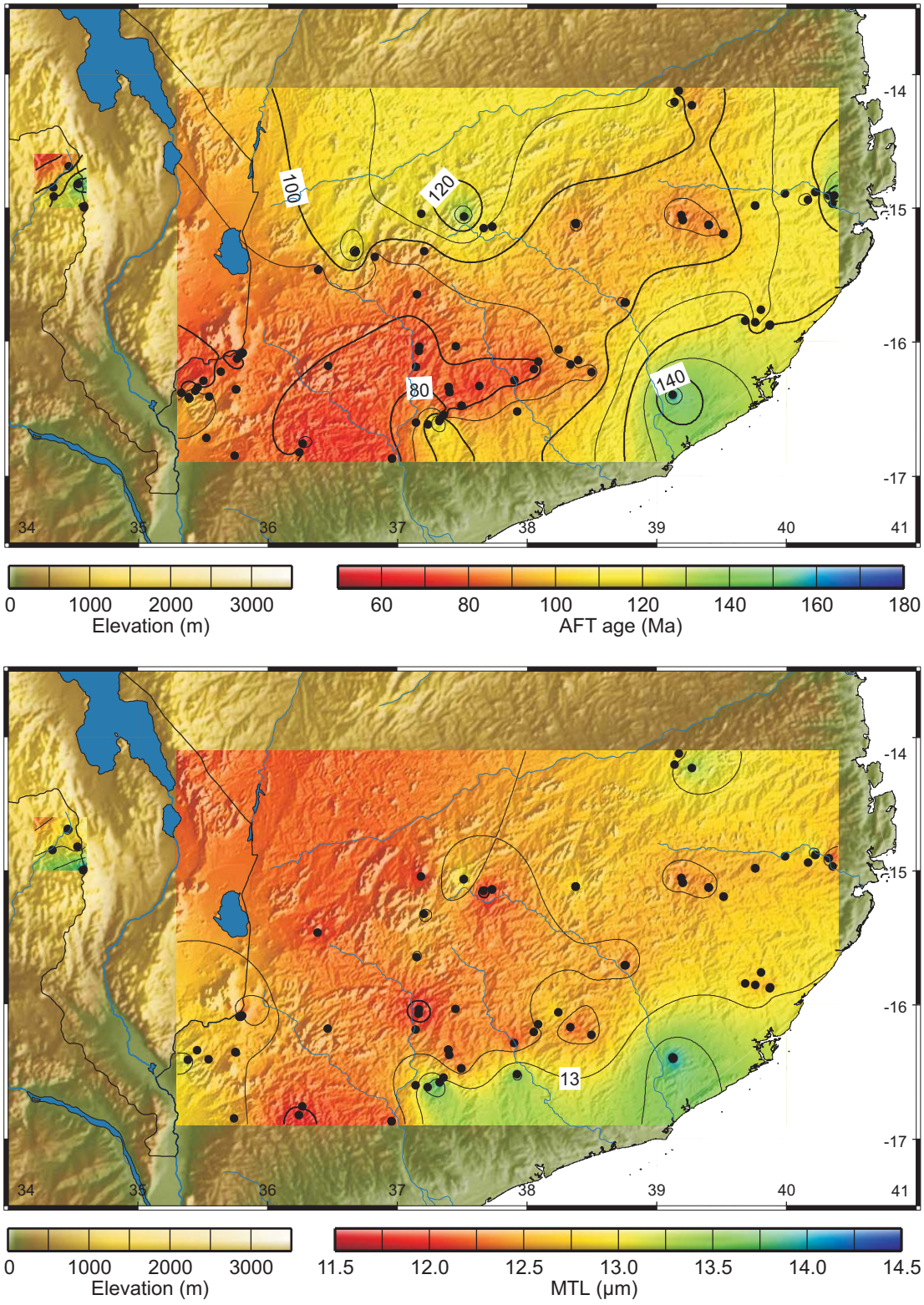

Figure 6.2: Topographic map of northern Mozambique with superimposed spatial distribution patterns of AFT ages (upper) and MTL data (lower). Contour lines were calculated using GMT 4.0, module surface. Sample locations are given as black circles.

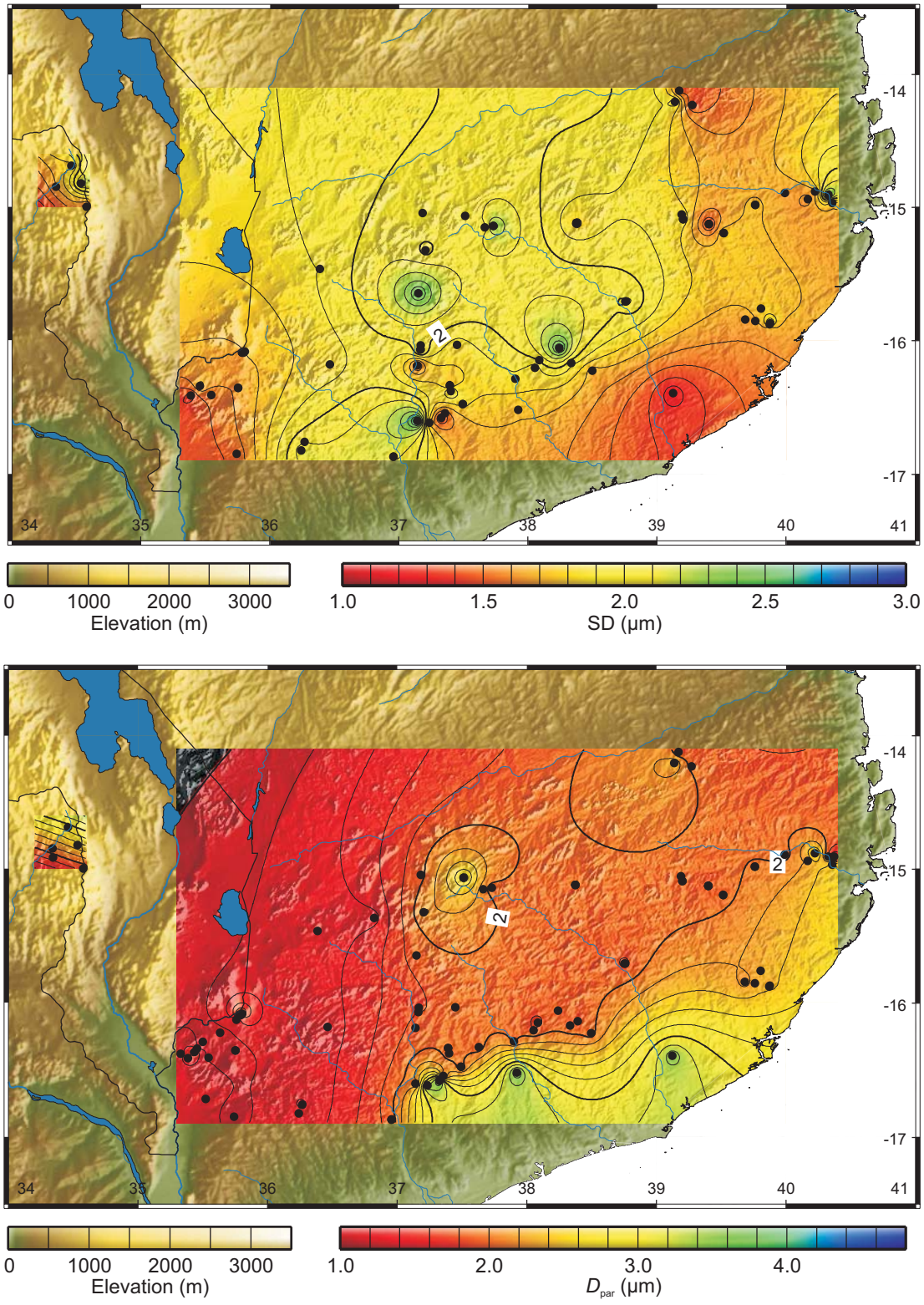

Figure 6.3: Topographic map of northern Mozambique with superimposed spatial distribution patterns of track length SD data (upper) and D_{par} values (lower). Contour lines were calculated using GMT 4.0, module surface. Sample locations are given as black circles.

6.1 Axial Granulite Complex

6.1.1 Results

Samples GZ 87, GZ 90, GZ 103 and PZ 37 were collected on the uplifted western flank of the Malawi rift zone, c. ≤ 50 km west of the western border fault (Figs. 4.6 and 6.1). All samples are derived from elevations > 1100 m (Tab. 6.1, Fig. 6.4a). The AFT ages show a large scatter, ranging from 163 ± 10 Ma to 79 ± 4 Ma. Their MTL span from 14.3 ± 0.1 μm to 12.6 ± 0.5 μm with associated SD ranging from 2.3 to 1.5 μm. Observed D_{par} values span between 2.89 ± 0.03 μm to 1.85 ± 0.01 μm (Tab 6.1, Fig 6.4a-d). All track length frequency distributions are unimodal. Samples GZ 90 and GZ 103 display a symmetric and sample PZ 37 a slightly negatively skewed shape of their track length histograms (Appendix B.1). The track length data of samples GZ 87 and GZ 99 are statistically critical and are omitted.

6.1.2 Interpretation

In the absence of track length information, the AFT ages of GZ 87 and GZ 90 are interpreted as minimum cooling ages. Two samples, GZ 90 and PZ 37 reveal moderate MTL values of less than 13.2 μm and probably experienced a significant amount of fission track length reduction. Their fairly broad SD of > 1.7 μm and symmetric and slightly negatively skewed unimodal track length frequency distributions (Tab. 6.1 and Appendix B.1) suggest, that both samples cooled, at least partially, slow and protracted through the AFT PAZ. The AFT ages of GZ 90 and PZ 37 are interpreted as minimum cooling ages.

AFT sample GZ 103 yields a long MTL value of 14.3 μm, a narrow SD of 1.5 μm and a unimodal, symmetric track length frequency distribution. These data argue for a relatively rapid cooling of GZ 103 through the AFT PAZ. The associated D_{par} value of 1.85 ± 0.01 μm (Tab. 6.1, Fig 6.4d) could indicate an annealing behaviour of GZ 103 similar to that of the Durango apatite standard. The AFT age of GZ 103 (106 ± 9 Ma) is interpreted as a cooling age and records the cooling to below c. 100°C in Early Cretaceous times.

Table 6.1: Results of apatite fission track analysis – Axial Granulite Complex

Sample	Lithology	Longitude	Latitude	Elevation (m)	No. of grains	ρ_s ($\times 10^6 cm^{-2}$) (N_s)	ρ_i ($\times 10^6 cm^{-2}$) (N_i)	ρ_d ($\times 10^6 cm^{-2}$) (N_d)	P(χ^2) (%)	Central age ± 1σ (Ma)	U (ppm)	MTL ± 1σ (µm)	SD (µm)	No. of tracks	Mean D_{par} ± 1σ (µm)	SD_{par} (µm)	No. of D_{par}
GZ 87	amphibolite	34.34556	-14.91611	1150	7	0.133 (69)	0.281 (146)	1.615 (11436)	92	123 ± 18	3	12.7		1	1.88 ± 0.05	0.29	30
GZ 90	gt-amphibolite	34.34167	-14.84944	1150	17	0.746 (453)	0.192 (1163)	1.570 (11436)	92	99 ± 6	18	13.0 ± 0.2	1.7	101	2.16 ± 0 .01	0.23	242
GZ 99	amphibolite	34.53417	-14.82306	1500	24	0.238 (496)	0.356 (740)	1.515 (11436)	100	163 ± 10	3	12.6 ± 0.5	2.3	19	2.54 ± 0.03	0.31	142
GZ 103	amphibolite	34.57889	-15.00000	1600	13	0.779 (268)	1.941 (668)	1.609 (11436)	48	106 ± 9	16	14.3 ± 0.1	1.5	117	1.85 ± 0.0 1	0.29	324
PZ 37	amphibolite	34.45778	-14.68889	1300	19	1.324 (619)	4.203 (1964)	1.559 (11436)	92	79 ± 4	38	13.2 ± 0.2	1.7	110	2.89 ± 0.03	0.39	213

U is the total uranium content of a sample, ρ_d is the standard glass track density, ρ_s and ρ_i represent the sample's spontaneous and induced track densities, with the total number of track counts given in parentheses. P (χ^2) represents the probability of the chi-square test. MTL is the horizontally confined mean track length and SD represents the corresponding standard deviation. Mean D_{par} is arithmetic mean of all c-axis parallel etch pit diameter measurements in a fission track sample and SD_{par} represents the corresponding standard deviation.

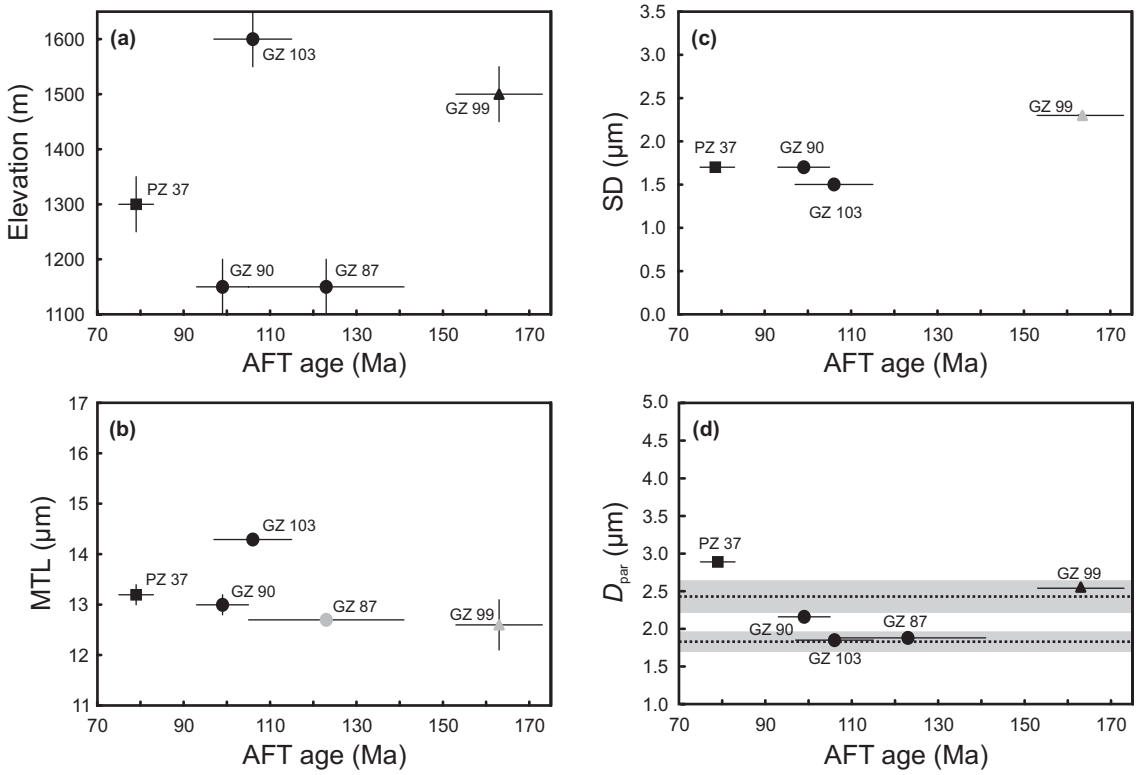

Figure 6.4: Diagrams depict the AFT ages versus elevation (a), horizontally confined MTL (b), SD (c) and D_{par} (d). Black triangles, circles and boxes represent different sample groups described in the text. Grey symbols indicate samples yielding statistically critical AFT track length data. In diagram (d) horizontally dotted lines represent D_{par} values of Fish Canyon (upper) and Durango (lower) AFT age standards with grey bars representing associated standard deviations from Donelick et al. (1999). An elevation error of ± 50 m is assumed for the GPS altitude determination.

Samples GZ 87 and GZ 90 are located in proximate distance on the same elevation at 1150 m and yield similar AFT ages of 123 ± 18 Ma and 99 ± 6 Ma, respectively. GZ 87 and GZ 90 also reveal similar D_{par} values of c. 1.88 µm and c. 2.16 µm, respectively which suggests similar annealing kinetics for both (Figs. 6.1, 6.4a, d and Tab. 6.1). These consistencies argue for a common *t-T* path for GZ 87 and GZ 90. Both samples are also very similar in their AFT age and their D_{par} values to sample GZ 103. (Figs. 6.1, 6.4a, d and Tab. 6.1). Sample GZ 103, however, yields an AFT cooling age whereas GZ 87 and GZ 90 reveal minimum AFT cooling ages (Fig. 6.4a-c and Tab. 6.1). GZ 87 and GZ 90 are located c. 500 m below GZ 103 and could represent a deeper crustal level. It is inferred that all three samples experienced cooling from a similar event in the Early Cretaceous but recorded it at different depths. The deeper seated samples (GZ 87,

GZ 90) probably experienced a more protracted cooling path than GZ 103 and did not cool entirely through the AFT PAZ whereas GZ 103 did during the common cooling event.

Sample GZ 99 yields the oldest AFT age of 163 ± 9 Ma in the region and is located at the same elevation as sample GZ 103 (Fig. 6.1, 6.4a and Tab 6.1). Its moderate D_{par} value of 2.54 ± 0.03 μm could indicate a higher annealing resistance than GZ 103 and likely accounts for a highest regional AFT age. However, the measured individual track lengths of less than c. 13 μm (Appendix B.1) indicate a distinct amount of fission track annealing. These moderate track lengths suggest a *t-T* path for GZ 99 that is distinctly different to GZ 103. It is supposed that the AFT age of GZ 99 documents a sample's cooling to below c. 110°C in the region at a time prior to the Early Cretaceous (c. 106 Ma).

Sample PZ 37 reveals the youngest minimum cooling age (79 ± 4 Ma) and the largest D_{par} value (2.98 ± 0.03 μm) of all samples (Figs. 6.1, 6.4d and Tab 6.1). Compared to the AFT standards (Durango, Fish Canyon; Fig. 6.4d), its higher D_{par} value could indicate a higher annealing resistance. The moderate MTL of 13.2 ± 0.01 μm, suggests that PZ 37 experienced a distinct amount of fission track annealing. All these facts indicate that PZ 37 experienced a *t-T* path distinctly different from the other samples in the region. As indicated by its youngest AFT age, PZ 37 presumably cooled at a younger time into the AFT PAZ than any other sample; at a time younger than c. 106 Ma (cooling age of GZ 103).

The modelled *t-T* paths of samples GZ 90, GZ 103 and PZ 37 are presented in Fig. 6.6. The *t-T* paths of GZ 90 and GZ 103, display both cooling into the AFT PAZ in the Early Cretaceous at c. 115-106 Ma but cool at different rates. GZ 103 displays a fast cooling through the AFT PAZ between c. 106 to 100 Ma at rates of c. 10-7°C/Ma, and thereby emphasizes that its age represents an AFT cooling age. GZ 90 displays a more rapid cooling step from c. 110°C to c. 80°-70°C. Subsequent cooling continued protractedly and cooling to below 60°C occurred in Palaeogene times. The similar timing of cooling into the AFT PAZ of GZ 90 and GZ 103 supports that both samples probably recorded

the same Early Cretaceous cooling event at different crustal levels, whereby GZ 90 (and by inference GZ 87) was seated approximately 0.5 km below GZ 103.

Sample PZ 37 displays a slow cooling into the PAZ in the Late Cretaceous at c. 82 Ma. Subsequently, slow cooling continued to below 60°C in the Neogene. This *t-T* path documents the youngest cooling period in the region and could be related to a cooling event in the Late Cretaceous at c. 90-80 Ma. The AFT results of PZ 37 could further indicate that among all samples of the region, PZ 37 represents the deepest exhumed crustal level.

Two distinct periods of cooling into the AFT PAZ are recognized in the region during Early (c. 115-100 Ma) and during Late Cretaceous (c. 90-80 Ma) times. These events are recorded by two sample sets which are located in fairly proximate distance to each other and at different present day elevations. Probably, these samples sets were seated at different crustal level in former times. As no apparent AFT age-elevation relationship is observed among these two sample sets (Fig. 6.4a), it is suggested that the Early and Late Cretaceous cooling histories are recorded in different crustal blocks. This in turn could indicate a tectonic segmentation of the region, with separating brittle faults supposedly aligned parallel to the regional, northerly ductile fabric trend.

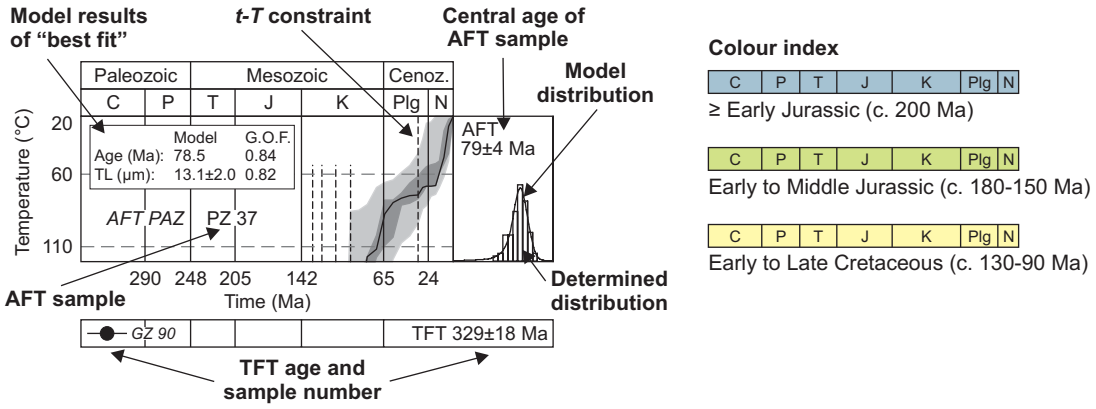

Figure 6.5: Illustration of the main elements of the AFT *t-T* path pictograms used in this study. **AFT *t-T* path:** The solid black line is the "best fit" model. The dark grey and light grey colours indicate the *t-T* space envelops of the "good fit" and "acceptable fit" *t-T* models, respectively. TFT model constraints are given in the lower panel and the sample number is quoted for a proximate TFT sample. The "best fit" model results Age = AFT age, TL = MTL ± SD and their probabilities of goodness of fit (G.O.F.) are given in the inset. **Colour index:** This colour scheme is used for modelled AFT *t-T* paths and indicates the earliest cooling of a sample to below c. 110°C.

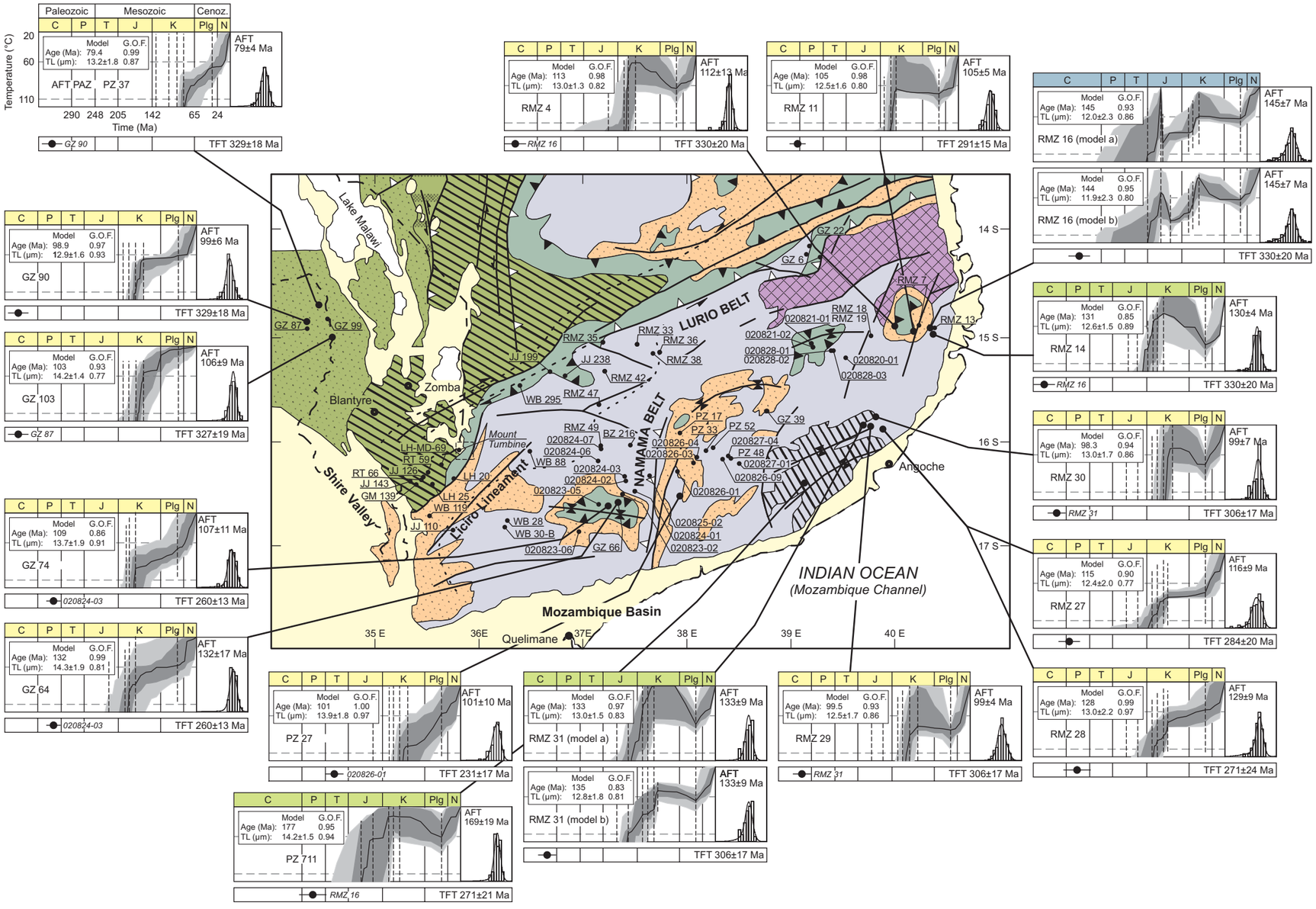

Fig 6.6: This map is a subset of Fig. 6.1 and depicts AFT sample locations in northern Mozambique. The large dots highlight samples from the western Axial Granulite Complex and samples from the eastern margin of the southern basement (*M* group) that were employed in the modelling of *t-T* paths. The corresponding *t-T* paths are given as pictograms. A detailed pictogram explanation is provided in Fig. 6.5.

6.2 Mount Tumbine

6.2.1 Results

Eight fission track analyses (RT 51 to RT 55 and RT-MD-94) were conducted on samples from a pseudo-vertical profile at Mt. Tumbine ranging from 788 to 1535 m altitude (Tab 6.2 and Fig. 6.8). The AFT ages span from 103 ± 5 Ma to 72 ± 8 Ma and do not correlate with elevation (Fig 6.7a). The MTL range from 14.2 ± 0.3 μm to 11.6 ± 0.2 μm with associated SD spanning from 2.3 to 0.7 μm. Observed D_{par} values span between 2.46 ± 0.02 μm to 1.22 ± 0.02 μm and indicate a negative trend on AFT age versus D_{par} plot (Fig. 6.6). Generally all samples display unimodal and negatively skewed track length frequency distributions though samples RT 52, RT 54 and RT-MD-94 indicate slightly symmetric tendencies (Appendix B.2). AFT ages of samples RT 50, RT-MD-94 and track length data of sample RT 53 are statistically critical and are omitted (Tab 6.2).

6.2.2 Interpretation

In the absence of track length information, the AFT age of RT 53 is interpreted as a minimum cooling age. The MTL values of less than 13.7 μm of samples RT 51, RT 52, RT 54 and RT 55 indicate a distinct amount of fission track length reduction. Their corresponding SD of > 1.3 μm and their unimodal, negatively skewed track length frequency distributions (Tab 6.2, Fig 6.7c and Appendix B.2) probably indicate a slow, protracted cooling of samples through the AFT PAZ. Therefore the AFT ages RT 51, RT 52, RT 54 and RT 55 are interpreted as minimum cooling ages.

On the AFT age versus D_{par} value plot sample RT 51 is represented twice (duplicate analyes) (Fig. 6.6d). Consequently, the observed negative trend line is solely considered as a qualitative trend estimate. The inverse AFT age-D_{par} value relation contrasts the predicted positively correlated increase of the AFT ages and D_{par} values. This contradiction probably indicates different etching characteristics that are unrelated to different annealing resistances of the analyses samples (e.g. Ketcham et al., 2000). On the other hand it could represent an AFT sample set that experienced distinctly different *t-T* paths. The latter suggestion is sustained as the majority of the samples reveal similar

Table 6.2: Results of apatite fission track analysis – Mount Tumbine

Sample	Lithology	Longitude	Latitude	Elevation (m)	No. of grains	ρ_s ($\times 10^6 cm^{-2}$) (N_s)	ρ_i ($\times 10^6 cm^{-2}$) (N_i)	ρ_d ($\times 10^6 cm^{-2}$) (N_d)	$P(\chi^2)$ (%)	Central age ± 1σ (Ma)	U (ppm)	MTL ± 1σ (μm)	SD (μm)	No. of tracks	Mean D_{par} ± 1σ (μm)	SD_{par} (μm)	No. of D_{par}
RT 54	syenite	35.80262	-16.08536	1535	11	1.307 (630)	2.777 (1338)	1.102 (7775)	11	82 ± 5	37	11.8 ± 0.2	1.9	102	2.46 ± 0.02	0.29	195
RT 53	syenite	35.80058	-16.08538	1480	20	0.229 (355)	0.495 (768)	1.110 (7775)	67	82 ± 6	7	14.2 ± 0.3	0.7	5	2.12 ± 0.02	0.16	89
RT 52	syenite	35.79303	-16.09021	1151	15	0.369 (285)	0.783 (605)	1.114 (7775)	89	84 ± 7	11	12.5 ± 0.3	2.1	58	1.86 ± 0.01	0.18	2 08
RT 51	bt-gneiss	35.79134	-16.09403	980	8	0.826 (361)	1.565 (684)	1.091 (7775)	73	92 ± 7	20	13.7 ± 0.2	1.6	56	1.29 ± 0.02	0.15	143
		35.79134	-16.09403	980	19	1.256 (971)	2.393 (1850)	1.227 (5836)	61	103 ± 5	28	13.1 ± 0.1	1.5	101	1.22 ± 0.02	0.17	266
RT 50	bt-orthogneiss	35.78660	-16.09402	842	3	1.050 (79)	2.259 (170)	1.099 (7775)	94	82 ± 11	30	12.8 ± 0.2	1.5	55	2.23 ± 0.02	0 .20	96
RT 55	bt-gneiss	35.78534	-16.09392	824	20	0.806 (899)	1.754 (1956)	1.095 (7775)	68	81 ± 4	23	11.6 ± 0.2	2.3	94	2.24 ± 0.02	0.31	280
RT-MD-94	bt-gneiss	35.78295	-16.09470	788	4	0.741 (118)	1.826 (291)	1.106 (7775)	76	72 ± 8	30	13.5 ± 0.2	1.3	52	2.41 ± 0.03	0.32	116

U is the total uranium content of a sample, ρ_d is the standard glass track density, ρ_s and ρ_i represent the sample's spontaneous and induced track densities, with the total number of track counts are given in parentheses. P (χ^2) represents the probability of the chi-square test. MTL is the horizontally confined mean track length and SD represents the corresponding standard deviation. Mean D_{par} is arithmetic mean of all c-axis parallel etch pit diameter measurements in a fission track sample and SD_{par} represents the corresponding standard deviation.

AFT ages of c. 82 Ma over an elevation spanning from c. 750 to 1550 m but do not show similar MTL, SD and D_{par} values (Fig. 6.7a-d and Tab. 6.2) as would be expected for a common cooling history of the sample set. In addition, the MTL do not show any trend with elevation as expected for a common history of the samples. Their clear scatter rather indicates diverse cooling histories recorded in the sample set (6.7a).

Duplicate analyses of sample RT 51 reveals the oldest AFT ages (> 90 Ma), long MTL (> 13 µm) and the lowest D_{par} values (< 1.3 µm) among all samples (Fig. 6.7a-d and Tab 6.2). These data could suggest that sample RT 51 experienced least significant fission track annealing than any other sample of the profile.

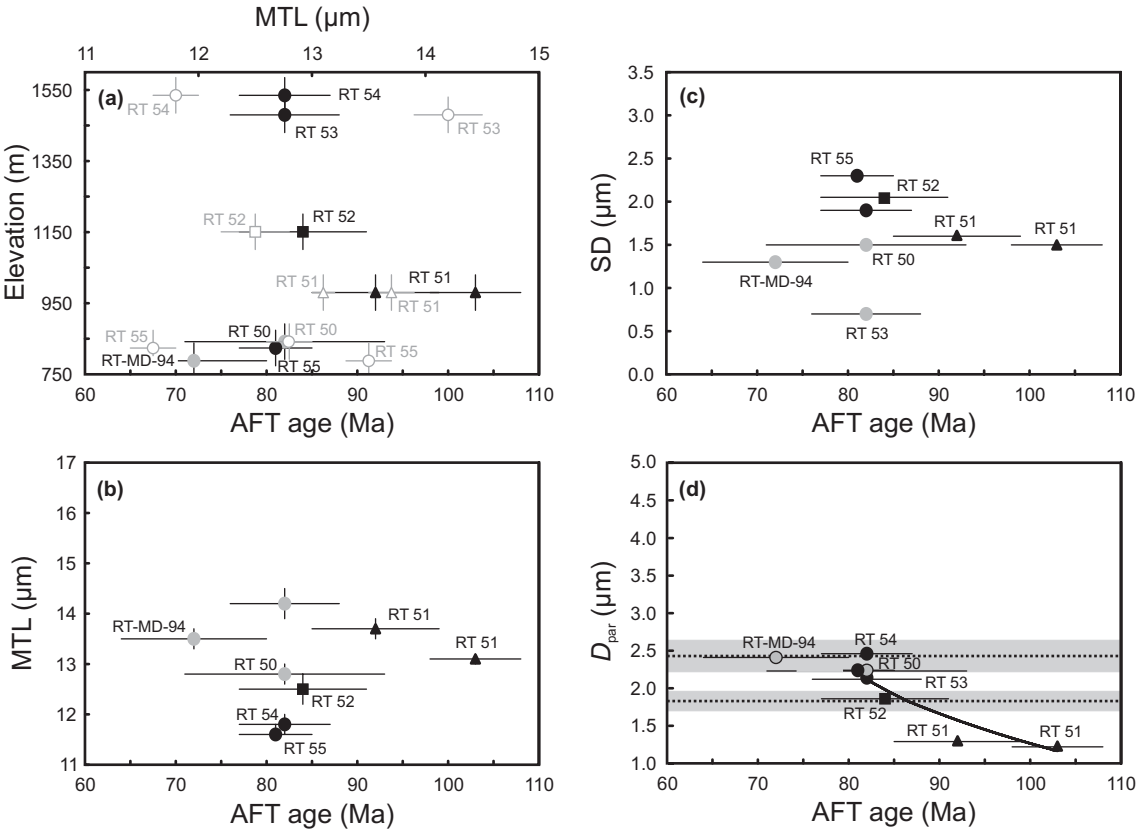

Figure 6.7: Diagram (a) depicts the AFT ages (filled symbols) and MTL (open symbols) versus elevation (a). Diagrams (b), (c) and (d) depict AFT ages versus horizontally confined MTL, SD and D_{par}, respectively. Black filled triangles, circles and boxes represent sample groups discussed in the text. Grey filled symbols indicate samples yielding statistically critical AFT track length data. In diagram (d) horizontally dotted lines represent D_{par} values of Fish Canyon (upper) and Durango (lower) AFT age standards with grey bars representing associated standard deviations from Donelick et al. (1999). An elevation error of ± 50 m is assumed for the GPS altitude determination.

Samples RT 54 and RT 55 display similar AFT ages, MTL, SD and D_{par} values (Tab. 6.2), indicating a very similar cooling history for both samples. Their MTL (≤ 11.8 μm) are the shortest of the sample set (Tab. 6.2, Fig. 6.7a, b) and document, that both samples experienced the highest degree of fission track annealing among the AFT samples of Mt. Tumbine. Proximate to RT 54 locates sample RT 53, which yield a similar AFT age and D_{par} value (Tab. 6.2 and Figs. 6.7d, 6.7). A similar cooling history is inferred for the three samples RT 53, RT 54 and RT 55. These samples were obtained from the syenite intrusion (RT 53, RT 54) and country rock gneiss lens (RT 55), and for the purpose of distinction, they are termed group *A* in this section.

RT 52 yield a similar AFT age and a SD value as the group *A* samples (Tab. 6.2). However, RT 52 reveals MTL (12.5 ± 0.3 μm) and D_{par} (1.86 ± 0.01 μm) values that range between the values of group *A* (RT 53, RT 54, RT 55) and sample RT 51 (Tab. 6.2, Fig. 6.7b-d). The *t-T* path of RT 52 could therefore be similar to group *A* or sample RT 51 and it is further explored by AFT *t-T* path modelling.

Modelled *t-T* paths of samples RT 51, RT 52, RT 54, and RT 55 are presented in Fig. 6.8. All samples display a consistent timing of more rapid cooling into the AFT PAZ in the Early Cretaceous (c. 115-100 Ma) and further cooling to below c. 80° in the Cretaceous. RT 51 and RT 52 display a fairly similar slow, protracted cooling through the AFT PAZ to below c. 60°C during the Late Cretaceous to Palaeogene times. However, RT 51 displays a somewhat earlier cooling to below c. 60°C in the Early-Late Cretaceous than RT 52 (Palaeogene). These AFT samples RT 51 and RT 52 are derived from a country rock gneiss lens and the syenite host rock, respectively (Fig 6.8). The difference in their cooling paths could be related to local variations in the palaeo-geothermal gradient. This could be attributed to minor variations in the thermal conductivity between the gneiss (RT 51) and the syenite (RT 52) or to localized, transient palaeo-heat flow values. Group *A* samples RT 54 and RT 55 solely yield good model reproductions of their AFT data if a cooling step suggesting a reheating up to c. 80-90°C in Palaeogene times is introduced. The more rapid cooling to below 60°C in Neogene times, however, could be a modelling artefact (e.g. Kohn et al., 2002).

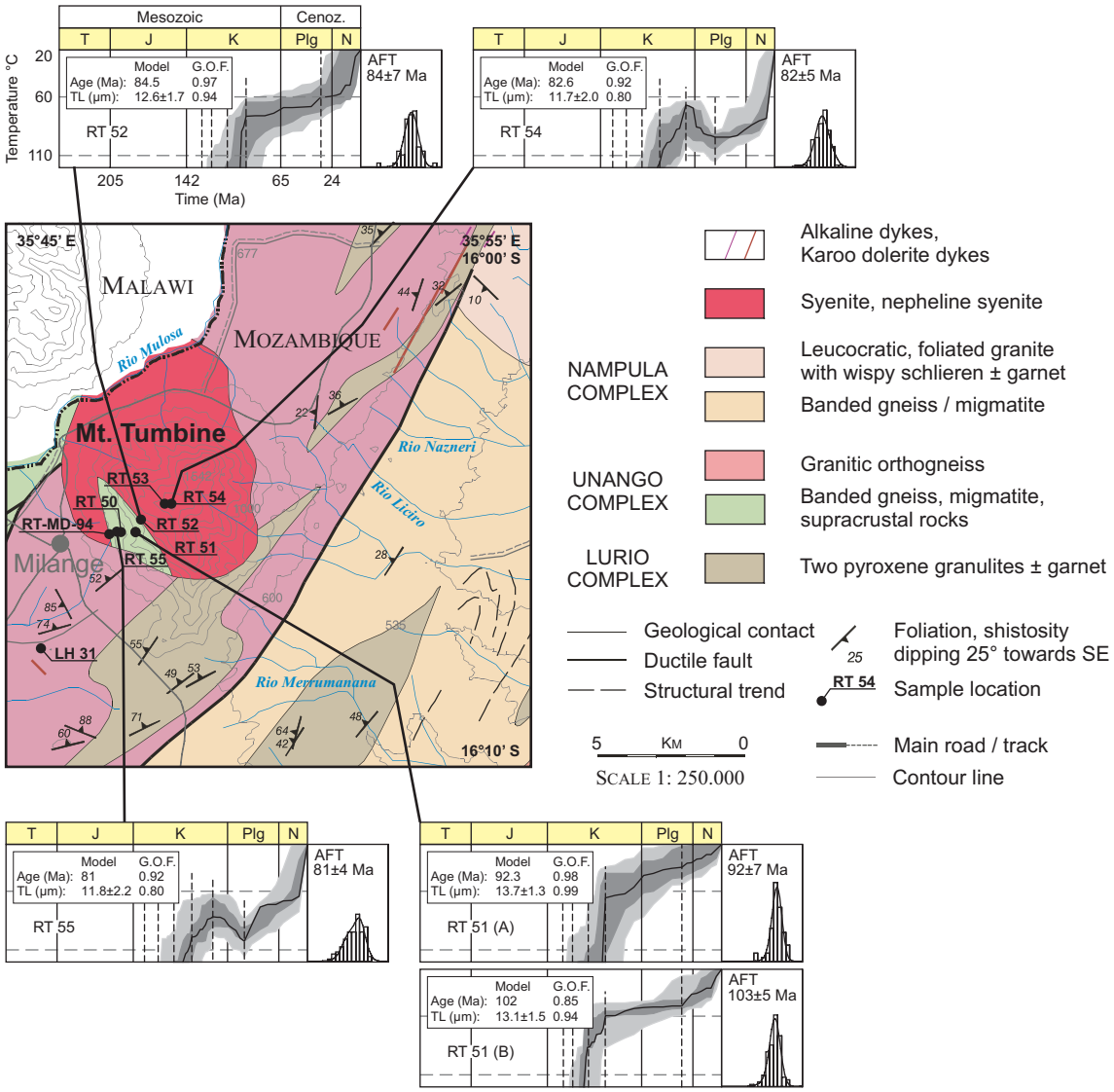

Figure 6.8: Map illustrating the geological situation of the Mt. Tumbine area. It is a subset of Map sheet 1635 – Milange (Thomas, 2006), which is part of the geological map of Mozambique (scale 1:250.000). Superimposed are the AFT sample locations of the pseudo vertical profile. The arranged pictograms display the modelled *t-T* paths.

6.3 Southern basement

6.3.1 Results

82 AFT samples were derived from the north Mozambican basement located between the Indian Ocean and the Malawi rift system. The majority of the samples are derived from the basement south of the Lurio Belt (Figs. 4.6 and 6.1). The AFT ages range from 169 ± 19 Ma to 61 ± 8 Ma. The samples MTL span between 14.5 ± 0.2 μm to 11.5 ± 0.2 μm with associated standard deviations ranging from 3.2 to 0.3 μm. The observed D_{par} values span between 4.97 ± 0.08 μm to 1.04 ± 0.04 μm (Tabs. 6.3, 6.4; Fig. 6.9). All track length frequency distributions are unimodal and display symmetrical to negatively skewed shapes (Appendix B.3, B.4).

6.3.2 Interpretation

Samples JJ 199, PZ 33, PZ 17, RT 59 and RMZ 36 (migmatite) yield statistically critical AFT data sets (Tab. 6.3) and are entirely omitted. It is indicated by Figs. 6.2 and 6.9a that samples, which are located within the central part of the basement, distant from the continental margin, generally reveal AFT ages younger than 100 Ma. These samples occur at elevations from c. 200 m to 900 m and are termed *C* (*central*) group samples. AFT samples which occur along the present continental margin generally yield AFT ages older than c. 100 Ma. These samples are located at elevations below c. 300 m and are termed *M* (*margin*) group samples. The grouping into two AFT sample populations is confirmed by a discriminant analysis (Bahrenberg et al., 1992). The AFT age, MTL, SD, latitudes, longitudes and elevations (Tabs. 6.3 and 6.4) are chosen as a sample's parameter values for this analysis. Solely samples yielding statistically trustworthy values in all six parameters are employed. Hence 47 *C* group and 15 *M* group samples are used in the analysis. A Wilks' Λ value of 0.28570 indicates a distinct class separation and a probability value of P (χ^2) 73.91% shows that the estimated discriminant functions are significant. 12 samples are located in the central part of the southern basement, which yield AFT ages of < 100 Ma but lack reliable track length data (Tab. 6.3). Due to of their similarities in AFT age and location these samples are incorporated in the *C* group. Samples RMZ 19, GZ 66 and RMZ 13 are located close to

the continental margin, yield AFT ages ≥ c. 100 Ma but lack reliable track length data (Tab. 6.4). Because of their similarities in AFT ages and location they are incorporated in the *M* group. In total the *C* and *M* groups comprise 59 and 18 AFT samples, respectively (Fig. 6.1 and Tabs. 6.3, 6.4).

C group samples

The *C* group samples yield AFT ages between 151 ± 9 Ma to 61 ± 8 Ma, with the majority being younger than c. 100 Ma. They display MTL between 13.4 ± 0.2 μm to 11.5 ± 0.2 μm with the majority being shorter than 13.0 μm (Tab 6.3 and Figs. 6.2, 6.9a, b). The associated SD ranges between 2.8 to 1.3 μm but cluster predominantly between 2.3 and 1.4 μm (Tab 6.3 and Figs. 6.3 6.9c). D_{par} values in the *C* group range from 3.20 ± 0.04 μm to 1.08 ± 0.01 μm but predominantly cluster tightly around a value of c. 1.8 μm. A subpopulation, which is generally restricted to the eastern part of the region, yields D_{par} values of 1.31 ± 0.02 μm to 1.08 ± 0.01 μm (Tab 6.3 and Figs. 6.3, 6.9d). The *C* group AFT samples consistently display unimodal and negatively skewed track length frequency distributions (Appendix B.3). 12 *C* group samples yield statistically critical track length data, which are omitted (Tab. 6.3). In the absence of track length information, their AFT ages are interpreted as minimum cooling ages. The moderate MTL values of the remaining 47 *C* group samples indicate a considerable amount of fission track annealing. Their fairly broad SD and their unimodal, negatively skewed track length distribution could suggest that track shortening resulted from a slow, protracted cooling through the AFT PAZ.

The majority of the *C* group samples display strong similarities in their AFT ages (c. < 100 Ma), their MTL (c. < 13 μm), their SD (c. 2.3-1.4 μm), their D_{par} values (c. 1.8 μm) and their track length frequency distributions (Tab 6.3, Figs. 6.2, 6.3, 6.9a, b and Appendix B.3). These similarities indicate that the majority of *C* group samples experienced fairly similar *t*-*T* paths. Few *C* group samples with AFT ages of ≤ c. 80 Ma display a slight tendency to decrease in MTL with AFT age (Fig. 6.9b), presumably indicating a higher degree of track annealing. However, all *C* group AFT ages of less than c. 100 Ma are interpreted as minimum cooling ages.

Table 6.3: Results of apatite fission track analysis – Southern basement : *C* group samples

Sample	Lithology	Longitude	Latitude	Elevation (m)	No. of grains	ρ_s (× 10^6cm^{-2}) (N_s)	ρ_i (× 10^6cm^{-2}) (N_i)	ρ_d (× 10^6cm^{-2}) (N_d)	P(χ^2) (%)	Central age ± 1σ (Ma)	U (ppm)	MTL ± 1σ (μm)	SD (μm)	No. of tracks	Mean D_{par} ± 1σ (μm)	SD_{par} (μm)	No. of D_{par}
BZ 216	amphibolite	37.44806	-16.03861	500	25	0.793 (962)	2.181 (2643)	1.500 (11436)	47	88 ± 4	21	12.4 ± 0.2	1.8	115	2.03 ± 0.01	0 .17	140
GZ 6	gneiss	39.27278	-14.23111	350	12	0.371 (382)	0.102 (1046)	1.512 (11436)	42	89 ± 6	11	13.5 ± 0.4	1.3	11	1.93 ± 0.03	0.27	74
GZ 22	gneiss	39.17139	-14.12139	500	5	0.432 (63)	0.117 (170)	1.533 (11436)	68	92 ± 14	14	12.8 ± 0.2	1.4	83	1.72 ± 0.02	0.24	212
GZ 39	gt-bt-gneiss	38.76139	-15.71056	250	20	0.556 (498)	1.341 (1202)	1.491 (11436)	99	100 ± 6	13	12.2 ± 0.3	2.3	54	1.68 ± 0.02	0 .23	196
GM 139	felsic gneiss	35.38598	-16.41710	289	7	1.072 (174)	1.874 (304)	1.210 (5836)	92	111 ± 11	22	13.3 ± 0.2	1.3	33	1.51 ± 0.02	0 .16	108
JJ 110	charnockite	35.74005	-16.85157	268	13	0.960 (750)	2.270 (1773)	1.258 (5836)	17	84 ± 5	25	12.7 ± 0.2	1.5	60	1.10 ± 0.01	0.15	200
JJ 126	metarhyolite	35.45539	-16.34469	474	18	1.093 (1042)	2.783 (2652)	1.294 (5836)	82	81 ± 4	31	12.6 ± 0.2	1.8	93	1.13 ± 0.01	0.16	177
JJ 143	amphibolite	35.32986	-16.38326	500	22	0.395 (648)	1.043 (1710)	1.254 (5836)	95	76 ± 4	12				1.32 ± 0.02	0.18	87
JJ 199	granulite	36.67493	-15.33184	711	2	1.310 (64)	1.964 (96)	1.276 (5836)	22	136 ± 22	21				1.10 ± 0.03	0.09	8
JJ 238	bt gneiss	36.82083	-15.37044	804	11	0.320 (210)	0.767 (504)	1.196 (5836)	86	80 ± 7	9				1.20 ± 0.02	0.16	44
LH 20	gneiss	35.75051	-16.35753	564	17	0.830 (934)	1.965 (2211)	1.214 (5836)	68	82 ± 4	23	12.6 ± 0.2	1.5	97	1.08 ± 0.01	0.17	146
	amphibolite	35.75051	-16.35753	564	18	0.602 (509)	1.376 (1163)	1.218 (5836)	41	86 ± 5	16	12.3 ± 0.2	1.7	85	1.18 ± 0.01	0.16	283
LH 25	amphibolite	35.54315	-16.41149	408	21	1.494 (1871)	3.272 (4097)	1.289 (5836)	32	94 ± 4	35	12.6 ± 0.1	1.5	101	1.12 ± 0.01	0. 15	188
LH 31	felsic gneiss	35.76124	-16.12972	568	5	0.544 (136)	1.419 (355)	1.174 (5836)	12	73 ± 9	17	11.7 ± 0.2	0.3	3	1.12 ± 0.02	0.12	29
LH-MD-69	felsic gneiss	35.63489	-16.22693	599	7	0.269 (147)	0.638 (349)	1.267 (5836)	48	85 ± 9	7				1.15 ± 0.03	0.16	28
RMZ 25	gabbroid	39.13778	-14.20472	358	30	1.021 (790)	2.088 (1615)	1.507 (11436)	90	119 ± 6	20	13.0 ± 0.2	2.1	112	2.56 ± 0.02	0.31	401
RMZ 33	amphibolite	37.51306	-15.06722	717	12	0.711 (474)	1.203 (802)	1.588 (11436)	81	151 ± 9	11	13.4 ± 0.2	2.0	101	3.20 ± 0.04	0. 57	212
RMZ 35	granitic gneiss	37.18194	-15.04722	794	27	1.006 (1797)	2.259 (4034)	1.653 (11436)	65	119 ± 4	19	11.9 ± 0.2	2.1	81	1.91 ± 0 .02	0.27	312
RMZ 36	gneiss	37.72972	-15.14361	657	25	0.453 (853)	1.279 (2405)	1.582 (11436)	49	91 ± 4	12	11.8 ± 0.3	2.7	72	1.85 ± 0.01	0.21	279
	migmatite	37.72972	-15.14361	657	5	0.294 (68)	0.609 (141)	1.593 (11436)	87	123 ± 18	8	12.4 ± 0.6	2.2	15			
RMZ 38	gneiss	37.66222	-15.15528	645	30	0.518 (415)	1.160 (929)	1.493 (11436)	96	108 ± 7	11	11.5 ± 0.2	2.0	94	2.03 ± 0.01	0.22	306
RMZ 42	bt-gneiss	37.20417	-15.32556	886	30	1.155 (1122)	3.216 (3125)	1.529 (11436)	22	89 ± 4	31	12.6 ± 0.2	1.9	98	2.27 ± 0.02	0.3 1	271
RMZ 47	granitic gneiss	37.14708	-15.64833	575	14	0.129 (142)	0.429 (472)	1.642 (11436)	100	80 ± 8	4	12.6 ± 0.5	2.7	31	1.95 ± 0.0 3	0.25	93
RMZ 49	charnockite	37.16639	-16.04111	495	27	0.838 (696)	3.016 (2506)	1.526 (11436)	49	69 ± 3	30	11.7 ± 0.2	2.0	98	1.66 ± 0.01	0. 23	379
RT 59	gneiss	35.50152	-16.29566	611	4	0.295 (53)	0. 945 (170)	1.271 (5836)	74	64 ± 10	10				1.04 ± 0.04	0.15	16
RT 66	microgranite	35.43654	-16.37018	485	7	0.825 (245)	1.659 (493)	1.223 (5836)	99	97 ± 8	19				2.00 ± 0.05	0.25	28
PZ 17	bt-gneiss	37.92833	-15.92194	550	3	0.107 (13)	0.396 (48)	1.548 (11436)	71	68 ± 21	3				1.94 ± 0.10	0.34	11
PZ 33	amphibolite	38.17444	-16.09139	250	1	0.195 (4)	0.292 (6)	1.524 (11436)		163 ± 106	3	13.7 ± 1.2	1.7	2	3.27 ± 0.21	0.70	11
PZ 52	amph. gneiss	38.24139	-16.06222	220	9	0.479 (83)	1.254 (217)	1.519 (11436)	99	94 ± 12	10	13.1 ± 0.3	2.8	80	1.93 ± 0.05	0.27	172
WB 28	k-fsp gneiss	36.26704	-16.76268	384	6	0.685 (152)	2.127 (472)	1.232 (5836)	7	61 ± 8	25	12.1 ± 0.4	2.1	29	1.11 ± 0.02	0.15	87
WB 30B	augengneiss	36.24128	-16.82791	336	19	0.539 (1001)	1.119 (2078)	1.103 (5836)	45	85 ± 4	14	11.6 ± 0.3	2.2	41	1.31 ± 0.02	0. 18	116
WB 88	charnockite	36.46199	-16.18425	567	8	1.850 (461)	4.148 (1034)	1.112 (5672)	94	79 ± 5	55	12.3 ± 0.3	1.8	58	1.24 ± 0.02	0.18	82
WB 119	metagabbro	35.52135	-16.71980	127	15	0.196 (219)	0.458 (513)	1.285 (5836)	88	88 ± 8	5				1.27 ± 0.02	0.16	60
WB 295	charnockite	36.38557	-15.46526	751	15	0.751 (560)	1.653 (1233)	1.152 (5836)	50	84 ± 5	21	12.0 ± 0.3	1.9	41	1.29 ± 0.02	0.21	156

Table 6.3: continued

Sample	Lithology	Longitude	Latitude	Elevation (m)	No. of grains	ρ_s (× 10^6cm^{-2}) (N_s)	ρ_i (× 10^6cm^{-2}) (N_i)	ρ_d (× 10^6cm^{-2}) (N_d)	P(χ^2) (%)	Central age ± 1σ (Ma)	U (ppm)	MTL ± 1σ (μm)	SD (μm)	No. of tracks	Mean D_{par} ± 1σ (μm)	SD_{par} (μm)	No. of D_{par}
020820-01	granite	39.51675	-15.19681	400	19	1.254 (613)	2.428 (1187)	0.986 (7775)	69	81 ± 5	35	13.1 ± 0.2	1.6	74	1.83 ± 0.02	0.22	181
	granite	39.51675	-15.19681	400	12	1.700 (811)	3.000 (1431)	1.044 (7775)	34	95 ± 5	40	12.3 ± 0.2	2.1	118	1.97 ± 0.01	0.18	161
020821-01	bt-gneiss	39.19008	-15.05664	420	13	0.591 (385)	1.335 (869)	1.058 (7775)	56	75 ± 5	19	12.1 ± 0.2	1.9	91	1.95 ± 0.01	0.19	226
020821-02	pink granite	39.20053	-15.09433	420	22	0.392 (695)	0.656 (1165)	1.001 (7775)	72	96 ± 5	10	12.2 ± 0.2	1.7	50	2.02 ± 0.02	0.25	169
	bt-gneiss	39.20053	-15.09433	420	16	0.364 (275)	0.746 (564)	1.019 (7775)	96	80 ± 6	11	12.8 ± 0.4	2.1	24	1.82 ± 0.02	0.21	123
020822-01	gt-bt-gneiss	38.75306	-15.71217	250	22	0.748 (776)	1.551 (1609)	0.986 (7775)	100	76 ± 4	22	12.4 ± 0.3	1.9	45	1.72 ± 0.01	0.19	190
020823-02	bt-granite	37.35775	-16.54864	210	25	0.366 (709)	0.912 (1766)	1.065 (7775)	60	69 ± 4	12	12.5 ± 0.2	1.5	39	1.80 ± 0.01	0.20	199
020823-05	gt-opx-gneiss	37.14056	-16.60700	350	10	0.353 (142)	0.651 (262)	1.006 (7775)	79	87 ± 9	9	12.8 ± 0.8	3.0	14	1.94 ± 0.03	0.18	82
020823-06	orthogneiss	36.95478	-16.87181	180	21	1.264 (804)	3.313 (2108)	1.032 (7775)	28	63 ± 3	46	11.8 ± 0.2	2.2	85	1.86 ± 0.02	0.22	198
	orthogneiss	36.95478	-16.87181	180	13	0.389 (287)	0.816 (602)	1.054 (7775)	100	81 ± 6	11	12.0 ± 0.3	2.0	50	1.82 ± 0.02	0.20	165
020824-01	microgranite	37.49197	-16.47936	330	18	0.931 (543)	2.161 (1261)	1.034 (7775)	62	71 ± 4	33	11.9 ± 0.2	2.0	73	1.82 ± 0.01	0.19	218
	gneiss	37.49197	-16.47936	330	12	1.221 (513)	2.524 (1061)	1.017 (7775)	59	79 ± 5	38	12.3 ± 0.2	1.7	96	1.79 ± 0.02	0.23	212
020824-02	bt-granite	37.40161	-16.37942	410	20	0.417 (485)	1.028 (1195)	1.029 (7775)	98	67 ± 4	15	12.1 ± 0.5	2.2	21	1.85 ± 0.02	0.24	114
020824-03	migmatite	37.39403	-16.33947	352	7	0.508 (201)	1.215 (481)	1.062 (7775)	8	75 ± 9	17	12.3 ± 0.3	1.4	22	1.99 ± 0.02	0.20	75
	leucosome	37.39403	-16.33947	352	22	1.464 (1775)	2.784 (3374)	0.996 (7775)	71	84 ± 4	46	12.3 ± 0.2	1.7	97	1.92 ± 0.02	0.23	200
020824-06	migmatite	37.13939	-16.19142	330	7	0.572 (236)	1.239 (511)	1.022 (7775)	90	76 ± 6	22	12.4 ± 0.3	1.3	27	1.88 ± 0.02	0.23	85
020824-07	charnockite	37.16511	-16.07128	480	18	0.551 (348)	1.185 (748)	1.004 (7775)	89	75 ± 5	18	11.4 ± 0.3	2.4	48	1.84 ± 0.02	0.20	174
020825-02	orthogneiss	37.62831	-16.33258	280	13	0.354 (307)	0.894 (775)	1.050 (7775)	56	67 ± 5	13	11.6 ± 1.4	3.2	5	1.80 ± 0.06	0.19	67
020826-01	gneiss	37.90036	-16.29083	240	9	0.636 (210)	1.404 (464)	1.039 (7775)	44	75 ± 7	22	11.9 ± 0.3	1.9	47	1.90 ± 0.02	0.21	124
020826-03	granite	38.05367	-16.21033	380	20	0.380 (459)	0.875 (1056)	1.037 (7775)	97	72 ± 5	12	12.3 ± 0.3	1.8	29	1.76 ± 0.02	0.23	143
020826-04	granite	38.08478	-16.15256	410	22	0.308 (185)	0.622 (374)	1.006 (7775)	100	80 ± 8	9	12.6 ± 0.4	2.0	28	1.68 ± 0.02	0.26	172
020826-09	granite	38.33333	-16.17339	290	11	0.886 (387)	1.648 (720)	1.011 (7775)	17	87 ± 6	24	12.0 ± 0.2	1.9	61	1.79 ± 0.02	0.21	166
020827-01	orthogneiss	38.49566	-16.22936	200	8	0.240 (66)	0.524 (144)	1.069 (7775)	31	78 ± 13	7	12.2 ± 0.3	1.6	23	1.81 ± 0.02	0.20	92
020827-04	orthogneiss	38.39200	-16.14103	200	5	0.109 (26)	0.181 (43)	0.991 (7775)	88	96 ± 24	3				1.77 ± 0.04	0.20	20
020828-01	gneiss	38.37297	-15.12233	450	17	0.401 (397)	0.779 (771)	1.042 (7775)	96	86 ± 6	11	13.2 ± 0.3	1.4	31	1.92 ± 0.02	0.18	126
020828-02	gneiss	38.37297	-15.12233	450	18	0.448 (445)	0.937 (931)	1.073 (7775)	22	82 ± 6	13	12.8 ± 0.2	1.9	92	1.93 ± 0.01	0.19	200
	microgranite	38.37297	-15.12233	450	12	0.689 (467)	1.413 (957)	1.088 (7775)	74	85 ± 5	23	12.9 ± 0.2	1.7	97	2.01 ± 0.02	0.21	166
020828-03	gneiss	39.39894	-15.12933	460	10	0.280 (225)	0.551 (443)	0.999 (7775)	100	81 ± 7	8	11.9 ± 0.3	1.7	35	1.64 ± 0.02	0.22	91
	pegmatite	39.39894	-15.12933	460	10	0.510 (344)	1.004 (677)	1.014 (7775)	88	83 ± 6	16	13.3 ± 0.3	1.2	13	1.74 ± 0.03	0.27	66
	granite	39.39894	-15.12933	460	23	0.273 (440)	0.467 (752)	1.027 (7775)	81	96 ± 6	7	12.3 ± 0.3	1.1	14	1.99 ± 0.02	0.21	129

U is the total uranium content of a sample, ρ_d is the standard glass track density, ρ_s and ρ_i represent the sample's spontaneous and induced track densities, with the total number of track counts are given in parentheses. P (χ^2) represents the probability of the chi-square test. MTL is the horizontally confined mean track length and SD represents the corresponding standard deviation. Mean D_{par} is arithmetic mean of all c-axis parallel etch pit diameter measurements in a fission track sample and SD_{par} represents the corresponding standard deviation.

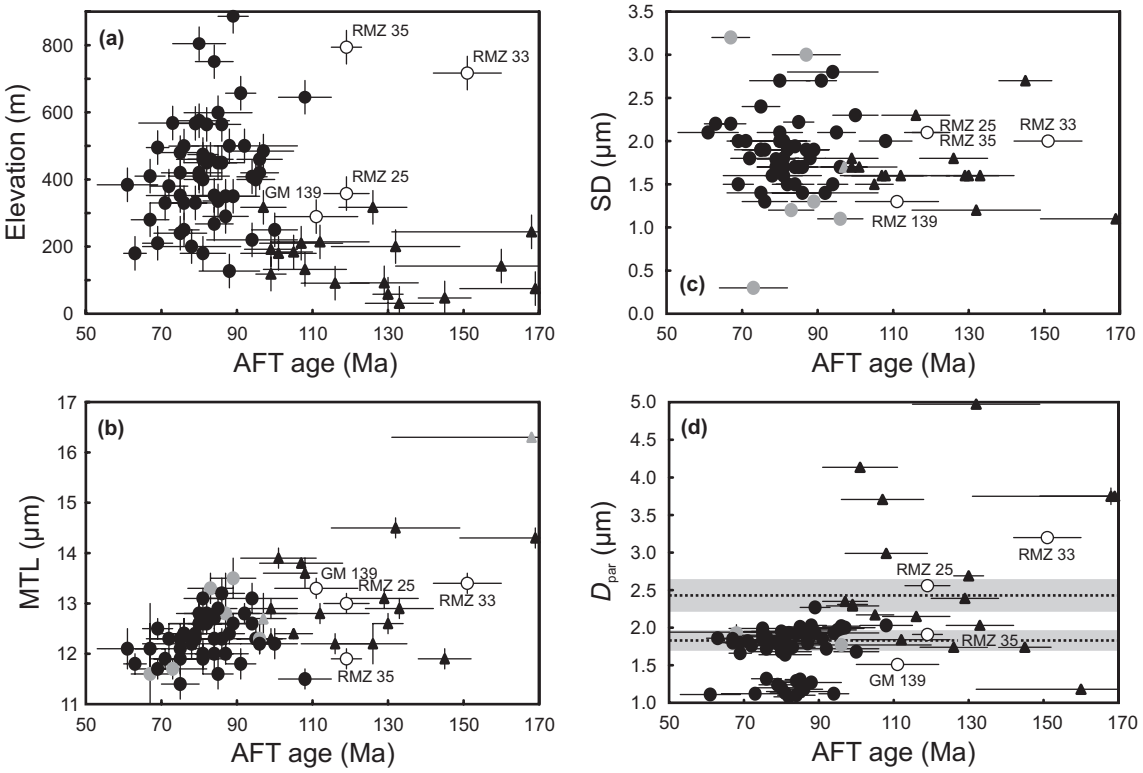

Figure 6.9: Diagrams depict the AFT ages versus elevation (a), horizontally confined MTL (b), SD (c) and D_{par} (d). Black triangles and circles denote the *C* group and *M* group samples, respectively. Grey symbols indicate samples yielding statistically critical AFT track length data. In diagram (d) horizontally dotted lines represent D_{par} values of Fish Canyon (upper) and Durango (lower) AFT age standards with grey bars representing associated standard deviations from Donelick et al. (1999). An elevation error of ± 50 m is assumed for the GPS altitude determination.

Four *C* group samples (GM 139, RMZ 25, RMZ 33 and RMZ 35) yield AFT ages of > 110 Ma and deviate from the general the *C* group AFT age pattern (Tab 6.3 and Fig. 6.9a-d). These samples are interpreted here in more detail. All four samples yield moderate MTL (< 13.4 µm), moderate to broad SD (< 2.1 µm) and negatively skewed track length frequency distributions (Tab. 6.3, Fig. 6.9a-d and Appendix B.3), indicating that they experienced some amount of fission track annealing and that track shortening probably resulted from slow cooling through the AFT PAZ. Therefore the AFT ages of GM 139 (111 ± 11 Ma), RMZ 25 (119 ± 6 Ma), RMZ 33 (151 ± 9 Ma) and RMZ 35 (119 ± 6 Ma) are interpreted as minimum cooling ages.

With exception of GM 139 (SD = 1.3 µm), their sample's broad SD suggest protracted cooling paths through the AFT PAZ. These 4 samples are all located at

marginal positions in the spatial distribution of the *C* group data set and proximate (≤ 20 km) to prominent tectonic zones. Sample GM 139 is located in the southwest of the *C* group data set, adjacent to Palaeozoic-Mesozoic rift basins of the Shire Valley (Fig. 6.1). Samples RMZ 25, RMZ 33 and RMZ 35 are located proximate to Lurio Belt, a high strain shear zone of late Neoproterozoic/Early Cambrian age that bounds the southern basement to the north. Compared to the majority of the *C* group samples GM 139 displays a larger MTL of 13.3 ± 0.2 μm and a narrower SD of 1.3 μm (Tab. 6.3 and Fig. 6.9b, c). This could indicate that GM 139 cooled more rapidly through the AFT PAZ and experienced a minor amount of track annealing. It is inferred, that the AFT age of > 100 Ma of GM 139 resulted from a cooling history that was broadly similar to but less protracted than the ones of the majority of *C* group samples.

Two samples, RMZ 25 and RMZ 33 yield D_{par} values of 2.56 ± 0.02 μm and 3.20 ± 0.04 μm, respectively. These values are larger than the average *C* group D_{par} values of c. 1.8 μm (Tab 6.3, Fig. 6.8d) and could indicate, compared to the *C* group, a higher fission track annealing resistance of both samples. This might explain their AFT ages of > 100 Ma even though both samples experienced *t-T* paths that were relatively similar to the majority of the *C* group samples. In the case of RMZ 33, its higher sample elevation at c. 717m (Tab. 6.3, Fig. 6.9a), compared to the majority of the *C* group samples, might additionally account for its AFT age. RMZ 33 yields a larger MTL of 13.4 ± 0.2 μm than the average *C* group samples (Fig. 6.9b). In conjunction with its higher elevation this could suggest that RMZ 33 was located at a more shallow crustal level and cooled slightly earlier through the AFT PAZ. It therefore retained a longer MTL and an older AFT age compared to the majority of the *C* group samples. The AFT age of RMZ 33 (151 ± 9 Ma) could result from a combined effect of increased track retention and slightly earlier cooling through the AFT PAZ, with respect to the *C* group sample set.

With exception of its AFT age, the AFT data (MTL, SD, D_{par}) of RMZ 35 are very similar to the majority of the *C* group samples (Tab. 6.3 and Figs 6.1, 6.2a-d). Sample RMZ 35 is located at an elevation of c. 794 m, distinctly higher than the average elevations (c. 300-500 m) of the *C* group samples. Therefore RMZ 35 could have been located at more shallow crustal level in former times and its AFT age > 100 Ma could

result from a slightly earlier cooling through the AFT PAZ with respect to the bulk *C* group sample set. However, the short MTL (11.9 ± 0.04 μm) indicate significant track annealing and appears to be less compatible with a simple "earlier cooling due to higher elevation" effect. It appears more reasonable, that the AFT age of RMZ 35 results from a *t-T* history that is distinctly different than that experienced by the majority of the *C* group samples. Hence RMZ 35 could represent an outlier. This is in particular reasonable, as RMZ 35 is derived from the high strain zone of the Lurio Belt and could reflect a cooling history related to tectonic activity along it.

The modelled AFT *t-T* paths of 21 *C* group samples are given in the Fig. 6.10. With the exception of the sample RMZ 35, they all display a fairly uniform cooling into the AFT PAZ in Early to Late Cretaceous times between c. 130 Ma to 90 Ma. The majority of the samples reveal a rapid cooling step in the Early/Late Cretaceous at c. 110-90 Ma. Subsequently, their cooling to from temperatures > c. 90°-80°C occurred protractedly during the Late Cretaceous to Palaeogene/Neogene times (Fig. 6.10). In general, the very similar *t-T* paths of the modelled *C* group samples are in good agreement with the uniform AFT data pattern of the population. This indicates that extensive parts of the southern basement experienced a very uniform cooling history since the Early/Late Cretaceous. All presented *C* group AFT *t-T* path models denote, that the southern basement had been definitely cooled to below 60°C by Palaeogene to Neogene times.

Sample GM 139 already indicates a cooling to below 60°C in the Late Cretaceous and thus reflects a more rapid cooling step through the AFT PAZ in the region adjacent to the Shire Valley (Fig. 6.10). RMZ 25, RMZ 33 and RMZ 36, located proximate to the Lurio Belt (Fig. 6.10), yield slow protracted cooling paths through AFT PAZ from the Late Cretaceous (c.130 Ma) onward to Palaeogene/Neogene times (below c. 60°C). Their *t-T* paths could indicate a subtle spatial difference of the southern basement's cooling history with proximity to the Lurio Belt (Fig. 6.10). Compared to the majority of the *C* group samples, their slightly earlier cooling into the AFT PAZ could reflect a cooling of a formerly more shallowly seated crustal level (see former section).

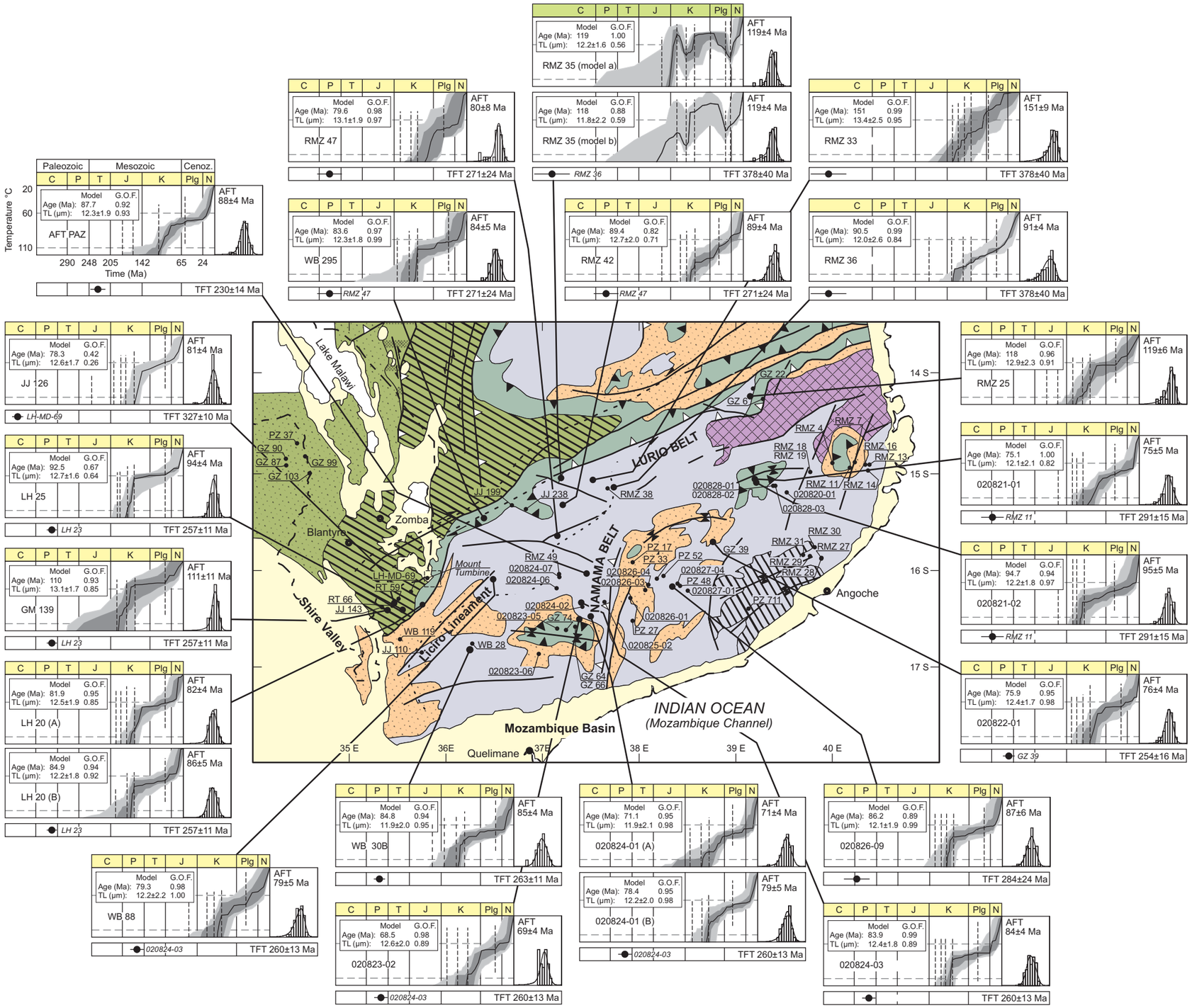

Fig 6.10: This map is a subset of Fig. 6.1 and depicts AFT sample locations in northern Mozambique. The large dots highlight samples from the central southern basement (*C* group) that were employed in the modelling of *t-T* paths. The corresponding *t-T* paths are given as the pictograms. A detailed pictogram explanation is provided in Fig. 6.5.

For sample RMZ 35 from the Lurio Belt, two *t-T* path models are presented (Fig. 6.10). Model *b* is a slight modification of model *a,* and results from *t-T* constraints adjusted in response to corresponding (U-Th)/He model results (see chapter 7, section 7.3). Reasonably good model reproductions of the determined AFT data of RMZ 35 are solely obtained, if a cooling into the AFT PAZ during Jurassic times (c. 170-150 Ma) and cooling steps linked to reheating (with $T \leq 90$°C) in the Early Cretaceous and in the Palaeogene are inferred. Additionally, at least one period of cooling to below 60°C had to be enforced prior to the reheating related final cooling step in the Palaeogene. The Jurassic timing of cooling into the AFT PAZ of RMZ 35 could suggest that this sample was seated at a more shallow crustal level than the majority of the *C* group samples.

M group samples

The AFT ages of the *M* group samples span from 169 ± 19 Ma to 97 ± 6 Ma. Their MTL range between 14.5 ± 0.2 μm to 11.9 ± 0.2 μm with most of them being larger than 12.3 μm. The associated SD range between 2.7 and 1.1 μm and cluster predominantly around c. 1.8 μm. Sample's D_{par} values span over a large range from 4.97 ± 0.08 μm to 1.18 ± 0.03 μm (Tab. 6.4 and Figs. 6.2, 6.3, 6.9a-d). Track length frequency distributions of the *M* group samples display unimodal symmetrical to negatively skewed shapes (Appendix B.4). The track length data of samples RMZ 19, GZ 66 and RMZ 13 are statistically critical and are therefore omitted (Tab 6.4). In the absence of track length information, their AFT ages are interpreted as minimum cooling ages.

With the exception of GZ 64 and PZ 711, the moderate MTL values of all *M* group samples indicate that they experienced a distinct amount of fission track annealing. Their track length frequency distributions point out that annealing probably resulted from protracted and rather complex cooling histories. Therefore these *M* group AFT ages are interpreted as mixed ages. A broad range of D_{par} values observed in the *M* group samples (Fig. 6.9d) suggests a diverse range of annealing kinetics, i.e. resistances to track shortening. As a consequence, some of the AFT age spread in the *M* group could be associated with variable track retention characteristics. Within the *M* group samples, no correlations are apparent between their AFT ages and elevation, MTL or

SD (Tab. 6.4 and Fig. 6.9a-c). Presumably, this suggests that the broad range of AFT ages might also represent a diversity of *t-T* histories in the *M* group.

The AFT samples GZ 64 and PZ 711 yield long MTL of > 14.3 μm and very narrow SD of < 1.2 μm (Tab. 6.4 and Fig. 6.9b, c). This could imply that both samples experienced minor amounts of fission track annealing and cooled fairly rapidly through the AFT PAZ. Their large D_{par} values of ≥ 3.75 μm (Tab 6.4, Fig 6.9d and Appendix B.4) likely argue for distinctly higher track annealing resistances compared to the Durango apatite standard. Their AFT ages, however, are interpreted as minimum cooling ages.

The modelled AFT *t-T* paths of 13 *M* group samples are presented in Fig. 6.6. and indicate more rapid cooling periods into the AFT PAZ during the Early Jurassic at c. 200 Ma, the Middle to Late Jurassic at c. 180-150 Ma and the Early to Late Cretaceous at c. 130-90 Ma. One modelled *t-T* path (RMZ 16) suggests a cooling to below c. 60°C in Early/Middle Jurassic times (c. 190 Ma) and a subsequent cooling step due to reheating to 90°-70°C in the Middle Jurassic (≥ 180 Ma). The majority of modelled *M* group *t-T* paths, however, show that the basement along the eastern continental margin cooled to below c. 60°C either in the Early to Late Cretaceous or at latest during Palaeogene to Neogene times. Several *t-T* paths indicate a cooling step due to a reheating of up to c. 80°-60°C during Palaeogene times approximately at c. 40-20 Ma.

Samples GZ 64, GZ 74, PZ 27, RMZ 27 and RMZ 28 indicate a more rapid cooling step into the AFT PAZ and further to below c. 90°C in Early to Late Cretaceous times. Subsequent, cooling continued protractedly to below c. 60°C during the Palaeogene to Neogene. These AFT *t-T* paths display very strong similarities to the *C* group *t-T* paths (Fig. 6.10). These sample's D_{par} values of > 2.1 μm are larger than the average D_{par} values of the *C* group samples of c. 1.8 μm. In particular samples GZ 64 and GZ 74, which display very large D_{par} values of > 3.5 μm (Tab. 6.4) and yield *t-T* paths, that appear to be very similar to *t-T* paths of adjacent *C* group samples 020823-02 and 020824-0 (Figs. 6.6 and 6.10), which reveal D_{par} values of c. 1.8 μm (Tab. 6.3). It is inferred, that the AFT ages (> 100 Ma) of GZ 64, GZ 74, PZ 27, RMZ 27 and RMZ 28

of are likely related to a higher resistance to track annealing, and therefore represent a further southward extension of *C* group cooling pattern.

The cooling paths of the very proximate samples RMZ 4 and RMZ 11 as well as RMZ 29 and RMZ 30 (Fig. 6.6) display all a similar rapid cooling step into the AFT PAZ in the Early Cretaceous. However, their following cooling histories appear to be somewhat ambiguous. Samples RMZ 11 and RMZ 29 indicate a rapid cooling step to below c. 80°C in the Early Cretaceous and a subsequent very slow and protractedly cooling to below c. 60°C during Neogene times. In contrast, RMZ 4 and RMZ 30 indicate a rapid cooling step through the entire AFT PAZ in Early Cretaceous times at c. 100 Ma (Fig. 6.6).

Samples RMZ 14, RMZ 31 and PZ 711 (Fig. 6.6) display cooling into the PAZ during Jurassic times at c. 160-150 Ma and at c. 170 Ma, respectively. In the following, slow cooling continued to below c. 60°C in the Early Cretaceous at c. 130 Ma. The three samples (RMZ 14, RMZ 31, PZ 711) document an earlier cooling through the AFT PAZ than the aforementioned *M* group samples. It is supposed, that their AFT data, compared to the previously interpreted *M* group samples, trace the *t-T* path of a formerly more shallow seated crustal level. Two modelled *t-T* paths (*a* and *b*) are presented for RMZ 31 (Fig. 6.6). While model *a* yields rapid cooling to below 60°C in the Early Cretaceous, model *b* suggests a prolonged residence close the low temperature threshold of AFT PAZ (≤ 60°C) since the Early Cretaceous. In contrast to model *a*, model *b* uses an additional tight temperature constraint in Cretaceous times. A refinement of these slightly ambiguous cooling paths is investigated by corresponding (U-Th)/He analyses (see chapter 7).

The *t-T* path of sample RMZ 16 indicates a more rapid cooling step into the AFT PAZ in the Early Jurassic at c. 200-190 Ma. It is therefore possible that, compared to the other *M* group samples, it reflects the *t-T* path of a formerly more shallowly seated crustal level. Two slightly varying *t-T* path models (*a* and *b*) indicate that the timing of the reheating is not too tightly to constrain but suggest a probable occurrence between c. 180 Ma and 160 Ma. The post Jurassic *t-T* path of RMZ 16 is very similar to that of the proximate samples RMZ 4 and RMZ 11 (Fig. 6.6). Alternatively, sample RMZ 16 could also represent the *t-T* path of a similar crustal level as the neighbouring samples RMZ 4,

Table 6.4: Results of apatite fission track analysis – Southern basement : *M* group samples

Sample	Lithology	Longitude	Latitude	Elevation (m)	No. of grains	ρ_s ($\times 10^6$cm^{-2}) (N_s)	ρ_i ($\times 10^6$cm^{-2}) (N_i)	ρ_d ($\times 10^6$cm^{-2}) (N_d)	P(χ^2) (%)	Central age ± 1σ (Ma)	U (ppm)	MTL ± 1σ (µm)	SD (µm)	No. of tracks	Mean D_{par} ± 1σ (µm)	SD_{par} (µm)	No. of D_{par}
RMZ 4	dolerite	39.98972	-14.89333	214	10	1.106 (174)	2.542 (400)	1.604 (11436)	15	112 ± 13	21	12.8 ± 0.2	1.6	48	1.84 ± 0.02	0.24	157
RMZ 7	carbonatite	40.22139	-14.88361	132	12	0.203 (159)	0.474 (370)	1.553 (11436)	100	108 ± 11	4	13.6 ± 0.3	1.6	24	2.99 ± 0.04	0. 41	118
RMZ 11	monzogranite	40.16833	-14.94222	184	15	2.728 (1288)	4.259 (2011)	1.024 (7775)	59	105 ± 5	61	12.4 ± 0.1	1.5	103	2.17 ± 0.0 3	0.25	99
RMZ 13	orthogneiss	40.37083	-14.91000	142	12	0.063 (55)	0.105 (91)	1.649 (11436)	100	160 ± 28	1				1.18 ± 0.03	0.21	47
RMZ 14	orthogneiss	40.35556	-14.97000	58	30	2.708 (2873)	5.273 (5594)	1.576 (11436)	66	130 ± 4	48	12.6 ± 0.2	1.6	108	2.69 ± 0.02	0.26	212
RMZ 16	orthogneiss	40.32722	-14.91028	47	13	2.025 (1049)	3.646 (1889)	1.621 (11436)	40	145 ± 7	31	11.9 ± 0.2	2.7	154	1.74 ± 0.03	0.38	190
RMZ 18	gneiss	39.75833	-14.98472	317	19	0.241 (314)	0.501 (654)	1.631 (11436)	63	126 ± 9	4	12.2 ± 0.4	1.8	23	1.74 ± 0.03	0.20	63
RMZ 19	leucogneiss	39.75833	-14.98472	317	30	0.179 (394)	0.456 (1002)	1.521 (11436)	96	97 ± 6	4	12.7 ± 0.5	1.7	11	2.35 ± 0.02	0.2 8	151
RMZ 27	granite	39.87333	-15.87722	91	17	0.379 (287)	0.842 (638)	1.599 (11436)	46	116 ± 9	8	12.2 ± 0.2	2.3	100	2.15 ± 0.02	0.29	24 1
RMZ 28	granite	39.87167	-15.88444	92	8	0.796 (324)	1.562 (635)	1.565 (11436)	86	129 ± 9	15	13.1 ± 0.2	1.6	54	2.39 ± 0.03	0.35	140
RMZ 29	granite	39.75944	-15.85639	118	20	1.157 (990)	2.894 (2475)	1.536 (11436)	68	99 ± 4	28	12.3 ± 0.2	1.7	102	2.31 ± 0.02	0.31	228
RMZ 30	leptite gneiss	39.80583	-15.76556	192	23	0.469 (296)	1.140 (719)	1.488 (11436)	90	99 ± 7	11	12.9 ± 0.2	1.8	65	2.29 ± 0.02	0.32	207
RMZ 31	gneiss	39.68361	-15.84694	31	27	0.546 (359)	1.012 (665)	1.531 (11436)	100	133 ± 9	10	12.9 ± 0.2	1.6	63	2.03 ± 0.02	0.25	26 6
PZ 711	amphibolite	39.12417	-16.39944	75	15	0.217 (134)	0.310 (193)	1.502 (11436)	99	169 ± 19	3	14.3 ± 0.2	1.1	47	3.75 ± 0.05	0.6 1	184
PZ 27	amphibolite	37.92167	-16.52389	180	13	0.505 (162)	1.213 (389)	1.509 (11436)	91	101 ± 10	11	13.9 ± 0.2	1.7	97	4.13 ± 0.04	0.67	220
GZ 64	amphibolite	37.32750	-16.58556	200	8	0.237 (96)	0.478 (194)	1.659 (11436)	97	132 ± 17	5	14.5 ± 0.2	1.2	38	4.97 ± 0.08	0.85	125
GZ 66	gneiss	37.32750	-16.58556	244	7	0.113 (35)	0.161 (50)	1.495 (11436)	98	168 ± 37	2	16.3		1	3.75 ± 0.11	0.60	29
GZ 74	amphibolite	37.23278	-16.62111	210	10	0.543 (165)	1.339 (407)	1.636 (11436)	29	107 ± 11	12	13.8 ± 0.1	1.6	122	3.70 ± 0.03	0 .49	284

U is the total uranium content of a sample, ρ_d is the standard glass track density, ρ_s and ρ_i represent the sample's spontaneous and induced track densities, with total the number of track counts are given in parentheses. P (χ^2) represents the probability of the chi-square test. MTL is the horizontally confined mean track length and SD represents the corresponding standard deviation. Mean D_{par} is arithmetic mean of all c-axis parallel etch pit diameter measurements in a fission track sample and SD_{par} represents the corresponding standard deviation.

RMZ 11 and RMZ 14. Thereby RMZ 16 could in turn indicate that these three proximate samples were completely annealed during a Jurassic reheating event and solely preserved a record of their post-Jurassic *t-T* histories.

In general, the modelled *M* group samples indicate a series of different *t-T* paths and emphasize that the population's heterogeneous AFT age pattern is related to diverse cooling histories. They also highlight that the *t-T* evolution of the present eastern continental margin is distinctly different from the homogenous *t-T* evolution of the central part of the southern basement. The spatially proximate occurrences of distinctly different *t-T* path along the eastern margin could imply that samples, which were formerly located at different crustal levels, are now juxtaposed at similar elevations due to a tectonic segmentation of the basement along the present eastern continental margin.

6.3.3 Remarks on the D_{par} values of the southern basement samples

The overwhelming majority of the apatite samples from the southern basement (*C* and *M* group samples) yield etch pit diameters that are very similar to D_{par} values of the Durango (c. 1.8 µm) and Fish Canyon (c. 2.5 µm) apatite standards, thus indicating that their annealing characteristics are very similar to these standard apatites. Few samples (e.g. RMZ 33, PZ 711), however, display very large D_{par} values of > 3.5-5 µm (Fig. 6.3). These apatite samples are all derived from amphibolitic lithologies and their AFT ages range among the oldest observed in the southern basement (Tabs 6.3, 6.4 and Figs. 6.2, 6.3). This could point out that the apatites obtained from amphibolitic lithologies yield distinctly higher fission track annealing resistances. These samples could have began to retain fission tracks at higher temperatures than the standard Durango apatites (> 110°C) and apparently, than the majority of the apatites sampled from the southern basement. The AFT ages of those "large D_{par}" samples could therefore also partly result from cooling and track accumulation that started in temperature regimes >> 110°C.

For an isothermal holding time of 100 Ma and D_{par} values of 5 µm, the annealing model of Ketcham et al. (1999) expands the AFT PAZ and places the high temperature threshold at c. 205°C. Accordingly, the AFT samples of the amphibolitic rocks could have already started to record the basement cooling history at temperatures as high as c. 200°C. This is almost twice the value of the high temperature PAZ threshold of

Durango apatite at c. 110°C (Carlson et al., 1999; Green et al., 1986; Ketcham et al., 1999; Laslett et al., 1987).

However, such extreme high temperature track retention can not be unambiguously inferred from the D_{par} parameter alone (see section 1.2.3.2). The etch pit diameter is related to the apatites solubility, which in turn depends on the apatites bulk chemical composition (e.g. Barbarand et al., 2003 and references therein). The chlorine content of apatites is a well known example, where the track retention behaviour is correlated to one chemical constituent and reflected in the etch pit size (Burtner et al., 1994). On the other hand, the presence of e.g. OH in apatites increases the etch pit size but apparently does not affect the fission track annealing kinetics (Ketcham et al., 2000). The observed etch pit diameters of > 3.5-5 µm represent rather extreme values for the annealing model of Ketcham et al., 1999 and might solely reflect a different apatite solubility, unrelated to their apatite annealing kinetics. Inferences on the fission track retention for temperatures >> 110°C may therefore not be simply deduced from such large D_{par} values without corresponding chemical analyses of the apatite samples from amphibolitic lithologies. They could assist to evaluate the dependence of the etch pit size on particular chemical constituents and their possible relation to annealing resistance. In *t-T* paths modelling of such samples (e.g. PZ 711, Tabs. 6.3, 6.4), the determined D_{par} values are employed as annealing kinetic proxies but the resultant *t-T* paths are cautiously interpreted within the usual temperature range of c. 110-60°C.

Independent *t-T* constraints from other thermochronological systems sensitive to temperatures between > 110°C and < 265°C (TFT) could provide information on the AFT retention characteristics of samples derived amphibolitic lithologies in northern Mozambique. Such additional thermochronological dating systems would permit an independent calibration for the temperature sensitivity of the samples displaying high D_{par} values. Suited thermochronological system would be zircon fission track dating, with an estimated PAZ of c. 320-210°C (Yamada et al., 1995) and U-Th/He dating on titanite and zircon which have closure temperatures of c. 200°C and c. 183°C (for cooling at 10°C/Ma), respectively (Reiners and Farley, 1999; Reiners et al., 2004).

Chapter 7

APATITE (U-TH)/HE ANALYSIS – RESULTS AND INTERPRETATION

The (U-Th)/He ages and the analytical details of 15 aliquot and 24 single grain analyses are presented in Tabs. 7.1, 7.2 and Figs. 7.1, 7.2, 7.4. All U-Th/He ages refer to F_T corrected ^{4}He ages unless quoted differently. The ^{4}He ages of the batch analyses range from 1459 ± 63 Ma to 40 ± 2 Ma. Their corresponding mass weighted average grain radii (MWAR) span from c. 74 to 48 μm. The associated standard deviations range from 8.8 to 2.9 μm. The single grain analyses yield ^{4}He ages between 523 ± 18 Ma to 46 ± 2 Ma. Their corresponding grain radii span from c. 83 to 38 μm.

Individual batch and single grain helium analyses are interpreted and grouped into (I) apparently reliable ^{4}He age results, (II) ambiguous ^{4}He ages and (III) rejected ^{4}He ages. The interpretation and grouping of the helium analyses is based on five criteria of which the first four are considered most significant:

(1) The relation between the observed ^{4}He age and corresponding AFT age is used to check the ^{4}He age consistency with ^{4}He production and diffusion model of Wolf et al. (1998). For a rock sample it predicts that an apatite ^{4}He age can not be older than its corresponding AFT age.

(2) An intra-sample ^{4}He age reproduction for similar grain radii is employed as a consistency criterion since grains with identical diameters are supposed to yield identical ^{4}He ages within a rock sample (Farley, 1996).

(3) The correlation of the ^{4}He ages with grain radii are evaluated for multiple intra-sample analyses in order to check for a grain size dependant helium retention; i.e. larger grains yield older ^{4}He ages (Farley, 2000) and very slow, protracted cooling histories can result in large ^{4}He age variations correlated with grain size (Reiners and Farley, 2001).

(4) Intra-sample ^{4}He age variations among grains of similar radii might result from dating grains containing different parent nuclide zoning patterns. ^{4}He age variations of up to ± 25 % around a "true age" can be expected for extreme cases of zoning (Farley, 2002; Fitzgerald et al., 2005). These variations are magnified by very slow cooling rates (< 3°C/Ma) or prolonged residence in the HePRZ (Fitzgerald et al., 2005). In order to evaluate the amount of the intra-sample single grain ^{4}He age variations, a maximum ^{4}He age spread relative to a mean ^{4}He age is estimated (Tab. 7.2).

(5) Individual ^{4}He analyses that are consistent with criteria (1) but do not fulfil criteria (2) and (3) are related to AFT and ^{4}He data of proximate samples. ^{4}He ages, the grain radii and the AFT cooling histories of the proximate samples are used to evaluate a regionally consistent cooling path of such particular ^{4}He ages.

Table 7.1: Results of (U-Th)/He batch analysis

Sample	Lithology	Longitude	Latitude	Elevation (m)	No. of grains	^{4}He (ncc)	U (ppm)	Th (ppm)	Th/U ratio	Raw age (Ma)	F_T	Corrected age ± 1σ (Ma)	MWAR (μm)	SD (μm)
BZ 216	amphibolite	37.44806	-16.03861	428	10	4.29	18.5	4.3	0.24	40	0.75	53 ± 2	58.0	5.8
					10	5.12	24.9	10.9	0.45	47	0.71	66 ± 3	50.4	3.5
					8	3.16	16.5	5.8	0.36	43	0.75	57 ± 2	56.8	5.6
RMZ 18	gneiss	39.75833	-14.98472	317	10†	1.02	2.6	1.2	0.48	77	0.73	106 ± 4	55.8	6.4
					10†	13.70	2.9	1.1	0.39	1052	0.72	1459 ± 63	51.7	5.6
					9	1.06	2.2	0.9	0.41	63	0.79	79 ± 3	67.6	8.8
					3	0.27	2.1	0.7	0.33	60	0.75	80 ± 3	59.1	3.2
					2	0.57	7.3	1.6	0.22	56	0.76	73 ± 3	66.9	7.4
RMZ 25	gabbro	39.13778	-14.20472	358	10	2.25	14.5	38.3	2.69	31	0.72	44 ± 3	53.1	6.5
					8	1.72	9.6	32.0	3.44	28	0.72	40 ± 2	54.2	5.1
					7	1.01	6.4	22.8	3.69	31	0.71	44 ± 2	52.5	4.9
					5†	1.58	8.6	30.0	3.60	55	0.70	78 ± 3	47.6	2.9
RMZ 47	granitic gneiss	37.14708	-15.64833	575	9	2.26	4.0	17.3	4.40	33	0.78	43 ± 3	73.9	8.7
					5	1.07	4.4	17.1	4.01	35	0.76	46 ± 2	68.1	7.8
RMZ 35	granitic gneiss	37.18194	-15.04722	794	8	5.73	16.4	41.0	2.55	60	0.67	89 ± 6	59.3	5.8

F_T represents the correction factor for α emission after Farley et al. (1996). MWAR is the mass weighted average radius of apatite crystals measured in an aliquot. SD is the associated standard deviation of the MWAR. Though standard deviations are not strictly valid for such small populations, they are provided as a rough guide of the spread of single grain radii in a sample. Analyses marked † represent rejected ^{4}He ages.

7.1 Apparently reliable ^{4}He ages (I)

The ^{4}He ages of all batch analyses of BZ 216 (c. 66-53 Ma), RMZ 47 (c. 46-43 Ma), of batch analyses *3-5* of RMZ 18 (c. 73-80 Ma) and of batch analyses *1-3* of RMZ 25 (c. 44-40 Ma) are younger than their corresponding AFT ages (Tabs. 6.3, 7.1, Fig. 7.1a).

These ^{4}He ages replicate within their ± 2 σ confidence levels and display similar MWAR (Tab. 7.1, Fig. 7.1a). All the helium data of these analyses are consistent with criteria (1) to (3) and thus their ^{4}He ages are considered to be reliable.

Table 7.2: Results of (U-Th)/He single grain analysis

Sample	Lithology	Longitude	Latitude	Elevation (m)	analysis	^{4}He (ncc)	U (ppm)	Th (ppm)	Th/U ratio	Raw age (Ma)	F_T	Corrected age ± 1σ (Ma)	Radius (µm)
020821-02	granite	39.20053	-15.09433	420	a*	0.60	9.2	8.1	0.91	39	0.81	48 ± 2	75.0
					b*	0.38	8.0	4.8	0.62	56	0.77	73 ± 3	60.5
					mean					*48*		*60*	
020824-02	bt-granite	37.40161	-16.37942	410	a†	2.28	11.4	13.2	1.19	86	0.84	102 ± 4	82.5
					b	0.67	11.5	12.7	1.14	37	0.81	46 ± 2	80.0
					c†	11.53	20.7	22.7	1.13	296	0.82	361 ± 13	77.5
020825-02	orthogneiss	37.62831	-16.33258	280	a†	0.53	6.8	5.7	0.87	100	0.76	132 ± 5	60.0
					b†	1.07	10.3	7.0	0.70	116	0.77	150 ± 5	65.0
					c†	0.33	4.9	4.1	0.86	76	0.77	99 ± 3	60.0
					mean					*97*		*127*	
020823-02	bt-gneiss	37.35775	-16.54864	210	a	0.41	8.6	8.8	1.05	44	0.77	57 ± 2	60.0
					b†	2.91	7.5	10.8	1.48	403	0.77	523 ± 18	60.0
					c†	0.28	8.5	9.2	1.12	54	0.73	74 ± 2	55.0
					d†	0.61	4.1	3.6	0.91	56	0.83	68 ± 3	75.0
					e†	0.10	8.0	23.2	3.00	42	0.6	70 ± 2	37.5
					mean c-e					*51*		*71*	
RMZ 31	bt-hbl-gneiss	39.68361	-15.84694	31	a*	0.33	6.3	30.4	4.96	74	0.68	109 ± 3	40.0
					b*	0.29	13.4	41.9	3.23	56	0.66	85 ± 2	37.5
					c*	0.21	6.4	14.3	2.32	39	0.74	52 ± 2	55.0
					d*	0.17	3.9	20.0	5.34	68	0.67	101 ± 3	40.0
					e*	1.15	4.8	21.9	4.69	85	0.78	109 ± 4	60.0
					mean					*64*		*91*	
RMZ 35	granitic gneiss	37.18194	-15.04722	794	a	0.55	25.7	84.0	3.38	41	0.68	61 ± 2	45.0
					b	0.23	14.9	35.6	2.48	39	0.68	58 ± 2	42.5
RMZ 42	biotite-gneiss	37.20417	-15.32556	886	a*	0.88	17.6	36.9	2.16	51	0.73	69 ± 2	50.0
					b*	1.77	29.0	52.6	1.87	61	0.76	80 ± 3	55.0
					c*	1.52	31.9	69.9	2.26	60	0.74	81 ± 2	55.0
					d*	1.00	20.4	29.5	1.50	41	0.77	53 ± 2	65.0
					mean					*53*		*71*	

F_T represents the correction factor for *α* emission after Farley et al. (1996). Radius is the single grain radius of the apatite crystals analysed. *Mean* is the arithmetic mean ^{4}He age of the denoted or of all individual analyses in a sample. Analyses marked * represent ambiguous ^{4}He ages and marked † represent rejected ^{4}He ages.

Sample RMZ 35 comprises only one batch and two single grain analyses (*a, b*) due to low grain quality and quantity. Batch analyses yield integrated ^{4}He ages of all grains present in an aliquot and are not unambiguously comparable to single grain ages. The batch analysis yields a ^{4}He age of 89 ± 6 Ma for an MWAR of c. 60 µm. This ^{4}He age is younger than the AFT age of the sample (Tabs. 6.3, 7.1, Fig. 7.1b). Likewise younger are the ^{4}He ages 61 ± 2 Ma and 58 ± 2 Ma of single grain analyses *a* and *b* (Tab. 7.2).

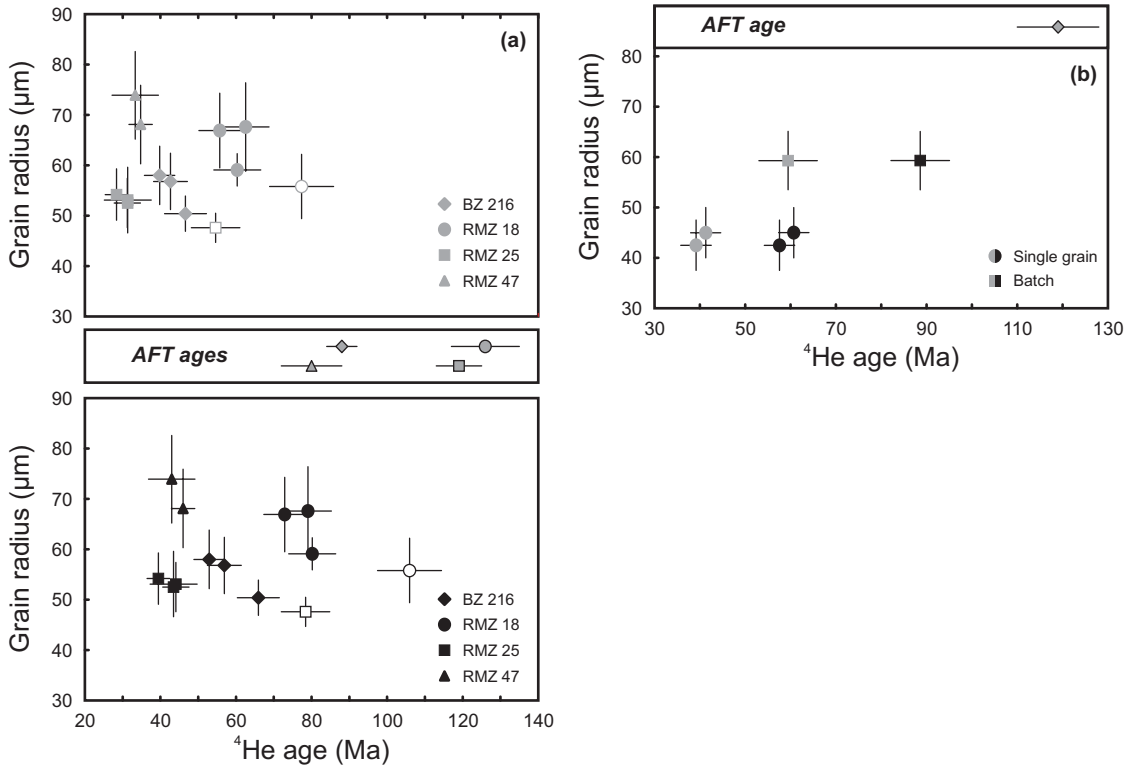

Figure 7.1: Diagrams depicting ^{4}He age versus grain size relation for batch analyses (a) and ^{4}He age versus grain size relation for batch and single grain analyses of sample RMZ 35 (b). In diagram (a) the raw and F_T corrected ^{4}He ages are plotted in the upper and lower panels, respectively. In diagram (b) raw and F_T corrected ^{4}He ages are indicated by grey and black colours, respectively. The error bars on ^{4}He ages represent 2 σ confidence levels. Open symbols denote rejected ^{4}He ages. Corresponding AFT ages are displayed as grey, black outlined symbols with their 1 σ confidence levels. For batch analyses the grain sizes are represented by the MWAR and their associated standard deviations. For single grain analyses, a grain radii error of ± 5 µm is estimated.

These single grain ages reproduce within their ± 2 σ confidence levels and display similar grain radii of c. 45 µm and c. 43 µm (Tab. 7.2 and Fig. 7.2b). Single grain and batch analyses of RMZ 35, however, show an apparent increase in their ^{4}He ages with their grain radii (Tabs. 7.1, 7.2 and Fig. 7.1b). Thus the batch and single grain analyses of RMZ 35 are apparently consistent with criteria (1) to (3) and their ^{4}He ages are considered to be reliable.

Analysis *a* of sample 020823-02 gives a ^{4}He age of 57 ± 2 Ma that is younger than the corresponding AFT age. The grain radius is c. 60 µm (Tabs. 6.3, 7.2 and Fig. 7.2b). This analysis displays strong similarities in ^{4}He age and grain size to the batch analyses of sample RMZ 47 (Tab. 7.1). In both samples, the AFT data uniformly indicate a very

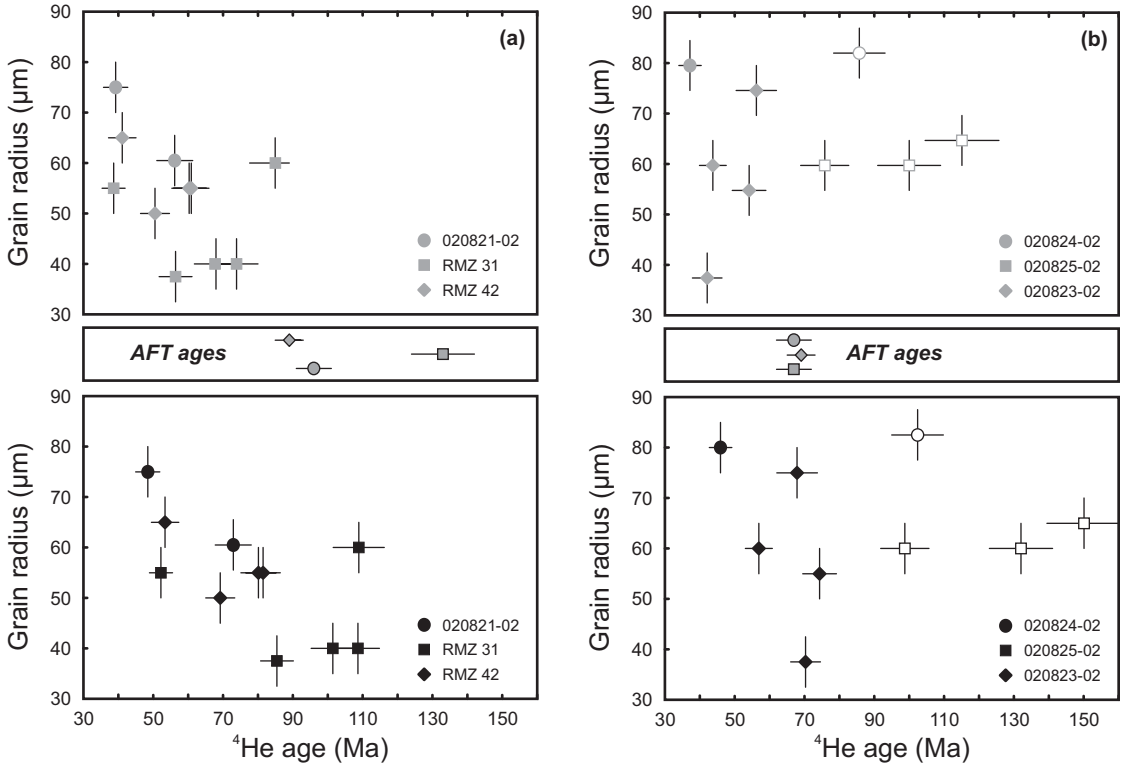

Figure 7.2: Diagrams (a) and (b) depict the ^{4}He ages versus grain size relation for single grain analyses. In both diagrams the raw and F_T corrected ^{4}He ages are plotted in upper and lower panels, respectively. The error bars on ^{4}He ages represent 2 σ confidence levels. Open symbols indicate rejected ^{4}He ages. Corresponding AFT ages are displayed as grey, black outlined symbols with their with their error bars indicating the 1 σ confidence levels. A grain radii error of ± 5 µm is estimated.

slow, protracted cooling into the HePRZ (c. 80°-60°C) (Fig. 6.10). This might suggest that both samples experienced a very similar cooling history through the HePRZ. Consequently, the ^{4}He age of analysis *a* of 020823-02 is considered to be reliable.

Analysis *b* of sample 020824-02 yields a ^{4}He age of 46 ± 3 Ma that is younger than its corresponding AFT age. The grain radius is c. 80 µm (Tabs. 6.3, 7.2 and Fig. 7.2b). This analysis displays remarkable similarities in ^{4}He age and grain size to the batch analyses of sample BZ 216 (Tab. 7.1). No AFT *t-T* path information is available for 020824-02. The proximate sample 020824-01 yields a similar AFT age as 020824-02 (Tab. 6.3) and its slow, protracted cooling into the HePRZ (c. 80-60°C) is regarded as representative for the region. AFT results of sample 020824-01 indicate an identical cooling history to BZ 216 (Fig. 6.10). These facts could suggest that sample 020824-02

and BZ 216 experienced a very similar cooling histories through the HePRZ. Accordingly, the ^{4}He age of analysis *b* of 020824-02 is interpreted as reliable.

7.2 Ambiguous ^{4}He ages (II)

All single grain ^{4}He ages of samples 020821-02 (c. 48-73 Ma), RMZ 31 (c. 52-109 Ma) and RMZ 42 (c. 53-81 Ma) are younger than their corresponding AFT ages. Their ^{4}He ages only partly replicate within their ± 2 σ confidence levels for similar grain radii (Tab. 7.2, Fig. 7.2a) and although their range in grain radii is fairly small, the grain sizes do not correlate with the ^{4}He ages (raw and F_T-corrected) (Tab. 7.2, Fig. 7.2a). The single grain ^{4}He analyses of samples 020821-02, RMZ 31 and RMZ 42 are consistent with criteria (1) but inconsistent with criteria (2) and (3). Therefore, these ^{4}He ages are interpreted as ambiguous. In each of these three samples the variations in single grain ages (raw and F_T-corrected ^{4}He ages) are fairly similar. They range between ± 15-27 % and reach in extreme cases ± 43 % (Tab. 7.2). For all three samples, corresponding AFT results indicate a very slow, protracted cooling into the HePRZ (c. 80°-60°C) (Fig. 6.10). As the ^{4}He ages do not correlate with the grain sizes, other reasons than differing grain radii might cause the observed scatter in single grain ages. Pre-screening results do not indicate strong or contrasting parent nuclide zoning patterns and exclude them as a cause for the age variations. However, minor amounts of excess ^{4}He* in some grains could account for the ^{4}He age scatter.

7.3 Rejected ^{4}He ages (III)

Batch analysis *2* of RMZ 18, single grain analyses *a, c* of 020824-02 and single grain analysis *b* of 020823-02 yield both raw and F_T corrected ^{4}He ages, which are older than their corresponding AFT ages (Tabs. 6.3, 7.1). Such old ^{4}He ages are inconsistent with criteria (1) and thus are rejected. Compared to their corresponding intra-sample ^{4}He analyses, their determined ^{4}He concentrations are over a magnitude higher whereas the U and Th concentrations are about the same (Tab. 7.1). This is interpreted to indicate significant amounts of excess ^{4}He*.

Batch analysis *1* of RMZ 18 (106 ± 4 Ma) and batch analysis *4* of RMZ 25 (78 ± 3 Ma) yield ^{4}He ages which are younger than their corresponding AFT ages

(Tabs. 6.3, 7.1 and Fig. 7.1a). These ^{4}He ages do not overlap within their ± 2 σ confidence levels with their replicating batch analyses and therefore regarded as potential outliers (see section 7.2). Compared to their corresponding replicates, the outliers of RMZ 18 and RMZ 25 yield slightly smaller MWAR of c. 56 µm and c. 48 µm, respectively but older ^{4}He ages (Tab. 7.1). Both analyses are consistent with criteria (1) but inconsistent with criteria (2) and (3). The ^{4}He ages of RMZ 18 batch *1* and RMZ 25 batch *4* are rejected. ^{4}He, U and Th concentrations of the outliers range within the same order of magnitude as their sample's replicates and preclude a significant influence of excess ^{4}He* (Tab. 7.1). In both samples the outlier analyses yield raw ^{4}He ages, which are older than the F_T-corrected ages of the intra-sample replicates (Tab.7.1). This indicates that a false F_T correction factor is unlikely to explain these two older ^{4}He ages (Farley, 2002; Fitzgerald et al., 2005). The fairly homogenous CL pre-screening results of RMZ 18 and RMZ 25 preclude significant influences by variable parent nuclide distribution patterns (Fitzgerald et al., 2005). No conclusive explanation is inferred for the non-replicating ^{4}He ages of samples RMZ 18 batch *1* and RMZ 25 batch *2*.

Single grain analyses *a-c* of 020825-02 yield raw and F_T-corrected ^{4}He ages that are older than the sample's AFT age (Tabs. 6.3, 7.2 and Fig. 7.2b). This contradicts criterion (1) and all single grain analyses of 020825-02 are rejected. The single grain ages of sample 020825-02 yield identical grain radii of c. 60-65 µm but do not replicate within their ± 2 σ confidence levels. Sample 020825-02 yields similar raw and F_T corrected single grain ^{4}He age variations in the range of ± 18-22 % (Tab. 7.2). The pre-screening revealed some grains displaying zoned CL (Fig. 7.3). This could indicate an influence of variable parent nuclide distribution patterns (Farley, 2002; Fitzgerald et al., 2005). AFT results of the proximate samples 020824-01, 020824-03 and BZ 216 argue for slow protracted cooling into the HePRZ (c. 80°-60°C) in the region (Fig. 6.10). The heterogeneous parent nuclide zoning and the very slow protracted cooling through the HePRZ could account for the non-reproducing single grain ^{4}He ages of 020825-02. However, these facts do not account for single ^{4}He ages that are older than the corresponding AFT age (Fig. 7.2b). Possibly, this is simply related to excess ^{4}He*.

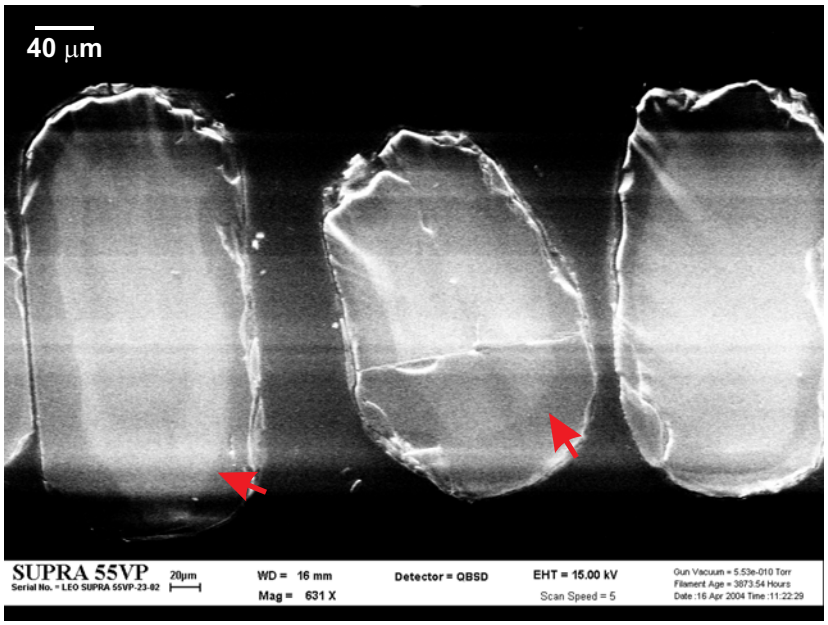

Figure 7.3: CL image of sample 020825-02 displaying grains with concentric alternating zoning patterns.

Single grain analyses *c-e* of 020823-02 yield ^{4}He ages (c. 68-74 Ma) that are older than the sample's AFT age and reproduce within their ± 2 σ confidence levels (Tabs. 6.3, 7.2 and Fig. 7.2b). These ^{4}He ages do not correlate with their corresponding grain radii of c. 37.5 to 75 µm. The single grain analyses *c-e* of sample 020823-02 are inconsistent with criteria (1) to (3) and are rejected. The corresponding raw ^{4}He ages are younger than the sample's AFT age, display an increase in age with grain size (Tabs. 6.3, 7.2 and Fig. 7.2b) and appear to be consistent with criteria (1) and (3). In addition, the raw ^{4}He ages of analyses *c-e* are fairly similar to the F_T corrected ^{4}He age of analysis *a* (Figs. 7.2b, Tab. 7.2). Following the F_T correction (Tab. 7.2) the variation in single grain ages decreases from ± 10-18 % to ± 4 %. As the single grain raw ^{4}He age variation is attributed to the range of grain radii (Tab. 7.2, Fig. 7.2b) the reduced variation in single grain F_T corrected ^{4}He ages could indicate incorrect F_T factors. Conclusively, it appears that subsequent to the F_T correction, the ^{4}He ages of sample 020823-02 become incompatible with model predictions for (U-Th)/He dating as the F_T factors overcorrect the raw ^{4}He ages of analyses *c-e* (Farley, 2002). Alternatively, minor amounts of excess ^{4}He* could also account for the inconsistencies between the raw and F_T corrected ^{4}He single grains ages in analyses *c-e* of sample 020823-02.

7.4 General considerations on (U-Th)/He dating

Recently it has been proposed, that as yet unexplained increases in ^{4}He retention might results in ^{4}He ages that are older than their corresponding AFT ages (Green and Duddy, 2006). It is problematic to reconcile "^{4}He ages with AFT data in the same sample as (U-Th)/He ages increase beyond c. 50 Ma years unless uranium contents are unusually low" (Green and Duddy, 2006). It has also been found that samples from silicic lithologies with high U and Th contents tend to be more susceptible to poor ^{4}He age reproduction than samples from basic host rocks with low U and Th contents (Lorencak et al., 2004).

The data presented do not show that particularly ^{4}He ages older than c. 50 Ma are incompatible with corresponding AFT ages. Additionally, the replication of the ^{4}He age does not appear to be related to specific lithologies or to U and Th concentrations (Tabs. 7.1 and 7.2). Batch analyses appear to yield slightly better ^{4}He age reproductions than single grain analyses. Presumably, inter-grain ^{4}He age variations (e.g. differing parent nuclide distributions) are "blurred" to a certain degree by aliquot dating.

7.5 Results of forward *t-T* path modelling of (U-Th)He ages

The helium *t-T* paths presented in Fig. 7.4 are the results of model approaches that aim to comply with the following criteria:

(a) The raw ^{4}He age must be reproduced by the modelled *t-T* path (Tab. 7.3).

(b) Within one sample, the temperature variations among modelled *t-T* paths of different helium analyses should be minimized within the HePRZ, i.e. ideally, the $He_{RMS} = 0$.

(c) The AFT and (U-Th)/He thermochronometer are both sensitive to record cooling from 80°C to 60°C (Laslett et al., 1987; Wolf et al., 1998). Therefore modelled helium *t-T* and corresponding AFT *t-T* paths should yield a similar timing for cooling to below c. 80°C. The modelled helium *t-T* paths should overlap at least with the corresponding AFT *t-T* path confidence envelops.

(d) The modelled helium *t-T* paths should yield a similar cooling trend as corresponding AFT *t-T* path. It should overlap at least with the AFT *t-T* paths

confidence envelops. The deviation of the mean helium cooling path from AFT cooling path should be minimized (ideally, $AFT_{RMS} = 0$).

(e) In samples with only one helium analysis modelled or with $He_{RMS} \geq 5$°C, the AFT_{RMS} values represents an estimates of the difference between the AFT *t-T* path and the single or least deviating helium *t-T* path, respectively.

For apparently reliable ^{4}He ages of samples BZ 216, RMZ 18, RMZ 25, RMZ 35, RMZ 47, 020823-02 and 020824-02 and for ambiguous ^{4}He ages of samples 020821-02, RMZ 31 and RMZ 42 forward modelling approaches are used to test if the their raw ^{4}He ages are compatible with their corresponding *t-T* paths derived from AFT analyses. In addition, the raw ^{4}He ages of the rejected analyses *c-e* of sample 020823-02 are subjected to a forward model approach together with its apparently reliable analysis *a* to test for a possible F_T factor overcorrection.

The modelled helium *t-T* paths are presented in two groups according to their general cooling path trends. Helium *t-T* paths from samples BZ 216, RMZ 25, RMZ 42, RMZ 47, 020821-02, 020823-02 and 020824-02 are characterized by slow, protracted cooling. The samples of these ^{4}He analyses are located within the central southern basement and correspond to the *C* group AFT data set (chapter 6, Tab. 6.3 and Fig. 6.10). The second group comprises helium *t-T* paths of samples RMZ 18 and RMZ 31 from the eastern margin of the southern basement (*M* group AFT data set; chapter 6, Tab. 6.4 and Fig. 6.6) and of sample RMZ 35 from the Lurio Belt (outlier of the *C* group, chapter 6, Tab. 6.3 and Fig. 6.10). These samples display periods of reheating in their *t-T* paths.

7.5.1 Slow and protracted cooling path models

Forward modelled helium age *t-T* paths of samples BZ 216 (all analyses, 2 models), RMZ 25 (all analyses, 2 models), RMZ 42 (grain *d*), RMZ 47 (all analyses), 020821-02 (grain *a*), 020823-02 (grains *a, d*) and 020824-02 (grain *b*) yield good fits with model criteria (a)-(e) (Fig. 7.4) and considered to be reliable. These modelled *t-T* paths indicate slow and protracted cooling to below c. 80°C in the central southern basement since the Late Cretaceous (c. < 100 Ma). They consistently display cooling to

Table 7.3: Summery of apatite (U-Th)/He model data

Sample	Analysis	MWAR / Radius (μm)	Length (μm)	Sphere radius (μm)	Uncorrected age (Ma)	Modelled age (Ma)
Apparently reliable ^{4}He ages						
BZ 216	batch 1	58	181	72	40	40
	batch 2	50	167	63	47	47
	batch 3	57	154	69	43	43
RMZ 18	batch 3	68	190	82	63	63
	batch 4	59	194	74	60	60
	batch 5	67	175	80	56	56
RMZ 25	batch 1	53	127	62	31	31
	batch 2	54	147	65	28	28
	batch 3	53	142	64	31	31
RMZ 47	batch 1	74	193	88	33	33
	batch 2	68	184	82	35	35
RMZ 35	batch	59	147	70	60	60
	grain a	45	120	54	41	41
	grain b	43	115	52	39	39
020823-02	grain a	60	200	75	44	44
020824-02	grain b	80	160	90	37	37
Ambigous ^{4}He ages						
020821-02	grain a	75	200	90	39	39
	grain b†	61	155	72	56	56
020823-02	grain c†	55	130	64	54	54
	grain d	75	320	97	56	56
	grain e*†	38	100	41	42	42
RMZ 31	grain a	40	170	52	74	74
	grain b	38	130	48	56	56
	grain c	55	155	67	39	39
	grain d	40	150	51	68	68
	grain e	60	310	80	85	85
RMZ 42	grain a*†	50	220	61	51	51
	grain b†	55	190	69	61	61
	grain c†	55	140	65	60	60
	grain d	65	175	78	41	41

MWAR and Radius are the mass weighted average radii and single grain radii of the batch and single grain analyses, respectively. Length is the mean and single grain length of the batch and single grain analyses, respectively. Analyses marked * denote idiomorphic apatite grains that are not corrected for grain breakage. Analyses marked † indicate rejected modelled helium age *t-T* paths Sphere radius is the radius of a model sphere with the same surface to volume ratio as the corresponding ^{4}He analysis.

below c. 60°C in the Palaeogene (c. 40 Ma) and further cooling to below c. 40°C in Neogene times (c. 20-10 Ma) (Fig. 7.4). With exception of sample RMZ 25, all corresponding AFT *t-T* path models indicate a more rapid cooling of their best-fit paths to below 60°C in Neogene time. This period of more rapid cooling to ambient temperatures in the recent geologic past is not reproduced by any of the corresponding helium *t-T* path models. This could suggest that such a period of rapid cooling represents a modelling artefact related to experimental uncertainties of AFT annealing

model (e.g. Kohn et al., 2002, see section 2.2.5.2). Therefore the cooling below c. 60°C in the Palaeogene and further to below c. 40°C in the Neogene is more likely expressed by the modelled helium *t-T* paths of the central southern basement.

The modelled helium *t-T* paths of BZ 216 only marginally overlap with confidence envelops of the related AFT *t-T* path and suggests a just acceptable consistency with the corresponding AFT data set. No AFT *t-T* path could be calculated for sample 020824-02 due to insufficient track length data (Appendix B.4). Therefore helium *t-T* path of analysis *b* of 020824-02 is modelled by using the AFT paths of the proximate samples 020824-01A and 020824-01B. The reliable helium model results of the initially rejected helium analysis *d* from sample 020823-02, could suggest that the inconsistency between its F_T corrected ^{4}He age and corresponding AFT ages is related to an incorrect F_T factor.

Helium models of analyses *a-c* of RMZ 42, analysis *b* of 020821-02 and analyses *c, e* of 020823-02 do not comply with criteria (a)-(e) and are rejected (Fig. 7.4). For analyses *c* and *e* of 020823-02, this suggests that the inconsistencies between their F_T corrected ^{4}He age and corresponding AFT age may not be related to an overcorrection of raw ^{4}He age by an incorrect F_T factor.

7.5.2 Cooling path models involving reheating events

Forward modelled helium age *t-T* paths of samples RMZ 18 (batch *3-5*), RMZ 31 (all analyses) and RMZ 35 (all analyses, 2 models) yield good fits with model criteria (a)-(e) (Fig. 7.4) and considered to be reliable. These modelled *t-T* paths indicate a more rapid cooling to below c. 60°C at the eastern margin of the southern basement and in the Lurio Belt in the Early Cretaceous (c. > 100 Ma). RMZ 18 and RMZ 31 also show further cooling to below c. 40°C during this time (Fig. 7.4). All these three samples consistently indicate a reheating up to c. 60°C in Palaeogene times (c. 40 Ma) followed by subsequent cooling to below c. 40°C in the Neogene at c. 20-10 Ma (Fig. 7.4).

No AFT *t-T* path is derived for sample RMZ 18 due to insufficient track length data (Appendix B.5). Therefore, its helium *t-T* paths are modelled by using AFT *t-T* paths of the proximate sample RMZ 4 as an initial model input.

The best-fit AFT *t-T* paths of RMZ 4, RMZ 31 and RMZ 35 indicate a reheating between 60°C and 75°-80°C in the Palaeogene related to a subsequent more rapid

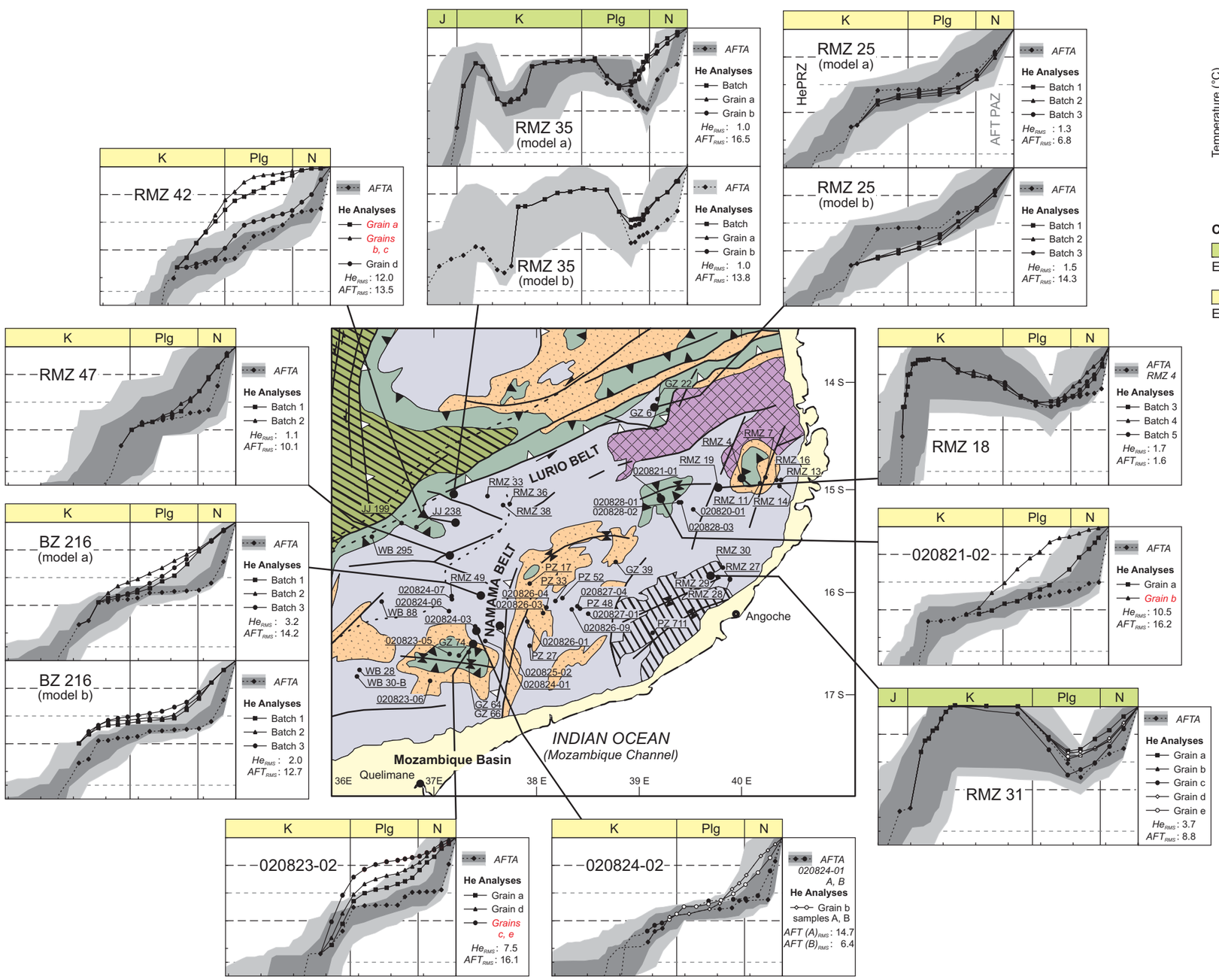

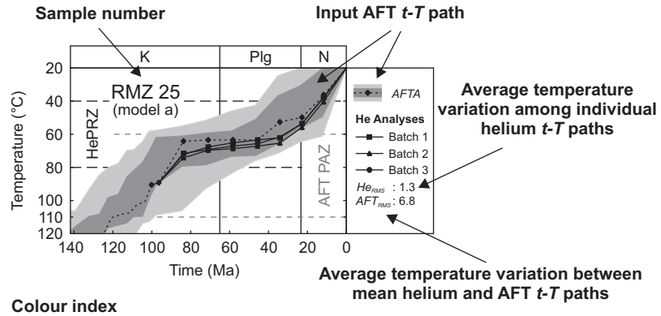

Colour index

J | K | Plg | N

Early to Middle Jurassic (c. 180-150 Ma)

J | K | Plg | N

Early to Late Cretaceous (c. 130-90 Ma)

Figure 7.4: The map is a subset of Fig. 6.1 and depicts AFT and (U-Th)/He sample locations. Large dots highlight sample locations of (U-Th)/He analyses in the southern basement. The arranged pictograms display the modelled helium *t-T* paths. Rejected ^{4}He *t-T* paths are denoted in red italics on the pictograms. The principle elements of the *t-T* path pictograms are indicated by the solitary top right example. The solid black lines represent the modelled *t-T* paths of individual analyses and the dots, triangles and circles are the employed *t-T* nodes. The dashed line and the grey envelops are the modelled *t-T* paths of corresponding AFT analyses (see Figs. 6.5, 6.10). The colour index corresponds to the colour scheme used for AFT *t-T* paths and indicates the sample's earliest cooling to below c. 110° C.

cooling step to below 60°C in the Neogene. Such more rapid cooling is not reproduced by any of the corresponding modelled helium age *t-T* paths. This could suggest that this period of rapid cooling represents a modelling artefact related to uncertainties in the AFT annealing model (e.g. Kohn et al., 2002, see section 2.2.5.2). Therefore cooling to below c. 60°C in the Palaeogene and further to below c. 40°C in the Neogene is more likely traced by the helium *t-T* paths of samples RMZ 18, RMZ 31 and RMZ 35.

Both, RMZ 31 and RMZ 35 display a difference of c. 15°-20°C in their maximum reheating temperatures between the best-fit AFT *t-T* and the helium *t-T* model paths. RMZ 31 helium *t-T* paths display good overlaps with their corresponding AFT *t-T* paths confidence envelops at time of reheating (Fig. 7.4). It is supposed that in this sample the temperature differences are related to uncertainties in both the AFT annealing and the helium diffusion models. In AFT dating these uncertainties originate from e.g. the limited knowledge of initial, non-annealed MTL (e.g. Kohn et al., 2002). In (U-Th)/He age modelling, the diffusion characteristics of Durango apatite are universally used. A possible influence of variable diffusion kinetics for different apatite species as proposed by Lippolt et al. (1994) is thereby not considered. The helium *t-T* paths of RMZ 35 do not display good overlaps with the AFT confidence envelops at times of maximum reheating (Fig. 7.3). The AFT MTL is not well reproduced by the modelled AFT data (Fig. 6.10). Besides uncertainties in the AFT annealing (section 2.2.5.2) and helium diffusion models, the rather less well reproduced AFT data are probably more crucial to account for the observed temperature difference. As the cooling step between 60°C to 40°C is best constrained by helium *t-T* paths, the temperature of c. 60°C and the timing of the reheating in the Palaeogene at c. 40-30 Ma are probably better estimated by modelled helium than by the AFT *t-T* paths of samples RMZ 31 and RMZ 35 (both models).

The *t-T* path of the single grain analysis *c* from samples RMZ 31 deviates slightly from the corresponding helium analyses *t-T* path models (Fig. 7.4) and might indicate an outlier ^{4}He analysis of RMZ 31. However, the single grain ^{4}He ages of RMZ 31 do not correlate with their grain radii (Tab. 7.2, Fig. 7.2a) but yield very consistent forward modelled *t-T* paths (Fig. 7.4). Meesters and Dunai (2002a) demonstrated that the average helium age does not strongly depend on the radius and shape of a crystal but

tends to be universal for identical surface to volume ratios (S/V). The helium age evolution can be modelled for a sphere with an identical S/V ratio. Consequently, the slightly larger length/width ratios of single grains *a, e* compared to *b, d* (Tab. 7.4) result in smaller S/V ratios and could account for higher helium retention, i.e. older ^{4}He ages. The lack of correlation between the raw ^{4}He ages and grain radii in single grain analyses of sample RMZ 31 might be simply explained by different single grain S/V ratios due to variations in grain length (Tabs. 7.2, 7.3).

Chapter 8

DISCUSSION – MESOZOIC-CENOZOIC COOLING AND DENUDATION HISTORY OF THE NORTH MOZAMBICAN BASEMENT

In this chapter, the results of the AFT and (U-Th)/He analyses are discussed together to deduce implications on the cooling and denudation history of the north Mozambican basement since middle Mesozoic times. They are presented in sections according to their sample locations and the sample groupings derived from the AFT analyses. These are the western *Axial Granulite Complex*, the *Mount Tumbine* and the *eastern* and *central southern basement* areas. The sections are ordered chronologically, starting with the oldest recorded cooling event in the region.

8.1 Axial Granulite Complex

The earliest cooling into the AFT PAZ, which is insinuated on the western rift shoulder of the Malawi rift system, (Figs. 4.6, 6.1, 8.1 and Tab. 6.1) most probably occurred prior to the Early Cretaceous. A Late Jurassic period (c. 150 Ma) of denudation due to rifting is inferred from AFT data on the western flanks of the Rukwa and Malawi rifts (Figs. 4.4, 8.2; Van der Beek et al., 1998). Nairn et al. (1991) and references therein suggest that earliest post-Karoo crustal extension occurred in southern Mozambique (SMGS in Fig. 4.4) between c. 195-140 Ma, prior to Gondwana break-up. Both areas of pre-Cretaceous rifting are superimposed onto the northerly trending MB and line up in N-S trend with the analysed samples from the western Axial Granulite Complex. This implies that the investigated region had cooled into the AFT PAZ in response to denudation during a Jurassic phase of rifting, which probably reactivated northerly trending ductile fabrics along the western MB. It further indicates that this Jurassic thermo-tectonic event is of continental scale relevance along the western edge of the MB, contrasting to the local importance ascribed by Van der Beek et al. (1998).

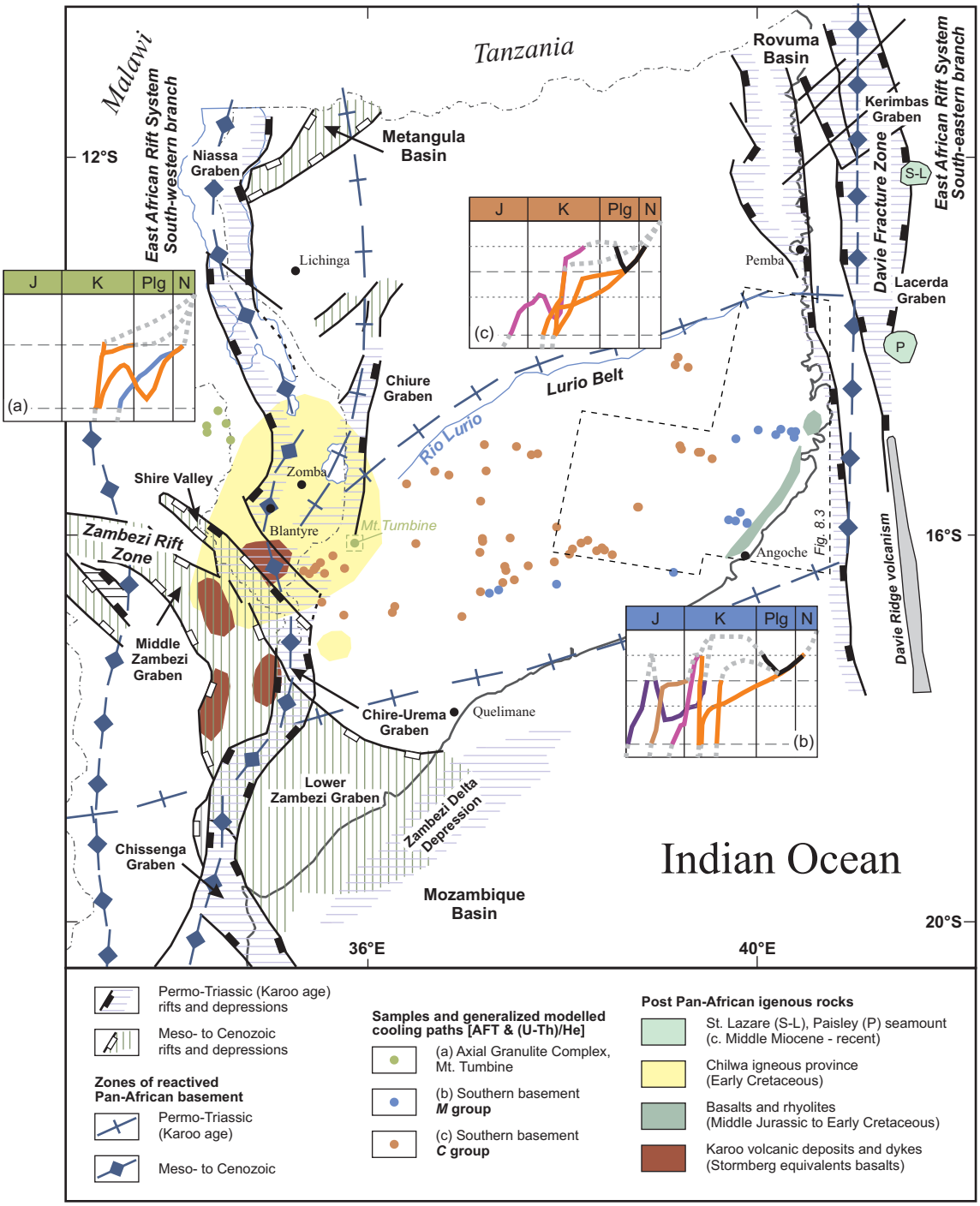

Figure 8.1: Map of post Pan-African tectonic lineaments in northern Mozambique. Modified and complied after Castaing (1991), Chorowicz (2005), Lächelt (2005), Mougneot et al. (1987), and references therein. The insets illustrate the generalized regional cooling paths for sample sets of the Axial Granulite Complex and Mt. Tumbine (*green*), the *C* group (*brown*) and the *M* group (*blue*) populations of the southern basement. The colours of the cooling paths represent similar periods of earliest cooling into the AFT PAZ (≤ 110°C): dark blue = c. 190-180 Ma, brown = c. 170 Ma, violet = c. 150 Ma, orange = c. 130-110 Ma, light blue = c. 90-80 Ma and dotted grey = unconstrained, but inferred.

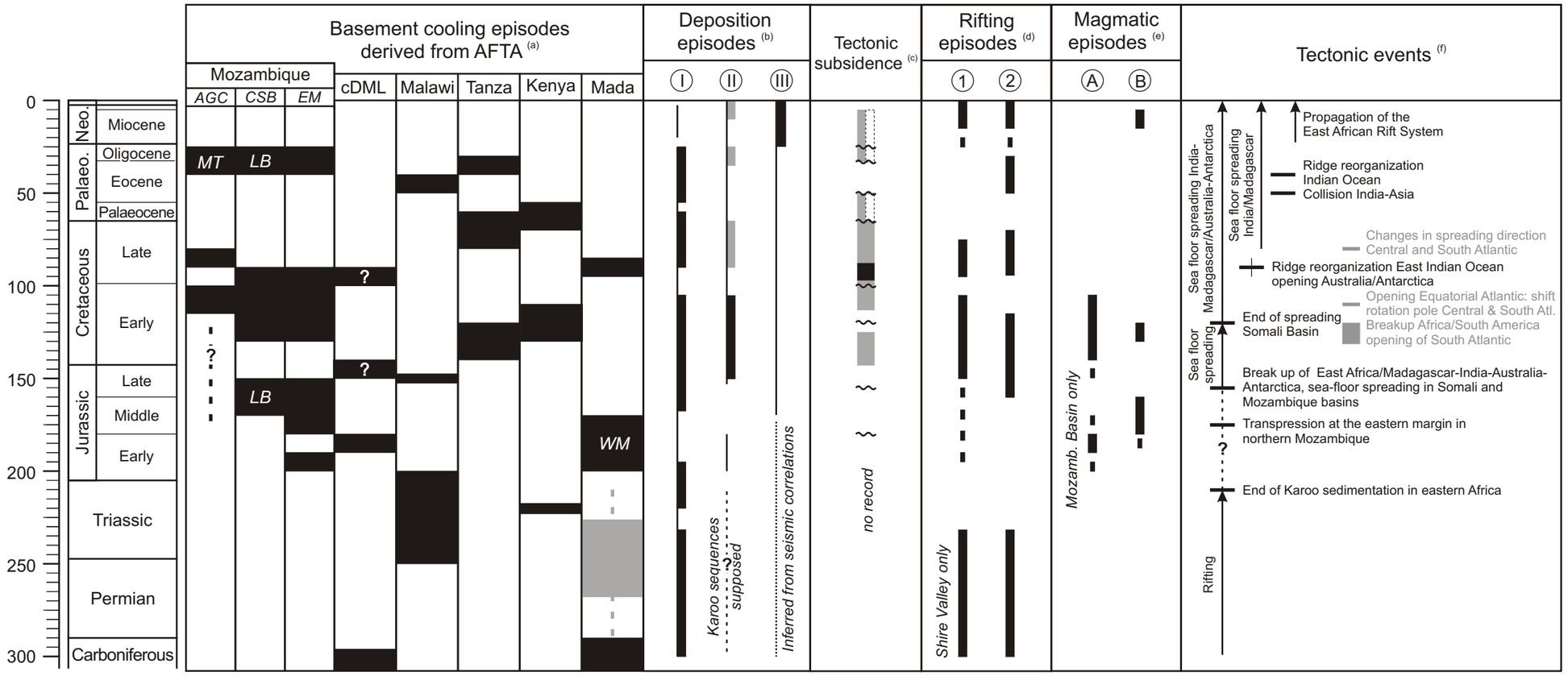

Figure 8.2: Comparison chart depicting: **(a)** episodes of more rapid basement cooling derived from AFT analyses in central East Africa and East Antarctica, **(b)** episodes of sediment deposition into East African basins, **(c)** episodes of tectonic subsidence in the Mozambique and Rovuma basins, **(d)** episodes of rifting in central East Africa, **(e)** episodes of magmatic activity in central East Africa and **(f)** regional/global tectonic events.

(a) Cooling periods derived by AFT analyses are: this study in northern Mozambique with *AGC* = Axial Granulite Complex and *MT* = Mt. Tumbine region, *CSB* = central southern basement (*C* group AFT samples, *LB* = Lurio Belt) and *EM* = eastern margin of the southern basement (*M* group AFT samples); cDML = central Dronning Maud Land from Meier et al. (2004) and Emmel et al. (2006b), ? = cooling periods uncertain; Malawi = Malawi and Rukwa rift flanks in northern Malawi and south western Tanzania from Van der Beek et al. (1998); Tanza = eastern Tanzania from Noble et al. (1997); Kenya = central Kenya Rift from Foster and Gleadow (1992, 1996) and Mada = southern and central Madagascar (WM = western margin of the basement) from Emmel et al. (2005, 2006a, b,c), grey shading and grey dashed lined indicate continuous cooling periods. **(b)** Deposition episodes: *I* = Deposition periods for the Anza Rift, the Lamu Embayment and the Tanzanian costal rift basins are adapted from Noble et al. (1997) and references therein. *II* = Deposition periods in the Mozambique Basin and *III* = Deposition periods in the southern Rovuma Basin after Salman and Abdula (1995). Thick black lines denote time periods when changes in style of sedimentation are related to rifting activities. Thick grey lines indicate increased sediment influx in the Zambesi Delta (Mozambique Basin) after Walford et al. (2005). **(c)** Episodes of tectonic basin subsidence and mean subsidence rates in the Mozambique and southern Rovuma basins after Janssen et al. (1995). Dashed outlines boxes represent slow subsidence (0-20 m/Ma) in part of the basins, grey boxes and black boxes indicate moderate (20-40 m/Ma) and fast subsidence (40-100 m/Ma), respectively. **(d)** Rifting episodes: *1* = southern Tanganyika-Rukwa-Malawi-Rift System, Shire Valley, Urema and southern Mozambique graben complied from Castaing (1991), Chorowicz (2005), Delveaux (2001), Flores (1973), Nairn et al. (1991), Salman and Abdula (1995), Van der Beek et al. (1998) and references therein. *2* = Anza Rift and costal basins of East Africa compiled from Chorowicz (2005), Mougenot et al. (1986), Noble et al. (1997) and references therein. **(e)** Time periods of magmatic activities: *A* = southern Tanganyika-Rukwa-Malawi-Rift System, the Shire Valley and Urema Graben compiled from Castaing (1991), Delvaux (2001), Eby et al. (1995), Flores (1973), Salman and Abdula (1995) and references therein. *B* = eastern margin of northern Mozambique, southern Rovuma Basin and Davie Fracture Zone compiled from Grantham et al. (2005), Jaritz et al. (1977) and Mougenot et al. (1986). **(f)** Regional tectonic events adapted and compiled after Chorowicz (2005), Grantham et al. (2005), Janssen et al. (1995) , Noble et al. (1997) and references therein.

During the Early Cretaceous a relatively swift cooling step with rates of up to 10°C/Ma is recorded at c. 115-100 Ma (Figs. 6.6, 8.1). This period coincides with the Early Cretaceous intrusive activity in the Chilwa Alkaline Province around southern Malawi between c. 138-105 Ma (Figs. 8.1, 8.2; Bloomfield, 1959; Eby et al., 1995; Woolley and Garson, 1970). Eby et al. (1995) suggested that the Chilwa magmatism was caused by crustal extension along pre-existing zones of weakness that lead to decompressional melting. The cooling of these intrusions to $T \leq 110°\text{-}60°C$ proceeded extremely rapid after their emplacement, implying that prolonged thermal influences on the surrounding basement are less likely and/or of very local importance. This argues that the Early Cretaceous cooling period is less likely related to a cooling from a thermally disturbed basement. In the Chilwa Alkaline Province, a sub-orthogonal system of NE and NW trending alkaline dykes indicates crustal extension in response to variable stress field settings. Castaing (1991) inferred a reorientation of the tensional stress field from NW-SE to NE-SW in Southeast Africa between Middle/Late Jurassic to Early/Late Cretaceous. The northerly trending Chire-Urema Graben, which crosscuts the Shire Valley, formed in the Early Cretaceous (Flores, 1973). It can be linked further southward via the Chissenga Graben into the horst and graben structures of southern Mozambique (Figs. 4.4, 4.5, 8.1, 8.2). The extension of theses graben was accompanied by the eruption of volcanics (Lupata, Movene basalts) from fissures at c. 137-115 Ma (Nairn et al., 1991; Lächelt, 2005 and references therein). Their tectonic activity presumably ended in the Late Cretaceous with the establishment of the rifting in Mascarene Basin in the Indian Ocean (Dingle and Scrutton, 1974). During the Early Cretaceous, crustal extension and related magmatism localized along the western MB is manifested from north to south in the Chilwa Alkaline Province, the Chire-Urema Graben and the southern Mozambican Graben (Figs. 4.4, 6.1, 8.1). These facts highlight a potential for brittle, extensional or transtensional reactivation of northerly trending ductile basement fabrics in the western MB. They further suggest that the middle Early Cretaceous swift cooling to $T \leq 70°\text{-}60°C$ in the Axial Granulite Complex was related to denudation due to rifting. Whether this Early Cretaceous exhumation also caused a basement exposure to sub aerial/aerial conditions is not resolved by the AFT system. However, the recorded amount of cooling suggests approximately 2.0-1.7 km of

associated denudation. Such an amount of denudation is in part supported by the fact that pre-existing NW trending faults in the Shire and Zambezi valleys (Fig. 8.1) experienced throws of up to 1 km during their intense extensional reactivation in Cretaceous times (Castaing, 1991). The rapid rift related denudation was most probably linked to the southward movement of Madagascar along the DFZ (Figs. 4.3, 4.4, 8.1, 8.4) as suggested by Castaing (1991). On the other hand, the opening of the South and Equatorial Atlantic at c. 130-110 Ma (Fig. 8.2) caused a reactivation of transcontinental shear zones and subsequently triggered reactivation of the MB fabrics and the superimposed extensional basins (Jansen et al., 1995 and references therein). The Mwembeshi Shear Zone extends across Africa from northern Namibia through Botswana, Zambia into Malawi, where it links up with the MB (Fig. 4.4, 4.5). In northern Namibia, the Early Cretaceous rifting and break-up was accompanied by the reactivation of NE-SW trending faults of the Mwembeshi Shear Zone (Clemenson et al., 1997) and fault related igneous activity at c. 137-124 Ma (Milner et al., 1995; Renne et al., 1992). Consequently, the Early Cretaceous (c. 115-100 Ma) phase of more rapid denudation and rifting in the Axial Granulite Complex was probably linked to the tectonic reactivation of the MB via the transcontinental Mwembeshi Shear Zone in response to the continental break-up and opening of the South Atlantic in West Africa (Fig. 4.4). The inferred sinistral sense of displacement along the Mwembeshi Shear Zone shear (Unternehr et al., 1988), however, conflicts with an associated right stepping extensional setting along the Axial Granulite Complex. This could in turn suggest that the Mwembeshi Shear Zone also experienced some dextral displacement in the Early Cretaceous. The Early and Late Cretaceous dextral movement and reactivation of Pan-African age shear zones and associated extensional and compressional tectonics in the perpendicular trending Cretaceous rift basins in response to the opening of the South and Central Atlantic are reported from the Central African Shear Zone and the Benue Trough (Fairhead and Brinks, 1991; Popoff, 1988). Alternatively, the Axial Granulite Complex was linked as a right stepping extensional/transtensional setting via the Tanganyika-Rukwa-Malawi System to the dextral Central African Shear Zone / Benue Trough (Figs. 4.4 and 4.5) and experienced rift related denudation due to far stresses transferred trough the Central African Shear Zone into Africa in Early Cretaceous times.

A Late Cretaceous cooling into the AFT PAZ at c. 90-80 Ma is recorded by one sample of the Axial Granulite Complex. The subsequent cooling through the AFT PAZ is rather slow and less rapid than the cooling during the Early Cretaceous denudation phase (Fig 8.1). The Late Cretaceous cooling period coincides with the highest tectonic subsidence rates (> 40 m/Ma) in the Mozambique Basin (Fig. 8.1; Jansen et al., 1995) and with the peak rifting rates (c. 50 m/Ma) in the now E-W extending South Mozambique Graben between c. 96-76 Ma (Fig. 4.4; Nairn et al., 1991). The recorded synchronous cooling is probably related to denudation by renewed crustal extension in the western Axial Granulite Complex. As cooling did not proceed too rapid this Late Cretaceous cooling phased could alternatively reflect, slow ongoing denudation due to erosion. Jansen et al. (1995), however, related the Late Cretaceous increase in subsidence in the Mozambique Basin to far field stresses of plate reorganization in the Indian Ocean, which therein led to the rapid opening of the Mascarene Basin (Fig. 8.2, section 8.3.1). Nairn et al. (1991) emphasized a broad synchronism between the peak rifting in southern Mozambique and a change in poles of rotation of South America relative to Africa (see references in Nairn et al., 1991). However, no significant tectonic changes/activities are reported along the entire Atlantic throughout the Cenomanian to Coniacian between c. 96 Ma and 85 Ma (Jansen et al. 1995). A tectonic quiescence since the break-up is also evidenced along the Mwembeshi Shear Zone in northern Namibia, where recent AFT data indicate earliest post break-up tectonic activity by transpression at around c. 70 Ma (Raab et al., 2002). This rather implies that tectonic activity and renewed extension in the western MB in northern Mozambique at c. 90-80 Ma were linked to changes in the spreading configuration in the Indian Ocean during the early Late Cretaceous.

The Late Cretaceous to Palaeogene period of slow cooling through the AFT PAZ represents c. 2.0-1.7 km of denudation. Since, subsequent cooling to surface conditions (c. 20°C) suggest additional 1.6-1.3 km of denudation. Together with Early Cretaceous denudation phase, this suggest at least locally up to 4.0-3.4 km of crust removal during Early Cretaceous to Palaeogene times and up to 5.6-4.7 km until today. An indicated pre-Cretaceous amount of denudation can not be exactly quantified but indicates, however, at least $\geq$ 3.6-3.0 km of removed crust since Mesozoic times. Since the Mesozoic, the Zambezi Delta was sourced from a palaeo-catchment area that comprised

the Middle Zambezi and the Shire fluviatile systems (Fig. 8.1; Goudi, 2004; Thomas and Shaw, 1988). According to Salman and Abdula (1995) the paleao-shelf outer edge of the Mozambique Basin gradually extended seawards by accumulation of younger sediment complexes since the Early Cretaceous. The presented AFT data evidence, that the Axial Granulite Complex provided material that was transported to and deposited in the Mozambique Basin since the Early Cretaceous. The Zambezi Delta experienced an elevated sediment influx in the Late Cretaceous between c. 90-65 Ma (Walford et al., 2005), synchronous to the second Cretaceous denudation period in the western Axial Granulite Complex at c. 90-80 Ma (Fig. 8.2). It further substantiates a material flux from the western Axial Granulite Complex into the Zambezi Delta of the Mozambique Basin in the Cretaceous.

The AFT modelling results of the western Axial Granulite Complex indicate that cooling to c. 60°C took places at latest in the Neogene (Fig. 8.1). This in turn could imply a subsequent more rapid cooling to subaerial conditions. As the development of the south-western Malawi Rift segment started in the Late Miocene (Chorowicz, 2005), this indirectly insinuated cooling in the recent past could be either related to renewed rifting in the Axial Granulite Complex in the Neogene or just a modelling artefact (see section 2.2.5.2)

8.2 Mount Tumbine

Mount Tumbine is an inselberg, made up of a circular syenite intrusion and belongs to a set of alkaline intrusions and dykes, the Chilwa Alkaline Province (Figs. 6.7, 8.1). The intrusion ages within this province range between c. 137-105 Ma (Bloomfield, 1968; Eby et al., 1995; Lächelt, 2004; Woolley and Garson, 1970).

A rapid cooling period into the AFT PAZ and presumably further below c. 80°-60°C occurred in the Early Cretaceous at c. 115-110 Ma. It is synchronous to the rapid cooling into the AFT PAZ of related alkaline intrusions, exposed near the city Zomba (Figs. 8.1, 8.2) to the north of Mt. Tumbine (Eby et al., 1995). This probably suggests that Mt. Tumbine cooled alike these plutons very rapidly to shallow ambient temperatures after its intrusion in the Early Creatceous at c. ≤ 115 Ma. Eby et al. (1995) related the rapid cooling of these alkaline granitoids to their emplacement into a shallow

intrusion level (c. 2-3 km depths) and to subsequent rapid unroofing due to local doming above the intrusions. Updomed and indurated Karoo sediments are also reported proximate to Early Cretaceous alkaline intrusions in the Shire Valley (Fig. 8.2) to the south of Mt. Tumbine (Cooper and Bloomfield, 1961). Consequently, the more rapid cooling of Mt. Tumbine is most probably as well related to an emplacement into a shallow crustal level and to subsequent rapid denudation (unroofing) in the Early Cretaceous. If the entire amount of rapid cooling is attributed to post-intrusive denudation, it equals to c. 2.0-1.7 km of crust removal during the Early Cretaceous. Such amount of denudation is similar to the synchronous rift related denudation in the western Axial Granulite Complex (section 8.1) and could suggest a primarily denudation (rift related) controlled cooling of Mt. Tumbine in the Early Cretaceous. This rapid Early Cretaceous cooling of the Mt. Tumbine syenite intrusion, however, further manifests a rifting and magmatic period in the western part of the north Mozambican MB during the Early Cretaceous at c. 130-100 Ma. The modelling results suggest that Mt. Tumbine cooled trough the 60°C isotherm in Late Cretaceous to Palaeogene times (Fig. 6.7). This subsequent exposure to sub aerial/aerial conditions is likely related to ongoing denudation and implies a maximum amount of 3.6-3.0 km of denudation since the Early Cretaceous.

A post-Cretaceous cooling step due to a reheating to temperatures up to 80°-90°C is inferred from the AFT modelling in Palaeogene times (c. 45-30 Ma). Field observations along the Mt. Tumbine sampling profile (Fig. 6.7) revealed cm-scale joints healed with quartz, feldspar and sulphides. These veins occur rather locally and are present within the gneiss and syenite host rock. Their formation thus clearly post-dates the timing of the syenite intrusion in the Early Cretaceous. It suggests, that the reheating is related to heat advection by fluids after the main intrusive activity. Because the timing of reheating broadly corresponds to the earliest rifting and igneous activity of the East African Rift System in the Afar region at c. 30 Ma (Fig. 4.6; Chorowicz, 2005 and references therein), the reheating might represent an early foreshadowed thermo-tectonic signal of the shortly after evolving south-eastern branch of the East African Rift System (Figs. 4.6 and 8.1).

8.3 Southern basement

8.3.1 The eastern margin

On the base of the interpretation from thermal history modelling of the AFT and (U-Th)/He data, a tectonic segmentation of the eastern margin of the southern basement is deduced (sections 6.3.2.2, 7.5.3). Satellite image analyses of the eastern margin reveal a prominent NNW-SSE trend in the photo-lineation pattern between c. 14.5° and 15.5° latitude (Riepshoff, 2005). These lineations crosscut the easterly trending ductile basement fabrics at high angles (Fig. 8.3) and display an obvious parallelism to the northerly trending DFZ, located offshore to the present continental margin (Figs. 8.1, 8.3). According to Riepshoff (2005) these photo-lineations represent brittle tectonic structures (faults) that resulted from associated tectonic activities of the DFZ in the Phanerozoic. The results of the AFT and apatite (U-Th)/He thermochronology and the satellite image analyses appear to be fairly complementary, inferring that the southern basement along the eastern continental margin exposes crustal segments that are separated by northerly trending brittle faults. These enclosed blocks were formerly located at different crustal levels and experienced exhumation and differential cooling during different stages of tectonic activity along the DFZ. The northerly trend of the brittle fault pattern coincides with northerly ductile basement trends of the MB, observed to the north of the Lurio Belt (Fig. 6.1). The matching northerly orientated trends of the ductile fabrics, brittle faults and DFZ imply that the formation of the DFZ reactivated pre-existing ductile basement fabrics to the north of the Lurio Belt.

Earliest rapid cooling through the AFT PAZ is recorded at c. 190-180 Ma and was followed by a second, slow cooling step starting in the Middle Jurassic due to reheating up to 70°-90°C at c. 180-160 Ma (Figs. 6.6, 8.1). The timings of the first cooling step and the reheating event correspond to the oldest crystallization K-Ar and Sm-Nd model ages (Jaritz et al, 1977; Grantham et al., 2005) of c. 180-160 Ma from primarily basaltic rocks exposed along the eastern margin (Fig. 8.3). A relation of these volcanic rocks to the Bouvet mantle plume derived Large Igneous Province (Fig. 4.2) is uncertain (Duncan et al., 1997; Grantham et al., 2005). Because of underlying terrestrial sedimentary remnants Jaritz et al. (1977) inferred surficial emplacement conditions.

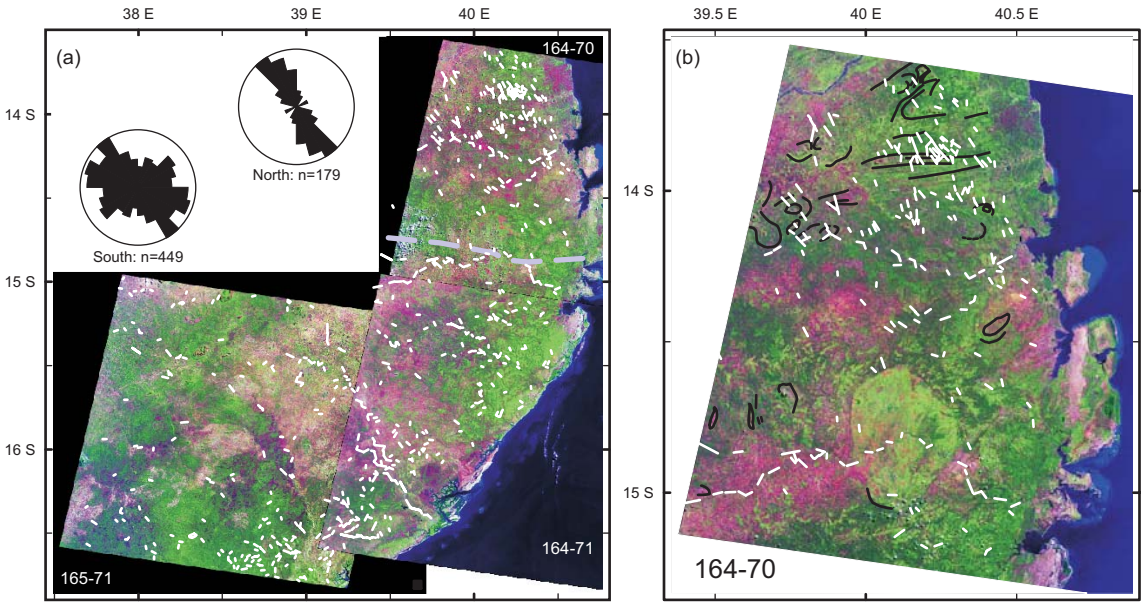

Figure 8.3: Image **(a)** displays the distribution of photo-lineations (white lines) superimposed on the interpreted satellite image mosaic of the eastern continental margin. The mosaic location at the eastern margin is depicted in Fig. 8.1 and the white numbers are the "*paths-row*" codes of individual Landsat TM 5 scenes. A dashed light blue line approximates the boundary between a northern and a southern region of photo-lineation trend patterns. Their corresponding rose diagrams are given in the inset. Image **(b)** displays the relationship between ductile basement fabrics (black lines) and photo-lineations (white lines) in the northern region. Images are modified after Riepshoff (2005).

This in turn suggests that the preceding cooling (at least for parts of the basement) took place from ≥ 110°C to aerial conditions at c. 190-180 Ma. Geiger et al. (2004) argued that the Gondwana break-up in the Morondava Basin of southern Madagascar (Figs. 4.1-4.4, 8.4) was preceded by a short-lived rifting period, the "Andafia rift", during the Early to Middle Jurassic at around 190-180 Ma (Toarcian-Aalenian). A series of AFT studies indicate that cooling by denudation along the western margin of Madagascar, parallel to the DFZ (Emmel et al., 2004; Seward et al., 2004) as well as exhumation and reworking of Permo-Triassic sedimentary strata within the Morondava Basin (Emmel et al., 2005) in the Early to Middle Jurassic are linked to the synchronous rifting event in the Morondava Basin (Figs. 4.3, 8.4). To the south of northern Mozambique, at the opposite site of the Mozambique Basin, an Early Jurassic cooling period is related to erosion along an evolving rift shoulder in central Dronning Maud Land, East Antarctica (Figs. 4.1-4.4, 8.2, 8.4; Emmel et al., 2006d; Meier et al., 2004). It indicates fairly synchronous rifting in the Mozambique and Somali basins during Early to Middle

Jurassic times, and prior to the Gondwana break-up. The orientation of the associated rift axis between northern Mozambique and central Dronning Maud Land is unknown. However, based on the easterly trending Permo-Triassic rift setting (chapter 3; Fig. 3.8) and the easterly orientated Mesozoic seafloor magnetic anomalies (Fig. 4.4; Coffin and Rabinowitz, 1992) an easterly rift axis trend, broadly parallel to the present southern passive margin of north Mozambique, is inferred. These Early to Middle Jurassic rifting phases in the future Somali and Mozambique basins could suggest a synchronous dextral movement and tectonic activity along the DFZ. The late Early Jurassic cooling period from ≥ 110°C to 20°C at around 190-180 Ma most probably reflects denudation of approximately 3.6-3.0 km due to tectonic activity along the DFZ and sustains synchronous transform faulting along the DFZ. Grantham et al. (2005) suggested a transpressive tectonic setting based on the chemical indications from the exposed volcanic rocks. In the absence of kinematic constraints, transtension and/or pure orthogonal crustal thinning might also account for denudation and cooling around 190-180 Ma. A Jurassic rifting period (c. 195-140 Ma) prior to break-up is also reported from southern Mozambique (Nairn et al., 1991 and references therein). There E-W to NW-SE tension resulted in N-S trending faults and produced a series of large horsts and grabens (Fig. 4.4; Castaing, 1991; Dingle and Scrutton, 1974; Nairn et al., 1991). Based on seismic interpretations an initial period (Jurassic-?Early Cretaceous) of wrench faulting is related to northerly trending strike slip movement during the early separation of East and West Gondwana (Dingle and Scrutton, 1974; Nairn et al., 1991). The late Early Jurassic period of transpressional and/or transtensional tectonics along the eastern margin of northern Mozambique appears to be of a similar nature as the synchronously active setting in southern Mozambique. These consistencies might indicate that the DFZ and the fault system of southern Mozambique were already active as associated systems of N-S trending transform structures during an Early Jurassic rifting event at c. 190-180 Ma (Figs. 4.3, 4.4, 8.4).

Subsequently to the Early Jurassic cooling a reheating up to 70°-90°C is inferred at c. 180-160 Ma (Figs. 6.6, 8.1, 8.2) and most probably related to the synchronous volcanic activity in the Middle Jurassic. Conclusively, an increased heat flow and/or re-

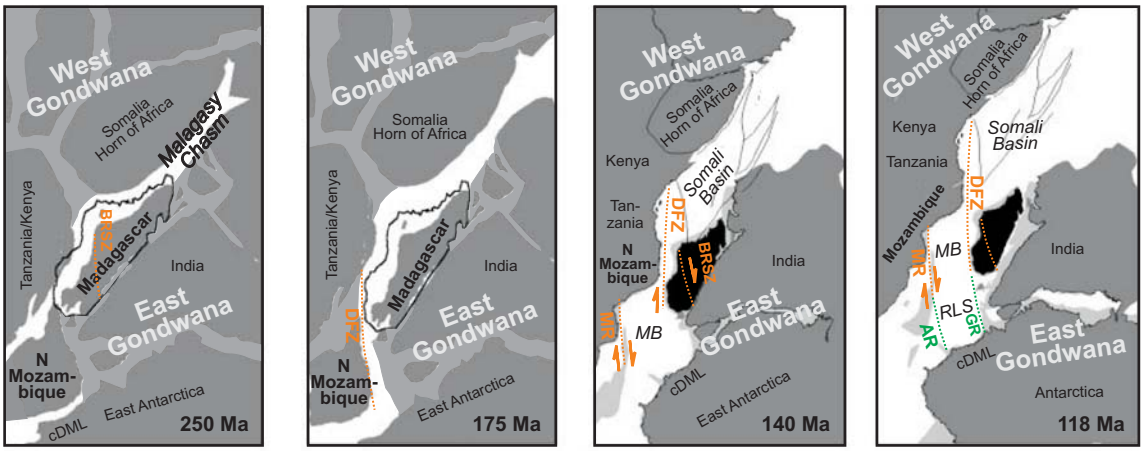

Figure 8.4: Palaeo-geographic reconstructions of Gondwana depicting the palaeo-positions of Madagascar, northern (N) Mozambique and central Dronning Maud Land (cDML) at the Permian/Triassic boundary (250 Ma), in the Middle Jurassic (175 Ma), Early Cretaceous (140 Ma) and late Early Cretaceous (118 Ma). White and medium grey zones in 250 Ma and 175 Ma timeframes represent zones of significant strain and limited intracontinental rifting during the late Palaeozoic to Early Mesozoic. Light grey zones in 140 Ma and 118 Ma timeframes represent shallow continental margins and oceanic plateaus. Orange and green lines represent transform faults. The maps are modified and compiled from de Wit (2003) and references therein and Roeser et al. (1996). Abbreviations: *Oceanic basins:* MB = Mozambique Basin, RLS = Riiser-Larsen Sea. *Transform and shear zones:* AR = Astrid Ridge, BRSZ = Bongolava-Ranotsara Shear Zone, DFZ = Davie Fracture Zone, GR = Gunnerus Ridge, MR = Mozambique Ridge.

burial due to volcanic rock emplacement are accounted for the observed reheating. Jaritz et al. (1977) estimated the present day maximum thickness of the volcanic rocks to be of c. 2.5-2.0 km. As these Jurassic volcanic rocks occur only as small remnants today, these estimates represent minimum values of their initial thickness. No information is available on the synchronously prevailing palaeo-geothermal gradient. Adopting an average value of 30°C/Ma suggests that reheating temperatures of 60°C to 75°C can be achieved by reburial from volcanic rocks of 2.5-2.0 km thickness alone. These values are in good agreement with reheating palaeo-temperatures of c. 70°-90°C derived from AFT modelling. Higher reheating temperatures up to 90°C are easily explained by a) an initial volcanic rock pile thickness of > 2.5 km and/or b) a palaeo-geothermal gradient of > 30°C/Ma, elevated by an increased palaeo-heat flow due to volcanism. Conclusively, reburial due to emplacement of volcanic rocks with a thickness of ≥ 2.0-2.5 km is accounted for as the prominent trigger of basement reheating (c. 70°-90°C) at the eastern margin in the Middle Jurassic at c. 180-160 Ma.

Broadly synchronous, during the Middle to Late Jurassic (c. 170-150 Ma) phases of more rapid cooling into the AFT PAZ are also recorded along the eastern margin (Figs. 6.6, 7.4, 8.1). They coincide with the timing of the incipient Gondwana break-up between c. 180-155 Ma (Fig. 8.2). Based on tectono-sedimentary evidences in the southern Somali Basin, Geiger et al. (2004) inferred a Middle Jurassic break-up (Bajocian unconformity) at c. 180 Ma. Whereas the oldest directly dated magnetic anomalies in the Somali and Mozambique basins indicate a break-up at c. 155-154 Ma (Coffin and Rabinowitz, 1992). Müller et al. (1997) inferred a similar time interval (c. 180-154 Ma) for oceanic crust formation between the continental shelf regions and the M25 anomaly in the Somali and Mozambique oceanic basins (Fig. 4.3). These data argue for tectonic activity along the DFZ as a result of the incipient rift to drift transition and ongoing southward movement of East Gondwana relative to West Gondwana in Middle to Late Jurassic times. Therefore the Middle to Late Jurassic (c. 170-150 Ma) cooling phases could reflect differential exhumation and denudation along the eastern margin in response to transpression and/or transtension along the DFZ in northern Mozambique. As the timing of this cooling period (c. 170-150 Ma) coincides with the period of basalt extrusion (c. 180-160 Ma), the observed cooling might not solely result from denudation but could also reflect the vanishing of an elevated palaeo-geothermal gradient, raised by an increased heat flow related to volcanism. An amount of denudation associated with this cooling episode is therefore not reliable to quantify. In combination with the denudation estimates associated with the Early Jurassic cooling phase, these AFT data suggest, that at least locally $\geq$ 3.6-3.0 km of material was removed between the Early Jurassic to Late Jurassic.

During the Early to Late Cretaceous (c. 130-90 Ma), a rapid cooling phase through the AFT PAZ to $\leq$ 60°C to 40°C occurred along the eastern margin (Figs. 6.6, 8.1, 8.2). Within that time, Madagascar stopped its southward drift (Fig. 8.4) due to cessation of sea floor spreading in the Somali Basin (magnetic anomaly M0: c. 118 Ma; Coffin and Rabinowitz, 1992). Therefore, the cooling periods between c. 130-110 Ma are likely associated with denudation due to transpression and/or transtension during the ceasing tectonic activity along the DFZ. In the Early Cretaceous, the opening of the South and Equatorial Atlantic (c. 130-110 Ma) (Figs. 4.5, 8.2) resulted in a dextral reactivation of

the NE to E trending Pan-African age shear zones fabrics along the Central African Shear Zone (Daly et al., 1989, Fairhead, 1988), and extension in the perpendicular trending rift basins superimposed on the N-S trending MB in East Africa (Jansen et al., 1995 and references therein). Jansen et al. (1995) related the increased tectonic subsidence in the Lamu Embayment (SE Kenya) and the Mozambique Basin (Figs. 4.4, 4.5, 8.2) to basement reactivation in response to the opening of the South Atlantic. Synchronously (c. 140-110 Ma), a more rapid denudation is indicated by AFT data in southern Kenya and along the costal margin of Tanzania (Fig. 4.3, 4.4, 4.5 8.2; Foster and Gleadow, 1996; Noble et al., 1997). In both areas this rapid denudation is related to block faulting and fault reactivation in response to far stresses of the opening of the South Atlantic. The eastern margin of northern Mozambique directly lines up with the Kenya rift valley and the coastal rift basins of Tanzania along the MB (Figs. 4.4, 4.5). This Early Cretaceous (c. 130-110) phase of more rapid cooling is therefore also related to denudation which resulted from basement reactivation (presumably northerly trending, pre-existing brittle and ductile fabrics) in response to far stresses of the South Atlantic opening. Thereby, the eastern margin (cf. the DFZ) formed via the costal Tanzania, Kenya and the Sudan rifts a regional right stepping extensional and/or transtensional setting to the dextrally displacing Central African Shear Zone.

The Early Cretaceous denudation period appears to be in good agreement with Early Cretaceous (Aptian-Lower Albian) sedimentary records from the southern Rovuma Basin. These records indicate an Early Cretaceous uplift and reworking of Jurassic strata due to tectonism and sea-level fluctuations (Hancox et al., 2002). Hancox et al. (2002) inferred sediment sources to the south and southwest of the southern Rovuma Basin. The presented AFT and (U-Th)/He data hereby evidence that the north Mozambican basement has been a region of denudation in the Early Cretaceous.

During the late Early Cretaceous to Late Cretaceous (c. 96-90 Ma), a reorganization of the spreading direction took place in the Indian Ocean (Fig. 8.2). It led to the rapid opening of the Mascarene Basin between the India/Seychelles/Madagascar block and Australia/Antarctica (Powell et al., 1988). Jansen et al. (1995) and references therein have argued that because the India/Seychelles/Madagascar block still formed an entity with the African Plate, the rapid rifting in the Mascarene Basin caused an accelerated

tectonic subsidence in the nearby coastal basins of Mozambique (Fig. 8.2). Consequently, rapid cooling along eastern margin in early Late Cretaceous times (c. 90 Ma) was possibly related to denudation by renewed crustal extension in reponse to far stress influences of the rapidly spreading Mascarene Basin. On the other hand, a base level lowering due to increased tectonic subsidence in the southern Rovuma Basin could have also triggered rapid erosion and cooling on the adjacent basement (Fig. 8.1). Compressional structures (flower structure), in the DFZ are associated with transpression along the DFZ due to a kinematic change related to the rifting in the Mascarene Basin (Malod et al., 1991). Hence, denudation due to transpression might too account for the more rapid denudation and cooling in the early Late Cretaceous.

However, this Early to Late Cretaceous period of cooling to sub aerial conditions (AFT and He model results: $T \leq 60°\text{-}40°C$) represents approximately 2.8-2.4 km of denudation along the eastern margin and potentially comprises up to 2.5-2.0 km of Jurassic basalts. Based on quantitative thermal models it is argued that an elevated transient geothermal gradient likely associated with the Early/Middle Jurassic magmatism in southern Africa would have been completely dissipated by Cretaceous times (Brown et al., 1994). Therefore the denudation estimates for the Early Cretaceous cooling period are less likely to be altered by an elevated geothermal gradient, related to the Early/Middle Jurassic magmatism along the eastern margin in northern Mozambique. Thermal effects of the Middle Jurassic to Early Cretaceous rifting along the northern Mozambican (south eastern basement) sector of the sheared margin of East Africa are unlikely to have caused elevated geothermal gradients within the upper 5 km of the crust for locations (all samples investigated; Figs. 6.1, 8.1) greater than c. 25 km inland of the continent-ocean boundary (Gadd and Scrutton, 1997).

The youngest, post Cretaceous slow cooling step at the eastern margin is related to a reheating to c. 60°C in Palaeogene times at c. 40-20 Ma (Figs. 6.6, 8.1, 8.2). Along the eastern margin Cenozoic marine sediments occur mainly in the Rovuma Basin and generally increase in thickness towards the basin's axis in the east (Salman and Abdula, 1995; von Daniels et al., 1977). This suggests that sedimentary burial is rather unlikely to explain the inferred basement reheating on the margin in the Palaeogene. Supposedly, the reheating reflects an increased paleao-geothermal gradient due to an increased heat

flow in Palaeogene times. As the eastern margin appears to be distinctly ruptured (e.g. Riepshoff, 2005; Fig. 8.3) advection of heat by fluid flow could account the observed reheating. The timing of this reheating event coincides with an Oligocene-Miocene unconformity observed in the sedimentary strata of Rovuma Basin. Jansen et al. (1995) and references therein "correlated" the unconformity with the development of the East African Rift System and/or with the India-Asia collision. Block faulting and extension along the south western branch of the East African Rift System, offshore to the eastern continental margin is evidenced since the Middle Miocene (Mougenot et al., 1986) and was accompanied by igneous activity (Figs. 4.6, 8.1). A synchronous reheating event at Mt. Tumbine is, alike the reheating at the eastern margin, localized within a broadly N-S trending zone of repeated Mesozoic tectonism, superimposed onto the MB. This consistency could point to a widespread Cenozoic reheating event confined to major zones of crustal weakness along the MB in northern Mozambique.

Since post Early to early Late Cretaceous times, final cooling from c. 60°-40°C to surface temperatures along the entire eastern margin of the southern basement is also partly related to denudation. This amount is not exactly to quantify as cooling caused by denudation is likely obscured by cooling from the Palaeogene reheating phase. However, it certainly did not exceed 0.8-0.7 km of denudation.

In total ≥ 6.4-5.4 km of material was removed from the eastern continental margin during the Jurassic (190-150 Ma) and Early to early Late Cretaceous (130-90 Ma) periods of denudation. If a potential post Cretaceous crust removal is considered then the total denudation amounts to approximately 7-6 km until today.

8.3.2 The central southern basement and the Lurio Belt

The earliest period of more rapid cooling into the AFT PAZ (≥ c. 110°C) is recorded by a sample from the Lurio Belt in the Middle to Late Jurassic at c. 170-150 Ma (Figs. 6.10, 8.3). This period coincides with the timing of the incipient break-up of Gondwana and the onset of seafloor spreading in the Somali and Mozambique basins (e.g. Müller et al., 1997). The Lurio Belt constitutes a prominent zone of crustal weakness that bounds the southern basement to the north. Its ENE to NE trend broadly parallels the axis of the seafloor spreading in the Mozambique Basin (Figs. 4.4, 6.1, 8.3). This could

suggest that the ductile fabrics of the Lurio Belt, were orientated in suited trend to have been affected by tectonism in response to the incipient seafloor spreading in the Mozambique Basin. Presumably, the observed period of more rapid cooling in the Lurio Belt represented exhumation due to reactivation of the ductile basement fabrics during the Jurassic. As the drift vector in the Mozambique Basin was orientated c. N-S (Fig. 4.3; Montenat et al., 1996), cooling could have been either related to c. N-S orientated crustal extension or to c. N-S orientated compressive uplift and subsequent denudation. Synchronously, the eastern margin of the southern basement experienced periods of denudation due to transpression and/or transtension along the DFZ in response to the incipient break-up and southward drift of East Gondwana relative to Africa (Fig. 8.1, section 8.3.1). A Jurassic period of rift related denudation is also supposed for the western edge of the MB along the Axial Granulite Complex (Fig. 8.1, section 8.1). These data could indicate that in northern Mozambique prominently N-S and subordinate ENE to NE trending ductile fabrics of the southern basement were reactivated by brittle deformation during the incipient Gondwana break-up in Middle to Late Jurassic times. While northerly trending ductile fabrics were primarily reactivated by transpression and/or transtension, ENE to NE aligned ductile trend were reactivated by c. N-S orientated extension or compression. Rapid cooling into the AFT PAZ up to c. 80°C due to denudation represents approximately 1.2-1.0 km of crust removal in Middle Jurassic times.

In the Early Cretaceous (c. 130-100 Ma), a rapid cooling through the AFT PAZ to $T \leq 70°\text{-}60°C$ is recorded from samples in the eastern Axial Granulite Complex (e.g. samples GM 139, LH 20; Figs. 6.10, 8.1). Their cooling through the AFT PAZ and the timing of cooling strongly resemble the Early Cretaceous cooling pattern of samples from the western Axial Granulite Complex (section 8.1) and the very proximate samples of Mt. Tumbine (section 8.2). These similarities suggest that the region at the western part of the southern basement cooled more rapidly in response to rapid denudation and crustal extension along the northerly trending Axial Granulite Complex and due to the reactivation of Karoo age NW-SE trending normal faults of the proximate Shire Valley (Figs. 6.1, 6.10, 8.1; Castaing, 1991) in the Early Cretaceous at c. 130-110 Ma. The synchronous amount of denudation is estimated to be of 2.0-1.7 km. As outlined in

section 8.1, this denudation was caused by rifting linked to the tectonic reactivation of the western MB either via the transcontinental Mwembeshi Shear Zone or the Central African Shear Zone in response to the continental break-up and opening of the South Atlantic in West Africa (Figs. 4.4, 8.2).

The Lurio Belt experienced a more rapid cooling step to sub aerial/aerial conditions, $T \leq 70°$-$40°C$, due to a reheating to $T \leq 90°C$ (samples RMZ 35, WB 295; Tab. 6.3; Figs. 6.10, 8.1) in the Early Cretaceous at c. 130-100 Ma. However, the timing and the intensity of this reheating event is not very tightly constrained (see sections 6.3.2.1 and 7.4). Both, the reheating and the subsequent rapid cooling are synchronous to

a) a period of crustal extension and magmatism in the Axial Granulite Complex (cf. southern Tanganyika-Rukwa-Malawi System, Figs. 4.4, 8.1) adjacent to the west (see section 8.1, 8.2 and 8.3.1) and
b) a period of denudation by block faulting due to northerly trending basement fabric reactivation along the eastern margin (section 8.3.1).

In both regions the tectonic reactivation along the northerly trending MB was triggered by far stress influences from the opening of the South Atlantic transfered via the reactivation of NE to E trending transcontinental shear zones (Central African Shear Zone, Mwembeshi Shear Zone in Fig. 4.5). The Lurio Belt links up to both regions of tectonic activity in the east and west (Fig. 4.4) and broadly parallels in its trend these transcontinental shear zones. It therefore supposed that the Lurio Belt was synchronously reactivated as it is linked via the MB to these transcontinental shear zones. A reactivation of the NE trending Limpopo Belt in south eastern Africa (Fig. 4.4) is also indicated by AFT data in the Early Cretaceous (pers. com. D.X. Belton). The reactivation of the Lurio Belt appears to be consistent with a widespread reactivation of NE to E trending Late Neoproterozoic/Early Palaeozoic shear zones in Eastern Africa during the Early Cretaceous. The inferred reheating ($T \leq 90°C$) could reflect advection of heat due to fluid flow in the Lurio Belt. In the Early Cretaceous, a NE-SW orientated regional tensional stress field prevailed in south-east Africa (Castaing, 1991). The subsequent cooling to aerial/subaerial conditions could therefore reflect the vanishing of an increased geothermal gradient and denudation due to transtensive and/or transpressive brittle reactivation of the ductile high strain fabrics of the Lurio Belt.

Certainly, the maximum amount of associated denudation was less 1.6-1.3 km (Figs. 6.10, 8.1.) and hence indicates a maximum of denudation of 2.8-2.3 km during the Middle to Late Mesozoic along the Lurio Belt.

The majority of the samples from the central southern basement display a very homogenous AFT data and cooling pattern (Fig. 6.2, 6.10, 8.1). They cooled more rapidly into the AFT PAZ up to ≤ 90°-70°C in the Early Cretaceous at c. 130-90 Ma. Subsequently, these samples cooled very slowly and protractedly through the AFT PAZ and to aerial conditions ($T \leq 40$°C) in the Neogene. The pronounced spatially homogenous cooling pattern could suggest that a large part of the central southern basement behaved as a uniform crustal segment during its post Jurassic thermo-tectonic evolution. The timing of cooling of the "uniform crustal segment" into the AFT PAZ coincides with episodes of more rapid cooling through the AFT PAZ ($T \leq 60$°C) in the adjacent regions of the eastern continental margin (cf. DFZ), the Axial Granulite Complex (cf. southern Tanganyika-Rukwa-Malawi System) and the Lurio Belt (Figs. 4.4, 6.1, 8.1). These regions were pronounced loci of repeated basement fabric reactivation (northerly trends of the MB) due to denudation and exhumation related to far field stress activities since the Jurassic (sections 8.1, 8.3.1). The uniformly cooled central southern basement appears to be "caught" between these regions (Figs. 6.6, 6.10, 8.1). Repeated differential denudation and exhumation presumably resulted in a lower, isostatically compensated local base level ("the lowest topographic point in a particular area" [Burbank and Anderson, 2001: page 160]) within these regions than in the central southern basement segment fringed by them. A resultant local base level gradient between the central southern basement and these adjacent N-S trending zones could have triggered gradient compensating denudation within the central southern basement. This denudation, probably erosion, could have caused the observed more rapid and spatially homogenous cooling into the AFT PAZ during the Early to early Late Cretaceous. Approximately 1.3-0.8 km of crustal material was removed during this denudation phase. No denudation induced more rapid cooling is recorded in the Axial Granulite Complex and along the eastern continental margin at times younger than the Late Cretaceous; $t \leq 90$ Ma (Figs. 4.4, 6.6, 6.10, 8.1). The early Late Cretaceous also marks the onset of very slow and protracted cooling through the AFT PAZ with the

central southern basement (Fig. 8.1). Such a significant reduction in the cooling could reflect a decrease of denudation, in correspondence to an attainment of a fairly similar, denudation compensated base level throughout the entire southern basement (to the south of the Lurio Belt) from the Axial Granulite Complex in the west to the eastern continental margin. It suggests, that the spatially homogenous cooling pattern of a large part of the central southern basement also resulted from global plate reorganization processes during the Mesozoic. In contrast to the Axial Granulite Complex (section 8.1) and the eastern continental margin (section 8.3.1), the basement cooling was related to exhumation that was indirectly linked to the reactivation of pre-existing ductile basement fabrics. However, the ductile basement fabrics in the central southern basement trend sub parallel to Lurio Belt (Fig. 6.1; Pinna, 1995). The Lurio Belt most likely experienced some denudation in the Early Cretaceous. Therefore it is also possible that denudation due to the reactivation of broadly easterly trending fabrics caused cooling in the southern central basement during the Early to onset of Late Cretaceous. Though this alternative cannot be strictly discarded it is regarded as less likely. It would infer a very homogenous fabric reactivation and exhumation in order to account for the observed AFT data (Tabs. 6.3 and Figs. 6.2, 6.10). Generally, the AFT and helium model results (Figs. 6.10, 7.4, 8.1) suggest, that the central southern basement cooled very slowly and protractedly to aerial conditions ($T \leq 40$°C) in Late Palaeogene to Early Neogene times (Fig.8.1), most probably to continuing slow erosional denudation. Since the Early Cretaceous, the central southern basement experienced approximately 3.6-3.0 km of crustal removal by denudation.

The youngest post Cretaceous cooling step, related to reheating up to c. 60°C occurred in the Lurio Belt in Palaeogene times at c. 40-20 Ma (Figs. 6.10, 8.1). Synchronous sediment deposition on the basement is not reported (Pinna, 1987 and Lächelt, 2005). As the Lurio Belt constitutes a crustal zone of weakness, heat advection by fluid flow appears to be the most reasonable explanation for the inferred reheating. This reheating temporally coincides with reheating events at Mt. Tumbine (section 8.2) and along the eastern continental margin (section 8.3.1). Similarly to them, a relation to the incipient formation of the East African Rift System is supposed for the Cenozoic reheating event along the Lurio Belt (section 8.2, 8.3.1). It, however, further manifests a

widespread Cenozoic reheating event, localized along major zones of crustal weakness in northern Mozambique.

8.4 Inferences on the Mesozoic Gondwana break-up

Within the north Mozambican basement the overwhelming majority of thermo-tectonic histories, recorded by the AFT and the apatite (U-Th)/ He systems are related to the post break-up evolution of the African continental crust (Figs. 6.6, 6.7, 6.10, 8.1). Solely along the sheared eastern continental margin, thermo-tectonic imprints of Early to Middle Jurassic age are related to the transform fault activities of the DFZ in response to rifting and subsequent drifting in the Early to Middle Jurassic (Fig. 6.6, 8.1). However, these data only provide an indirect thermo-tectonic record of Gondwana's rift and break-up history in the north Mozambican sector. They neither permit direct inferences on the Jurassic rift geometry nor do they permit the quantification of rift related denudation. The post Jurassic thermo-tectonic basement evolution, recorded by the AFT and apatite (U-Th)/He data likely obscured any potential previous thermo-tectonic patterns related to the Gondwana break-up in the Jurassic. It cannot be concluded if the supercontinent's break-up either left a thermo-tectonic imprint that has been obscured by younger thermo-tectonic events or if it did not leave an imprint at all on the north Mozambican basement. Rifting in the north Mozambican sector could have been a more a less slow, continuous process of crustal attenuation since the earliest rift undertaking in the Permian (cf. chapter 3). The rift axis and the loci of continuous crustal extension were likely located to the south of the present continental margin and therefore may have not left a thermo-tectonic record on the basement. In addition, a new rift axis might have formed at a rather distant location to the south of northern Mozambique and rifting did not affect the basement at all in the Early Jurassic. Such a rift setting would be fairly similar to a proposed "Andafia rift" in the Somali Basin in the Early Jurassic (Geiger et al., 2004). There, the Jurassic rift event initiated a new rift axis by a rift jump to the north of the Morondava Basin (Fig. 4.3), abandoned the "Karoo age" rift axis and did not leave an imprint in the AFT thermo-tectonic record of the basement in south-western Madagascar (see chapter 9).

8.4.1 Denudation estimates for the Permo-Jurassic

AFT and (U-Th)/He data indicate that throughout the entire southern basement of northern Mozambique at least 3.6-3.0 km and locally up to c. 5.6 km of high grade metamorphic crust was removed by denudation since Jurassic to Cretaceous times. Corresponding TFT data suggest c. 12-9 km of denudation since the Early Carboniferous to Late Permian. As pointed out in chapter 3, this amount of denudation equals approximately 1/3-1/5 of an average continental crust thickness and is regarded as the upper limit estimate of denudation. In particular as this estimation is very sensitive to the palaeo-geothermal gradient employed and as independent evidences of significantly thinned crust are absent in northern Mozambique. However, it suggests that on average $\leq$ 8-6 km of high grade metamorphic crust could have been removed between the Late Permian (c. 250 Ma) and the Early Jurassic to Early Cretaceous (c. 190-130 Ma) by very slow denudation ($\leq$ 0.13 km/Ma).

Chapter 9

THE NORTH MOZAMBICAN – SOUTH CENTRAL MALAGASY RELATIONS: INFERENCES FROM FISSION TRACK ANALYSES

This chapter summarizes the main results from TFT and AFT fission track analyses in south central Madagascar of Emmel et al. (2004, 2006a, b, c) and relates them to this study in northern Mozambique. It aims to outline the principle differences and similarities in the thermo-tectonic histories of the two passive continental margins in order to evaluate a coeval and possibly linked margin evolution. Both margins evolved from the long term Gondwana disintegration during Late Palaeozoic to Mesozoic times. Today, southern Madagascar and northern Mozambique are separated by the DFZ transform fault system, whose tectonic activity resulted in a sheared continental margin in the northern Mozambican sector of central East Africa (Figs. 4.3, 4.4, 8.4). A comparison of their basement's thermo-tectonic histories could thereby contribute to infer, if the supercontinent's disintegration between both regions was favoured along one prominent long lasting transcontinental mega shear system, the Falkland-East Africa-Tethys shear system (Figs. 3.10, 4.1) as proposed by Visser and Praekelt (1996, 1998). In addition, the south western Malagasy and north Mozambican passive continental margins could represent opposite shoulders of a common large scale rift structure between East and West Gondwana, offset by the DFZ (Fig. 4.3).

In pure shear models of crustal attenuation the extension is inferred to be symmetrically distributed around the rift zone (McKenzie, 1978). Within this model, the upper and lower crusts are symmetrically stretched by brittle and ductile deformation, respectively. Consequently, this mode of extension could suggest that the exhumation due to crustal attenuation is also fairly symmetrically distributed (Fig. 9.1A). It further suggests that relative similar cooling, i.e. thermo-tectonic histories are to be expected on

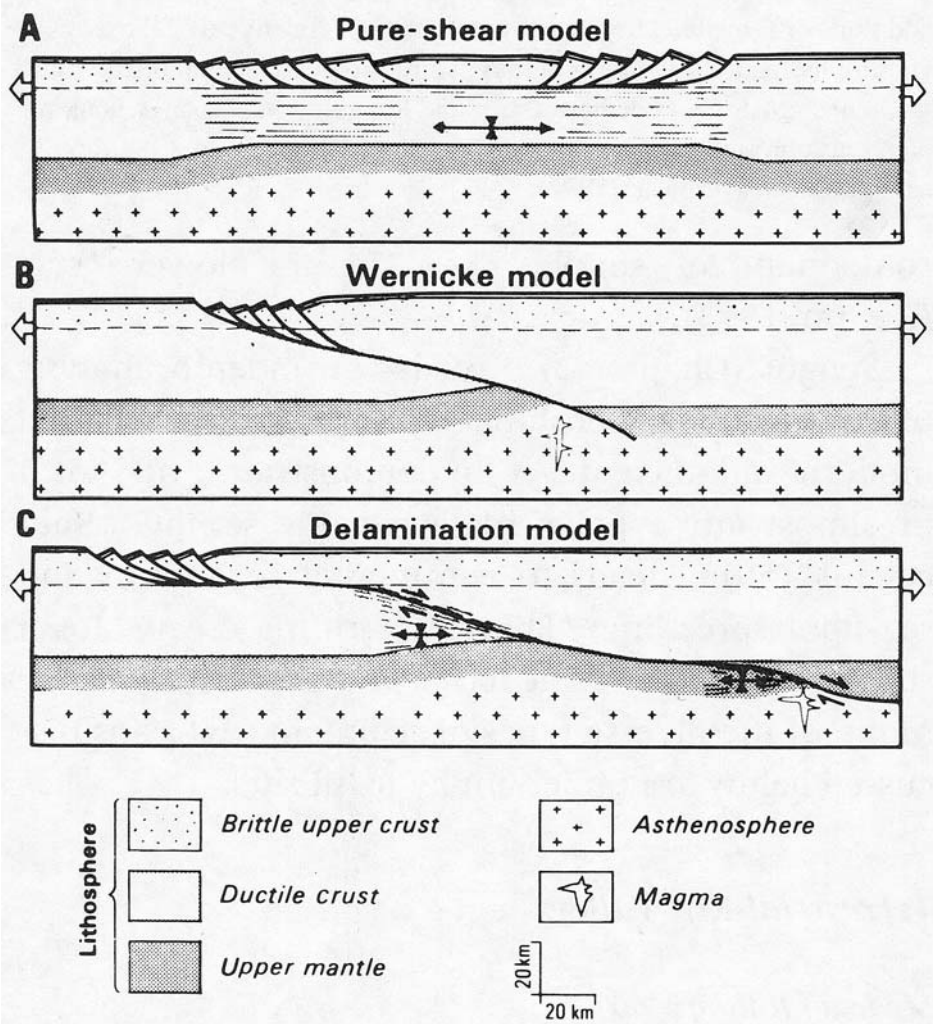

Figure 9.1: Three end-member models for continental extension after Lister et al. (1986).

either side of the rifted margins. In contrast, simple shear models of non-uniform continental extension (Fig. 9.1B, C) are characterized either by low angle detachment faults that cut through the crust and may even dissect the entire lithosphere (Wernicke, 1985) or by a complex delamination of the lithosphere, with a crustal detachment at the brittle-ductile transition connecting with the Mohorovičić discontinuity, (Lister et al., 1986). Both, the simple (Wernicke model) and combined shear model (delamination model) predict a strong asymmetry in the distribution of the crustal extension to either side of the detachment (Fig. 9.1B, C). These detachment models indicate that the lower plate margin experienced a distinctly higher degree of crustal attenuation than the upper plate margin (Fig. 9.2). Consequently, the associated cooling and denudation histories

should be significantly different on the evolving margins. The non-uniform shear models predict that the lower plate margin should display a much broader zone of thinned crust, which thus experienced a higher amount of exhumation and denudation than the corresponding upper plate margin (Fig. 9.2).

Comparing the thermo-tectonic and related denudations histories (cf. amounts of cooling) from the basements of south western Madagascar and northern Mozambique, it should be possible to identify symmetric or asymmetric distributed denudation patterns across the rift (upper versus lower plate margin) and to derive inferences on the type of crustal extension (pure shear versus simples shear model). In the case of a non-uniform stretching model it might even be possible to infer the dip direction of the continental crust's dissecting detachment.

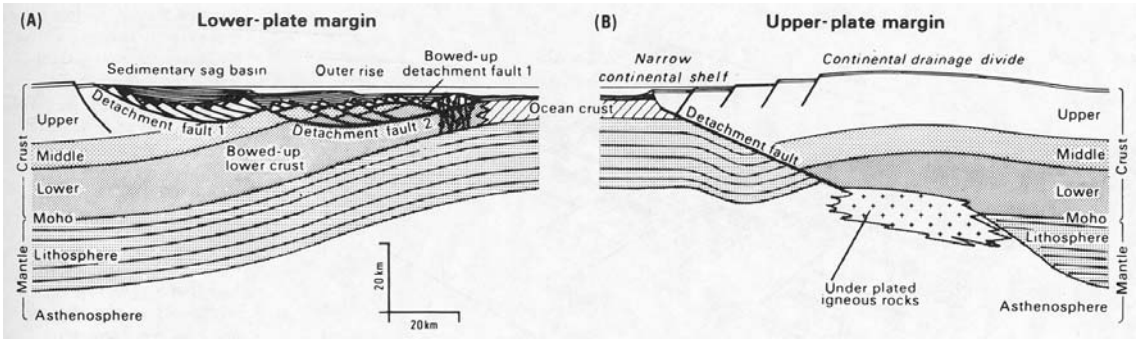

Figure 9.2: Sketch of the detachment-fault model of intraplate continental margins with lower-plate and upper-plate characteristics. "lower plate" and "upper plate" terminology refer to the position during terrestrial-rift stage; both types of margins evolve into intraplate continental margins during seafloor spreading. The lower-plate margin (A) has a complex structure; tilted blocks are remnants from the upper plate, above a bowed-up detachment faults. Multiple detachments have led to two generations of tilted blocks. The upper-plate margin (B) is relatively coherent. A rise of the asthenosphere during detachment faulting would cause uplift of the adjacent margin but "underplating of igneous rocks" would result in subsidence as asthenospere converts to lithosphere during cooling as an intraplate margin. Taken from Busby and Ingersoll (1995) after Lister et al. (1986).

After the latest tectono-metamorphic imprint related to the Gondwana amalgamation at c. 500 Ma, south central Madagascar experienced a long, protracted period of slow cooling in response to slow denudation lasting until the Early Carboniferous at c. 350 Ma (see references in Emmel et al. 2004). The titanite fission track ages from south central Madagascar range from 483 ± 33 Ma to 266 ± 13 Ma (Fig. 9.3). Generally, TFT

ages of ≤ 300 Ma are partially reset due to a post cooling thermal influence and are mainly located proximate to Cretaceous volcanic dykes. The AFT ages range from 460 ± 21 Ma to 79 ± 5 Ma (Fig. 9.3). AFT ages that are younger than c. 100 Ma are mainly located along the eastern margin of Madagascar and relate to the Madagascar-India separation while ages of around 200 Ma are partially reset due to a post cooling thermal influence by Cretaceous volcanism. These results are fairly similar to AFT ages of Seward et al., 2004, which range between 431 ± 21 Ma to 68 ± 5 Ma.

TFT data with ages of c. ≥ 300 Ma and AFT data with ages of c. ≥ 200 Ma from the basement suggest that the south western margin of Madagascar cooled more rapidly by denudation (≤ 0.2-0.1 km/Ma) to $T \leq 110°C$ in the Early Carboniferous and to subaerial/aerial conditions ($T \leq 60°C$) in the Late Carboniferous/Early Permian. The denudation was either related to wet based glacial abrasion or to differential exhumation due to brittle reactivation of NW-SE trending basement structures in response to intracontinental compression. Synchronously more protracted cooling to $T \leq 60°C$ due to very slow denudation (≤ 0.11-0.025 km/Ma) is recorded further inland to the east. Throughout the Permian more rapid cooling ($T \leq 60°C$) is related to differential denudation which continued east of the Morondava Basin and progressed eastwards inland. This differential exhumation occurred along N-S trending basement structures during the evolution of the eastward retreating rift shoulder of the Morondava Basin. Synchronously and subsequently, the western part of the basement (Morondava Basin) was subjected to reheating ($T \geq 110°C$) due to burial by Permo-Triassic sediments. The Morondava Basin had its largest eastward extension at this time. Along the NW-SE trending Bongolava Ranotsara Shear Zone differential cooling was related to exhumation and indicated graben formation during the Permo-Triassic. South central Madagascar experienced a more or less continued basement cooling due to differential exhumation along NW-SE and N-S trending structures during Carboniferous to Triassic times. It was related to block faulting due to potential reactivation of late Neoproterozoic/Early Cambrian basement structures during the formation of the Morondava Basin. Importantly, the AFT data indicate, that except for the western basin area, the south central Malagasy basement had cooled to $T \leq 60°C$ by the Middle Triassic.

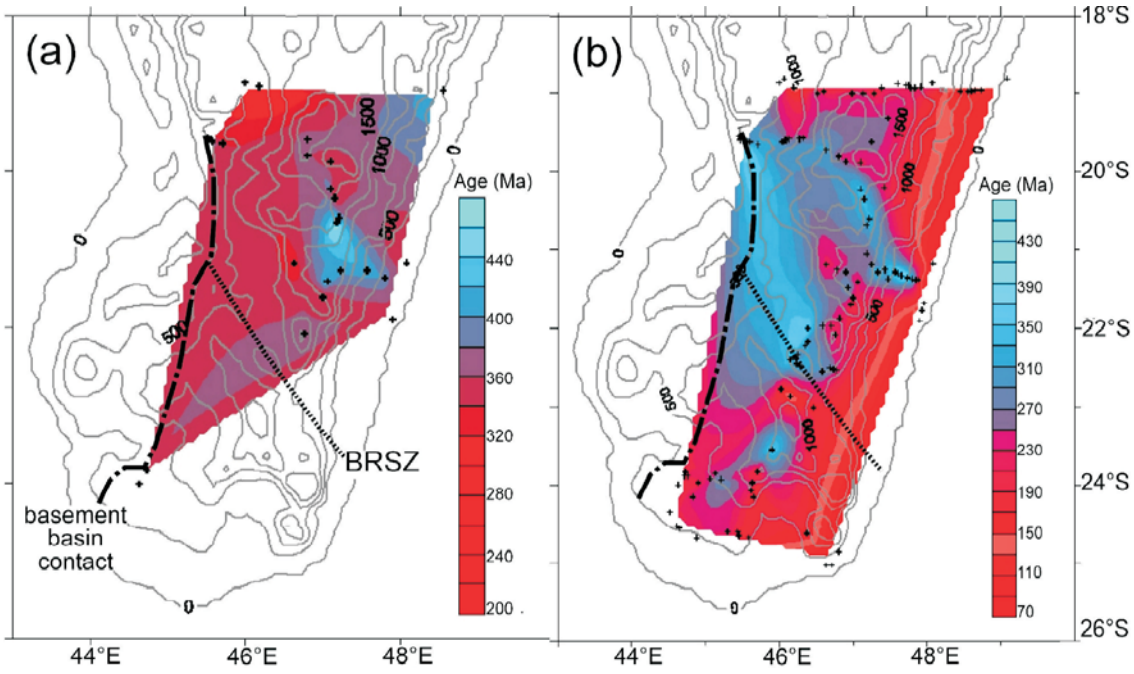

Figure 9.3: TFT (a) and AFT (b) age distribution pattern from the basement of central and southern Madagascar with sample locations (black crosses) from Emmel (2004). BRSZ = Bongalova Ranotsara Shear Zone.

Palaeostress analyses in the southern Morondava Basin (Schandelmeier et al., 2004) indicate that

a) an early period (Late Carboniferous/Early Permian) of sinistral strike-slip faulting resulted in c. N-S trending pull apart basins; bounded by conjugated sets of N-S and NW-SE trending faults
b) and it was successively replaced by pure NW-SE orthogonal rifting in the Early to Middle Triassic and resulted in NE-SW trending graben structures.

Recent palaeo-geographic reconstructions suggest that Madagascar experienced a slight counter clockwise rotation subsequent to its Carboniferous-Triassic rifting (Reeves et al., 2004; Reeves et al., 2002). The axis of crustal extension had therefore a c. NNE to NE alignment. It was part of a large intracontinental rift zone, the Malagasy Chasm (Wopfner, 1994) that extended from the southern Tethyian margin into Gondwana (Figs. 3.2, 8.4: 250 Ma time frame).

The basement of northern Mozambique experienced its latest metamorphic imprint, related to supercontinent amalgamation, between c. 550-500 Ma (chapter 3) and was

followed by a very slow and protracted cooling in response to denudation from the Early Ordovician to the Late Devonian/Early Carboniferous (c. 350 Ma). This slow long term cooling (c. 200-150 Ma) appears to be similar to the post metamorphic basement cooling of south central Madagascar.

The TFT ages from northern Mozambique (384±20 Ma to 219±12 Ma) are generally younger than the ages of south central Madagascar. They indicate that

a) more rapid cooling occurred in the late Early to Late Permian (280-260 Ma); distinctly later than in Madagascar
b) the cooling was related to denudation due to the onset of rifting and slightly postdates the incipient rifting in Madagascar
c) the exhumation likely occurred along an uplifted rift flank, parallel to an E-W trending rift basin that was supposedly linked to the Zambezi rift system
d) the basement did not cool to $T \leq 275$°C prior to the Triassic ($\leq$ 250 Ma) and remained at distinctly higher temperature than south central Madagascar in Late Palaeozoic to Early Mesozoic times.

Importantly, the TFT age pattern on the north Mozambican basement reflects the thermo-tectonic imprint of an uplifted rift flank, where the total amount of exhumation is related to a complex, coupled interaction of flexural tectonic uplift, denudation and isostatic compensation (chapter 3.0) during the Permian to Triassic. In south western and central Madagascar, the differential exhumation during the Permo-Triassic period is related to a retreating rift shoulder and to crustal extension (graben formation). Clearly, the thermo-tectonic basement records of the Permo-Triassic rifting event that affected south western Madagascar and northern Mozambique resulted from two fundamentally different rifting induced processes. Rift flank uplifts are common rifting induced features that do not relate to a particular mode of crustal extension (Ziegler and Cloething, 2004). As a consequence, no inferences on the type continental margin can be made for northern Mozambique and no conclusion can be drawn on the mode of crustal extension (pure versus simple shear) for the intracontinental Gondwana rifting in the Malagasy-Mozambican sector during the Permo-Triassic.

The kinematic constraints from the southern Morondava Basin in Madagascar (Schandelmeier et al., 2004) strongly argue that there has been no tectonic activity along the Tanzania-Mozambican sector of the East African margin during the Permo-Triassic. In conjunction with the strongly E-W aligned exhumation pattern in northern Mozambique these inferences suggest that there has been no apparent direct linkage between the c. NE-SW trending Malagasy Trough rift system and the c. E-W trending North Mozambique-Zambezi Rift System along the Tanzania-Mozambican sector of the East African margin (Fig. 3.2, 8.4). This could imply that the Falkland-East Africa-Tethys Shear System did not exist between northern Mozambique and Madagascar during the Permo-Triassic rifting period (Fig. 3.10). It appears more reasonable, that the Malagasy Trough and the North Mozambique-Zambezi Rift System constituted two discrete rift zones with two individual detachments during the Permo-Triassic period of intracontinental rifting in Gondwana. How and if these zones were linked further to the west within Central Africa (Fig. 3.2) is beyond the scope of this fission track data set.

The AFT ages of northern Mozambique (169 ± 19 Ma to 61 ± 8 Ma) are generally younger than the ages of south central Madagascar and indicate that

a) more rapid cooling to $T \leq 110°C$ and to subaerial / aerial conditions ($T \leq 60°$-40°C) took place between the late Early Jurassic (c. 190-180 Ma) and the Late Cretaceous (c. 90-80 Ma); distinctly later than in Madagascar
b) alike south central Madagascar the cooling was related to differential denudation and primarily confined along N-S trending zones of crustal weakness that also parallel the Mozambique Belt trend
c) in contrast to southern Madagascar, brittle reactivation and the stepwise exhumation along these N-S trending zones are related to repeated transpression and/or transtension due to the Gondwana break-up but mainly to post break-up far field stress influences from global plate re-organizations; by tectonic events that occurred in post Triassic times.

Subsequent to the Permo-Triassic rifting along the Malagasy Chasm, the Morondava Basin experienced a short lived Early Jurassic (c. 190-180 Ma) rifting event, the

"Andafia rift". This rifting event initiated the supercontinent break-up and seafloor spreading in the Somali Basin. Subsequently, the southward drift of Madagascar relative to Africa started at c. 180-154 and lasted until c. 118 Ma (Geiger et al., 2004, Coffin and Rabinowitz, 1987). Palaeo-reconstructions of Madagascar's movement along the DFZ suggest, that its south western margin passed northern Mozambique between c. 175-140 Ma (de Witt, 2003 and references therein) when they attained their spatially closest palaeo-geographic position during the Gondwana dispersal (Fig. 8.4).

A potential mutual influence during this period is therefore discussed now in more detail. During the incipient break-up and drift of E and W Gondwana, basaltic lavas of Early to Middle Jurassic age (c. 180-160 Ma) erupted on the eastern margin of northern Mozambique (Fig. 8.1; Jaritz et al., 1977, Grantham et al., 2005). Volcanic rocks of Jurassic age are completely absent in Madagascar (Besairie, 1961; Besairie, 1973). This likely suggests that south western Madagascar did not pass northern Mozambique prior to the Middle Jurassic (c. ≥ 170-160 Ma). Hence they likely were located at common latitude during the late Middle Jurassic to the onset of the Early Cretaceous (c. 160-140 Ma). Synchronously (c. 170-150 Ma), parts of the eastern margin of Mozambique experienced more rapid denudation due to transpression along the DFZ (section 8.3.1). This could indicate that the denudation along the eastern margin of northern Mozambique provided sedimentary infill to the passing Morondava Basin during the late Middle to Late Jurassic. Detrital AFT central ages from Middle Jurassic strata (Lower Bajocian to Lower-Middle Callovian; c. 174-156 Ma) of the Morondava Basin suggest that these sediments were sourced by reworking the older Permo-Carboniferous basin strata (Emmel et. al, 2006a). Reworking was triggered by the previously formed "Andafia rift". It exposed the eastern parts of the Morondava Basin into the position of a denuding rift shoulder. Palaeo-current indicators consistently suggest a sediment source in the east and appear to exclude an East African source region throughout the Middle Jurassic. (Emmel et al., 2006a; Geiger, 2004). These facts rather preclude a sediment delivery from northern Mozambique into the adjacent Morondava Basin during this time. Thus the question arises where these sediments were deposited instead. In the southern Rovuma Basin (Figs. 6.1, 8.1), Middle to Late Jurassic strata are inferred, based on seismic interpretation (Salman and Abdula, 1995). Hancox et al.

(2002) have shown that Early Cretaceous strata of the southern Rovuma Basin in northern Mozambique were sourced from the south and southwest. It could imply that a similar source region can be assumed for the Middle to Late Jurassic sediments of the southern Rovuma Basin. Thereby the Rovuma Basin "collected" the denuded material from northern Mozambique and prevented a material transport further east into the Morondava Basin. Such a scenario broadly resembles the Mesozoic graben setting in southern Mozambique (Fig. 4.4). These graben also accumulated the Mesozoic sediments (Jurassic to Late Cretaceous) that were delivered from the African continent and prevented a further eastward transport into the developing Mozambique Basin (Dingle and Scrutton, 1974).

The comparison of the TFT and AFT data from south central Madagascar and northern Mozambique clearly shows that both regions experienced a distinctly different thermo-tectonic evolution since the Early Carboniferous. While cooling to $T \leq 60°C$ occurred differentially in south central Madagascar during the Karoo rifting period (Carboniferous-Triassic), northern Mozambique did not cool $T \leq 110°C$ prior to the Early Jurassic. The cooling of the north Mozambican basement to $T \leq 60°C$ and further to surface temperatures was strongly linked to the post break-up evolution of south central East Africa. Common to both regions is a repeated differential denudation along pre-existing late Neoproterozoic/Early Cambrian zones of crustal weakness due to their repeated reactivation since the Palaeozoic. The basements of south western Madagascar and northern Mozambique did not yield thermo-tectonic FT records that are directly linked to the Jurassic rifting events in the Somali and Mozambique basins, respectively. In northern Mozambique, a thermo-tectonic imprint related to the Jurassic rifting might have existed but has been subsequently overprinted by younger, post break-up tectonic events. It is therefore not possibly to derive inferences on the types of continental margins and on the modes of crustal extension in the Malagasy-Mozambican sector during the Jurassic rifting episode of the disintegrating Gondwana supercontinent.

Many continental rifts are asymmetric in their nature of extension (Busby and Ingersoll, 1995 and references therein). As the Jurassic rifting event ultimately led to the Gondwana break-up and proceeded along the DFZ in the Malagasy-Mozambican sector, it could be likely that south western Madagascar and northern Mozambique constituted

asymmetric rift margins and shared a common detachment during the short lived Jurassic rifting period. On the other hand, the DFZ constitutes a major transform fault (Droz and Mougenot, 1987). Therefore, separated by the DFZ, independent rift basin yielding individual detachments of even opposite dip directions could have existed between Madagascar-Kenya/Tanzania and northern Mozambique-central Dronning Maud Land (Antarctica) during the Jurassic rifting.

The youngest thermo-tectonic event recorded by AFT data in south central Madagascar is a thermal overprint in Early to Late Cretaceous times. It is associated with the magmatism of the Marion hot spot (c. 90-83 Ma) that initiated the India Madagascar break-up (Storey et al., 1995). In northern Mozambique, the youngest event recorded by AFT data is a basement reheating confined to N-S and ENE to NE trending zones of crustal weakness in Palaeogene times. It reflects an increased geothermal gradient due to heat advection by fluid flow and potentially foreshadows the subsequent incipient rifting in northern Mozambique in the Neogene. These different youngest thermo-tectonic events further manifest the distinct spatial separation and independent thermo-tectonic evolution of Madagascar and Mozambique following the cessation of Madagascar's southward drift in the Early Cretaceous (c. 118 Ma).

Chapter 10

CONCLUSION

$^{40}Ar/^{39}Ar$ hornblende and biotite cooling ages record the cooling from the latest Pan-African metamorphic imprint at c. 550-500 Ma, linked to the formation of the Namama thrust Belt, at slow rates of about 11°-7°C/Ma in Early to Late Ordovician times. Syn- to post-tectonic granitoid and pegmatite emplacements at c. 500-450 Ma locally delayed cooling and a widespread basement cooling to < 350°C occurred in the Late Ordovician to Early Silurian.

The TFT results in the northern part of the basement record the very slow cooling (rates < 1°C/Ma) between the Late Ordovician/Early Silurian and the Late Devonian/Early Carboniferous, that is related to decreasing denudation due to the establishment of pre-Karoo peneplains within central Gondwana. In southern part of the basement the TFT results record the cooling of a denuding and approximately E-W trending uplifted rift flank. It formed in the Early to Late Permian and marks the onset of rifting and incipient Gondwana dispersal in the vicinity of northern Mozambique. Associated crustal extension proceeded in an oblique mode in response to a NW-SE tensional stress field. Thereby easterly trending ductile basement fabrics were supposedly reactivated by brittle extensional faulting; emphasizing that the ductile structural heritage of the late Neoproterozoic/Early Cambrian MB (cf. EAAO) influenced the location and orientation of the zone of rifting and exhumation in Permian times. A linkage of the north Mozambican rift structure to the Zambezi Rift via the Zambezi pre-transform system is inferred. The denudation estimates derived from the TFT data suggest a maximum crustal removal of ≤ 9-11 km in the hinterland and ≤ 10-12 km on the rift flank since Late Carboniferous and Early/Late Permian, respectively.

AFT and (U-Th)/He data of the north Mozambican basement can be broadly grouped into three regions. These are the zone of the Axial Granulite Complex including Mt. Tumbine, the eastern margin of the southern basement and the central part of the

southern basement, located between the former two regions. Common to all regions is an AFT cooling history record since the Jurassic to Cretaceous. These thermo-tectonic histories show, that the location and the orientation of the zones of repeated Mesozoic-Cenozoic exhumation appear to be controlled by prominently N-S and subordinately ENE-WSW trending ductile fabrics of the MB, which formed in late Neo-proterozoic/Early Cambrian times. However, the origin of the brittle basements fabric reactivation by exhumation is intrinsically linked to post break-up and opening histories of the Atlantic and Indian oceans; global plate reorganization process that exerted far field stresses onto the north Mozambican sector of the African continental crust since Middle Mesozoic time.

Two periods of more rapid cooling due to denudation are record by the AFT data in northern Mozambique, a first during the Early to Late Jurassic (c. 190-150 Ma) and a second during the Early to early Late Cretaceous. A third cooling stage is presumably related to a reheating event in the Palaeogene (c. 40-20 Ma).

The Jurassic period is related to reactivation of N-S trending zones of crustal weakness along the MB, i.e. along the orogenic root of the former East African-Antarctic Orogen. In the western Axial Granulite Complex a potential Jurassic (? 195-145) cooling stage is related to crustal extension along a generally N-S orientated zone that extents from the southern Tanganyika-Rukwa-Malawi Rift System via northern Mozambique into the graben system of southern Mozambique. Along the eastern margin of the southern basement denudation in the Early Jurassic (c. 190-180 Ma) was caused by transpression tectonics along the N-S trending DFZ, which was active as a transform zone and interlinked the short-lived Early Jurassic rifting events in the Somali and Mozambique basins. A subsequent reheating to c. 70°-90°C resulted from the emplacement of at least 2.5-2.0 km of volcanics rocks, presumably related to transform faulting the late Early to Middle Jurassic at c. 180-160 Ma. Synchronous (c. 170- 150 Ma) differential cooling to $T \leq 60$°C reflects either the fading of a volcanism induced elevated transient palaeo-geothermal gradient and/or denudation related to transpressive /transtensive tectonics along the DFZ during the incipient southward drift of East relative to West Gondwana. Within the Lurio Belt (central southern basement) a Jurassic denudation induced cooling phase is also attributed to a brittle reactivation of

the ductile high strain basement fabrics by exhumation in response to the early southward drift of East Gondwana.

The second denudation period triggered cooling that was recorded throughout the entire southern basement during the Early to Late Cretaceous (c. 130-90 Ma). In the Axial Granulite Complex denudation resulted from crustal extension in response to NE-SW orientated tensional stresses. It occurred along the N-S aligned zone stretching from the Axial Granulite Complex in the north via the contemporaneously formed Urema Graben to the graben system of southern Mozambique. The associated alkaline intrusion of Mount Tumbine was probably emplaced into a shallow crustal level (c. ≤ 3km) and sub-sequently cooled rapidly in response to denudation in the Early Cretaceous. Crustal attenuation along the western MB has been triggered by the reactivation of pre-existing N-S trending zones of weakness and can be linked to the influence of far field stresses of the opening of the South and Equatorial Atlantic. Changes in the spreading configuration in the Indian Ocean are accounted for denudation by renewed crustal extension in the western MB in the Late Cretaceous (c. 90-80 Ma). Palaeo-drainage pattern and sediment flux estimates suggest that material denuded in the western Axial Granulite Complex was deposited within the Zambesi Delta of the Mozambique Basin during Cretaceous times and potentially since. At the eastern margin more rapid denudation during the Early to Late Cretaceous is linked to transpressive and/or transtensive and extensional tectonics along the DFZ, which in turn are linked to the cessation of Madagascar's southward drift (130-118 Ma), to far field stresses of the opening of the South and Equatorial Atlantic (c. 130-110 Ma) and to changes in the spreading configuration in the Indian Ocean (c. 90 Ma). Material denuded from the eastern margin of the basement was deposited into the southern Rovuma Basin during Early Cretaceous times. In the Lurio Belt an Early Cretaceous cooling phase is linked to the fading of a basement reheating by fluid flow and to denudation by transpressive and/or transtensive brittle reactivation of the ENE to NE trending ductile high strain fabrics, which both are caused by far field stresses of the South Atlantic opening. In the central southern basement the AFT and the apatite (U-Th)/He data indicate a spatially homogenous and very similar thermo-tectonic history since the Early Cretaceous. The basement experienced an episode of more rapid denudation during the Early to the Late

Cretaceous (c. 130-90 Ma) and subsequently a very slow and protracted denudation until Palaeogene to Neogene times. This very uniform pattern is related to an erosional compensation of a potential local base level gradient between the central southern basement and its bounding N-S trending zones of contemporaneous crustal extension to the west (Axial Granulite Complex) and east (eastern continental margin).

A Palaeogene cooling stage (c. 40-20 Ma), linked to a basement reheating to c. 60°C by heat advection of fluids, is observed at Mt. Tumbine, in the Lurio Belt and along the eastern continental margin; within zones of crustal weakness. It temporally coincides with the earliest tectonic activity of the initiating EARS at c. 30 Ma and probably displays a tectonic foreshadow of the Late Miocene rifting in northern Mozambique.

Denudation estimates suggest that in the Axial Granulite Complex (incl. Mt. Tumbine) c. 3.6-3.0 km, and locally up to 5.6-4.7 km of crust were removed since the Early Cretaceous, whereby the post Cretaceous amount of denudation was less 0.8 km. Along the eastern continental margin denudation amounted to at least 6.4-5.4 km between the Early Jurassic to early Late Cretaceous. An additional post Cretaceous quantity of denudation of less 0.8 km suggests an approximated total amount of 7-6 km since the Jurassic. In the Lurio Belt and in the central southern basement a total of 3.6-3.0 km of denudation is recognized since the Middle Jurassic and since the Early to Late Cretaceous, respectively. The post Cretaceous amount of denudation has been less than 0.8-0.7 km in the Lurio Belt area and less than 2.3-2.2 km throughout the central southern basement.

The comparison of the thermo-tectonic histories from the passive continental margins of northern Mozambique and south central Madagascar yield the following results. Though the timings of cooling during the Karoo age rifting episode are broadly similar in south central Madagascar (Carboniferous to Permian) and northern Mozambique (Permian to Triassic), the associated rifting induced processes responsible for the observed cooling are fundamentally different in both regions and do not permit inferences on the prevailing geometry of crustal extension. South central Madagascar experienced differential denudation by crustal extension and rift shoulder retreat in the Morondava Basin whereas the basement of northern Mozambique was exhumed and denuded due to

an uplifted rift flank. The different alignment of the Karoo age rift axes in southern Madagascar (c. NE-NNE) and northern Mozambique (c. E-W) rather suggest independent rift shoulder evolutions within the independent rift systems of Malagasy Chasm and the Mozambique-Zambezi system during the Permo-Triassic, respectively. In conjunction with structural data from southern Madagascar these results suggest a kinematic linkage of both rift systems via Falkland-East Africa-Tethys Shear System did not exist in Permian times.

No thermo-tectonic records of the Jurassic rifting and subsequent Gondwana break-up histories (c. 180-160 Ma) are preserved in the basement rocks of south central Madagascar as extensive parts to the east the present Morondava Basin had been cooled to $T \leq 60°C$ prior to Triassic times. Detrital AFT data from the Morondava Basin evidence an influence of the Jurassic rifting episode in southern Madagascar but do not permit inferences on the amount of associated exhumation and denudation. In northern Mozambique cooling $T \leq$ 110-60°C is not evidenced prior to the late Early Jurassic and is not directly related to Jurassic Gondwana break-up in the Mozambique Basin. The majority of north Mozambican basement experienced cooling $T \leq 60°C$ by thermo-tectonic events associated with the post break-up history of the eastern African continent. The thermochronological data sets from south western Madagascar and northern Mozambique imply that both rift shoulders were not directly linked throughout their passive margin evolution during the Gondwana dispersal in Palaeozoic to Mesozoic times. The youngest thermo-tectonic events recorded by AFT data in south central Madagascar (Late Cretaceous) and northern Mozambique (Palaeogene) further manifest the distinct spatial separation and independent thermo-tectonic evolution of Madagascar and Mozambique following the cessation of Madagascar's southward drift in the Early Cretaceous (c. 118 Ma).

Common to both regions is brittle reactivation of ductile basement fabrics, formed during the late Neoproterozoic/Early Cambrian development of East African-Antarctic Orogen by differential exhumation during their post Pan African rift and drift evolutions. In Permian times broadly northerly and easterly trending fabrics were reactivated in Madagascar and northern Mozambique, respectively. Since the Jurassic,

exhumation was prominently localized to the reactivation of northerly fabrics in northern Mozambique.

Bibliography

Andreoli, M.A.G., 1984. Petrochemistry, tectonic evolution and metasomatic mineralisations of Mozambique Belt granulites from S Malawi and Tete (Mozambique). Precambrian Research, 25: 161-186.

Bahrenberg, G., Giese, G. and Nipper, J., 1992. Statistische Methoden in der Geographie, Bd.2. Borntraeger, Stuttgart, 220 pp.

Barbarand, J., Hurford, T. and Carter, A., 2003a. Variation in apatite fission-track length measurement: implications for thermal history modelling. Chemical Geology, 198: 77-106.

Barbarand, J., Carter, A., Wood, I. and Hurford, T., 2003b. Compositional and structural control of fission-track annealing in apatite. Chemical Geology, 198: 107-137.

Baxter, E.F., 2003. Quantification of the factors controlling the presence of excess ^{40}Ar or ^{4}He. Earth and Planetary Science Letters, 216: 619-634.

Baxter, E.F., DePaolo, D.J. and Renne, P.R., 2002. Spatially correlated anomalous ^{40}Ar/^{39}Ar "age" variations in biotites about a lithologic contact near Simplon Pass, Switzerland; a mechanistic explanation for excess Ar. Geochimica et Cosmochimica Acta, 66: 1067-1083.

Belton, D.X., Kohn, B.P. and Gleadow, A.J.W., 2004a. Quantifying "excess helium": some of the issues and assumptions in combined (U-Th)/He and fission track analysis. In: P. Andriessen (Editor), 10th international Fission track dating conference, Amsterdam, pp. 18.

Belton, D.X., Lorencak, M., Carter, T.J., Norman, M. and Kohn, B.P., 2004b. Samarium in apatite: contributions to radigenic helium and the effect on the (U-Th)/He thermochronology. In: P. Andriessen (Editor), 10th international Fission track dating conference, Amsterdam, pp. 40.

Bergmann, S.C. and Corrigan, J., 1996. Compositional variations of natural apatites subjected to fission track analysis, 8th Int. Workshop Fission-Track Dating, Ghent, pp. 7.

Besairie, H., 1961. Madagascar carte géologique, 1:1.000.000. Sérvice Géologique de Madagascar, Antananarivo.

Besairie, H., 1973. Carte géologique a 1:2.000.000 de Madagascar. Sérvice Géologique de Madagascar, Antananarivo.

Biagazzi, G., 1981. The problem of the decay constant λ_f of ^{238}U. Nuclear Tracks, 5: 35-44.

Bloomfield, K., 1968. The pre-Karoo geology of Malawi. Memoir Geological Survey Malawi, 5.

Boschmann-Käthler, W., 1986. Uran und Helium in Erzmineralen und die Frage ihrer Datierbarkeit. Heidelberger Geowissenschaftliche Abhandlungen, 4: 135.

Brewer, T.S., Hergt, J.M., Hawkesworth, C.J., Rex, D.C. and Storey, B.C., 1992. Coats Land dolerites and the generation of Antartic continental flood basalts. In: B.C. Storey, T. Alabaster and R.J. Pankhurst (Editors), Magmatism and the cause of

continental break-up. Geological Society Special Publications, London, pp. 185-208.

Brown, R.W., 1992. A fission track thermochronology study of the tectonic and geomorphic development of the sub-aerial continental margins of southern Africa. PhD Thesis, La Trobe University, Victoria, 407 pp.

Brown, R.W., Gallagher, K. and Duane, M., 1994. A quantitive assessment of the effects of magmatism on the thermal history of the Karoo sedimentary sequence. Journal of African Earth Sciences, 18: 227-243.

Burbank, D.W. and Anderson, R.S., 2001. Tectonic Geomorphology. Blackwell Sciences, Oxon, 274 pp.

Burtner, R., Nigrin, A. and Donelick, R., 1994. Thermochronology of lower Cretaceous source rocks in the Idaho-Wyoming Thrust Belt. American Association of Petroleum Geologists Bulletin, 78: 1613-1636.

Busby, B.J. and Ingersoll, R.V., 1995. Tectonics of Sedimentary Basins. Blackwell Science, Oxford, 579 pp.

Carlson, W.D., 1990. Mechanisms and kinetics of apatite fission-track annealing. American Mineralogist, 75: 1120-1139.

Carlson, W.D., Donelick, R.A. and Ketcham, R.A., 1999. Variability of apatite fission-track annealing kinetics: I. Experimental results. American Mineralogist, 84: 1213-1223.

Castaing, C., 1991. Post-Pan-African tectonic evolution of South Malawi in relation to the Karroo and Recent East African Rift Systems. Tectonophysics, 191: 53-73.

Catuneanu, O. et al., 2005. The Karoo basins of south-central Africa. Journal of African Earth Sciences, 43: 211-253.

Chorowicz, J., 2005. The East African rift system. Journal of African Earth Science, 43: 379-410.

Chorowicz, J. et al., 1998. The Tana basin, Ethiopia: intra-plateau uplift, rifting and subsidence. Tectonophysics, 295: 351-367.

Clemenson, J., Cartwright, J. and Booth, J., 1997. Structural segmentation and the influence of the basement structure on the Namibian passive margin. Journal of the Geological Society of London, 154: 477-482.

Coffin, M.F. and Rabinowitz, P.D., 1987. Reconstruction of Madagascar and Africa; evidence from the Davie fracture zone and western Somali Basin. Journal of Geophysical Research, 92: 9385-9406.

Coffin, M.F. and Rabinowitz, P.D., 1992. The Mesozoic East African and Madagascan conjugate continental margins; stratigraphy and tectonics. In: J.S. Watkins, Z. Feng and K.J. McMillen (Editors), AAPG Memoir, pp. 207-240.

Cooper, W.G.G. and Bloomfield, K., 1961. The geology of the Tambani-Salambidwe area. Bulletin of the Geological Survey Nyasaland, 13 pp.

Cowan, G.A. and Adler, H.H., 1976. The variability of natural abundance of ^{235}U. Geochimia et Cosmochimia Acta, 40: 1487-1490.

Coyle, D.A. and Wagner, G.A., 1998. Positioning the titanite fission-track partial annealing zone. Chemical Geology, 149: 117-125.

Crowley, K.D., Cameron, M. and Schaefer, R.L., 1991. Experimental studies of annealing of etched fission tracks in fluorapatite. Geochimica et Cosmochimica Acta, 55: 1449-1465.

Dalrymple, B.G. and Lanphere, M.A., 1974. $^{40}Ar/^{39}Ar$ age spectra of some undisturbed terrestrial samples. Geochimia et Cosmochimia Acta, 38: 715-738.

Daly, M.C., Chorowicz, J. and Fairhead, J.D., 1989. Rift basin evolution in Africa: The influence of reactivated steep basement shear zones. In: M.A. Cooper and G.D. Williams (Editors), Inversion tectonics. Geological Society Special Publication, London, pp. 309-334.

Daly, M.C., Lawrence, S.R., Kimun, a.D. and Binga, M., 1991. Late Palaeozoic deformation in Central Africa; a result of distant collision? Nature, 350: 605-607.

Damon, P.E., 1968. Potassium-argon dating of igneous and metamorphic rocks with applications to the Basin ranges of Arizona and Sonora. In: E.I. Hamilton and R.M. Farquhar (Editors), Radiometric dating for geologists. Intersciences, London, pp. 1-71.

Delvaux, D., 2001. Tectonic and palaeostress evolution of the Tanganyika-Rukwa-Malawi rift segment, East African Rift System. In: P.A. Ziegler, W. Cavazza, A.H.F. Robertson and S. Crasquin-Soleau-Sylvie (Editors), Peri-Tethys memoir 6: Peri-Tethyan rift/wrench basins and passive margins. Edition du Museum National d'Histoire Naturelle, Paris, pp. 545-556.

De Wit, M., 2003. Madagascar: Heads it's a continent tail it's an island. Annual Review of Earth and Planetary Sciences, 31: 213-248.

Di Vincenzo, G., Viti, C. and Rocchi, S., 2003. The effect of chlorite interlayering on ^{40}Ar-^{39}Ar biotite dating; an ^{40}Ar-^{39}Ar laser-probe and TEM investigations of variably chloritised biotites. Contributions to Mineralogy and Petrology, 145: 643-658.

Dickin, A.P., 1995. Radigenic isotope geology. Cambrige University Press, Cambridge, 452 pp.

Dingle, R.V. and Scrutton, R.A., 1974. Continental breakup and the development of the Post-Paleozoic sedimentary basins around southern Africa. Geological Society of America Bulletin, 85: 1467-1474.

Dodson, M.H., 1973. Closure temperature in cooling geochronological and petrological systems. Contributions to Mineralogy and Petrology, 40: 259-274.

Donelick, R.A., 1991. Crystallographic orientation dependence of mean etchable fission track length in apatite: An empirical model and experimental observations. American Mineralogist, 76: 83-91.

Donelick, R.A., 1993. A method of fission track analysis utilizing bulk chemical etching of apatite, U.S.A. patent no. 5.267.274.

Donelick, R.A., Ketcham, R.A. and Carlson, W.D., 1999. Variability of apatite fission-track annealing kinetics: II. Crystallographic orientation effects. American Mineralogist, 84: 1224-1234.

Donelick, R.A., Roden, M.K., Mooers, J.D., Carpenter, B.S. and Miller, D.S., 1990. Fission track annealing in minerals. In: S.A. Durrani and E.V. Benton (Editors), Proceedings of the 6th international fission track dating workshop. Nuclear Tracks and Radiation Measurements. Pergamon, Oxford, pp. 261-265.

Droz, L. and Mougenot, D., 1987. Mozambique upper fan; origin of depositional units. AAPG Bulletin, 71: 1355-1365.

Duddy, I.R., Green, P.F. and Laslett, G.M., 1988. Thermal annealing of fission tracks in apatite. 3. Variable temperature behaviour. Chemical Geology (Isotope Geoscience Section), 73: 25-38.

Dumitru, T., 1991. A new computer-automated microscopic stage system for fission track analysis. On Track, 1: 1-7.

Dumitru, T.A., 1993. A new computer-automated microscope stage system for fission-track analysis. Nucl. Tracks Radiat Meas., 21: 575-580.

Duncan, R.A., Hooper, P.R., Rehacek, J., Marsh, J.S. and Duncan, A.R., 1997. The timing and duration of the Karoo igneous event, southern Gondwana. Journal of Geophysical Research, 102: 18127-18138.

Eby, G.N. et al., 1995. Geochronology and cooling history of the northern part of the Chilwa alkaline province, Malawi. Journal of African Earth Sciences, 20: 275-288.

Ehlers, T.A. and Farley, K.A., 2003. Apatite (U-Th)/He thermochronometry; methods and applications to problems in tectonic and surface processes. Earth and Planetary Science Letters, 206: 1-14.

Emmel, B., 2004. Reconstruction of the Phanerozoic tectono-thermal history of central and southern Madagascar, based on fission track thermochronology. PhD Thesis, University of Bremen, Bremen, 166 pp.

Emmel, B., Geiger, G. and Jacobs, J., 2006a. Detrital apatite fission-track ages in Middel Jurassic strata at the rifted margin of W Madagascar – an indicator for a protratced resedimentation history. Sedimentary Geology, 186: 27-38.

Emmel, B., Jacobs, J., Dassinnies, M.C. and Razakamanana, T., 2006b. The drainage system along the Ranotsara Shear Zone: An inheritance from early Gondwana break-up tectonics? In: C. Schwitzer et al. (Editors), Proceedings of the German-Malagasy Research Cooperation in Life and Earth Sciences. Concept Verlag Berlin, Antananarivo, Madagascar, pp. 19-28.

Emmel, B., Jacobs, J., Kastowski, M. and Graser, G., 2006c. Phanerozoic upper crustal tectono-thermal development of basement rocks from central Madagascar; an integrated fission-track and structural study. Tectonophysics, 412: 61-86.

Emmel, B., Jacobs, J., Dassinnies, M.C. and Crowhurst, P., 2006d. Combined apatite fission track and single grain apatite (U-Th)/He ages - a possibility to identify thermally overprinted crustal segments in Dronning Maud Land (East Antartica). In: F. Lisker, B. Ventura, M. Olesch and U.A. Glasmacher (Editors), European Conference on Thermochronology July 30 - August 4, 2006. Schriftenreihe der Deutschen Gesellschaft für Geowissenschaften, Bremen, pp. 40.

Emmel, B., Jacobs, J. and Razakamanana, T., 2004. Titanite and apatite fission track analyses on basement rocks of central-south Madagascar: contraints on exhumation and denudation rates along the eastern rift shoulders of the Morondava basin. Journal of African Earth Sciences, 38: 343-361.

Enkelmann, E., Jonckheere, R. and Ratschbacher, L., 2005. The effect of radiation damage accumulation and annealing of fission-track dating in titanite. Nuclear Instruments and Methods in Physics Research B, 227: 567-576.

Fairhead, J.D., 1988. Late Mesozoic rifting in Africa. In: W. Manspeizer (Editor), Triassic-Jurassic rifting; continental breakup and the origin of the Atlantic

Ocean and passive margins. Developments in Geotectonics. Elsevier, Amsterdam, pp. 821-831.

Fairhead, J.D. and Binks, R.M., 1991. Differential opening of the Central and South Atlantic oceans and the opening of the West African rift system. Tectonophysics, 187: 191-203.

Fanale, F.P. and Kulp, J.L., 1962. Dating of magnetite and other ore minerals by the U, Th-He method. Special papers - Geological Society of America: 174-175.

Farley, K.A., 2000. Helium diffusion from apatite: General behavior as illustrated by Durango fluorapatite. Journal of Geophysical Research, 105: 2903-2914.

Farley, K.A., 2002. (U-Th)/He dating: Techniques, calibrations and applications. In: D.P. Porcelli, C.J. Ballentine and R. Wieler (Editors), Noble Gases. Reviews in Mineralogy and Geochemistry, pp. 819-844.

Farley, K.A., Reiners, P.W. and Nenow, V., 1999. An apparatus for high-precision helium diffusion measurements from minerals. Analytical Chemistry, 71: 2059-2061.

Farley, K.A., Wolf, R.A. and Silver, L.T., 1996. The effects of long alpha-stopping distances on (U-Th)/He ages. Geochimica et Cosmochimica Acta, 60: 4223-4229.

Ferreira, M.P. et al., 1975. Rare-gas dating. II. Attempted Unranium-Helium dating of young volcanic rocks from the Madeira archipelago. Earth and Planetary Science Letters, 25: 140-150.

Fitzgerald, P.G., Baldwin, S.L., Webb, L.E. and O'Sullivan, P.B., 2005. Interpretation of (U-Th)/He single grain ages from slowly cooled crustal terranes: A case study from the Transantarctic Mountains of southern Victoria Land. Chemical Geology, 225: 91-120.

Fleck, R.J., Sutter, J.F. and Elliot, D.H., 1977. Interpretation of discordant $^{40}Ar/^{39}Ar$ spectra of Mesozoic tholeiites from Antarctica. Geochimia et Cosmochimia Acta, 41: 15-32.

Fleischer, R.L., 1983. Theory of alpha recoil effects on radon release and isotopic disequilibrium. Geochimia et Cosmochimia Acta, 47: 779-784.

Fleischer, R.L., Price, P.B. and Walker, R.M., 1965a. Effects of temperature, pressure, and ionization of the formation and stability of fission tracks in minerals and glasses. Journal of Geophysical Research, 70: 1497-1502.

Fleischer, R.L., Price, P.B. and Walker, R.M., 1965b. The ion explosion spike mechanism for formation of charged particle tracks in solids. Journal of Applied Physics, 36: 3645-3652.

Fleischer, R.L., Price, P.B. and Walker, R.M., 1975. Nuclear Tracks in Solids: Principles and Applications. University of California Press, Berkeley, 605 pp.

Flores, G., 1973. The Cretaceous and Tertiary sedimentary basins of Mozambique and Zululand. In: G. Glant (Editor), Sedimentary basins of the African Coast, Part 2, South and East Coasts. Association of African Geological Survey, Paris, pp. 81-111.

Foster, D.A. and Gleadow, A.J.W., 1992. The morphotectonic evolution of rift-margin mountains in central Kenya: constraints from apatite fission-track thermochronology. Earth and Planetary Science Letters, 113: 157-171.

Foster, D.A. and Gleadow, A.J.W., 1996. Structural framework and denudation history of the flanks of the Kenya and Anza Rifts, East Africa. Tectonics, 15: 258-271.

Gaber, L.J., Foland, K.A. and Corbato, C.E., 1988. On the significance of argon release from biotite and amphibole during $^{40}Ar/^{39}Ar$ vacuum heating. Geochimica et Cosmochimica Acta, 52: 2457-2465.

Gadd, S.A. and Scrutton, R.A., 1997. An integrated thermomechanical model for transform continental margin evolution. Geo Marine Letters, 17: 21-30.

Galbraith, R.F., 1990. The radial plot; graphical assessment of spread in ages. In: S.A. Durrani and E.V. Benton (Editors), Proceedings of the 6th international fission track dating workshop. Nuclear Tracks and Radiation Measurements. Pergamon, Oxford, pp. 207-214.

Galbraith, R.F. and Laslett, G.M., 1993. Statistical models for mixed fission track ages. Nuclear Tracks and Radiation Measurements, 21: 459-470.

Gallagher, K., Brown, R.W. and Johnson, C., 1998. Fission track analysis and its application to geological problems. Annual Review Earth and Planetary Sciences, 26: 519-572.

Gallagher, K. and Sambridge, M., 1994. Genetic algorithms: a powerful method for large scale non-linear optimisation problems. Computers and Geosciences, 20: 1229-1236.

Geiger, M., 2004. Sedimentary and stratal patterns in Jurassic successions of western Madagascar. PhD Thesis, University of Bremen, Bremen, 146 pp.

Geiger, M., Clark, D.N. and Mette, W., 2004. Reappraisal of the timing of the break-up of Gondwana based on sedimentological and seismic evidence from the Morondava Basin, Madagascar. Journal of African Earth Sciences, 38: 363-381.

Gleadow, A.J.W., 1978. Anisotropic and variable track etching characteristics in natural sphenes. Nuclear Track Detection, 2: 105-117.

Gleadow, A.J.W., 1981. Fission track dating methods: What are the real alternatives? Nuclear Tracks and Radiation Measurements, 5: 3-14.

Gleadow, A.J.W., Belton, D.X., Kohn, B.P. and Brown, R.W., 2002. Fission track dating of phosphate minerals and ther thermochronology of apatite. In: J.M. Hughes, M.J. Kohn and J. Rakovan (Editors), Phosphates, Geochemical, Geobiological and Material Importance. Reviews in Mineralogy and Geochemistry, pp. 579-630.

Gleadow, A.J.W. and Duddy, I.R., 1981. A natural long-term track annealing experiment for apatite. Nuclear Tracks, 5: 169-174.

Gleadow, A.J.W., Duddy, I.R., Green, P.F. and Lovering, J., 1986. Confined fission track lengths in apatite: a diagnostic tool for thermal history analysis. Contributions to Mineralogy and Petrology, 94: 405-415.

Gleadow, A.J.W., Duddy, I.R. and Lovering, J.F., 1983. Fission track analysis: A new tool for the evaluation of thermal histories and hydrocarbon potential. Australian Petroleum Exploration Association, 23: 93-102.

Gleadow, A.J.W. and Lovering, J.F., 1977. Geometry factor for external detectors in fission track dating. Nuclear Track Detection, 1: 99-106.

Götze, J., 2002. Potential of cathodoluminescence (CL) microscopy and spectroscopy for the analysis of minerals and materials. Analytical and Bioanalytical Chemistry, 374: 703-708.

Goudi, A., 2004. The drainage system of Africa since the Cretaceous. Geomorphology, 67: 437-456.

Grantham, G.H. et al., 2005. The chemistry and age of Karoo-age andesitic lavas along the northern Mozambique coast. In: R.J. Pankhurst and G.D. Veiga (Editors), Gondwana 12, Mendoza, pp. 183.

Green, P.F., 1981. A new look at statistics in fission-track dating. Nuclear Tracks and Radiation Measurements, 5: 77-86.

Green, P.F., 1988. The relationship between track shortening and fission track age reduction in apatite: combined influences of inherent instability, annealing anisotropy, length bias and system calibration. Earth and Planetary Science Letters, 89: 335-352.

Green, P.F. and Duddy, I.R., 2006. Interpretation of apatite (U-Th)/He ages and fission track ages from cratons. Earth and Planetary Science Letters, 244: 541-547.

Green, P.F., Duddy, I.R., Gleadow, A.J.W. and Tingate, P.R., 1986. Fission-Track annealing in apatite: Track length measurements and the form of the Arrhenius plot. Nuclear Tracks and Radiation Measurements, 10: 323-328.

Green, P.F., Duddy, I.R., Gleadow, A.J.W., Tingate, P.R. and Laslett, G.M., 1986. Thermal annealing of fission tracks in apatite 1. A Qualitative Description. Chemical Geology (Isotope Geoscience Section), 59: 237-253.

Green, P.F., Duddy, I.R. and Laslett, G.M., 1988. Can fission track annealing in apatite be described by first-order kinetics? Earth and Planetary Science Letters, 87: 216-228.

Green, P.F. and Durrani, S.A., 1977. Annealing studies of tracks in crystals. Nuclear Track Detection, 1: 33-39.

Grove, M. and Harrison, T.M., 1996. ^{40}Ar* diffusion in Fe-rich phlogopite. American Mineralogist, 81: 940-951.

Hancox, P.J., Brandt, D. and Edwards, H., 2002. Sequence stratigraphic analysis of the Early Cretaceous Maconde Formation (Ruvuma Basin), northern Mozambique. Journal of African Earth Sciences, 34: 291-297.

Harrison, T.M., 1981. Diffusion of ^{40}Ar in hornblende. Contributions to Mineralogy and Petrology, 78: 324-331.

Harrison, T.M., Duncan, I. and McDougall, I., 1985. Diffusion of ^{40}Ar in biotite: temperature, pressure and compositional effects. Geochimia et Cosmochimia Acta, 49: 2461-2468.

Harrison, T.M. and Fitz Gerald, J.D., 1986. Exsolution in hornblende and its consequences for ^{40}Ar/^{39}Ar age spectra and closure temperature. Geochimia et Cosmochimia Acta, 50: 247-253.

Hawkesworth, C.J., Kelly, S.P., Turner, S., Le Roex, A. and Storey, B.C., 1999. Mantle processes during the Gondwana break-up and dispersal. Journal of African Earth Sciences, 28: 239-261.

Hess, J.C., Lippolt, H.J., Gurbanov, A.G. and Michalski, I., 1993. The cooling history of the late Pliocene Eldzhurtinskiy granite (Caucasus, Russia) and the potential of grain-size/age relationships. Earth and Planetary Science Letters, 117: 393-406.

Hodges, K.V., Hames, W.E. and Bowring, S.A., 1994. ^{40}Ar/^{39}Ar age gradients in micas from a high-temperature-low-pressure metamorphic terrane: evidences for very

slow cooling and implications for the interpretation of age spectra. Geology, 22: 55-58.

Hoffmann, C. et al., 1997. Timing of the Ethiopian flood basalt event: implication for plume birth and global change. Nature, 389: 838-841.

Honess, A.P., 1927. The nature, origin and interpretation of the etch figures on crystals. John Wiley and Sons, New York, pp. 154.

House, M., Farley, K.A. and Stockli, D.F., 2000. Helium chronometry of apatite and titanite using Nd-YAG laser heating. Earth and Planetary Science Letters, 183: 365-368.

House, M., Wernicke, B. and Kohn, B., 1999. An empirical test of helium diffusion in apatite: borehole data from the Otway basin, Australia. Earth and Planetary Science Letters, 170: 463-474.

Hughes, J.M., Cameron, M. and Crowley, K.D., 1990. Crystal structure of natural ternary apatites: Solid solution in the $Ca_5(PO_4)_3X$ (X=F, Cl, OH) system. American Mineralogist, 75: 295-304.

Hughes, J.M., Cameron, M. and Mariano, A.N., 1991. Rare element ordering and structural variations in natural rare-earth-bearing apatites. American Mineralogist, 76: 1165-1173.

Hurford, A.J., 1990a. International Union of Geological Sciences Subcommission on Geochronology Recommendation for standardization of fission track dating calibration and data reporting. Nuclear Tracks and Radiation Measurements, 17: 233-236.

Hurford, A.J., 1990b. Standardization of fission track dating calibration: Recommendation by the Fission Track Working Group of the I.U.G.S. Subcommission on Geochronology. Chemical Geology, 80: 171-178.

Hurford, A.J., Carter, A., Barbarand, J. and Walgenwitz, F., 2000. Acid and chloro-tincles, rare earths and differing angles, just what might be important in understanding track annealing in apatite? Geological Society Australia Abstracts, 58: 175-176.

Hurford, A.J. and Green, P.F., 1983. The zeta age calibration of fission track dating. Isotope Geoscience, 1: 285-317.

Hurley, P.M., 1954. The helium method and the distribution and migration of helium in rocks. In: H. Faul (Editor), Nuclear Geology. Wiley, New York, pp. 187.

Jacobs, J., Fanning, C.M., Henjes-Kunst, F., Olesch, M. and Paech, H.-J., 1998. Continuation of the Mozambique Belt into East Antarctica: Grenville-age metamorphsim and polyphase Pan-African high-grade events in central Dronning Maud Land. Journal of Geology, 106: 385-406.

Jaffey, A.H., Flynn, K.F., Glendenin, L.E., Bentley, W.C. and Essling, A.M., 1971. Precision measuments of the half-lives and specific activities of ^{235}U and ^{238}U. Physical Review, C4: 1889-1906.

Janssen, M.E., Stephenson, R.A. and Cloethingh, S., 1995. Temporal and spatial correlations between changes in plate motions and the evolution of rifted basins in Africa. Geological Society of America Bulletin, 107: 1317-1332.

Jokat, W., Boebel, T., König, M. and Meyer, U., 2003. Timing and Geometry of early Gondwana breakup. Journal of Geophysical Research, 108: 2428-2442.

Jolivet, M., Dempster, T. and Cox, R., 2003. Distribution of U and Th in apatites: Implications for (U-Th)/He thermochronology. Comptes Rendus de l'Academie des Sciences, Serie II Sciences de la Terre et des Planetes, 355: 899-906.

Jonckheere, R., Ratschbacher, L. and Wagner, G.A., 2003. A repositioning technique for counting induced fission tracks in muscovite external detectors in single-grain dating of minerals with low and inhomogeneous uranium concentrations. Radiation Measurements, 37: 217-219.

Jonckheere, R.C. and Wagner, G.A., 2000. On the thermal stability of fossil and neutron-induced fission-tracks in natural titanite. Nuclear Instruments and Methods - Physics Research B, 168: 78-87.

Jones, D.L., Duncan, R.A., Briden, J.C., Randall, D.E. and MacNiocaill, C., 2001. Age of Batoka basalts, northern Zimbabwe, and the duration of Karoo Igneous Province magmatism. Geochemisty, Geophysics, Geosystems - G^3, 2: paper number 2000GC000110.

Keevil, N.B., 1941. Terminology in age work. American Journal of Science, 239: 608-611.

Kelley, S.P., 2002. Excess argon in K-Ar and Ar-Ar geochronology. Chemical Geology, 188: 1-22.

Ketcham, R.A., Donelick, M.B. and Carlson, W.D., 1999. Variability of apatite fission-track annealing kinetics: III. Extrapolation to geological time scales. American Mineralogist, 84: 1235-1255.

Ketcham, R.A., Donelick, R.A. and Donelick, M.B., 2000. AFTSolve: A program for multi-kinetic modeling of apatite fission-track data. Geological Materials Research, 2: 1-32.

Kohn, B.P. et al., 2002. Shaping the Australian crust over the last 300 million years: insights from fission track thermotectonic imaging and denudation studies of key terranes. Australian Journal of Earth Sciences, 49: 679-717.

Kohn, B.P., Wagner, M.E., Lutz, T.M. and Organist, G., 1993. Anomalous Mesozoic thermal regime, central Appalachian Piedmont; evidence from sphene and zircon fission-track dating. Journal of Geology, 101: 779-794.

Kuiper, Y.D., 2002. The interpretation of inverse isochron diagrams in $^{40}Ar/^{39}Ar$ geochronology. Earth and Planetary Science Letters, 203: 499-506.

Kusky, T.M., Abdelsalam, R.D., Tucker, R.D., and Stern, R.J., 2003. Evolution of the East African and related orogens and the assembly of Gondwana. Precambrian Research, 123: 81-85.

Lächelt, S., 2004. The Geology and Mineral Resources of Mozambique. Direcção Nacional de Geologia Moçambique (DNG), Maputo, 515 pp.

Lanphere, M.A. and Dalrymple, G.B., 1978. The use of $^{40}Ar/^{39}Ar$ data in evaluation of disturbed K-Ar systems. U.S. Geological Survey Open-file Report 78-701, pp. 241-243.

Laslett, G.M. and Galbraith, R.F., 1996. Statistical modelling of thermal annealing of fission tracks in apatite. Geochimica et Cosmochimica Acta, 60: 5117-5131.

Laslett, G.M., Green, P.F., Duddy, I.R. and Gleadow, A.J.W., 1987. Thermal annealing of fission tracks in apatite 2. A Quantitative Analysis. Chemical Geology (Isotope Geoscience Section), 65: 1-13.

Lawver, L.A., Royer, J.-Y., Sandwell, D.T. and Scotese, C.R., 1991. Evolution of the Antarctic continental margins. In: M.R.A. Thomson, J.A. Crame and J.W. Thomson (Editors), Geological Evolution of Antarctica. Cambridge University Press, Cambridge, pp. 533-540.

Lee, J.K.W., 1993. The Argon release mechanisms of hornblende in vacuo. Chemical Geology, 106: 133-170.

Lee, J.K.W., 1995. Multipath diffusion in geochronology. Contributions to Mineralogy and Petrology, 120: 60-82.

Lee, J.K.W., Onstott, T.C., Cashman, K.V., Cumbest, R.J. and Johnson, D., 1991. Incremental heating of hornblende in vacuo: Implications for ^{40}Ar-^{39}Ar geochronology and the interpretation of thermal histories. Geology, 19: 872-876.

Lippolt, H.J., Leitz, M., Wernicke, R.S. and Hagedorn, B., 1994. (Uranium +thorium)/helium dating of apatite: experience with samples from different geochemical environments. Chemical Geology (Isotope Geoscience Section), 112: 179-191.

Lister, G.S., Etheridge, M.A. and Symonds, P.A., 1986. Detachment faulting and the evolution of passive continental margins. Geology, 14: 246-250.

Lo, C.H., Lee, J.K.W. and Onstott, T.C., 2000. Argon release mechanisms of biotite in vacuo and the role of short-circuit diffusion and recoil. Chemical Geology, 165: 135-166.

Lorencak, M., Kohn, B.P., Osadetz, K.G. and Gleadow, A.J.W., 2004. Combined apatite fission track and (U-Th)/He thermochronology in a slowly cooled terrane: results from a 3440 m deep drill hole in the Canadian Shield. Earth and Planetary Science Letters, 227: 87-104.

Ludwig, K.R., 2001. Isoplot 2.49 - A Geochronological Toolkit for Microsoft Excel, Berkeley Geochronology Center Special Publication 1a.

Malod, J.A., Mougenot, D., Raillard, S. and Maillard, A., 1991. Nouvelles constraintes sur la cinematique de Madagascar; les structures de la Caine Davie. Comptes Rendus de l'Academie des Sciences, Serie II Sciences de la Terre et des Planetes, 312: 1639-1646.

Mamyrin, B.A. and Tolstikhin, I.N., 1984. Helium isotopes in nature. Elsevier, Amsterdam, pp. 352.

McDougall, I. and Harrison, T.M., 1999. Geochronology and Thermochronology by the $^{40}Ar/^{39}Ar$ Method. Oxford University Press, New York, 269 pp.

McIntyre, G.A., Brooks, C., Compston, W. and Turek, A., 1966. The statistical assessment of Rb-Sr isochrons. Journal of Geophysical Research, 71: 5459.

McKenzie, D., 1978. Some remarks on the development of sedimentary basins. Earth and Planetary Science Letters, 40: 25-32.

Meesters, A.G.C.A. and Dunai, T.J., 2002a. Solving the production-diffusion equation for finite diffusion domains of various shapes; Part I, Implications for low-temperature (U-Th)/He thermochronology. Chemical Geology, 186: 333-344.

Meesters, A.G.C.A. and Dunai, T.J., 2002b. Solving the production-diffusion equation for finite diffusion domains of various shapes; Part II, Application to cases with alpha-ejection and nonhomogeneous distribution of the source. Chemical Geology, 186: 347-363.

Meesters, A.G.C.A. and Dunai, T.J., 2005. A noniterative solution of the (U-Th)/He age equation, Geochemistry, Geophysics, Geosystems - G^3. 6: Q04002, doi: 10.1029/2004GC000834.

Meier, S., 1999. Paleozoic and Mesozoic tectono-thermal history of central Dronning Maud Land, East Antarctica - evidence from fission-track thermochronology. PhD Thesis, University of Bremen, Bremen, 150 pp.

Meier, S., Jacobs, J. and Olesch, M., 2004. Tectono-thermal Evolution of Central Dronning Maud Land, East Antarctica, from Mid-Palaeozoic to Cenozoic Times: Zircon and Apatite Fission-Track Data from the Conradgebirge and Östliche Petermannkette. In: H.-J. Paech (Editor), International Geomaud Expedition of the BGR to central Dronning Maud Land in 1995/96 - Volume 1: Geological results. Geologisches Jahrbuch: Reihe B, Regionale Geologie Ausland, Polar Issue No. 10. Bundesanstalt für Geowissenschaften und Rohstoffe, Hannover, pp. 562.

Merrihue, C.M. and Turner, G., 1966. Potassium-argon dating by activation with fast neutrons. Journal of Geophysical Research, 71: 2852-2857.

Miller, D.S., Eby, N., McCorkell, R., Rosenberg, P.E. and Suzuki, M., 1990. Results of interlaboratory comparison of fission-track ages for the 1988 Fission Track Workshop. Nuclear Tracks and Radiation Measurements, 17: 237-245.

Milner, S.C., le Roex, A.P. and O'Connor, J.M., 1995. Age of Mesozoic igneous rocks in northwestern Namibia, and their relation to the continetal breakup. Journal of the Geological Society of London, 152: 97-104.

Mougenot, D., Recq, M., Virlogeux, M. and Lepvrier, C., 1986. Seaward extension of the East African Rift. Nature, 321: 599-603.

Müller, R.D., Roest, W.R., Royer, J.-Y., Gahagan, L.M. and Sclater, J.G., 1997. Digital Isochrons of the world's ocean floor. Journal of Geophysical Research, 102: 3211-3214.

Naeser, C.W. and Forbes, R.B., 1976. Variation of fission track ages with depth in two deep drill holes. Transactions of the American Geophysical Union, 57: 353.

Naeser, C.W. and McKee, E.H., 1970. Fission-track and K-Ar ages of Tertiary ash-flow tuffs, north-central Nevada. Geological Society of America Bulletin, 81: 3375-3384.

Nairn, A.E.L., Lerche, I. and Iliffe, J.E., 1991. Geology, basin analysis, and hydrocarbon potential of Mozambique and the Mozambique Channel. Earth Science Reviews, 30: 81-124.

Nier, A.O., 1950. A redetermination of the relative abundances of the isotopes of carbon, nitrogen, oxygen, argon and potassium. Physical Review, 77: 789-793.

Noble, W.D., Foster, D.A. and Gleadow, A.J.W., 1997. The post-Pan-African thermal and extensional history of crystalline basement rocks in eastern Tanzania. Tectonophysics, 275: 331-350.

Nyblade, A.A., Pollack, H.N., Jones, D.L., Podmore, F. and Mushayandedbvu, M., 1990. Terrestrial heat flow in east and southern Africa. Journal of Geophysical Research, 95: 17371-17384.

O'Sullivan, P.B. and Parrish, R.R., 1995. The importance of apatite composition and single-grain ages when interpreting fission track data from plutonic rocks, a case

study from the Coast Ranges, British Columbia. Earth and Planetary Science Letters, 132: 213-224.

Perits, F. et al., 2002. Map showing geology, oil and gas fields and geological provinces of Africa, Ver. 2.0. U.S. Department of the Interior and U.S. Geological Survey, Open File Report 97-470A.

Pinna, P. and Marteau, P., 1987. Carta geologica de Moçambique, 1:1,000,000 scale with explanatory notes, Instituto Naçional de Geologica, Maputo.

Popoff, M., 1988. The Benue Trough; its evolution in the Atlantic equatorial fracture zone. Journal of African Earth Sciences, 7: 480-509.

Powell, C.M., Roots, S.R. and Veevers, J.J., 1988. Pre-breakup continental extension in Eastern Gondwanaland and the early opening of the eastern Indian Ocean. Tectonophysics, 155: 261-283.

Price, P.B. and Walker, R.M., 1962a. Observation of charged-particle tracks in solids. Journal of Applied Physics, 33: 3400-3406.

Price, P.B. and Walker, R.M., 1962b. Chemical etching of charged-particle tracks in solids. Journal of Applied Physics, 33: 3407-3412.

Raab, M., Brown, R.W., Gallagher, K., Carter, A. and Weber, K., 2002. Late Cretaceous reactivation of major crustal shear zones in northern Namibia: constrains from apatite fission track analysis. Tectonophysics, 349: 75-92.

Ravenhurst, C.E., Roden, M.K., Willett, S.D. and Miller, D.S., 1992. Dependence of fission track annealing kinetics on apatite crystal chemistry, 7th International Workshop on Fission-Track Thermochronology, Philadelphia.

Reeves, C.V., De Wit, M. and Sahu, B.K., 2004. Tight reasssembly of Gondwana exposes Phanerozoic shears in Africa a global tectonic player. In: B.C. Storey, H. Hiller, N. Mortimer, H.J. Campell and T.A. Moore (Editors), Gondwana 11 - Correlations and Connections, Christchurch, pp. 15.

Reeves, C.V., Sahu, B.K. and de Wit, M., 2002. A re-examination of the paleo-position of Africa's eastern neighbours in Gondwana. Journal of African Earth Sciences, 34: 101-108.

Reiners, P.W. and Farley, K.A., 1999. Helium diffusion and (U-Th)/He thermochronometry of titanite. Geochimia et Cosmochimia Acta, 63: 3825-3859.

Reiners, P.W. and Farley, K.A., 2001. Influence of crystal size on apatite (U-Th)/He thermochronology: an example from the Bighorn Mountains, Wyoming. Earth and Planetary Science Letters, 188: 413-420.

Reiners, P.W., Spell, T.L., Nicolescu, S. and Zanetti, K.A., 2004. Zircon (U-Th)/He thermochronometry: He diffusion and comparison with $^{40}Ar/^{39}Ar$ dating. Geochimica et Cosmochimica Acta, 68: 1857-1887.

Renne, P.R. et al., 1992. The age of the Paraná flood volcanism, rifting of Gondwanaland, and the Jurassic-Cretaceous boundary. Science, 258: 975-979.

Riepshoff, H., 2005. Auswertung und Interpretation tektonischer Strukturen am Kontinentalrand Nordmoçambiques basierend auf Satellitenbildern. Universität Bremen, pp. 34.

Roddick, J.C., 1978. The application of isochron diagrams in $^{40}Ar/^{39}Ar$ dating: A discussion. Earth and Planetary Science Letters, 41: 233-244.

Roeser, H.A., Fritsch, J. and Hinz, K., 1996. The development of the crust off Dronning Maud Land, East Antarctica. In: B.C. Storey, E.C. King and R.A. Livermore (Editors), Weddell Sea Tectonics and Gondwana Break-up. Geological Society Special Publication, London, pp. 243-264.

Rutherford, E., 1906. The Production of Helium from Radium and the Transfromation of Matter, Radioactive Transfromations. Yale University Press.

Salman, G. and Abdula, I., 1995. Development of the Mozambique and Ruvuma sedimentary basins, offshore Mozambique. Sedimentary Geology, 96: 7-41.

Schandelmeier, H., Bremer, F. and Holl, H.-G., 2004. Kinematic evolution of the Morondava rift basin of SW Madagascar - from wrench tectonics to normal extension. Journal of African Earth Sciences, 38: 321-330.

Seward, D., Grujic, D. and Schreurs, G., 2004. An insight into the breakup of Gondwana; identifying events through low-temperature thermochronology from the basement rocks of Madagascar. Tectonics, 23: 3-22.

Spencer, A.S. et al., 2004. The importance of residing in good neigbourhood: rechecking the rules of the game for apatite (U-Th)/He thermochronology. In: P. Andriessen (Editor), 10th international Fission track dating conference, Amsterdam, pp. 20.

Steiger, R.J. and Jäger, E., 1977. Subcommission on geochronology: Convention on the use of decay constants in geo- and cosmochronology. Earth and Planetary Science Letters, 36: 359-362.

Stockli, D.F., Farley, K.A. and Dumitru, T.A., 2000. Calibration of the apatite (U-Th)/He thermochronometer on an exhumed fault block, White Mountains, California. Geology, 28: 983-986.

Stoenner, R.W., Schaeffer, O.A. and Katcoff, S., 1965. Half-lives of argon-37, argon-39 and argon-42. Science, 148: 1325-1328.

Stollnhofen, H., 1999. Karoo Syn-rift-Sedimentation und ihre tektonische Kontrolle am entstehenden Kontinentalrand Namibias. Zeitschrift der deutschen geologischen Gesellschaft, 149: 519-632.

Storey, B.C., 1995. The role of mantle plumes in continental breakup: case histories from gondwana breakup. Nature, 377: 301-308.

Strutt, R.J., 1908. On the accumulation of helium in geological time. Royal Society Proceedings, A 81: 272-277.

Strutt, R.J., 1909. The accumulation of helium in geological time-II. Royal Society Proceedings, A83: 96-99.

Sudarsanan, K. and Young, R.A., 1978. Structural interactions of F, Cl and OH in apatites. Acta Crystallographica, B34: 1401-1407.

Summerfield, M.A., 1985. Plate tectonics and landscape development on the African continent. In: M. Morisawa and T.J. Hack (Editors), Tectonic Geomorphology. Unwin Hyman Ltd, Winchester, pp. 27-51.

Summerfield, M.A., 1991. Sub-aerial denudation of passive margins: regional elevation versus local relief models. Earth and Planetary Science Letters, 102: 460-469.

Thomas, D.S.G. and Shaw, P., 1988. Late Cainozoic drainage evolution in the Zambezi Basin: geomorphologic evidence from the Kalahari rim. Journal of African Earth Sciences, 7: 611-618.

Turekian, K., Kharkar, D.P., Funkhouser, J. and Schaeffer, O.A., 1970. An evaluation of the uranium-helium method of dating fossil bones. Earth and Planetary Science Letters, 7: 420-424.

Unternehr, P., Curie, D., Olivet, J.L., Goslin, J. and Beuzart, P., 1988. South Atlantic fits and intraplate boundaries in Africa and South America. Tectonophysics, 155: 169-179.

Van der Beek, P.A., Mbede, E., Andriesssen, P. and Delvaux, D., 1998. Denudation history of the Malawi and Rukwa Rift flanks (East African Rift System) from Apatite fission track thermochronology. Journal of African Earth Sciences, 26: 363-385.

Verniers, J., Jourdan, P.P., Paulis, R.V., Frasca-Spada, L. and Bock, F.R.D., 1989. The Karroo Graben of Metangula Northern Mozambique. Journal of African Earth Sciences, 9: 137-158.

von Daniels, C.H., Gramann, F., Jaritz, W., Kemper, E. and Wilhelm, K., 1977. Zum Vorkommen von Sedimentgesteinen des Mesozoikums und des Tertitärs im Küstengebiet von Nordmoçambique. Geologisches Jahrbuch. Reihe B: Regionale Geologie Ausland, 26: 167-172.

Wagner, G.A., 1981. Fission-track ages and their geological interpretation. Nuclear Tracks and Radiation Measurements, 5: 15-25.

Wagner, G.A. and Van den haute, P., 1992. Fission-Track Dating. Ferdinand Enke Verlag, Stuttgart, 285 pp.

Wagner, M., Altherr, R. and Van den haute, P., 1992. Apatite fission-track analysis of Kenyan basement rocks: constraints on the thermotectonic evolution of the Kenya dome. A reconnaissance study. Tectonophysics, 204: 93-110.

Walford, H.L., White, N.J. and Sydow, J.C., 2005. Solid sediment load history of the Zambesi Delta. Earth and Planetary Science Letters, 238: 49-63.

Warnock, A.C., Zeitler, P.K., Wolf, R.A. and Bergmann, S.C., 1997. An evaluation of low-temperature apatite (U-Th)/He thermochronometry. Geochimia et Cosmochimia Acta, 61: 5371-5377.

Wernicke, B.P., 1985. Uniform-sense normal simple shear of the continental lithosphere. Canadian Journal of Earth Sciences, 22: 108-125.

Wolf, R.A., Farley, K.A. and Kass, D.M., 1998. Modeling of the temperature sensivity of the apatite (U-Th)/He thermochronometer. Chemical Geology, 148: 105-114.

Wolf, R.A., Farley, K.A. and Silver, L., 1996a. Assessment of (U-Th)/He thermochronometry: the low-temperature history of the San Jacinto Mountains, California. Geology, 25: 65-68.

Wolf, R.A., Farley, K.A. and Silver, L., 1996b. Helium diffusion and low temperature thermochronology of apatite. Geochimia et Cosmochimia Acta, 60: 4231-4240.

Woolley, A.R. and Garson, M.S., 1970. Petrochemical and tectonic relationship of the Malawi carbonatite-alkaline province and the Lupata-Lebombo volcanics. In: T.N. Clifford and I.G. Gass (Editors), African Magmatism and Tectonics. Oliver and Boyd, Edinburgh, pp. 237-262.

Wopfner, H. and Kaaya, C.Z., 1991. Stratigraphy and morphotectonics of Karoo deposits of the northern Selous Basin, Tanzania. Geological Magazine, 128: 319-334.

Yamada, R., Tagami, T., Nishimura, S. and Ito, H., 1995. Annealing kinetics of fission tracks in zircon: an experimental study. Chemical Geology (Isotope Geoscience Section), 122: 249-258.

York, D., 1969. Least squares fitting of a straight line with correlated errors. Earth and Planetary Science Letters, 5: 320-324.

Zeitler, P.K., Herczig, A.L., McDougall, I. and Honda, M., 1987. U-Th-He dating of apatite: a potential thermochronometer. Geochimia et Cosmochimia Acta, 51: 2865-2868.

Ziegler, P.A. and Cloething, S., 2004. Dynamic processes controlling the evolution of rifted basins. Earth-Science Reviews, 64: 1-50.

Appendix A

TITANITE FISSION TRACK – RADIAL PLOTS

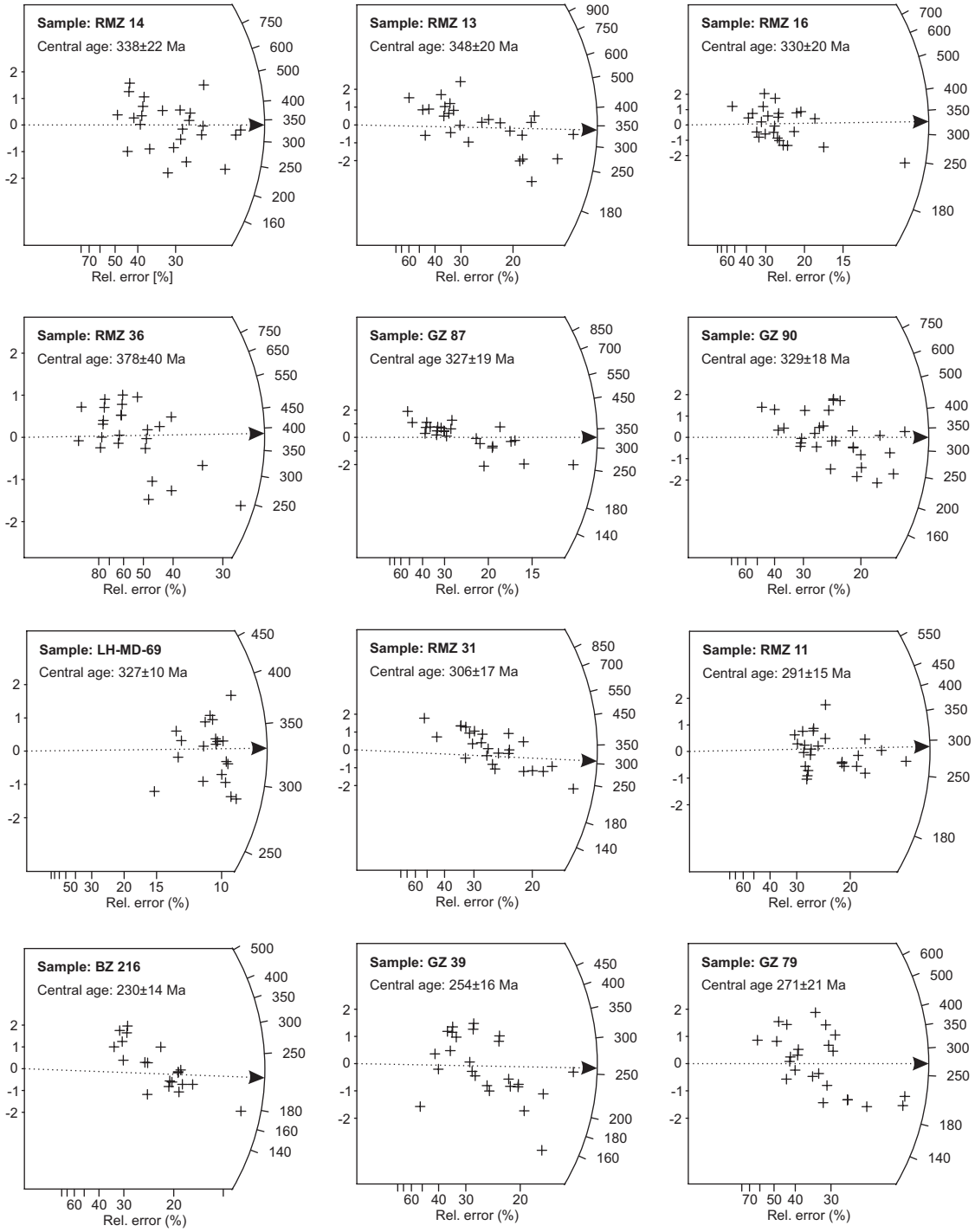

Appendix A

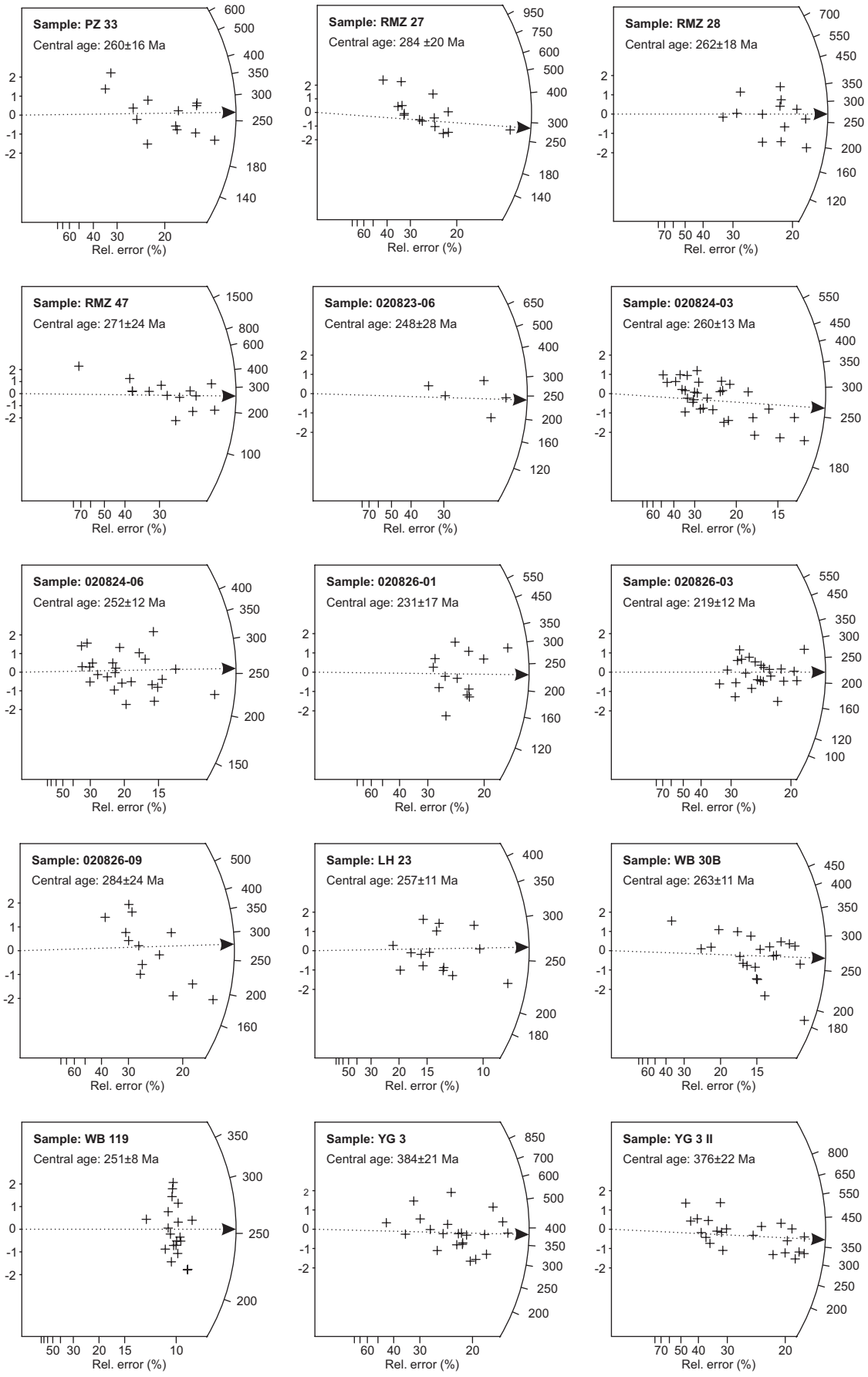
Sample: PZ 33
Central age: 260±16 Ma
Sample: RMZ 27
Central age: 284 ±20 Ma
Sample: RMZ 28
Central age: 262±18 Ma
Sample: RMZ 47
Central age: 271±24 Ma
Sample: 020823-06
Central age: 248±28 Ma
Sample: 020824-03
Central age: 260±13 Ma
Sample: 020824-06
Central age: 252±12 Ma
Sample: 020826-01
Central age: 231±17 Ma
Sample: 020826-03
Central age: 219±12 Ma
Sample: 020826-09
Central age: 284±24 Ma
Sample: LH 23
Central age: 257±11 Ma
Sample: WB 30B
Central age: 263±11 Ma
Sample: WB 119
Central age: 251±8 Ma
Sample: YG 3
Central age: 384±21 Ma
Sample: YG 3 II
Central age: 376±22 Ma
Rel. error (%)

Appendix B

APATITE FISSION TRACK – DATA PLOTS

B.1 Western Axial Granulite Complex

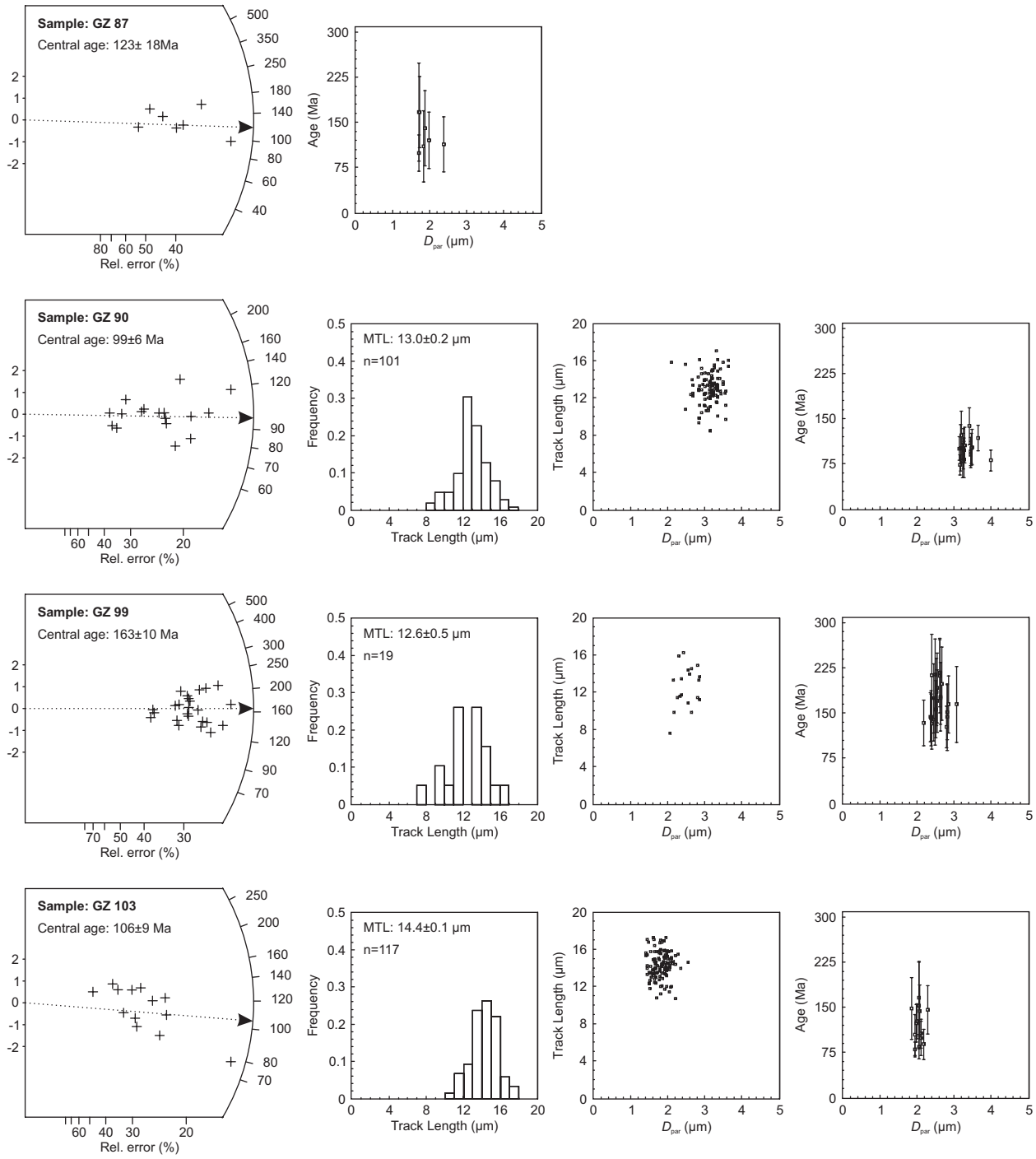

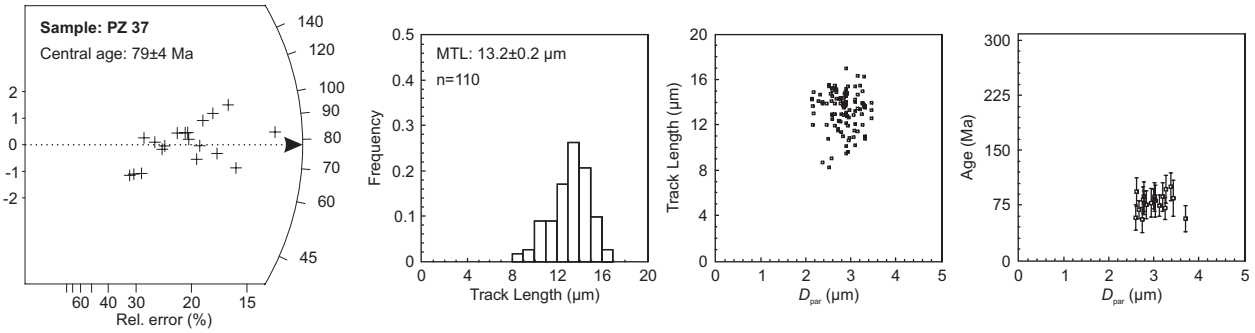

B.2 Mount Tumbine

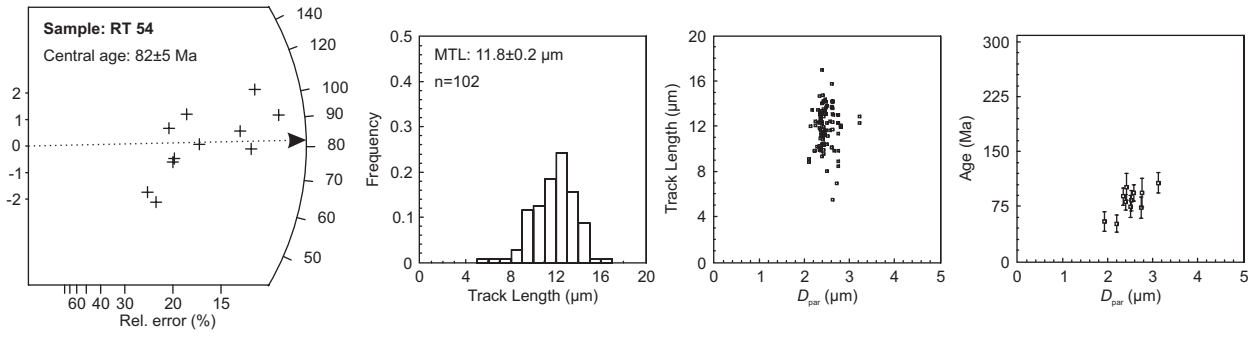

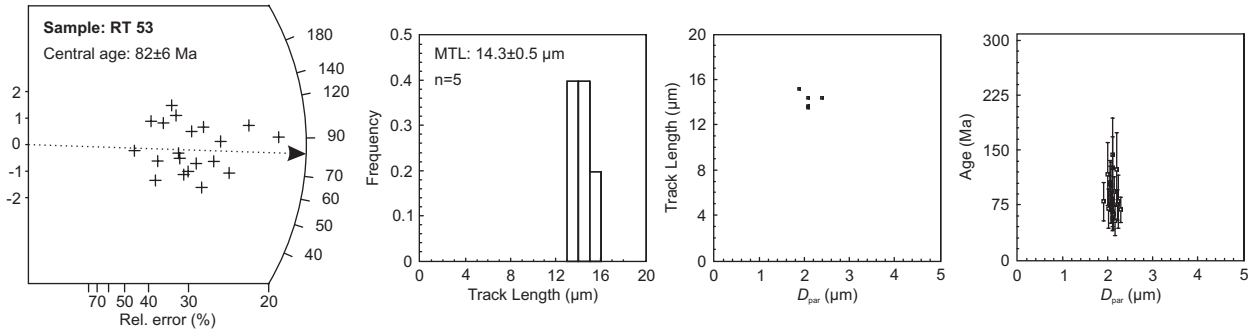

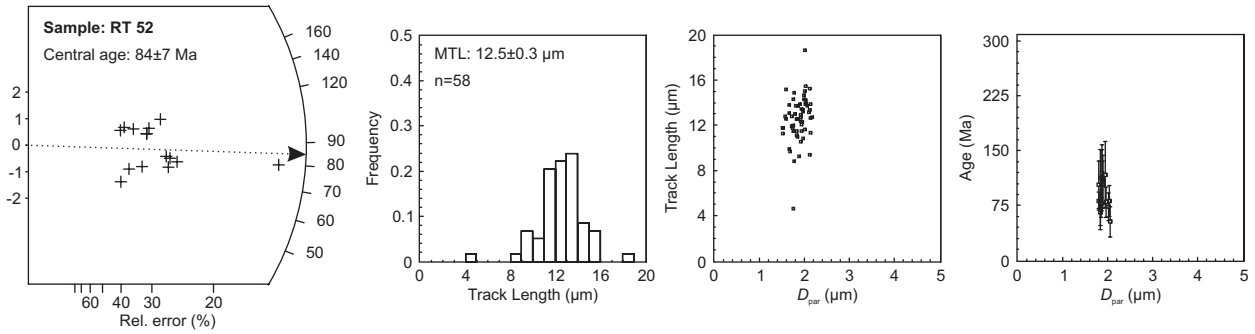

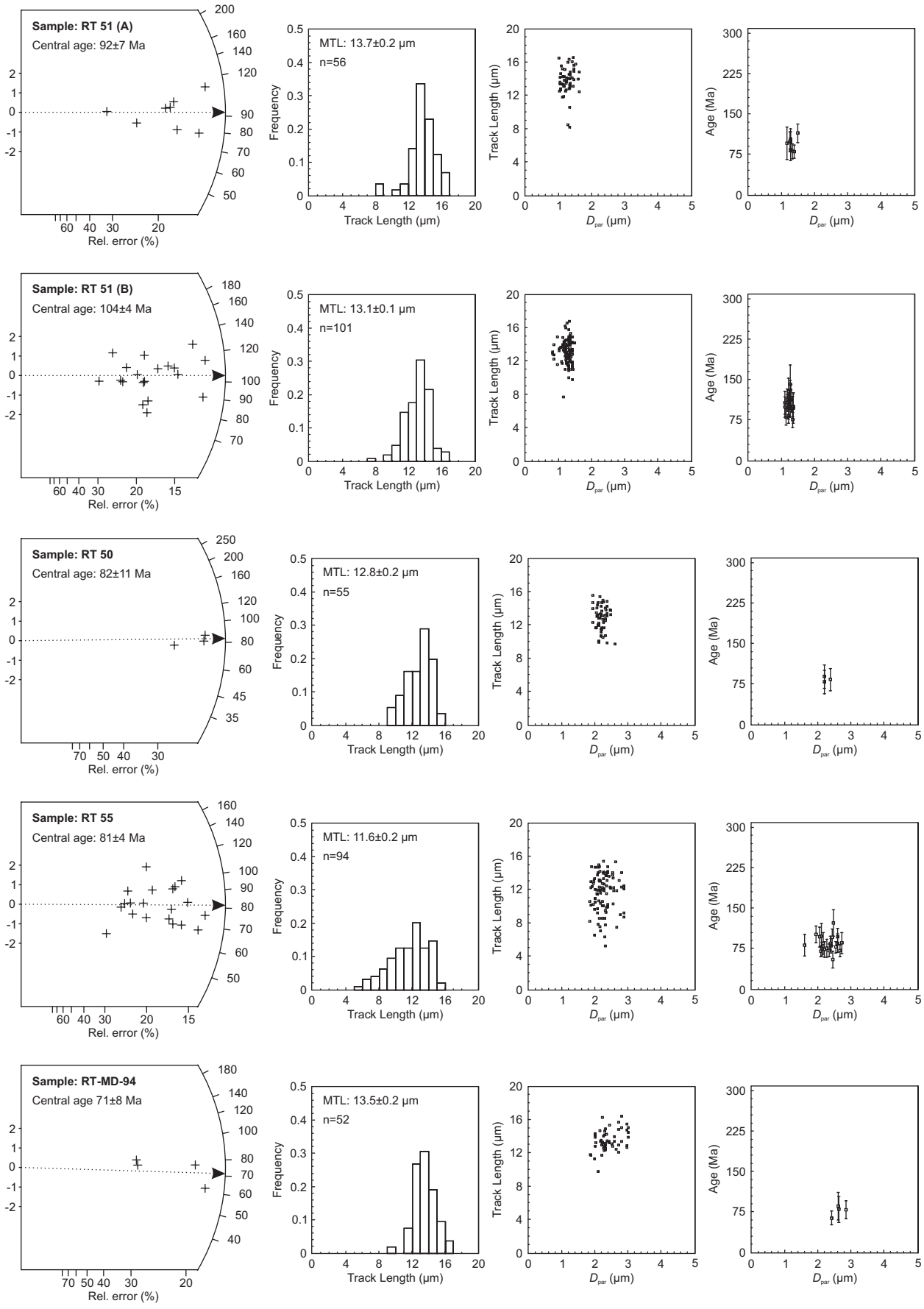
Sample: RT 51 (A)
Central age: 92±7 Ma
Rel. error (%)
MTL: 13.7±0.2 µm
n=56
Frequency
Track Length (µm)
Track Length (µm)
Age (Ma)
D_{par} (µm)
Sample: RT 51 (B)
Central age: 104±4 Ma
MTL: 13.1±0.1 µm
n=101
Sample: RT 50
Central age: 82±11 Ma
MTL: 12.8±0.2 µm
n=55
Sample: RT 55
Central age: 81±4 Ma
MTL: 11.6±0.2 µm
n=94
Sample: RT-MD-94
Central age 71±8 Ma
MTL: 13.5±0.2 µm
n=52

B.3 Southern basement – *C* group

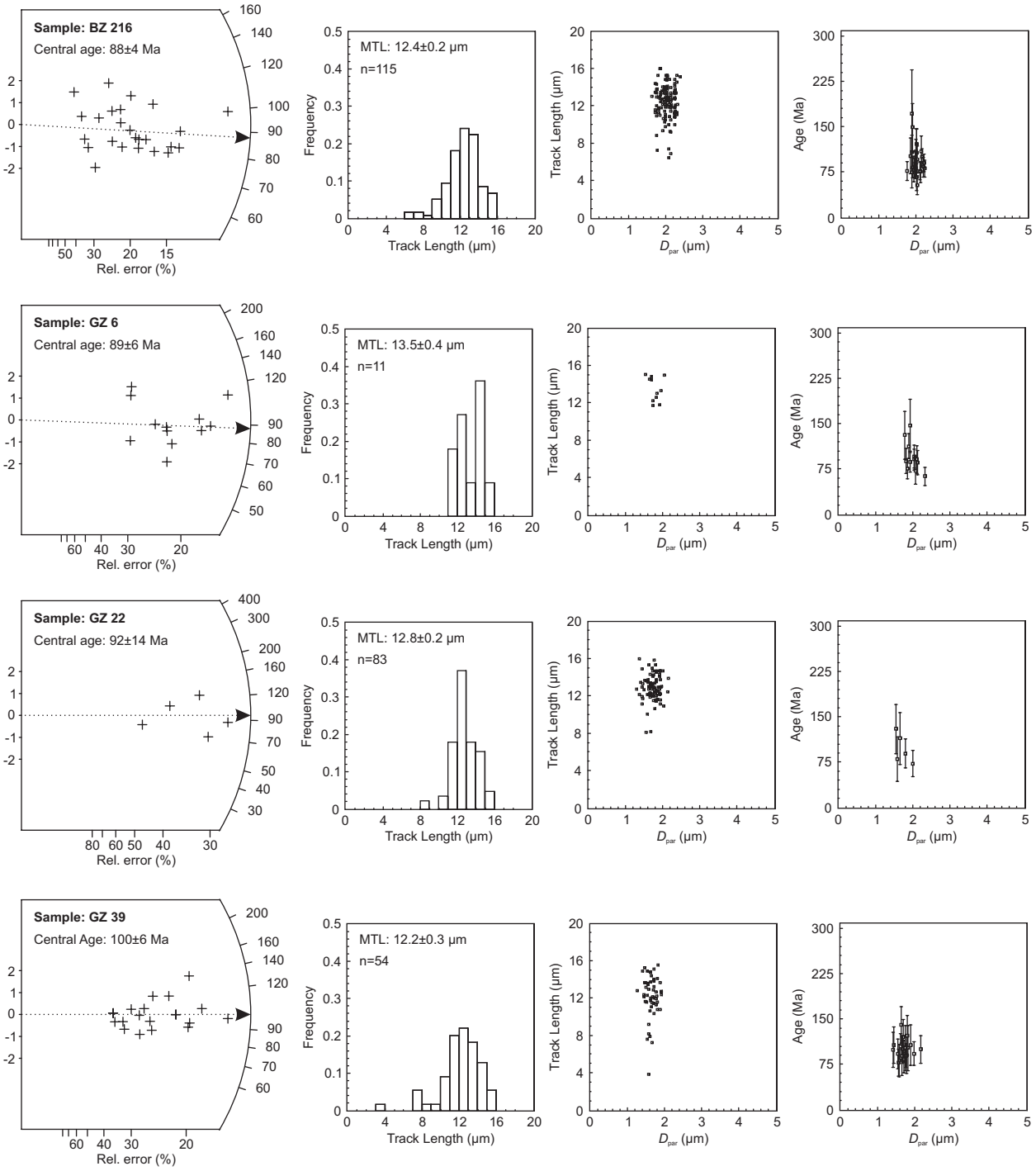

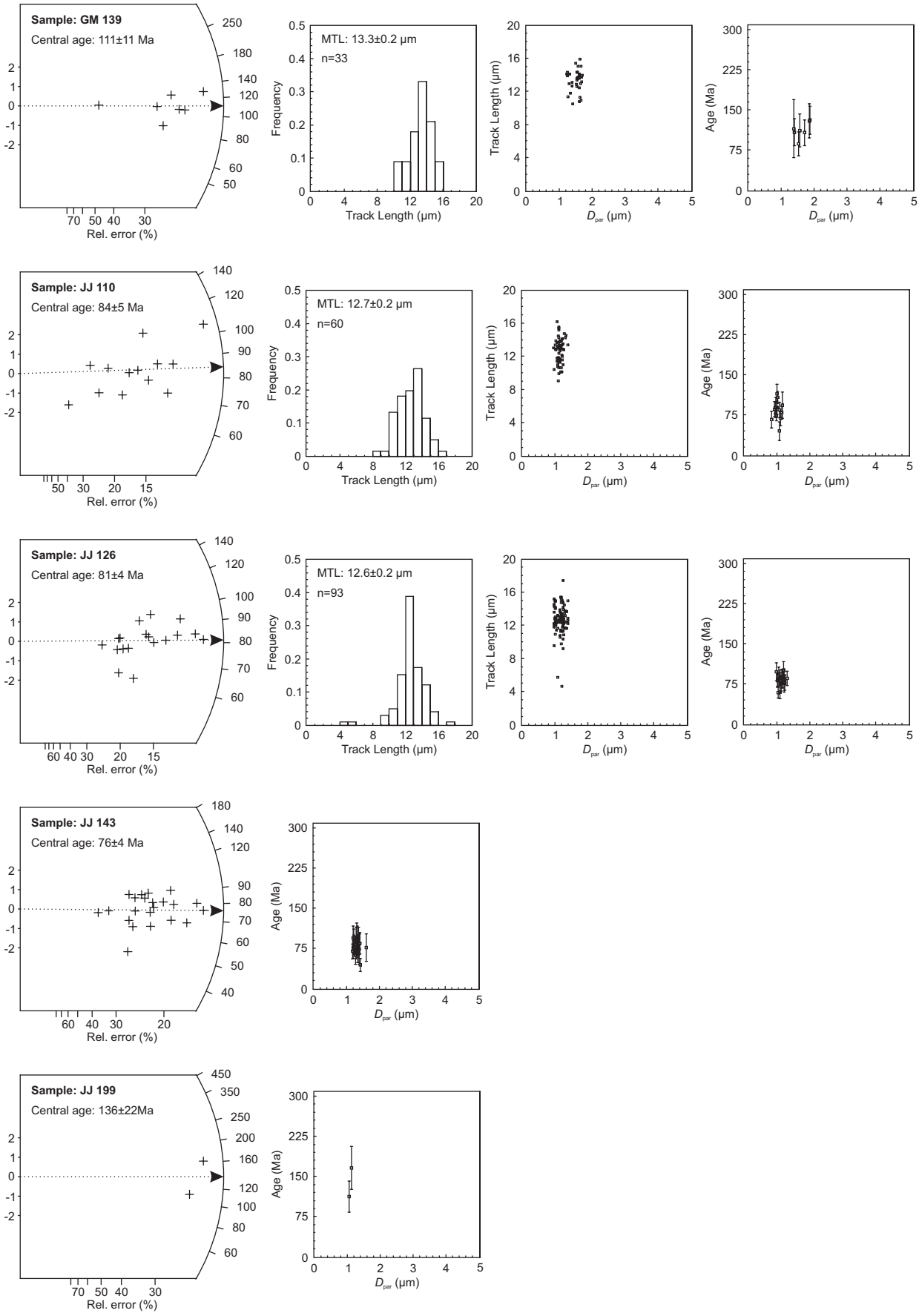
Sample: GM 139
Central age: 111±11 Ma
Rel. error (%)
MTL: 13.3±0.2 µm
n=33
Frequency
Track Length (µm)
Track Length (µm)
Age (Ma)
D_{par} (µm)
Sample: JJ 110
Central age: 84±5 Ma
Rel. error (%)
MTL: 12.7±0.2 µm
n=60
Frequency
Track Length (µm)
Track Length (µm)
Age (Ma)
D_{par} (µm)
Sample: JJ 126
Central age: 81±4 Ma
Rel. error (%)
MTL: 12.6±0.2 µm
n=93
Frequency
Track Length (µm)
Track Length (µm)
Age (Ma)
D_{par} (µm)
Sample: JJ 143
Central age: 76±4 Ma
Rel. error (%)
Age (Ma)
D_{par} (µm)
Sample: JJ 199
Central age: 136±22Ma
Rel. error (%)
Age (Ma)
D_{par} (µm)

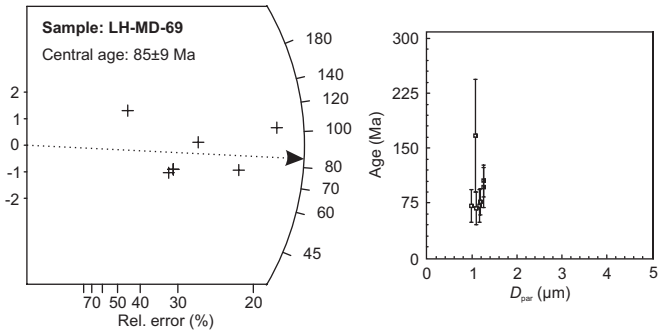
Sample: LH-MD-69
Central age: 85±9 Ma
Rel. error (%)
Age (Ma)
D_{par} (μm)

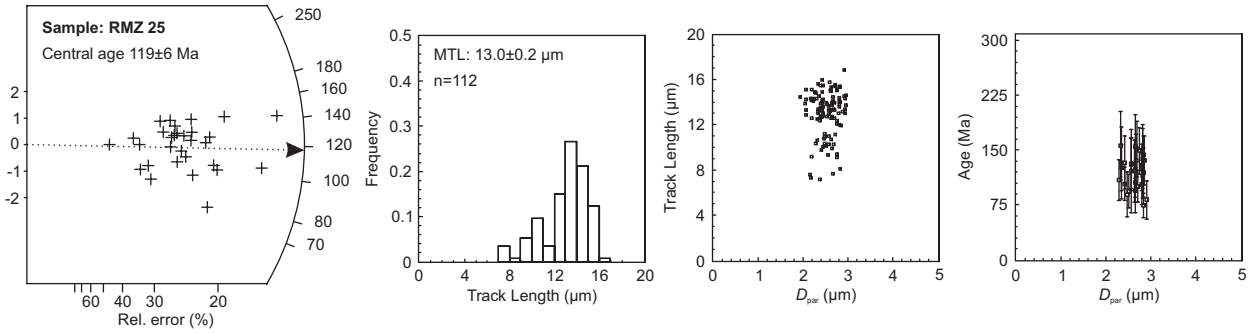
Sample: RMZ 25
Central age 119±6 Ma
Rel. error (%)
MTL: 13.0±0.2 μm
n=112
Frequency
Track Length (μm)
Track Length (μm)
D_{par} (μm)
Age (Ma)
D_{par} (μm)

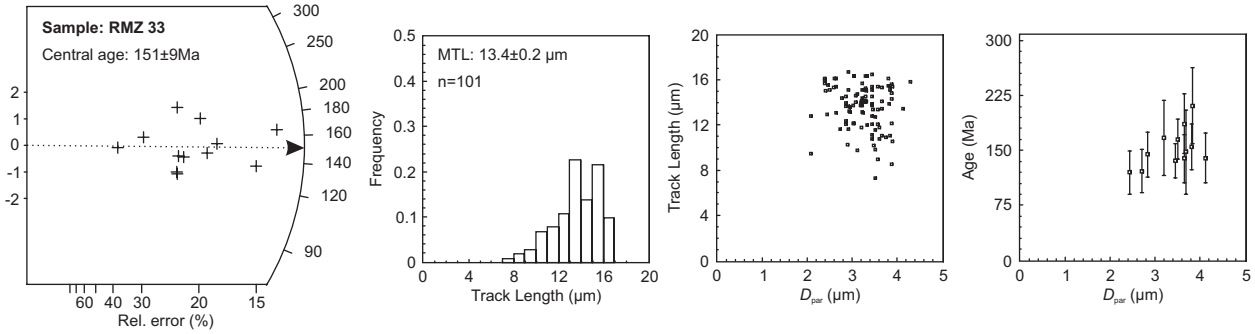
Sample: RMZ 33
Central age: 151±9Ma
Rel. error (%)
MTL: 13.4±0.2 μm
n=101
Frequency
Track Length (μm)
Track Length (μm)
D_{par} (μm)
Age (Ma)
D_{par} (μm)

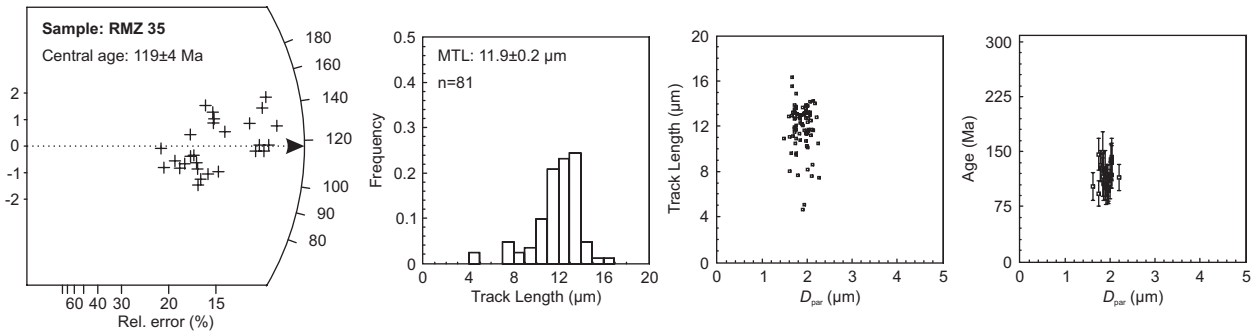
Sample: RMZ 35
Central age: 119±4 Ma
Rel. error (%)
MTL: 11.9±0.2 μm
n=81
Frequency
Track Length (μm)
Track Length (μm)
D_{par} (μm)
Age (Ma)
D_{par} (μm)

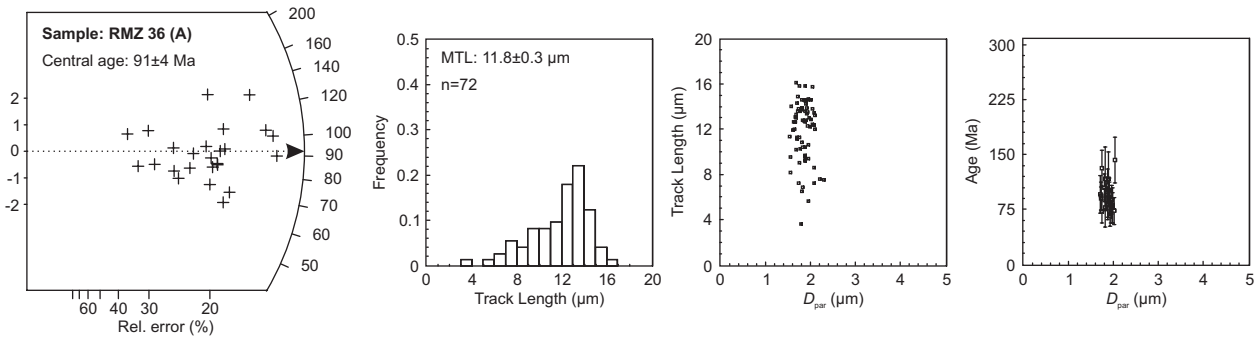
Sample: RMZ 36 (A)
Central age: 91±4 Ma
Rel. error (%)
MTL: 11.8±0.3 μm
n=72
Frequency
Track Length (μm)
Track Length (μm)
D_{par} (μm)
Age (Ma)
D_{par} (μm)

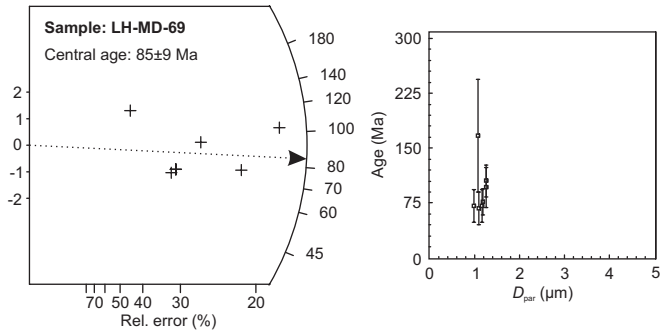
Sample: LH-MD-69
Central age: 85±9 Ma
Rel. error (%)
Age (Ma)
D_{par} (µm)

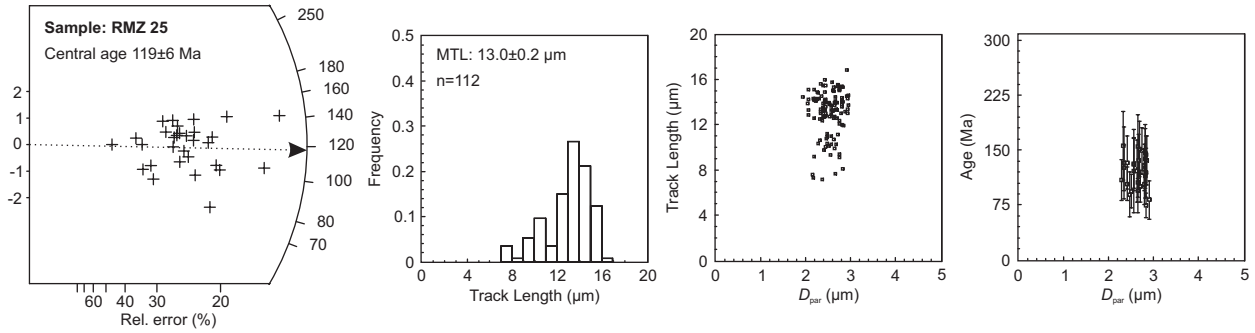
Sample: RMZ 25
Central age 119±6 Ma
Rel. error (%)
MTL: 13.0±0.2 µm
n=112
Frequency
Track Length (µm)
Track Length (µm)
D_{par} (µm)
Age (Ma)
D_{par} (µm)

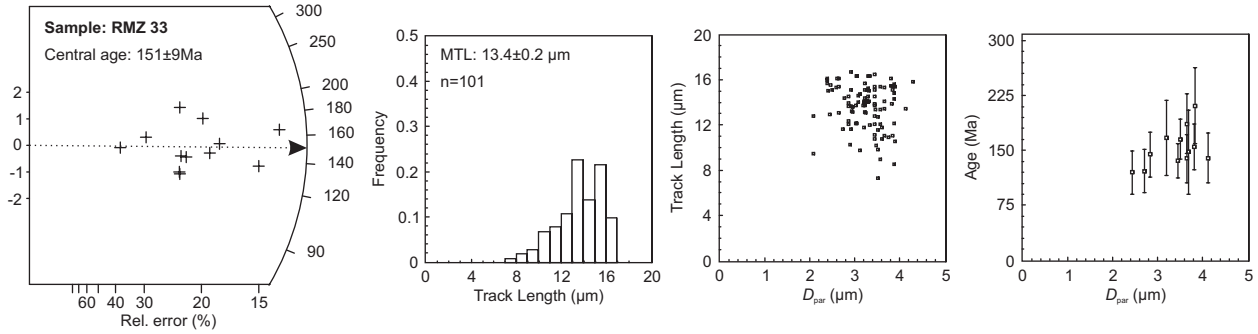
Sample: RMZ 33
Central age: 151±9Ma
Rel. error (%)
MTL: 13.4±0.2 µm
n=101
Frequency
Track Length (µm)
Track Length (µm)
D_{par} (µm)
Age (Ma)
D_{par} (µm)

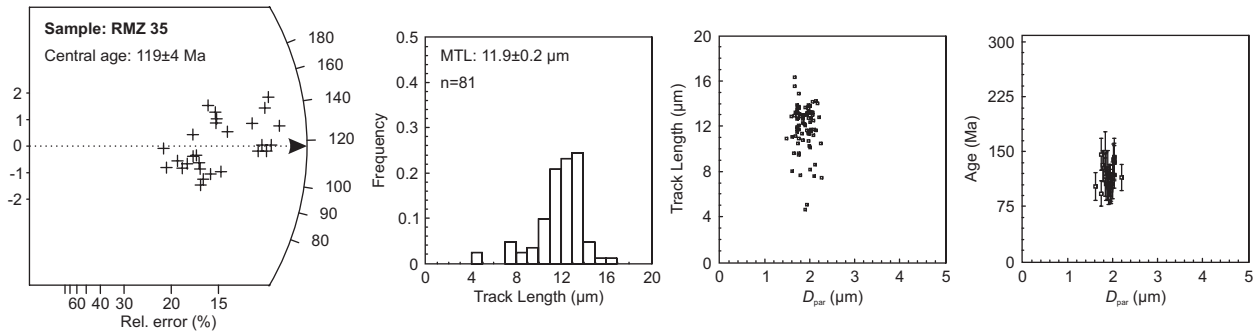
Sample: RMZ 35
Central age: 119±4 Ma
Rel. error (%)
MTL: 11.9±0.2 µm
n=81
Frequency
Track Length (µm)
Track Length (µm)
D_{par} (µm)
Age (Ma)
D_{par} (µm)

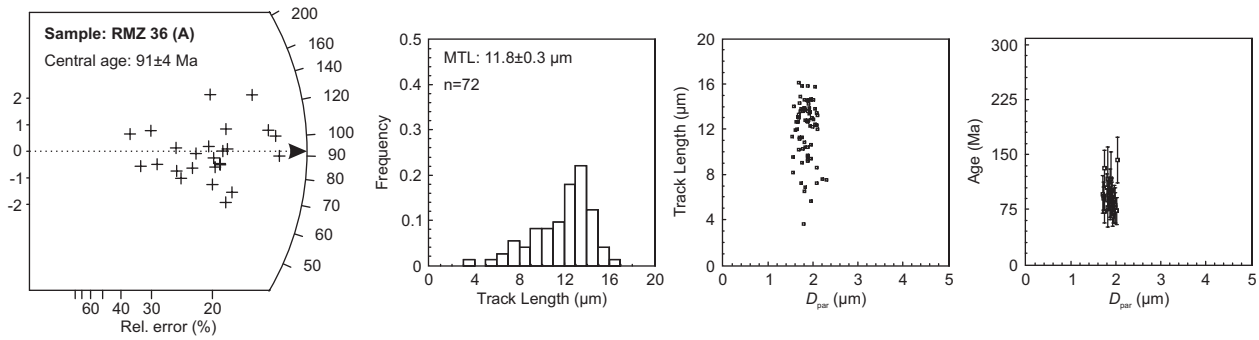
Sample: RMZ 36 (A)
Central age: 91±4 Ma
Rel. error (%)
MTL: 11.8±0.3 µm
n=72
Frequency
Track Length (µm)
Track Length (µm)
D_{par} (µm)
Age (Ma)
D_{par} (µm)

Appendix B

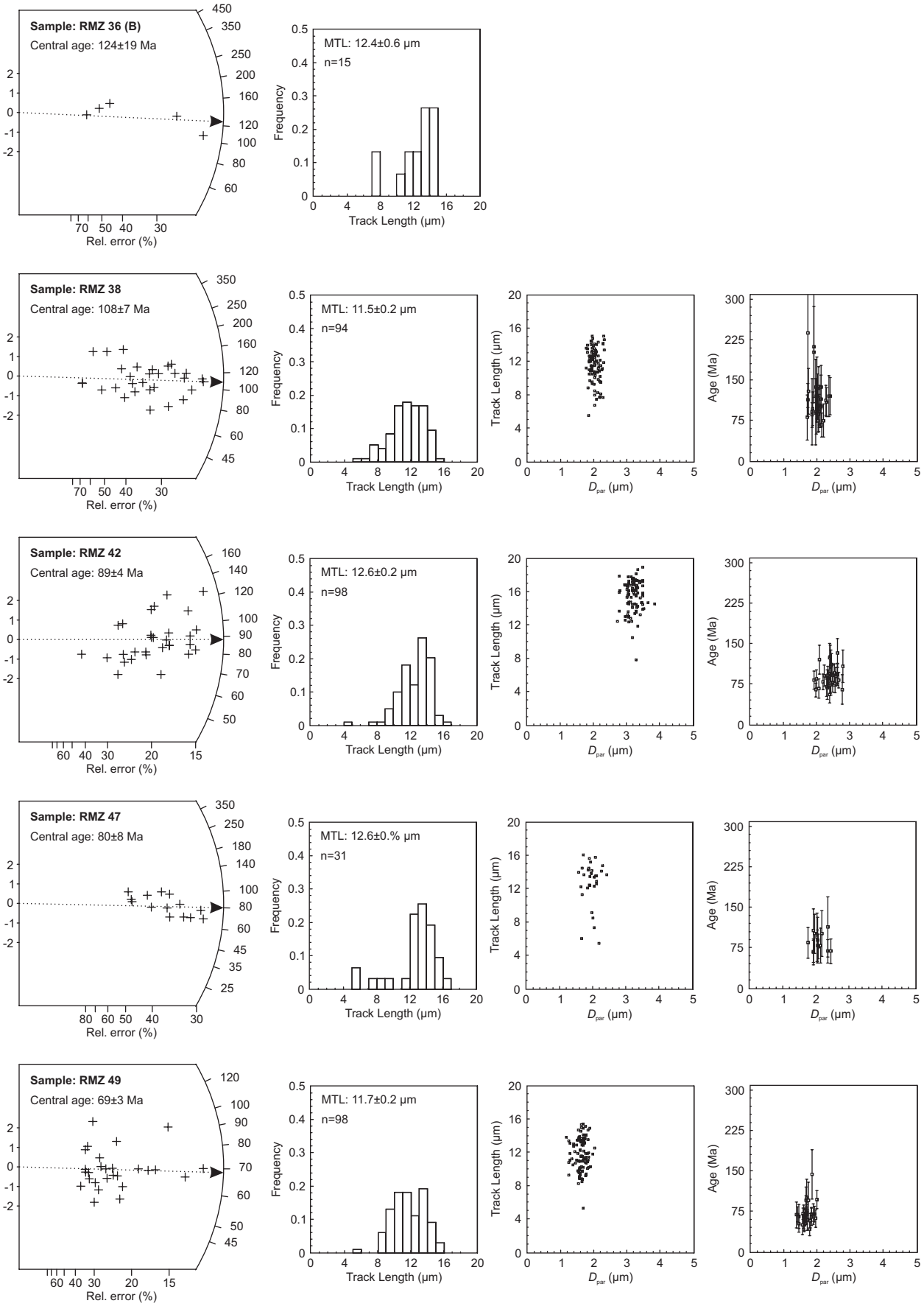
Sample: RMZ 36 (B)
Central age: 124±19 Ma
Rel. error (%)
MTL: 12.4±0.6 µm
n=15
Frequency
Track Length (µm)
Sample: RMZ 38
Central age: 108±7 Ma
MTL: 11.5±0.2 µm
n=94
Track Length (µm)
D_{par} (µm)
Age (Ma)
Sample: RMZ 42
Central age: 89±4 Ma
MTL: 12.6±0.2 µm
n=98
Sample: RMZ 47
Central age: 80±8 Ma
MTL: 12.6±0.% µm
n=31
Sample: RMZ 49
Central age: 69±3 Ma
MTL: 11.7±0.2 µm
n=98

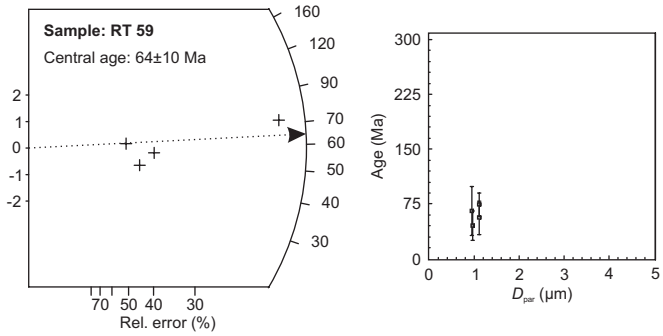
Sample: RT 59
Central age: 64±10 Ma
Rel. error (%)
Age (Ma)
D_{par} (µm)

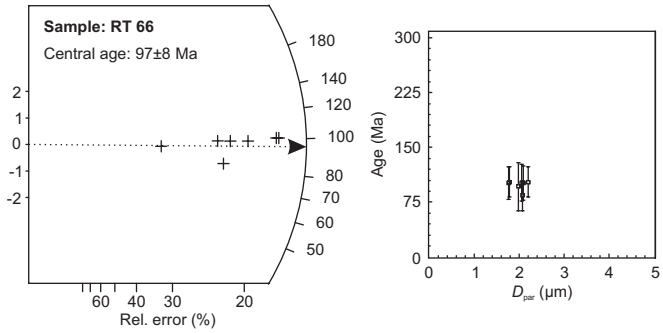
Sample: RT 66
Central age: 97±8 Ma
Rel. error (%)
Age (Ma)
D_{par} (µm)

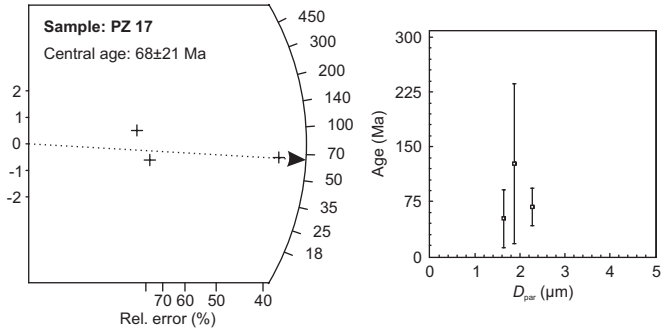
Sample: PZ 17
Central age: 68±21 Ma
Rel. error (%)
Age (Ma)
D_{par} (µm)

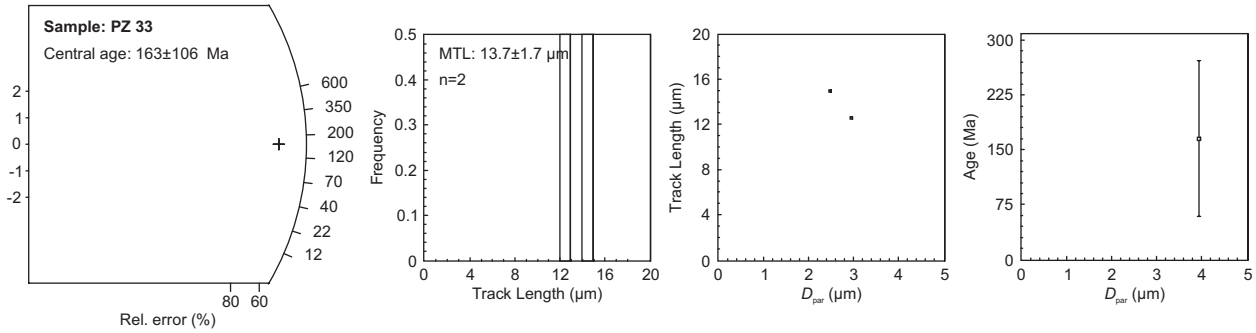
Sample: PZ 33
Central age: 163±106 Ma
Rel. error (%)
MTL: 13.7±1.7 µm
n=2
Frequency
Track Length (µm)
Track Length (µm)
D_{par} (µm)
Age (Ma)
D_{par} (µm)

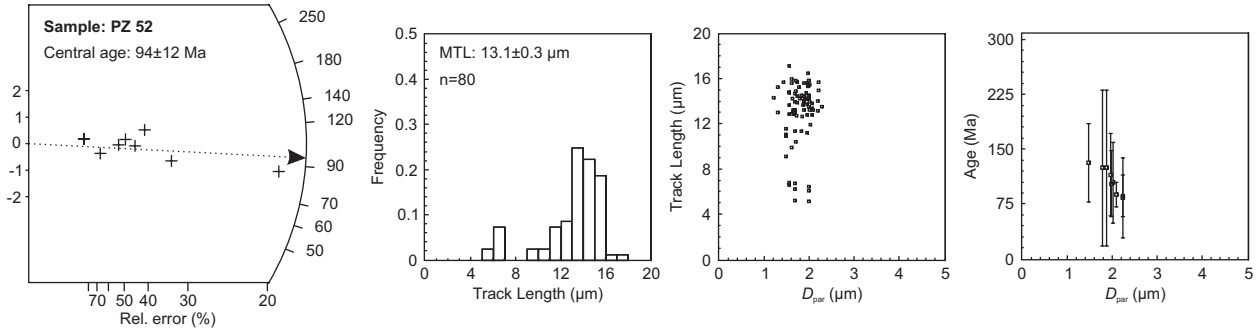
Sample: PZ 52
Central age: 94±12 Ma
Rel. error (%)
MTL: 13.1±0.3 µm
n=80
Frequency
Track Length (µm)
Track Length (µm)
D_{par} (µm)
Age (Ma)
D_{par} (µm)

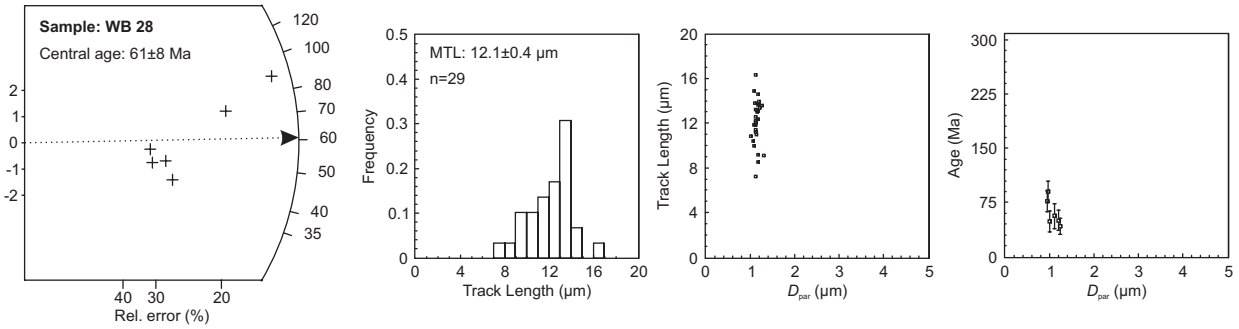
Sample: WB 28
Central age: 61±8 Ma
Rel. error (%)
MTL: 12.1±0.4 µm
n=29
Frequency
Track Length (µm)
Track Length (µm)
D_{par} (µm)
Age (Ma)
D_{par} (µm)

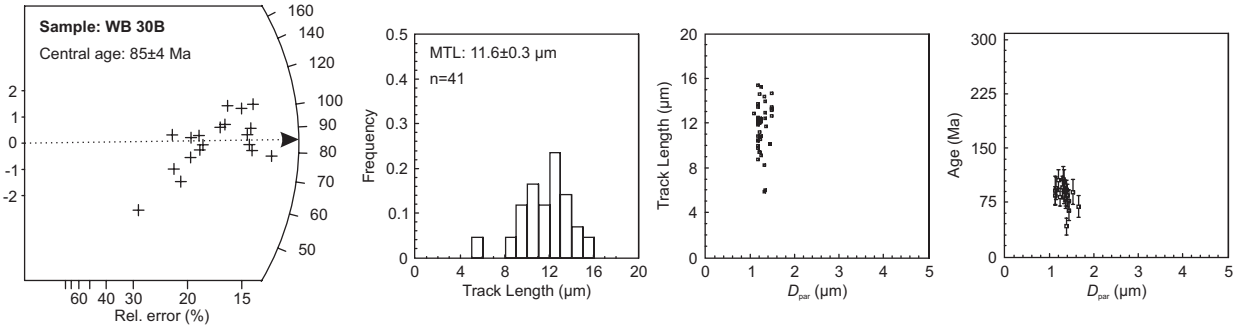
Sample: WB 30B
Central age: 85±4 Ma
Rel. error (%)
MTL: 11.6±0.3 µm
n=41
Frequency
Track Length (µm)
Track Length (µm)
D_{par} (µm)
Age (Ma)
D_{par} (µm)

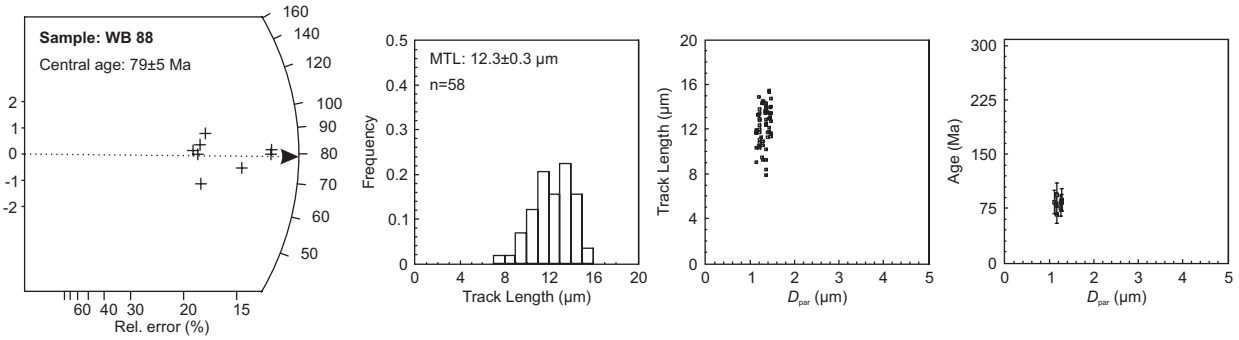
Sample: WB 88
Central age: 79±5 Ma
Rel. error (%)
MTL: 12.3±0.3 µm
n=58
Frequency
Track Length (µm)
Track Length (µm)
D_{par} (µm)
Age (Ma)
D_{par} (µm)

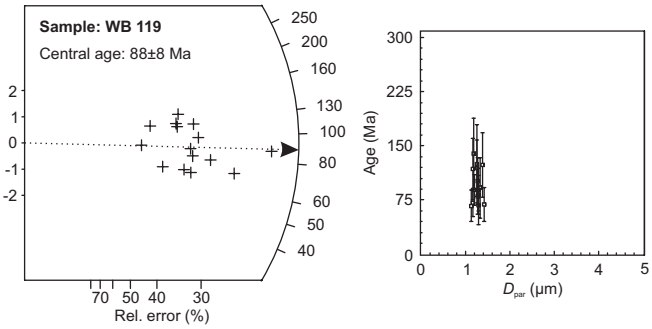
Sample: WB 119
Central age: 88±8 Ma
Rel. error (%)
Age (Ma)
D_{par} (µm)

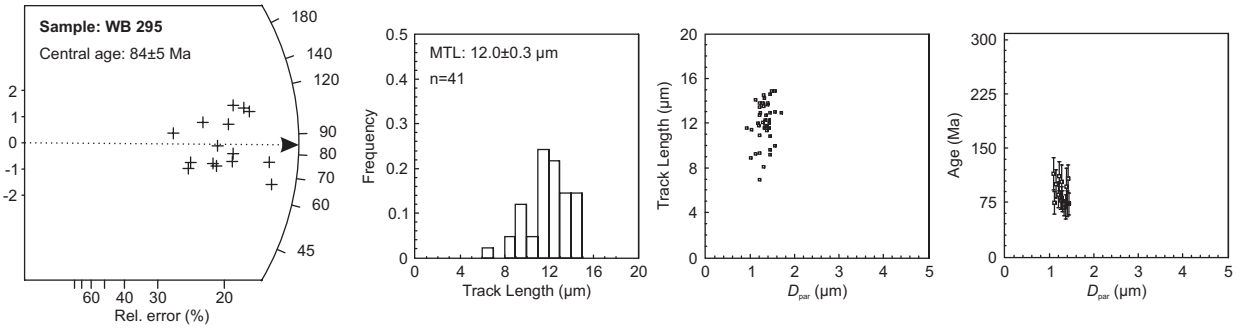
Sample: WB 295
Central age: 84±5 Ma
Rel. error (%)
MTL: 12.0±0.3 µm
n=41
Frequency
Track Length (µm)
Track Length (µm)
D_{par} (µm)
Age (Ma)
D_{par} (µm)

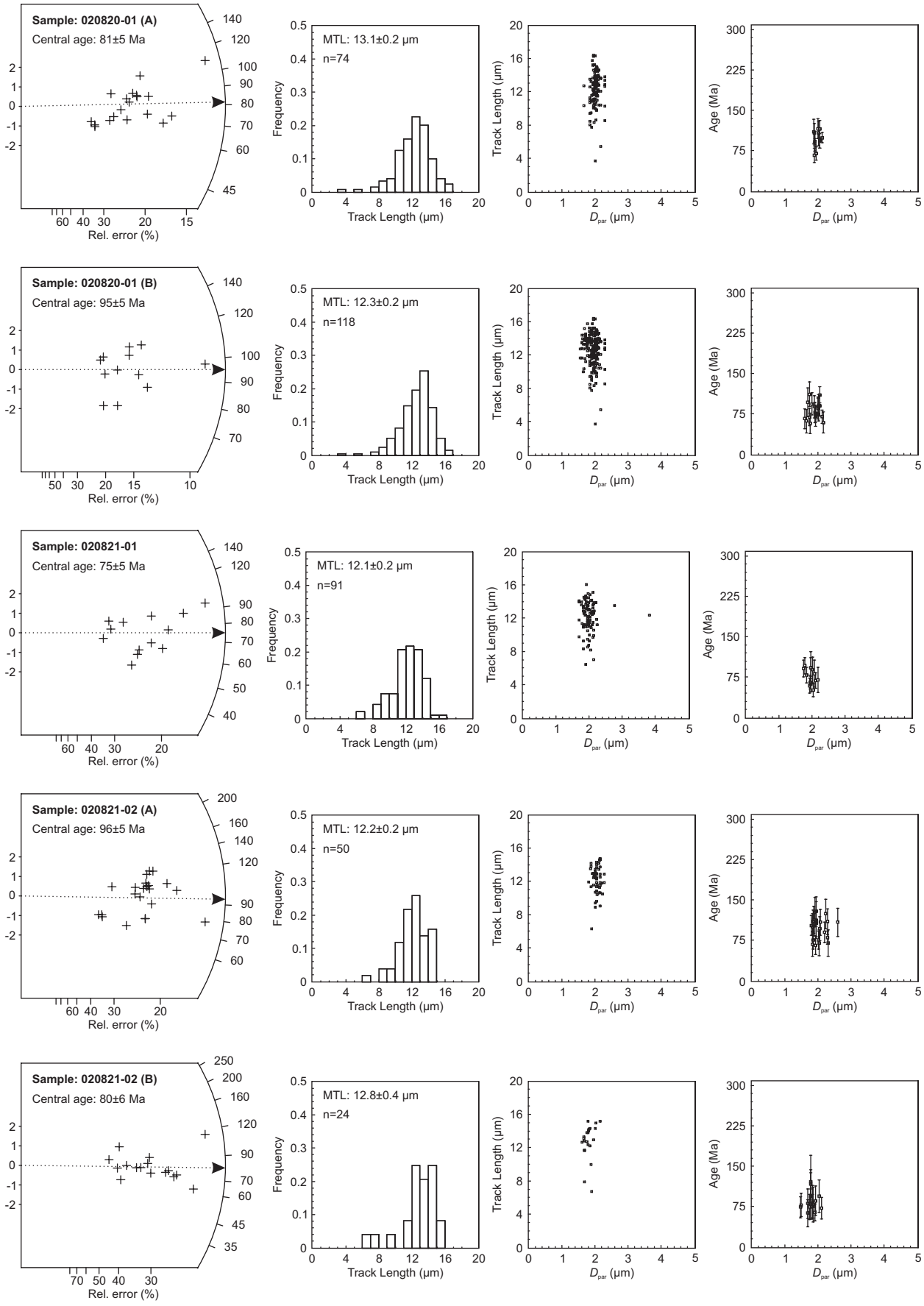
Sample: 020820-01 (A)
Central age: 81±5 Ma
Rel. error (%)
MTL: 13.1±0.2 µm
n=74
Frequency
Track Length (µm)
Track Length (µm)
D_{par} (µm)
Age (Ma)
D_{par} (µm)
Sample: 020820-01 (B)
Central age: 95±5 Ma
Rel. error (%)
MTL: 12.3±0.2 µm
n=118
Frequency
Track Length (µm)
Track Length (µm)
D_{par} (µm)
Age (Ma)
D_{par} (µm)
Sample: 020821-01
Central age: 75±5 Ma
Rel. error (%)
MTL: 12.1±0.2 µm
n=91
Frequency
Track Length (µm)
Track Length (µm)
D_{par} (µm)
Age (Ma)
D_{par} (µm)
Sample: 020821-02 (A)
Central age: 96±5 Ma
Rel. error (%)
MTL: 12.2±0.2 µm
n=50
Frequency
Track Length (µm)
Track Length (µm)
D_{par} (µm)
Age (Ma)
D_{par} (µm)
Sample: 020821-02 (B)
Central age: 80±6 Ma
Rel. error (%)
MTL: 12.8±0.4 µm
n=24
Frequency
Track Length (µm)
Track Length (µm)
D_{par} (µm)
Age (Ma)
D_{par} (µm)

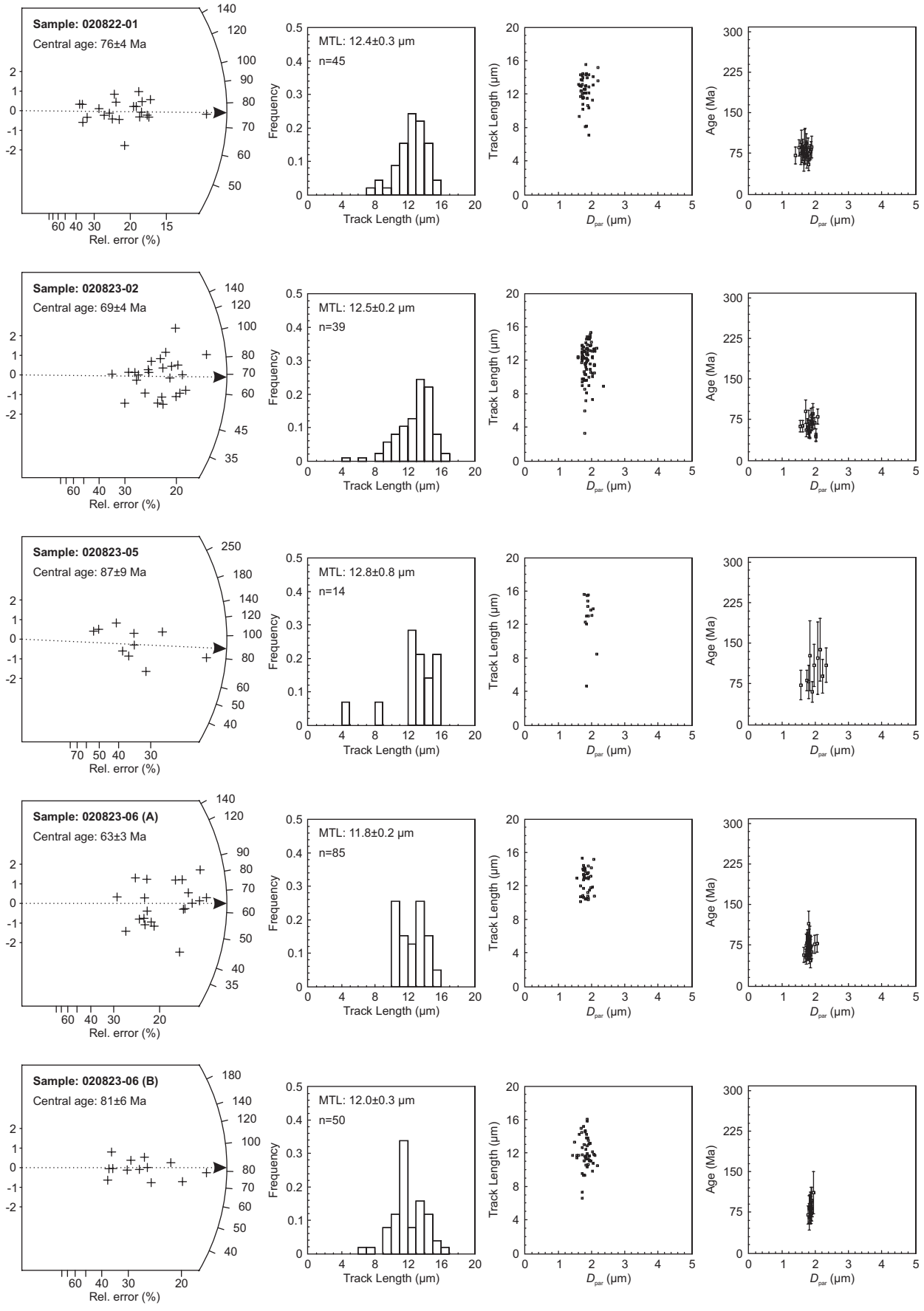
Sample: 020822-01
Central age: 76±4 Ma
MTL: 12.4±0.3 µm
n=45
Sample: 020823-02
Central age: 69±4 Ma
MTL: 12.5±0.2 µm
n=39
Sample: 020823-05
Central age: 87±9 Ma
MTL: 12.8±0.8 µm
n=14
Sample: 020823-06 (A)
Central age: 63±3 Ma
MTL: 11.8±0.2 µm
n=85
Sample: 020823-06 (B)
Central age: 81±6 Ma
MTL: 12.0±0.3 µm
n=50
Rel. error (%)
Frequency
Track Length (µm)
Track Length (µm)
Age (Ma)
D_{par} (µm)

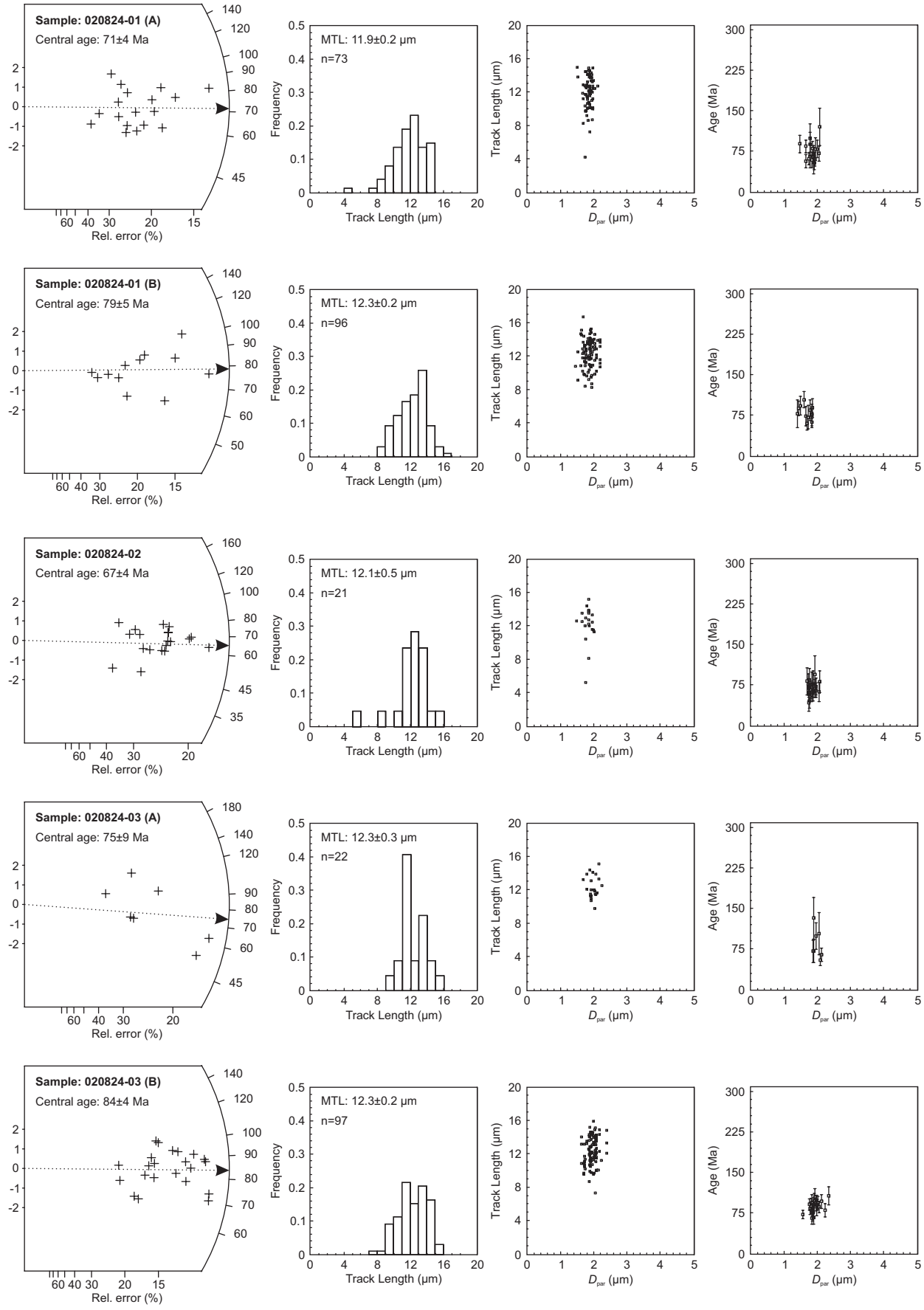
Sample: 020824-01 (A)
Central age: 71±4 Ma
Rel. error (%)
MTL: 11.9±0.2 µm
n=73
Frequency
Track Length (µm)
Track Length (µm)
D_{par} (µm)
Age (Ma)
D_{par} (µm)
Sample: 020824-01 (B)
Central age: 79±5 Ma
Rel. error (%)
MTL: 12.3±0.2 µm
n=96
Frequency
Track Length (µm)
Track Length (µm)
D_{par} (µm)
Age (Ma)
D_{par} (µm)
Sample: 020824-02
Central age: 67±4 Ma
Rel. error (%)
MTL: 12.1±0.5 µm
n=21
Frequency
Track Length (µm)
Track Length (µm)
D_{par} (µm)
Age (Ma)
D_{par} (µm)
Sample: 020824-03 (A)
Central age: 75±9 Ma
Rel. error (%)
MTL: 12.3±0.3 µm
n=22
Frequency
Track Length (µm)
Track Length (µm)
D_{par} (µm)
Age (Ma)
D_{par} (µm)
Sample: 020824-03 (B)
Central age: 84±4 Ma
Rel. error (%)
MTL: 12.3±0.2 µm
n=97
Frequency
Track Length (µm)
Track Length (µm)
D_{par} (µm)
Age (Ma)
D_{par} (µm)

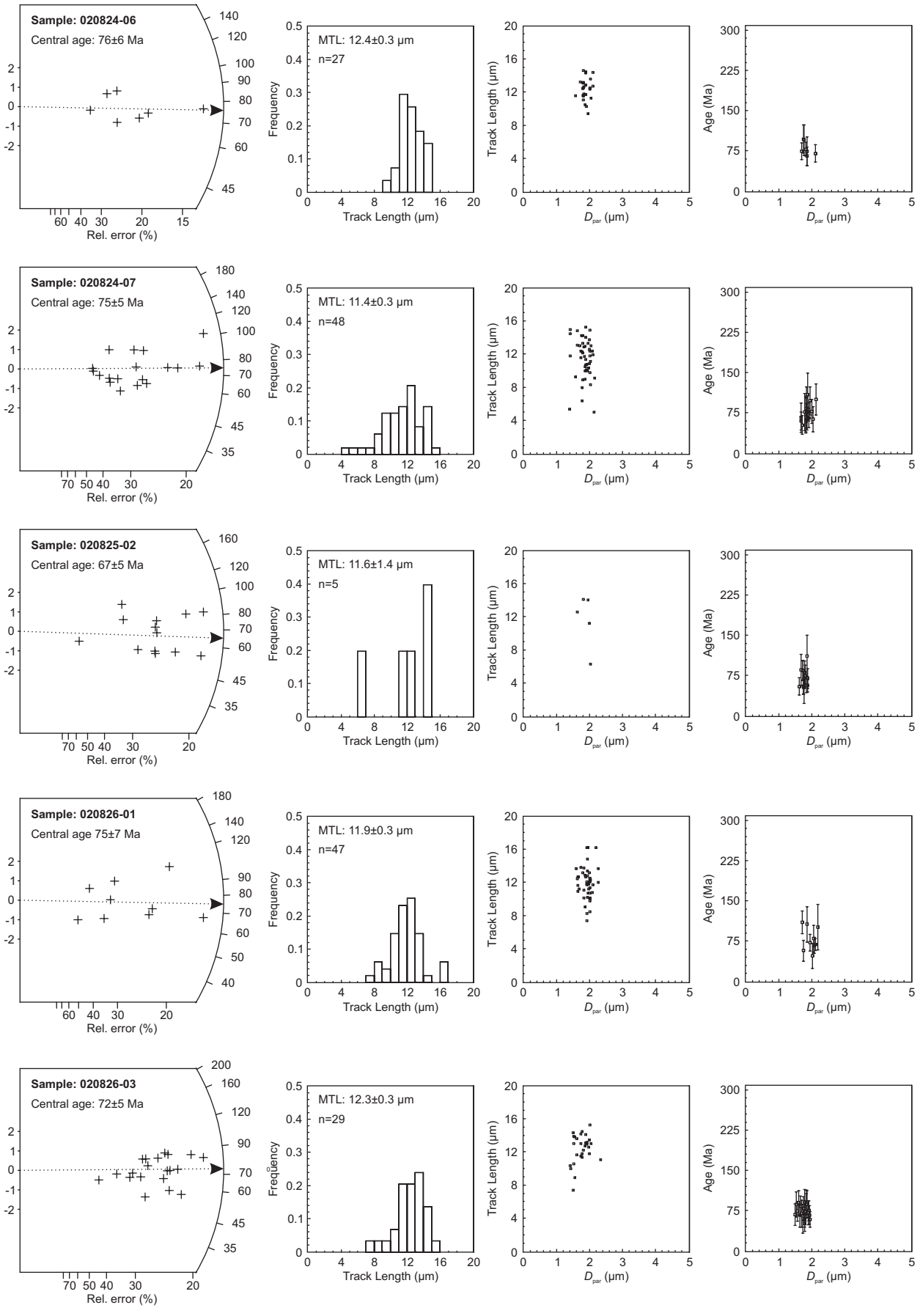
Sample: 020824-06
Central age: 76±6 Ma
Rel. error (%)
MTL: 12.4±0.3 µm
n=27
Frequency
Track Length (µm)
Track Length (µm)
D_{par} (µm)
Age (Ma)
D_{par} (µm)
Sample: 020824-07
Central age: 75±5 Ma
Rel. error (%)
MTL: 11.4±0.3 µm
n=48
Frequency
Track Length (µm)
Track Length (µm)
D_{par} (µm)
Age (Ma)
D_{par} (µm)
Sample: 020825-02
Central age: 67±5 Ma
Rel. error (%)
MTL: 11.6±1.4 µm
n=5
Frequency
Track Length (µm)
Track Length (µm)
D_{par} (µm)
Age (Ma)
D_{par} (µm)
Sample: 020826-01
Central age 75±7 Ma
Rel. error (%)
MTL: 11.9±0.3 µm
n=47
Frequency
Track Length (µm)
Track Length (µm)
D_{par} (µm)
Age (Ma)
D_{par} (µm)
Sample: 020826-03
Central age: 72±5 Ma
Rel. error (%)
MTL: 12.3±0.3 µm
n=29
Frequency
Track Length (µm)
Track Length (µm)
D_{par} (µm)
Age (Ma)
D_{par} (µm)

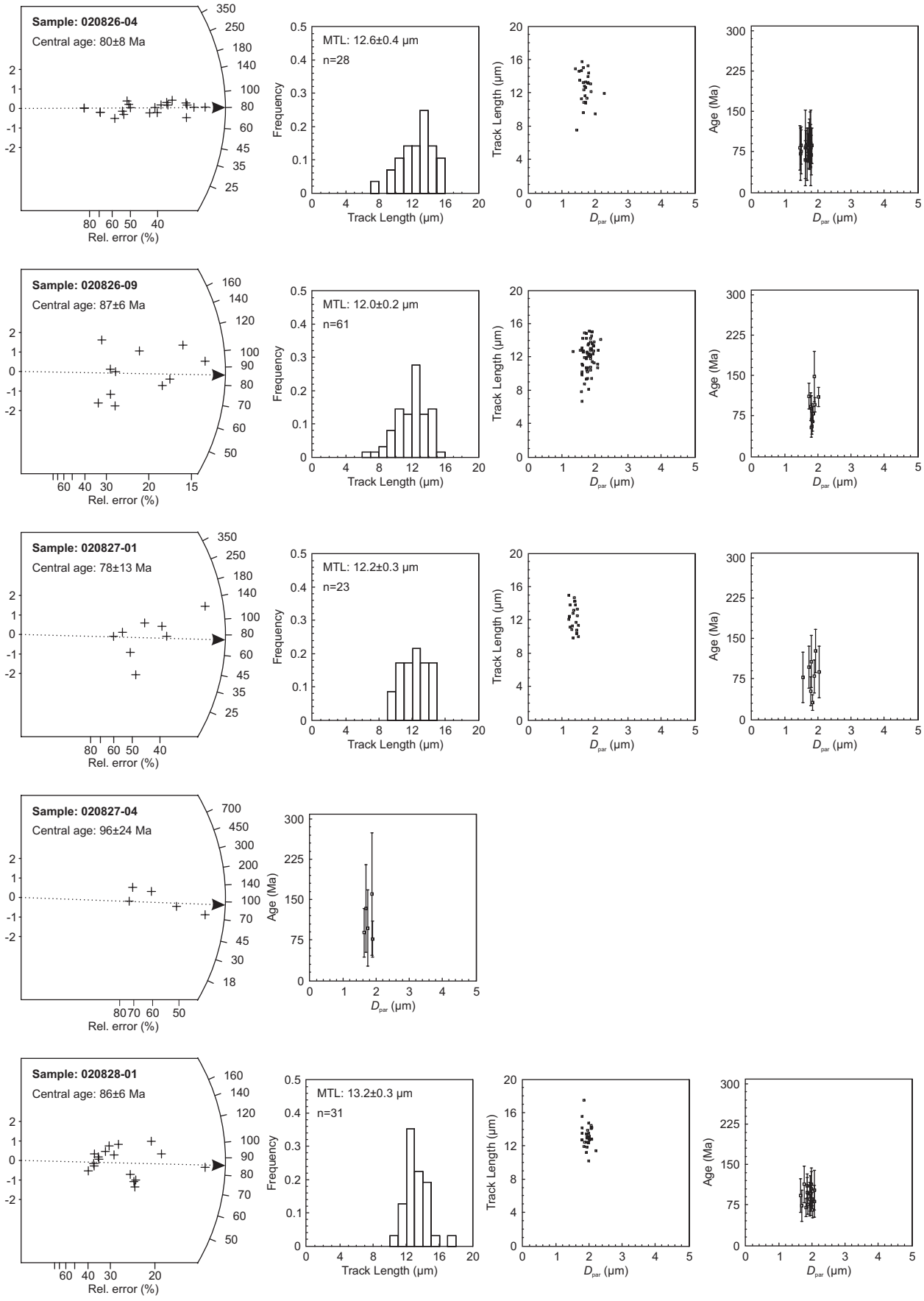
Sample: 020826-04
Central age: 80±8 Ma
Rel. error (%)
MTL: 12.6±0.4 µm
n=28
Frequency
Track Length (µm)
Track Length (µm)
D_{par} (µm)
Age (Ma)
D_{par} (µm)
Sample: 020826-09
Central age: 87±6 Ma
Rel. error (%)
MTL: 12.0±0.2 µm
n=61
Frequency
Track Length (µm)
Track Length (µm)
D_{par} (µm)
Age (Ma)
D_{par} (µm)
Sample: 020827-01
Central age: 78±13 Ma
Rel. error (%)
MTL: 12.2±0.3 µm
n=23
Frequency
Track Length (µm)
Track Length (µm)
D_{par} (µm)
Age (Ma)
D_{par} (µm)
Sample: 020827-04
Central age: 96±24 Ma
Rel. error (%)
Age (Ma)
D_{par} (µm)
Sample: 020828-01
Central age: 86±6 Ma
Rel. error (%)
MTL: 13.2±0.3 µm
n=31
Frequency
Track Length (µm)
Track Length (µm)
D_{par} (µm)
Age (Ma)
D_{par} (µm)

Appendix B

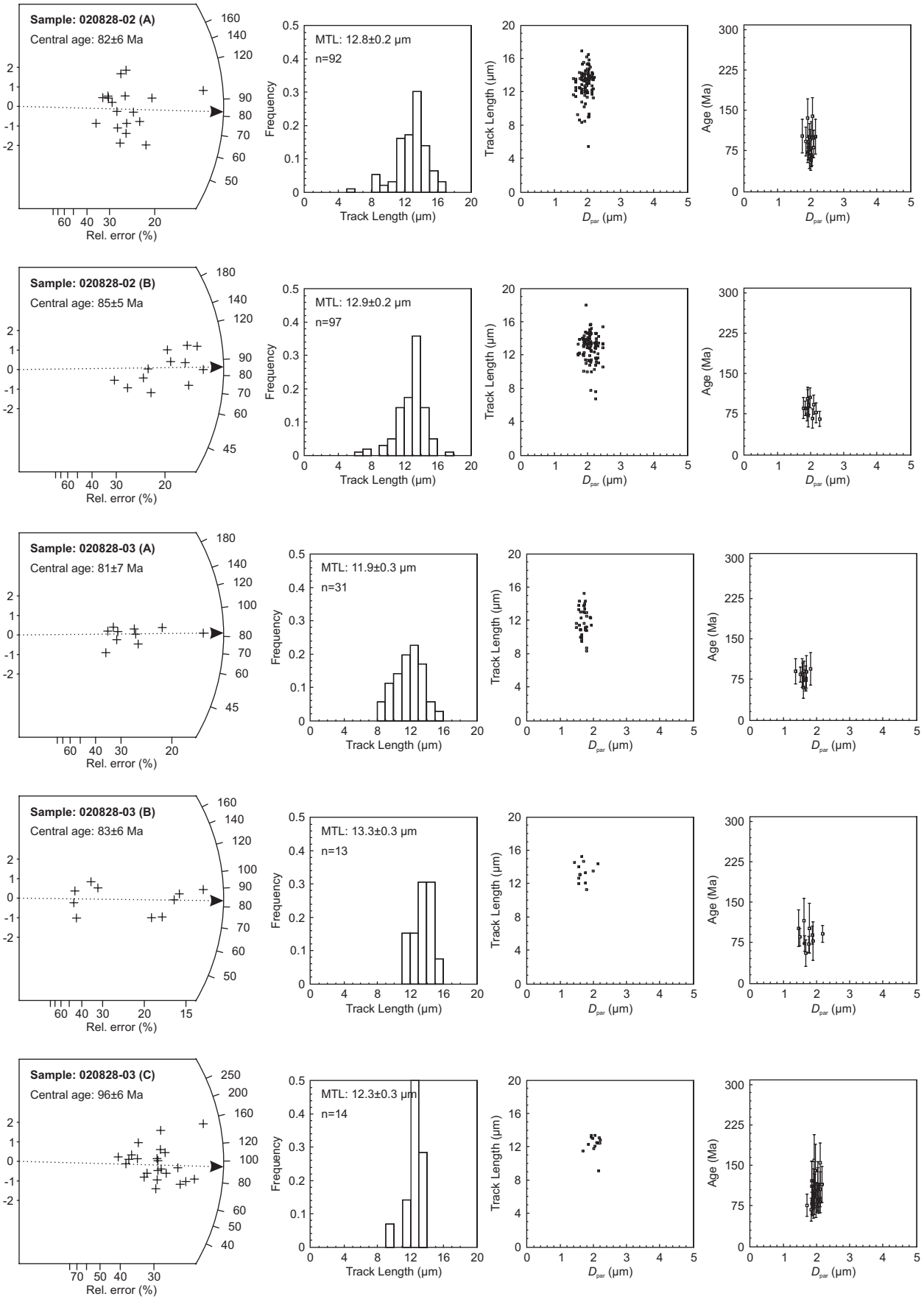
Sample: 020828-02 (A)
Central age: 82±6 Ma
Rel. error (%)
MTL: 12.8±0.2 µm
n=92
Frequency
Track Length (µm)
Track Length (µm)
Age (Ma)
D_{par} (µm)
Sample: 020828-02 (B)
Central age: 85±5 Ma
Rel. error (%)
MTL: 12.9±0.2 µm
n=97
Frequency
Track Length (µm)
Track Length (µm)
Age (Ma)
D_{par} (µm)
Sample: 020828-03 (A)
Central age: 81±7 Ma
Rel. error (%)
MTL: 11.9±0.3 µm
n=31
Frequency
Track Length (µm)
Track Length (µm)
Age (Ma)
D_{par} (µm)
Sample: 020828-03 (B)
Central age: 83±6 Ma
Rel. error (%)
MTL: 13.3±0.3 µm
n=13
Frequency
Track Length (µm)
Track Length (µm)
Age (Ma)
D_{par} (µm)
Sample: 020828-03 (C)
Central age: 96±6 Ma
Rel. error (%)
MTL: 12.3±0.3 µm
n=14
Frequency
Track Length (µm)
Track Length (µm)
Age (Ma)
D_{par} (µm)

B.4 Southern basement – *M* group

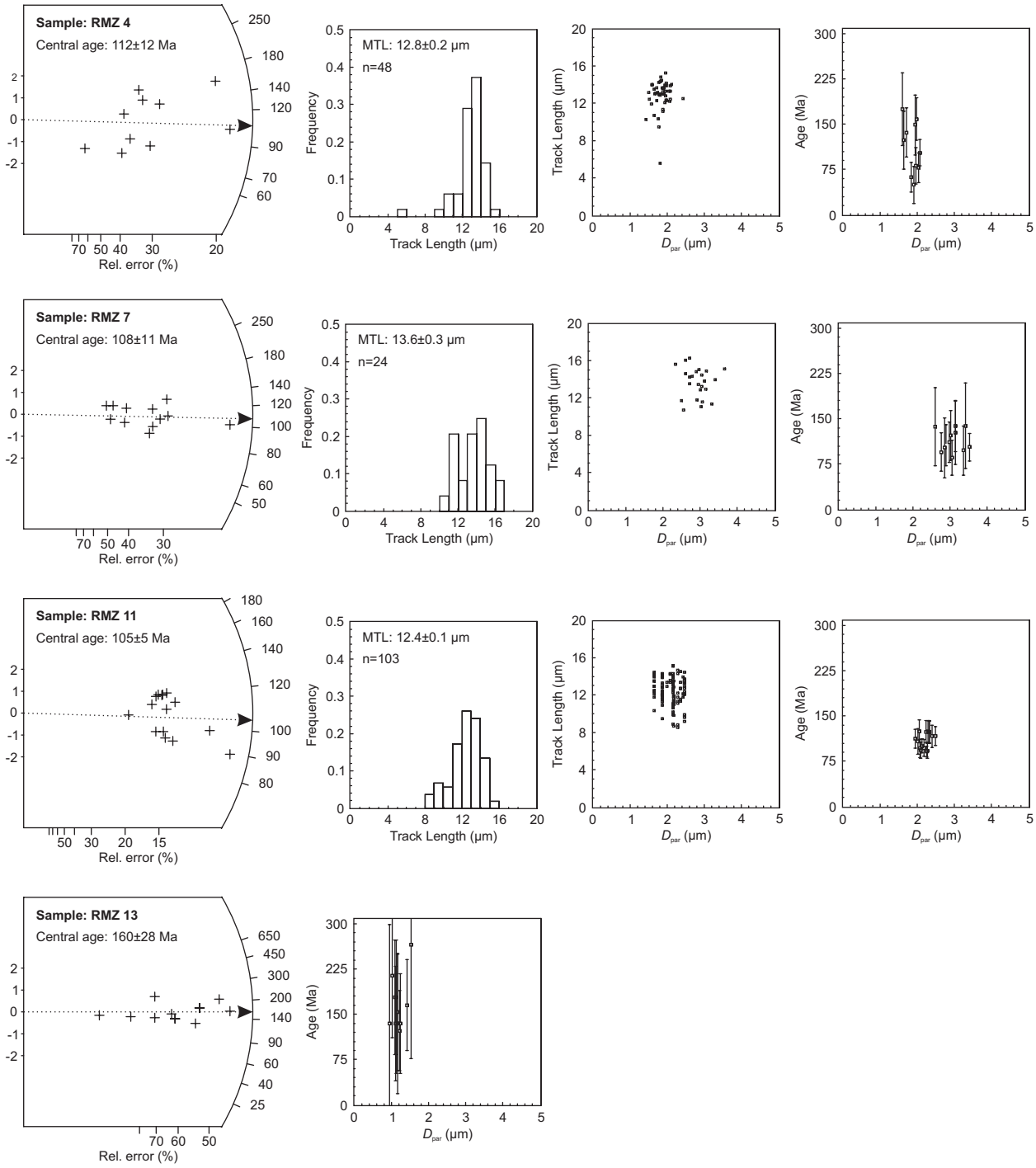

Appendix B

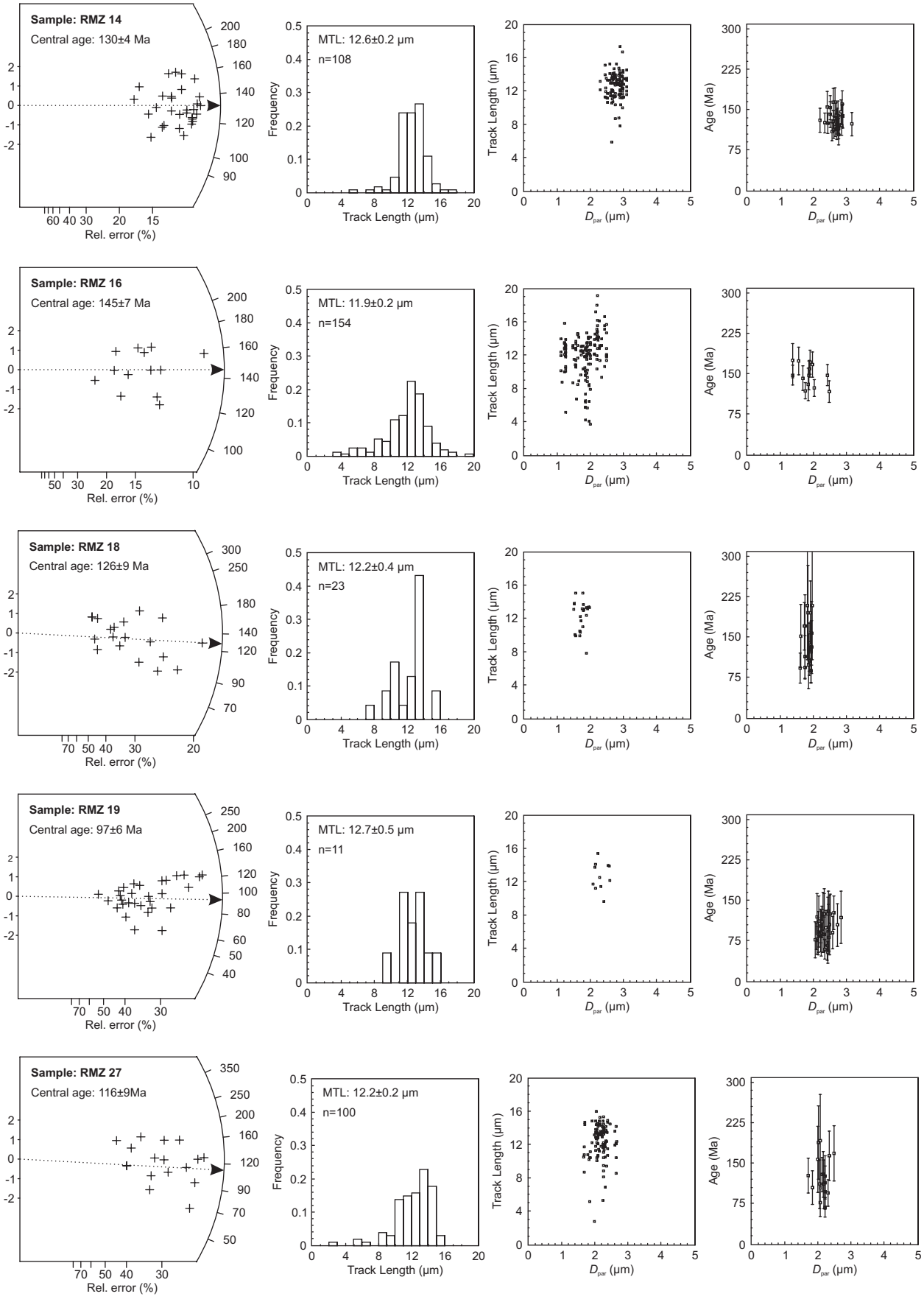
Sample: RMZ 14
Central age: 130±4 Ma
Rel. error (%)
MTL: 12.6±0.2 µm
n=108
Frequency
Track Length (µm)
Track Length (µm)
D_{par} (µm)
Age (Ma)
D_{par} (µm)
Sample: RMZ 16
Central age: 145±7 Ma
Rel. error (%)
MTL: 11.9±0.2 µm
n=154
Frequency
Track Length (µm)
Track Length (µm)
D_{par} (µm)
Age (Ma)
D_{par} (µm)
Sample: RMZ 18
Central age: 126±9 Ma
Rel. error (%)
MTL: 12.2±0.4 µm
n=23
Frequency
Track Length (µm)
Track Length (µm)
D_{par} (µm)
Age (Ma)
D_{par} (µm)
Sample: RMZ 19
Central age: 97±6 Ma
Rel. error (%)
MTL: 12.7±0.5 µm
n=11
Frequency
Track Length (µm)
Track Length (µm)
D_{par} (µm)
Age (Ma)
D_{par} (µm)
Sample: RMZ 27
Central age: 116±9Ma
Rel. error (%)
MTL: 12.2±0.2 µm
n=100
Frequency
Track Length (µm)
Track Length (µm)
D_{par} (µm)
Age (Ma)
D_{par} (µm)

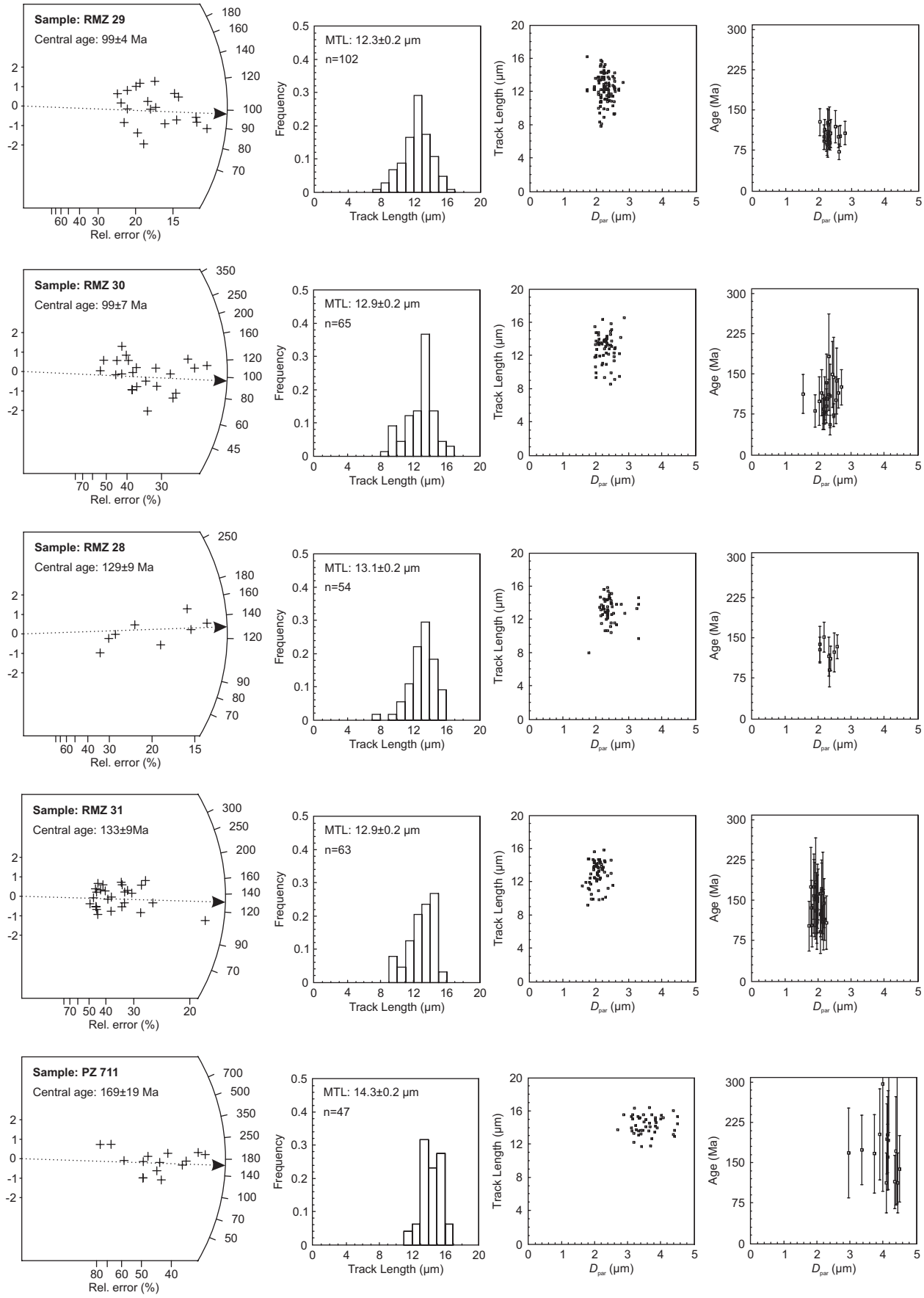
Sample: RMZ 29
Central age: 99±4 Ma
Rel. error (%)
MTL: 12.3±0.2 µm
n=102
Frequency
Track Length (µm)
Track Length (µm)
D_{par} (µm)
Age (Ma)
D_{par} (µm)
Sample: RMZ 30
Central age: 99±7 Ma
Rel. error (%)
MTL: 12.9±0.2 µm
n=65
Frequency
Track Length (µm)
Track Length (µm)
D_{par} (µm)
Age (Ma)
D_{par} (µm)
Sample: RMZ 28
Central age: 129±9 Ma
Rel. error (%)
MTL: 13.1±0.2 µm
n=54
Frequency
Track Length (µm)
Track Length (µm)
D_{par} (µm)
Age (Ma)
D_{par} (µm)
Sample: RMZ 31
Central age: 133±9Ma
Rel. error (%)
MTL: 12.9±0.2 µm
n=63
Frequency
Track Length (µm)
Track Length (µm)
D_{par} (µm)
Age (Ma)
D_{par} (µm)
Sample: PZ 711
Central age: 169±19 Ma
Rel. error (%)
MTL: 14.3±0.2 µm
n=47
Frequency
Track Length (µm)
Track Length (µm)
D_{par} (µm)
Age (Ma)
D_{par} (µm)

Appendix B

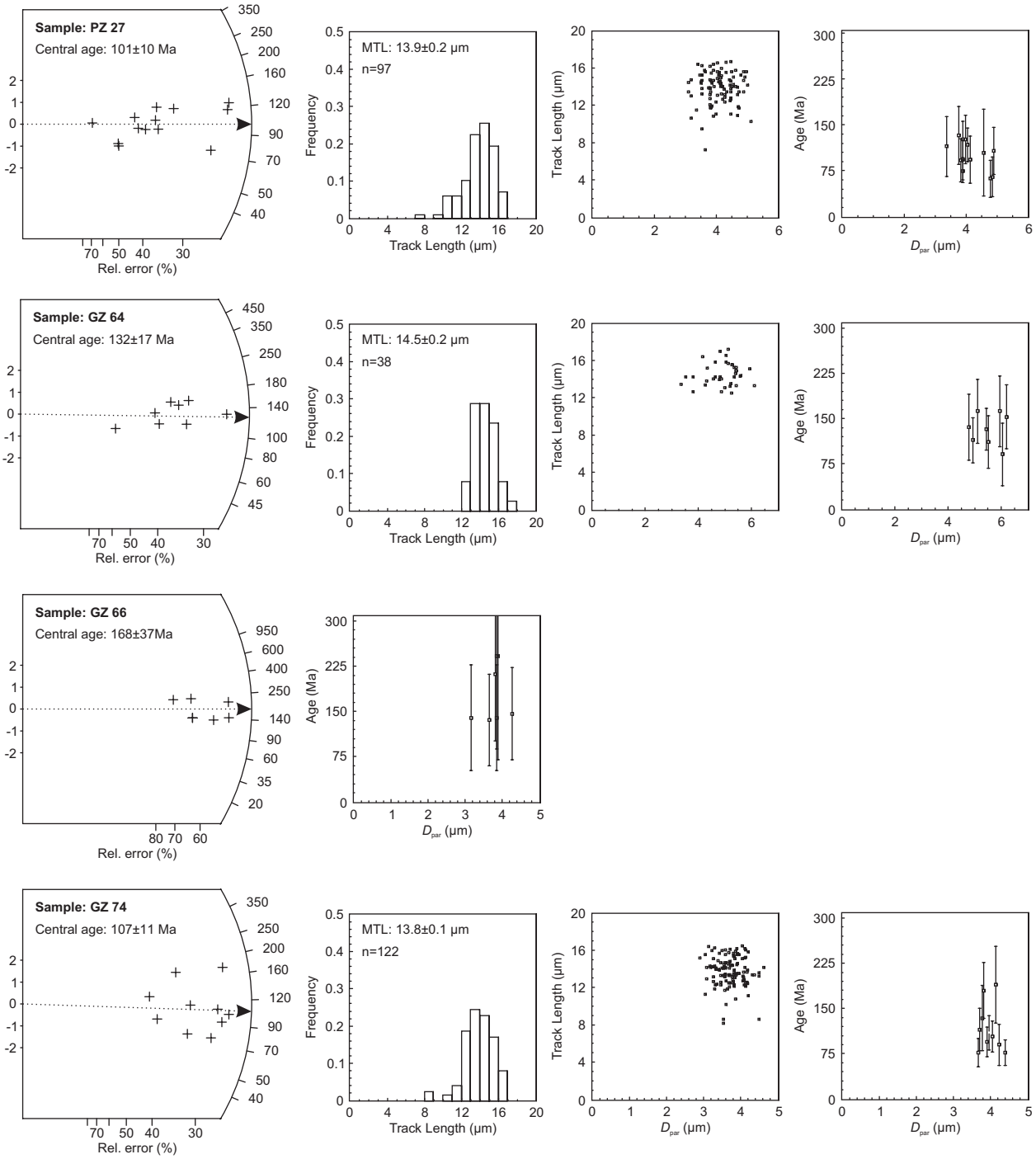
Sample: PZ 27
Central age: 101±10 Ma
Rel. error (%)
MTL: 13.9±0.2 µm
n=97
Frequency
Track Length (µm)
Track Length (µm)
Age (Ma)
D_{par} (µm)
Sample: GZ 64
Central age: 132±17 Ma
Rel. error (%)
MTL: 14.5±0.2 µm
n=38
Frequency
Track Length (µm)
Track Length (µm)
Age (Ma)
D_{par} (µm)
Sample: GZ 66
Central age: 168±37Ma
Rel. error (%)
Age (Ma)
D_{par} (µm)
Sample: GZ 74
Central age: 107±11 Ma
Rel. error (%)
MTL: 13.8±0.1 µm
n=122
Frequency
Track Length (µm)
Track Length (µm)
D_{par} (µm)
Age (Ma)
D_{par} (µm)

Appendix C

BASH SCRIPT – GMT 4.0

```
#!/bin/bash
#
# GMT script for plotting spatial distribution patterns of apatite and titanite fission
track data
# Copyright M.Daszinnies:University of Bremen:Department of Geosciences
#
#
if [ "x$1" != "x-a" ] && [ "x$1" != "x-t" ]; then # check 1st parameter
        cat << EOF >&2

Usage: sh ft_age.sh -option1 -option2

 option 1      -a apatites -> inputfilename ap_age_a.txt etc...
               -t titanites -> inputfilename tit_age_a.txt etc...

 option 2      -s gridding using surface
               -t gridding using triangulation
Example
EOF
exit
else
        if [ "x$2" != "x-s" ] && [ "x$2" != "x-t" ]; then # check 2nd parameter
        echo Check your parameters !
        echo sh ft_age.sh -h for help
        exit
        fi
fi

# ---Save existing GMT defaults---
echo Saving GMT defaults...
rm /home/mat/work_gmt/tmp/gmtdefaults$$ -v -f
gmtdefaults -L > /home/mat/gmt_work/tmp/gmtdefaults$$
#
# ---Set new GMT defaults---
echo Setting new GMT defaults...
gmtset MEASURE_UNIT cm
gmtset PAPER_MEDIA A4
gmtset ANOT_FONT Helvetica
gmtset LABEL_FONT Helvetica
gmtset ANOT_FONT_SIZE 8
gmtset LABEL_FONT_SIZE 8
gmtset HEADER_FONT_SIZE 12
gmtset FRAME_WIDTH 0.075
gmtset TICK_LENGTH 0.15
gmtset PAGE_ORIENTATION PORTRAIT
gmtset COLOR_BACKGROUND 0/0/0
gmtset COLOR_FOREGROUND 255/255/255
gmtset COLOR_NAN 255/255/255
gmtset DEGREE_FORMAT 3
gmtset BASEMAP_TYPE FANCY
#
# ---Definition of general variables---
cpt=/home/mat/gmt_work/cpt/mozambique.cpt # cpt-file for topography grid
grid=/home/mat/gmt_work/grids/mozambique_base.grd # base topography grid
grad_grid=/home/mat/gmt_work/grids/mozambique_shade.grd
# base shaded topography grid (intensity parameter for topography grid)
grad_grid_a=/home/mat/gmt_work/grids/mozambique_shade_sub_a.grd
# sub shaded topopography grid (intensity parameter - trend grid)
# grad_grid_b=/home/mat/gmt_work/grids/mozambique_shade_sub_b.grd
# (like a "grad_grid_a" but for additional area)
```

```
project=M
scale=16
trend_cpt=/home/mat/gmt_work/cpt/trend_ft_age.cpt # cpt-file for trend grids
trend_grid_a=/home/mat/gmt_work/grids/tit_ft_age_a.grd # trend grid
trend_grid_b=/home/mat/gmt_work/grids/tit_ft_age_b.grd # trend grid
trend_grid_x=/home/mat/gmt_work/grids/tit_ft_age_x.grd # trend grid
#
# ---General graphic features---
#
# ---Creating colour palaette for topography (only once required)---
# echo Creating color palette -cpt- for topography...
# makecpt -Crelief -T-3500/3500/200 -Z > $cpt
#
# ---Illumination option; creating shaded relief from topography grid---
echo Creating shaded relief...
grdgradient $grid -Ne0.6 -A120 -M -G$grad_grid -V # creating topographic gradient grid
# grdimage $grid -R$region -J$project$scale -I$grad_grid -C$cpt -Y15 -E150 -K -V > $out
# shaded topography image using intensity parameter of grad_grid
#
#
if [ "x$1" == "x-a" ]; then # gridding apatite ft ages
        echo Apatite Fission Track....
           # ---Input variables---
                txt_in_a=/home/mat/gmt_work/ap_age_a.txt # eastern area - data file
                txt_in_b=/home/mat/gmt_work/ap_age_b.txt # western area - data file
                region=34/41/-17.5/-13.5 # total area dimension variables
                #
                if [ "x$2" = "x-s" ]; then # gridding with surface
                        out=/home/mat/gmt_work/ps/mozambique_ap_ft_ages_surface.ps
                        # output variables
                        echo Plotting basemap relief...
                        grdimage $grid -R$region -J$project$scale -I$grad_grid -C$cpt -Y15
                        -E150 -K -V > $out
                        # shaded topography image using intensity parameter of grad_grid
                        prep_grid_a=/home/mat/gmt_work/tmp/ft_age_prep_a.gmt
                        # ---trendsurface variables surface--prep for
                        blockmean
                        prep_grid_b=/home/mat/gmt_work/tmp/ft_age_prep_b.gmt
                        # ---trendsurface variables surface--prep for
                        blockmean
                        #
                   # ---Preprocessing data for SURFACE---
                        echo Preprocessing fission-track data...
                        blockmedian $txt_in_a -I0.5m `minmax $txt_in_a -I0.1` -V >
                        $prep_grid_a
                        blockmedian $txt_in_b -I0.5m `minmax $txt_in_b -I0.2` -V >
                        $prep_grid_b
                        echo done!
                   # ---Interpolation of data (in plane)---
                        echo Gridding -surface- fission-track data...
                        surface $prep_grid_a -I0.5m `minmax $txt_in_a -I0.1` -T0.5 -A0.965
                        -G$trend_grid_x
                        grdsample $trend_grid_x -T -G$trend_grid_a
                        # ---transforming grid: node to pixel registration ---
                        surface $prep_grid_b -I0.5m `minmax $txt_in_b -I0.2` -T0.5 -A0.965
                        -G$trend_grid_x
                        grdsample $trend_grid_x -T -G$trend_grid_b
                        # ---transforming grid: node to pixel registration---
                        echo done!
                        #
                else
                        # gridding with triangulate -- using remaining alternative for
                        option2 "-t "
                        out=/home/mat/gmt_work/ps/mozambique_ap_ft_ages_triangulate.ps
                        # output variables
                        echo Plotting basemap relief...
                        grdimage $grid -R$region -J$project$scale -I$grad_grid -C$cpt -Y15
                        -E150 -K -V > $out
                        # shaded topography image using intensity parameter of grad_grid
                        tria_grid_a=/home/mat/gmt_work/tmp/ft_age_tria_a.grd
```

```
                    # ---trendsurface variables triangulation---
                    tria_grid_b=/home/mat/gmt_work/tmp/ft_age_tria_b.grd
                    # ---trendsurface variables triangulation---
                    #
               # ---Triangulating data---
                    echo Gridding -triangulation- fission-track age data...
                    triangulate $txt_in_a `minmax $txt_in_a -I0.1` -J$project$scale -
                    I0.5m -F -G$tria_grid_a
                    triangulate $txt_in_b `minmax $txt_in_b -I0.2` -J$project$scale -
                    I0.5m -F -G$tria_grid_b
               # ---Postprocessing of data after triangulation (smoothing)---
                    echo Smoothing triangulated trendsurface...
                    grdfilter $tria_grid_a -D0 -Fc1 -G$trend_grid_a
                    grdfilter $tria_grid_b -D0 -Fc1 -G$trend_grid_b
                    echo done!
               fi
               #
          # ---Creating colour palatte of trendsurface---
               makecpt -Cseis -T50/180/10 -Z > $trend_cpt # adjust range manually
               #
          # ---Cutting sub-grid of shaded topography using dimensions of trendsuface---
               echo Cutting subgrid from shaded relief...
               grdcut /home/mat/gmt_work/grids/mozambique_shade.grd
               -G/home/mat/gmt_work/grids/mozambique_shade_sub_a.grd
               `minmax /home/mat/gmt_work/ap_age_a.txt -I0.1` # grdcut absolut path - ?
               grdcut /home/mat/gmt_work/grids/mozambique_shade.grd
               -G/home/mat/gmt_work/grids/mozambique_shade_sub_b.grd
               `minmax /home/mat/gmt_work/ap_age_b.txt -I0.2` # grdcut absolut path - ?
               #echo loop okay
fi
#
if [ "x$1" = "x-t" ]; then
        echo Titanite Fission Track....
               # ---Input variables---
               txt_in_a=/home/mat/gmt_work/tit_age_a.txt # eastern area - data file
               txt_in_b=/home/mat/gmt_work/tit_age_b.txt # western area - data file
               region=34/41/-18/-14 # total area dimension variables
               #
               if [ "x$2" = "x-s" ]; then # grdding with surface
                       out=/home/mat/gmt_work/ps/mozambique_tit_ft_ages_surface.ps
                       # output variables
                       echo Plotting basemap relief...
                       grdimage $grid -R$region -J$project$scale -I$grad_grid -C$cpt -Y15
                       -E150 -K -V > $out
                       # shaded topography image using intensity parameter of grad_grid
                       prep_grid_a=/home/mat/gmt_work/tmp/ft_age_prep_a.gmt
                       # ---trendsurface variables surface--prep for blockmean
                       #
                  # ---Preprocessing data for SURFACE---
                       echo Preprocessing fission-track data...
                       blockmedian $txt_in_a -I0.5m `minmax $txt_in_a -I0.1` -V >
                       $prep_grid_a
                       echo done!
                  # ---Interpolation of data (in plane)---
                       echo Gridding -surface- fission-track data...
                       surface $prep_grid_a -I0.5m `minmax $txt_in_a -I0.1` -T0.5 -A0.965
                       -G$trend_grid_x
                       grdsample $trend_grid_x -T -G$trend_grid_a
                       # ---transforming grid: node to pixel registration---
                       echo done!
                       #
               else
                       # gridding with triangulate -- using remaining alternative for
                       option2 "-t "
                       out=/home/mat/gmt_work/ps/mozambique_tit_ft_ages_triangulate.ps
                       # Output variables
                       echo Plotting basemap relief...
                       grdimage $grid -R$region -J$project$scale -I$grad_grid -C$cpt -Y15
                       -E150 -K -V > $out
                       # shaded
```

```
                    topography image using intensity parameter of grad_grid
                    tria_grid_a=/home/mat/gmt_work/tmp/ft_age_tria_a.grd
                    # ---trendsurface variables triangulation---
                    #
               # ---Triangulating data---
                    echo Gridding -triangulation- fission-track age data...
                    triangulate $txt_in_a `minmax $txt_in_a -I0.1` -J$project$scale
                    -I0.5m -F -G$tria_grid_a
               # ---Postprocessing of data after triangulation (smoothing)---
                    echo Smoothing triangulated trendsurface...
                    grdfilter $tria_grid_a -D0 -Fc1 -G$trend_grid_a

               fi
               #
          # ---Creating colour palatte of trendsurface---
               makecpt -Cseis -T200/380/10 -Z > $trend_cpt # adjust range manually
               #
          # ---Cutting sub-grid of shaded topography using dimensions of trendsuface---
               echo Cutting subgrid from shaded relief...
               grdcut /home/mat/gmt_work/grids/mozambique_shade.grd
               -G/home/mat/gmt_work/grids/mozambique_shade_sub_a.grd
               `minmax /home/mat/gmt_work/tit_age_a.txt -I0.1`
               # grdcut uses only absolute path - ?
               #echo loop okay
fi
#
#
# ---Plottin of trendsurfaces using intensity parameter of shaded topography---
echo Plotting trendsurfaces...
grdimage $trend_grid_a -J$project$scale -R$region -
I/home/mat/gmt_work/grids/mozambique_shade_sub_a.grd
-C/home/mat/gmt_work/cpt/trend_ft_age.cpt -K -O -V >> $out # grdimage akzeptiert nur
direkte Pfade - ?
if [ "x$1" == "x-a" ]; then
       grdimage $trend_grid_b -J$project$scale -R$region -I/home/mat/gmt_work/
       grids/mozambique_shade_sub_b.grd -C/home/mat/gmt_work/cpt/trend_ft_age.cpt -K -O
       -V >> $out
       # grdcut uses only absolute path - ?
fi
# grdimage $trend_grid_b -J$project$scale -R$region -I$grad_grid_sub_b -C$trend_cpt -K -
O -V >> $out
# obsolete - 2nd area only
#
# ---Plotting isolines of data distribution---
echo Plotting isolines of data distribution...
grdcontour $trend_grid_a -J$project$scale -R$region -C10 -A20 -K -O -V >> $out
if [ "x$1" == "x-a" ]; then
       grdcontour $trend_grid_b -J$project$scale -R$region -C20 -A20 -K -O -V >> $out
fi
#
# ---Plotting of sample locations---
echo Plotting sample locations...
psxy -R$region -J$project $txt_in_a -G0/0/0 -Sc0.15 -K -O -V >> $out
psxy -R$region -J$project $txt_in_b -G0/0/0 -Sc0.15 -K -O -V >> $out
#
# ---Plotting geography---
echo Plotting rivers, coastline...
pscoast -J$project$scale -R$region -Df -C50/100/150 -I1/3/50/100/150 -I2/2/50/100/150
-I3/1/50/100/150 -I4/1/50/100/150 -I5/1/50/100/150 -I6/1/50/100/150 -I8 -N1/2/0/0/0
-N3/1/0/0/0 -W0.25p -O -K -V >> $out
#
# ---Creating basemap---
echo Plotting color scale bar of topography
psscale -C$cpt -D6/-1/12/0.4h -I0.5 -B500g500":Elevation (m):" -K -O -V >> $out # scale
bar topography
echo Plotting color scale bar of trendsurface
if [ "x$1" == "x-a" ]; then
       psscale -C$trend_cpt -D6/-3/12/0.4h -I0.8 -B20g10":Apatite FT-Ages (Ma):" -K -O
       -V >> $out
       # scale bar trendsurface
```

```
else
        # remaining option is x-t
        psscale -C$trend_cpt -D6/-3/12/0.4h -I0.8 -B20g10":Titanite FT-Ages (Ma):" -K -O
        -V >> $out
        # scale bar trendsurface
fi
echo Plotting basemap...
if [ "x$1" == "x-a" ]; then
        psbasemap -J$project$scale -R$region -B1/1:."Distribution of Apatite FT-Ages": -O
        -V >> $out
        # map frame etc...; adjust image title manually
else
        psbasemap -J$project$scale -R$region -B1/1:."Distribution of Titanite FT-Ages":
        -O -V >> $out
        # map frame etc...; adjust image title manually
fi
#
# ---Cleaning up---
echo Cleaning up...
rm $grad_grid $grad_grid_a $grad_grid_b -v -f
rm $trend_grid_a $trend_grid_a $trend_grid_x $trend_cpt -v -f
rm $tria_grid_a $tria_grid_a $prep_grid_a $prep_grid_a -v -f
#
echo Restoring GMT defaults...
/bin/mv /home/mat/gmt_work/tmp/gmtdefaults$$ .gmtdefaults
rm /home/mat/work_gmt/tmp/gmtdefaults$$ -v -f
echo Finished !
```